Università Politecnica delle Marche

DOCTORAL THESIS

Self-assembled nanomaterials: an extended structural characterization of lipid nanoparticles and guanosine-based hydrogels

PhD student: Federica Carducci

Supervisor: Prof. Paolo Mariani

Department of Life and Environmental Sciences (DiSVA)

XXX cycle

Ancona, 2016-2017

Al mio papà, che è stato il primo a credere in me
e a mia madre, perché la sua forza è unica al mondo

Una corrente di eventi ha inizio dalla decisione, facendo sorgere a nostro favore ogni tipo di incidenti imprevedibili, incontri e assistenza materiale, che nessuno avrebbe sognato potessero venire in questo modo.
Tutto quello che puoi fare, o sognare di poter fare, incomincialo. Il coraggio ha in sé genio, potere e magia. Incomincia adesso.

[Wolfgang J. Goethe]

Declaration of Authorship

I, Federica Carducci, declare that this thesis titled "*Self-assembled nanomaterials: an extended structural characterization of lipid nanoparticles and guanosine-based hydrogels*" and the work presented it are my own and has been generated by me as the result of my own original research.

I confirm that:

- This work was done wholly or mainly while in candidature for a research degree at this University;
- where any part of this thesis has previously been submitted for a degree or any other qualification at the University or any other institution, this has been clearly stated;
- where I have consulted the published work of others, this is always clearly attributed;
- where I have quoted from the work of others, the source is always given. With the exception of such quotations, this thesis is entirely my own work;
- where the thesis is based on work done by myself jointly with others, I have made clear exactly what done by others and what I have contributed myself.
- parts of this work have been published in the following papers:

- Elisabetta Esposito, Maddalena Sguizzato, Markus Drechsler, Paolo Mariani, **Federica Carducci**, Claudio Nastruzzi, Rita Cortesi "**Data on Scaling up and in vivo human study of progesterone lipid nanoparticles**", Data in Brief 14 (**2017d**) 639-642

- Elisabetta Esposito, Maddalena Sguizzato, Markus Drechsler, Paolo Mariani, **Federica Carducci**, Claudio Nastruzzi, Rita Cortesi **"Progesterone lipid nanoparticles: Scaling up and in vivo human study",** Eur J Pharm Biopharm 119 (**2017c**) 437-446

- Elisabetta Esposito, Markus Drechsler, Paolo Mariani, **Federica Carducci**, Michela Servadio, Francesca Melancia, Patrizia Ratano, Partizia Campolongo, Viviana Trezza, Rita Cortesi, Claudio Nastruzzi **"Lipid nanoparticles for administration of poorly water soluble neuroactive drugs"***,* Biomed Microdevices (**2017b**) 19:44 DOI 10.1007/s10544-017-0188-x

- Rita Cortesi, Enrica Cappellozza, Markus Drechsler, Catia Contado, Anna Baldisserotto, Paolo Mariani, **Federica Carducci**, Alessandra Pecorelli, Elisabetta Esposito, Giuseppe Valacchi **"Monoolein aqueous dispersions as delivery system for quercetin"***,* Biomed Microdevices (**2017**) 19:41 DOI 10.1007/s10544-017-0185-0;

- Maddalena Sguizzato, Elisabetta Esposito, Markus Drechsler, Eleonora Gallerani, Riccardo Gavioli, Paolo Mariani, **Federica Carducci**, Rita Cortesi, Paola Bergamini "**Nafion®-Containing Solid Lipid Nanoparticles as a Tool for Anticancer Pt Delivery: Preliminary Studies**", *Hindawi Journal of Chemistry* (**2017b**)*,* DOI 10.1155/2017/3206298;

- Maddalena Sguizzato, Rita Cortesi, Eleonora Gallerani, Markus Drechsler, Lorenza Marvelli, Paolo Mariani, **Federica Carducci**, Riccardo Gavioli, Elisabetta Esposito, Paola Bergamini **"Solid lipid nanoparticles for the delivery of 1,3,5- triaza-7-phosphaadamantane (PTA) platinum (II) carboxylates"**, Mater Sci Eng C 74, (**2017a)**, 357-364;

- Elisabetta Esposito, Markus Drechsler, Paolo Mariani, Anna Maria Panico, Venera Cardile, Lucia Crascì, **Federica Carducci**, Adriana Carol Elena Graziano, Rita Cortesi, Carmelo Puglia **"Nanostructured lipid dispersions for topical administration of crocin, a potent antioxidant from saffron (Crocus sativus L.)"**, Mater Sci Eng C 71 (**2017a**), 669-677.

Signed.....

Date.....

Abstract

This thesis presents an extended work concerning the structural characterization of Drug Delivery Systems (DDS) made by lipidic nanoparticles and hydrogels based on DNA-derivatives. The link between these two completely different DDS is represented by the phenomenon of *self-assembly*, at the base of the formation of these extraordinarily versatile materials.

Self-assembly can be defined as the autonomous organization of components into patterns or structures, without the human intervention (Whitesides and Grzybowsky, Science, 2002). In the present case, and both for lipids and DNA-derivatives, the obtainment of complex supramolecular structures leads to the possibility to use these systems as powerful tools in the controlled delivery of drugs. For example, fundamental is the role played by lipidic nanoparticles in the delivery of anticancer drugs in which the biggest challenge is to avoid the unwanted side-effects and thus to develop always well-tolerated formulations.

In the first part of the thesis I present a thorough structural characterization of several nanoparticle systems tested to transport different antioxidants, anticancer drugs and other active principles. In the second part attention will be focused into hydrogels prepared by using guanosine derivatives. An almost completed characterization made by coupling macroscopical (e.g. microscopy observations, inverted-vial test) with microscopic techniques (e.g. Small-Angle X-ray Scattering and “classical” X-ray diffraction), lead us to move towards possible applications of these self-assembled hydrogels in the biological field, not yet explored for this specific kind of nanomaterials.

List of Abbreviations

DDS: Drug **D**elivery **S**ystems

EE: Encapsulation **E**fficiency

EM: **E**lectron **M**icroscopy

G: **G**uanosine

GMP: Guanosine 5'-**M**ono**P**hosphate

HPH: **H**igh-**P**ressure **H**omogenization

IEC: Ion-**E**xchange **C**hromatography

LC: Loading **C**apacity

LDC: Lipid **D**rug **C**onjugates

MAD: **M**onoolein **A**queous **D**ispersions

NLC: **N**anostructured **L**ipid **C**arriers

NLD: **N**anostructured **L**ipid **D**ispersions

NPs: **N**ano**P**article**s**

OM: Optical **M**icroscopy

PCS: Photon **C**orrelation **S**pectroscopy

SAFiN: Self-**A**ssembled **Fi**brillary **N**etwork

SAN: Self-**A**ssembled **N**anomaterials

SAS: Small-**A**ngle **S**cattering

SAXS: **S**mall **A**ngle **X**-ray **S**cattering

SLN: **S**olid **L**ipid **N**anoparticles

SWAXS: **S**mall- and **W**ide-**A**ngle **X**-ray **S**cattering

TAGs: Triacyl**G**licerol**s**

U: **U**ltrasonication

UH: Ultra**-H**omogenization

XRD: **X**-**R**ay **D**iffraction

Thesis organization

This thesis is organized into **9** chapters. **Chapter 1** provides at first an introduction to DDS, with an emphasis on lipid self-assembling nanoparticles. In the second part, I report basic principles about Lipid/Water polymorphism and phase identification using X-ray diffraction (a preamble about this extraordinary technique is given in "Material and Methods", Chapter 9). **Chapter 2** summarizes main results obtained considering different lipid nanoparticles. Each analysed system has been discussed in separated sections, focusing attention to the specific kind of nanoparticle used, active principle tested and method of production. In each section, as declared at the beginning of this thesis, reference to the published paper (if any) is always given. In **Chapter 3** a brief introduction about guanosine self-assembly and Lyotropic Liquid-Crystalline behavior is given. Details about the phase identification of columnar mesophases observed in such derivatives can be also found. **Chapter 4** introduces to guanosine-based hydrogels. Here, after a brief introduction, results about the macroscopical characterization can be found, together with the X-ray diffraction analysis of less-hydrated guanosine hydrogels. Results on fully hydrated hydrogels obtained by Small-Angle X-Ray Scattering are presented and discussed in **Chapter 5,** in which attention is focused on the analysis of circularly averaged 1D-profiles. Finally, in **Chapter 6**, a possible application of guanosine hydrogels is presented. **Chapter 7** summarizes results obtained on two different guanosine derivatives by osmotic stress measurements, performed in order to provide information on force effects on hydrogel formation and stability. **Chapter 8** provides conclusions and insights into the ongoing and future works concerning DDS and finally, in **Chapter 9,** can be found details about the sample preparation and experimental procedures.

Chapter 1

Chapter 1

Lipid nanoparticles

1.1 Introduction: The Drug Delivery revolution in science

Wanted to find a starting point in the development of controlled drug delivery systems, this can be the 1952, when Smith Kline & French developed the first sustained release formulation for 12-hour delivery of dextroamphetamine (Dexedrine). Many efforts have been done in the last two decades in the development of DDS, and now the next goal will be the third generation of DDS (Park, 2014). The necessity to develop homogeneous formulations of nanoparticles started a revolution in science. In DDSs and in general in *nanoscience,* self-assembled nanomaterials (SAN) occupy a special place. SAN can be defined as matter structured rationally at scale less than 100nm (Whitesides *et al.*, 2005) in which the nanoscale order is provided by the spontaneous assembly of biomolecules.

1.1.1 Nanoparticle-based Drug Delivery Systems (DDS)

A Nanoparticle-based drug delivery system is defined as a formulation or device of nanometric size, produced using lipids or natural and synthetic polymers, that enables the introduction of a therapeutic substance into the body. The process of drug delivery consists in the improvement of the efficacy and safety controlling the rate, time and place of release of drugs in the body. The prefix *nano-* in nanoparticles refers to solid or colloidal particles consisting of macromolecular substance that vary in dimensions from 10nm to 1000nm (Kreuter, 1994)

Nanoparticle-based DDS can be classified into two main typologies:

- produced using natural or synthetic polymers (e.g. poly- lactic acid, PLA or poly-lactide-co-glycolide, defined as PGLA) in which can be found Hydrogel-nanoparticles, Micelles and Liposomes (made in this case using amphiphilic copolymer), Nanomaterial formulations, Nanosystems, Nanocells, Dendrimers, Nanotubes, Polymersomes (block copolymer vesicles) and Quantum dots;

- Metal Nanoparticles (e.g. Iron-oxide Nanoparticles, Gold Nanoparticles, Nanoshells and Nanocages, Silver Nanoparticles, (Mody *et al.,* 2010));

- lipidic-based NPs produced using *homolipids*, lipids containing only carbon (C), hydrogen (H) and oxygen (O); *heterolipids*, containing nitrogen (N) and phosphorous (P) in addition to C, H, O and finally *complex lipids*, more complex lipids such as lipoproteins, phospholipids.

Nanoparticulate systems made using natural or synthetic polymers represent an alternative and exciting way to overcome limitations such the facilitation of transport of drugs across the Blood Brain Barrier (BBB). What remains a challenge is the precise characterization of molecular targets, ensuring the action of the drug only to the targeted organ (Singh and Lillard, 2009).

In this thesis, attention will be focused on Lipid-based nanoparticles.

In the second half of this dissertation, the almost completed structural characterization of guanosine hydrogels made using binary mixtures of guanosine (G) and guanosine 5'-monophosphate (GMP) will be presented and

widely discussed, together with the first tentative to approach them in the field of biological applications, starting from the study of interaction of those DNA-based systems with model proteins.

The first report on the potential use of hydrogels in medical science is probably due to Wichterle and Lim (Wichterle and Lim, 1960). A gel is a substance characterized by a continuous microscopic structure with macroscopic dimensions (Peters and Davis, 2016). The solid-like network (gel) has the ability to entrap and retain the solution, which analyzing gel constituents is the predominant (in weight, often accounting for > 97-99% of the material). When gels are made using organic solvents, those materials are referred to the so-called *organogel*, whereas gels formed with water are defined as *hydrogels*. A distinct classification can be made about gels: *physical* or "reversible" gels, in which the 3D-network is held by noncovalent interaction such as Van der Waals forces, hydrogen bonds and Coulombic interactions (Peters and Davis, 2016) and *chemical* or "permanent" gels, where the 3D network is constitute of covalent crosslinks.

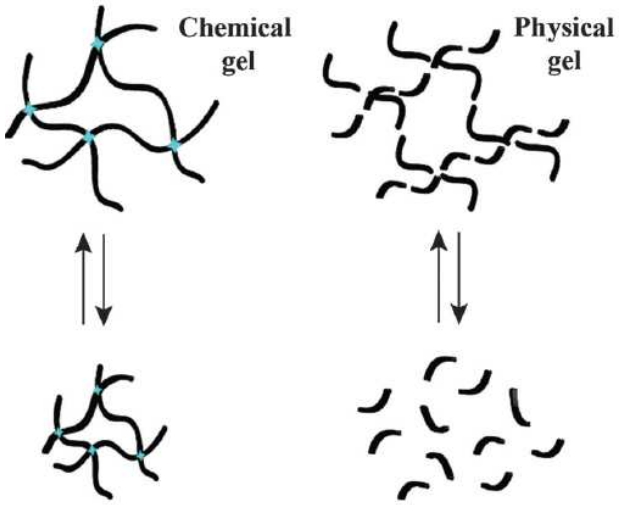

Figure 1.1 difference between chemical and physical gels. Figure taken form the paper of Peters and Davis, 2016 "Supramolecular gels made from nucleobase, nucleoside and nucleotide analogs"

Weak forces, at the base of the generation of the 3D-network of physical gels, confer to them the characteristic of *stimuli-responsiveness,* thus the ability to respond when exposed to variation of pH, temperature and pressure, ionic strength and enzymatic ability. A more detailed classification can be made in the case of physical gels, which are given by:

- simple entanglement systems, in which the network is held together by molecular entanglements or crystallites;
- ion-mediated or "ionotropic" networks, in which the network is stabilized by interaction between polyelectrolyte and multivalent ions of opposite charges (e.g. alginate);
- thermally induced networks, in which the heating (or the cooling) induces the structure formation;
- self-assembly process.

Thus, hydrogels can be made using:

- natural polymers (such as pectin (Yoshimura, 2005), cellulose (Navarra, 2015), agarose, alginate, carrageenan (Reis, 2008) etc…);

- synthetic polymers (PLA, PEG, PGLA, acrylates etc…);
- mixture of synthetic and natural polymers;
- DNA (Kahn *et al.*,2017; Bomboi *et al.,* 2016) and DNA derivatives (Peters *et al.,* 2015a; Peters *et al.,* 2015b; Adhikari *et al.,* 2014).

The spontaneous assembly at the base of the formation of the structure of lipid nanoparticles and DNA-based systems is what makes those compounds comparable.
The development of innovative supramolecular materials obtained by self-assembling of biomolecules is an extremely attractive field for nanotechnology.

1.2 Lipid Nanoparticles

Lipid nanoparticles drug delivery systems are an accepted, proven, commercially viable strategy to formulate pharmaceuticals for topical, oral, pulmonary or parenteral delivery (Attama *et al.*, 2012).
Tailoring lipid formulations, a very wide range of different drug delivery systems can be listed:

- Solid Lipid Nanoparticles (SLN);
- Nanostructured Lipid Carriers (NLC);
- Monoolein Aqueous Dispersions (MAD);
- Lipid drug conjugates (LDC)-nanoparticles;
- Liposomes;
- Transfersomes;
- Niosomes;
- Liquid Crystal Drug Delivery systems;
- Nanoemulsions.

During my PhD work, attention has been focused on the structural characterization of SLN and NLC and MAD. I report here a brief introduction and description of these systems.

1.2.1 Solid Lipid Nanoparticles (SLN)

Developed in 1990s as alternative carrier systems to the existing liposomes, SLN can be defined as a solid matrix nanodisperse phase of crystalline solid lipids (Esposito *et al.*, 2016) which can be composed of biocompatible lipids, well-tolerated when administered in vivo. One of the main advantage is the possibility to prepare SLN without using organic solvent. Other benefits are the modulation of the release of drug, the preservation of degradation of molecules and the enhancement of the specificity toward cells with the consequent increase of bioavailability of drug (Siekmann and Westesen, 1992; Muller *et al.*, 2000; Lippacher *et al.*, 2001) and the ability to incorporate lipophilic drugs. Major limitations are instead particle growth, gelation tendency, instability in terms of tendency of polymorphic transitions and low incorporation rate due to the crystalline structure of these NPs (Attama, 2008). The latter is probably the major limitation of SLN. Muller (Muller *et al.*, 2000) conducted many investigations to overcome this limitation developing NLC, defined by Esposito (Esposito *et al.*, 2016) as an improvement of SLN.

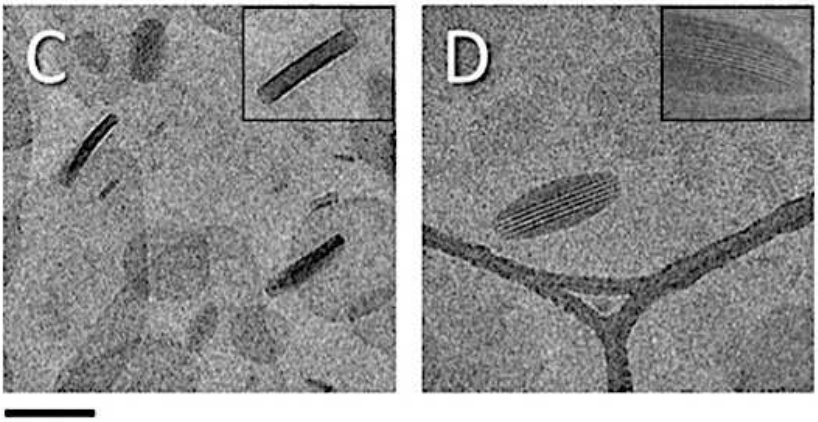

Figure 1.2 figures have been obtained using Cryo-TEM and taken from the paper "Progesterone lipid nanoparticles, scaling up and in vivo human study" (Esposito *et al.*, 2017) are showed empty-SLN (C) and empty-NLC (D). In this latter, in particular in microphotography, it is possible to observe bulges corresponding to the oil fraction typical of NLC composition. Bar corresponds to 150 nm

1.2.2 Nanostructured Lipid Carriers (NLC)

The main components of a NLC are a solid lipid matrix and a liquid lipid phase with a mean particle size in the nanometer range. The unique nanostructure of the lipid matrix (Muller *et al.*, 2000) makes these nanoparticles able to improve drug loading and firmly retain drug during storage. Examples of studies made using NLC are the topical administration of Retinol/Coenzym Q_{10} (Müller *et al.*, 2002; Pardeike *et al.*, 2009) or the parenteral route of administration of bromocriptine (Esposito *et al.*, 2008)

1.2.3 Monoolein Dispersions

Two different kinds of monoolein dispersions can be distinguished: the first one, Monoolein Aqueous Dispersions (MAD) can be defined as aqueous nanostructured dispersion of an amphiphilic lipid of complex lyotropic liquid crystalline phases (Cortesi *et al.*, 2017); monoolein is able to adopt different mesophases simply varying lipid and water concentration (see section 1.3). The nature of MAD dispersed phase is influenced by the type of emulsifier (Worle *et al.*, 2007). Poloxamer 407 copolymer is one of the most used emulsifier in the case of monoolein. This compound leads to aqueous solution composed by hexasomes, cubosomes ad vesicles (Gustafsson *et al.*, 1996**;** Larsson, 2000**;** Siekmann, 2002). The possibility to explore the monoolein:water phase diagram make those DDS able to incorporate poorly water-soluble drugs, enhancing encapsulation efficacy.

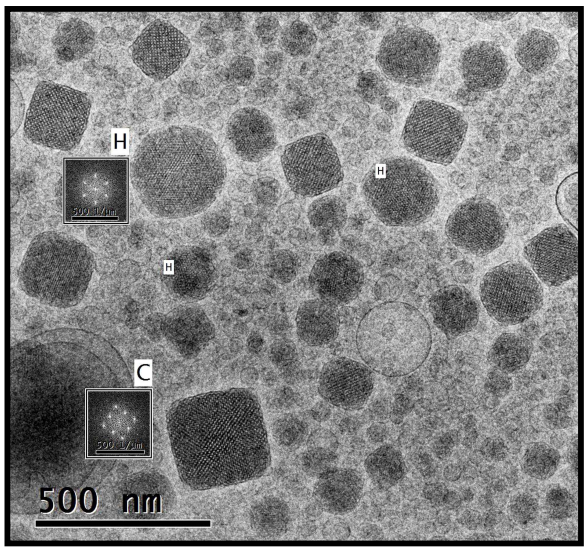

The second one, NLD, can be defined as Nanostructured Lipid Dispersions. A work has been published recently using those nanoparticles and *crocin* as active principle (Esposito *et al.*, 2017a) and it will be discussed widely in section 2.2. Nanostructured Lipid dispersion (NLD) is a particular kind of dispersion made using monoolein, together with sodium cholate and caseinate as stabilizing agents (Srinivasan *et al.*,1996; Jeongh *et al.*, 2014)

Figure 1.3 MAD observations using Cryo-TEM. Figure obtained from Markus Drechsler of the University of Bayreuth, Germany

1.3 Polymorphism of Lipid/Water Systems: a brief overview

Lipids can organize into a variety of structures (such as lamellar, hexagonal and cubic phase) due to their amphiphilic nature and thus to their Lyotropic Liquid Crystalline behavior.
Simply varying composition (concentration of emulsifier, kind of lipid) and temperature, a wide range of structures can be obtained.
This paragraph wants to give a brief description of different mesophases observable in lipid-water systems. In Figure 1.4 it is possible to appreciate how large is the number of lipid morphologies achievable simply varying the content of water and temperature, while in table 1.1 the structural and topological properties of the different lipidic phases have been summarized.

The first mesophase observed in a temperature-composition phase diagram (as the one reported in Figure 1.3) in the highly hydrated region is the *micellar* phase, constituted by spheres or ellipsoids, in which lipids are organized with polar heads kept in contact with aqueous medium and aliphatic chains direct within the core of micelle (note that in the less hydrated side of the phase diagram a second micellar phase, the *inverse micellar* phase, can be found, in which lipids organize exactly in the opposite way, with water inside the micelles and the hydrocarbon chains that form a continuous hydrocarbon moiety). Micelles form above a critical value of concentration, defined as *critical micelle concentration* (CMC). Below this value lipid molecules are presents as monomers, dimers and small aggregates. The addition of other lipidic molecules to micelle solution can't provoke the increase of number of monomers in solution but the formation of new micelles. Bile salts can form micelles, they play a key role because of their ability of incorporate in their cavity high quantity of lipids and of consequence cholesterol.
Lamellar phase is a 1D-lipid phase constituted of a bilayer (the same structure of biological membranes). Most of lipids are able to adopt this structure.
Considering 2D (two-dimensional) structure of lipid, *hexagonal phase* can be mentioned. In this case, long cylinders are localized at the vertex and the center of a hexagon with polar head directed in the aqueous medium and with hydrocarbon chains in the middle of the cylindrical structure (in Type *I,* direct). In Type *II* the orientation of lipids is inverted: as aforementioned for the micellar phase, in the inverted-hexagonal phase the way in which lipids organize is exactly the opposite of the *direct* one. Phases adopted by lipids can be related also to the geometry of lipid molecule itself (Micellar: conical configuration of lipid; Hexagonal (*I*, direct): truncated conical configuration; Lamellar: cylindrical; Hexagonal (*II*, inverse): inverted conical truncated. The organization of lipids in a cubic phase is more complicated. Bicontinuous cubic phase can be imagined as an interconnection of rods reciprocally intertwined and unconnected (Mariani *et al.,* 1988). Among the seven cubic phases so far identified in lipids, of greatest interest are the inverted bicontinuous cubic phases, where Q^{224} (*Pn3m*), Q^{230} (*Ia3d*) and Q^{229} (*Im3m*) can be mentioned. The bicontinuous phases can be imagined as the paradigm of the IPMS (Infinite Periodic Minimal Surface).
The Q^{224} (*Pn3m*) can be related to the diamond *D*-surface in which rods are tetrahedrally joined 4 by 4; Q^{229} (*Im3m*) 6 by 6, cubically, related to a IPMS gyroid *G*-surface and finally the coplanarly joined 3 by 3, related to a primitive *P*-surface Q^{230} (*Ia3d*) (Esposito *et al.*, 2016). As showed in Table 2 *Ia3d* can be found both in type *I* and *II*.

Table 1.1 structural and topological properties of some of the lipidic phases

PHASE	STRUCTURAL UNIT	CLASS	TYPE
***Lamellar* (1D)**	Lamellae	-	-
***Hexagonal* (2D)**	Infinite long rods	Rod-like	*I* (direct) or *II* (inverse)
***Cubic P4$_3$32* (3D)**	Rod network and micelles	Mixed rod-like and micellar	*II*
***Cubic Pm3n* (3D)**	Micelles	Micellar	*I*
***Cubic Pn3m* (3D)**	Interwined rod networks	Bicontinous	*II*
***Cubic Fd3m* (3D)**	Micelles	Micellar	*II*
***Cubic Im3m* (3D)**	Interwined rod networks	Bicontinous	*II*
***Cubic Ia3d* (3D)**	Interwined rod networks	Bicontinous	*I* or *II*

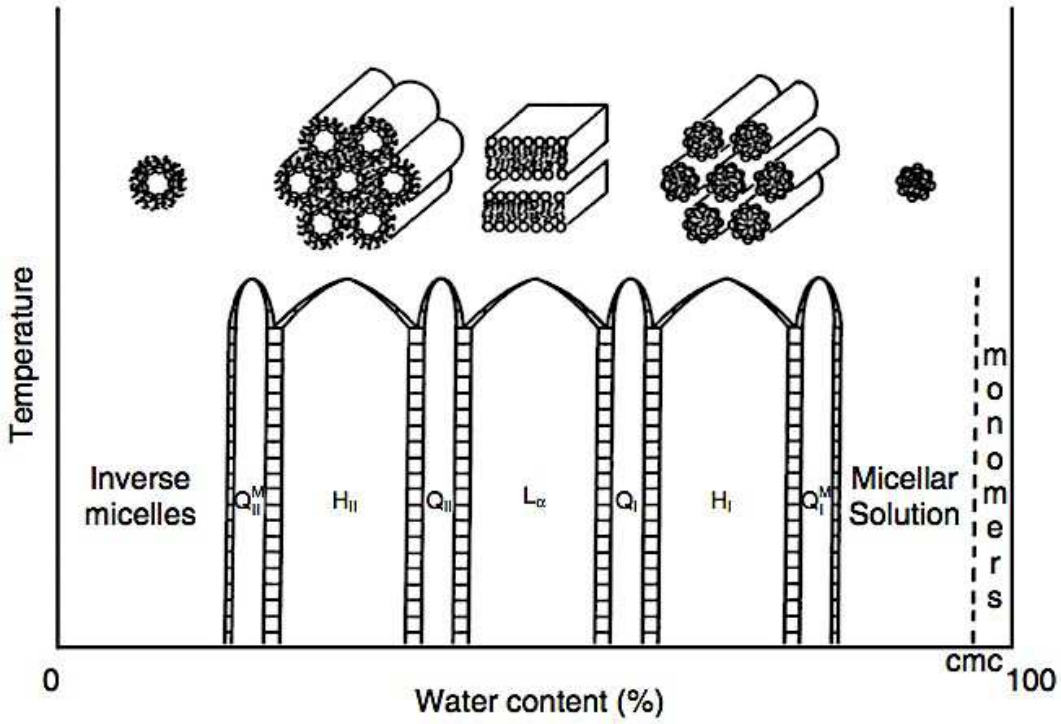

Figure 1.4 theoretical lyotropic lipid-water phase diagram for phospholipid

Figure 1.5 examples of various lipid phases **I**: different types of gel (A) subgel, L_c; (B) gel, untilted chains, L_β; (C) gel, tilted chains L_β; (D) rippled gel, P_β'; (E) fully interdigitated gel L_β^{int}; (F) partially interdigitated gel; (G) mixed interdigitated gel; (H) liquid crystalline, L_α. **II** Liquid crystalline morphologies: (A) spherical micelles; (B) cylindrical micelles (tubules); (C) disks; (D) inverted micelles; (E) part of a rhombohedral phase; (F) lamellae; (G) inverted hexagonal phase; (H) inverted micellare cubic; (J) bilayer cubic Im3m phase; (K) bilayer cubic Pn3m phase; (L) bilayer cubic Ia3d phase. (Figure taken from "*Lipid, Phase Transitions of*", Rumiana Koynova and Boris Tenchov, 2008)

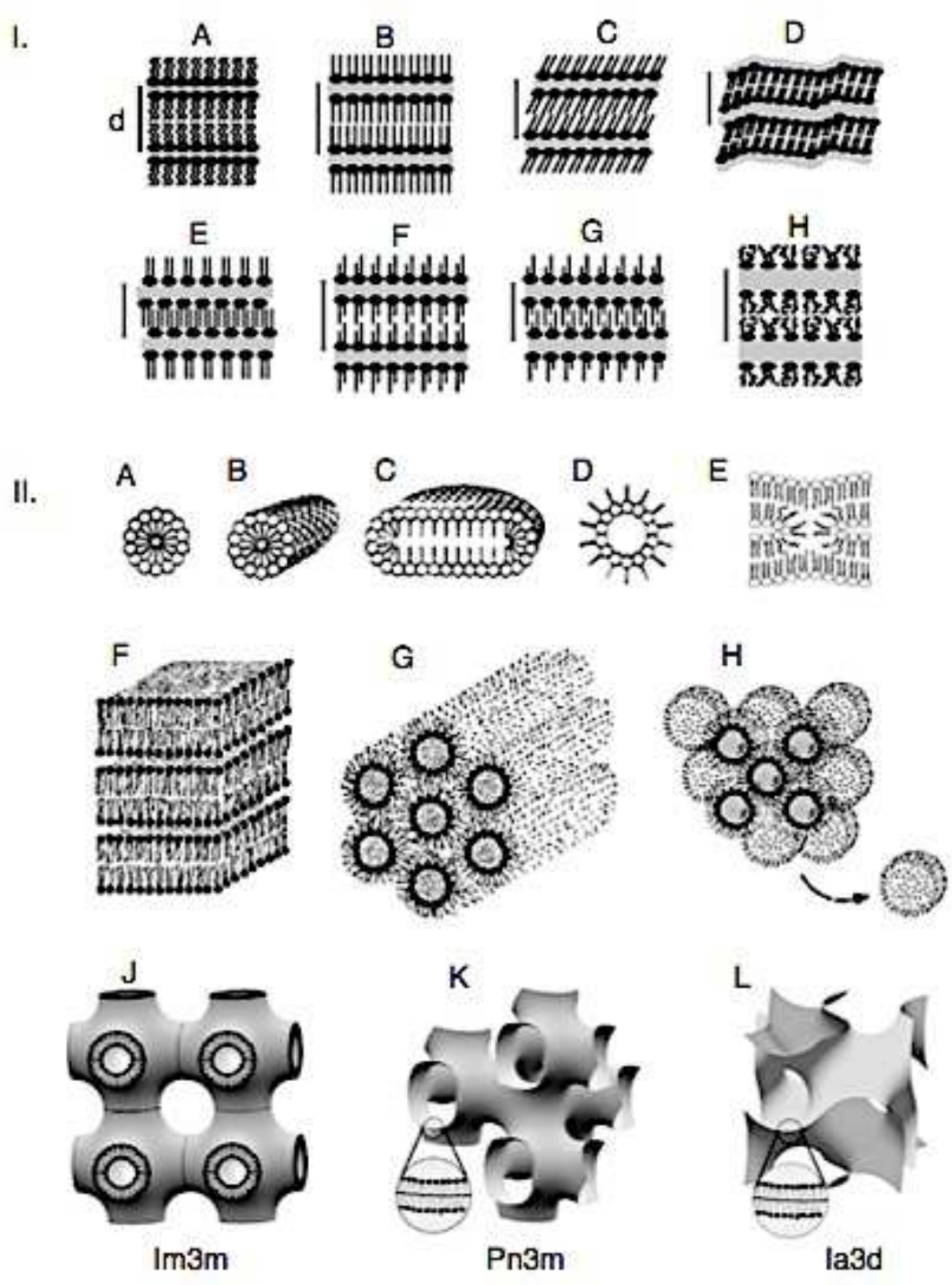

1.4 Structural characterization using X-Ray Diffraction (XRD)

Structural characterization of lipid and DNA derivatives polymorphism can be made using both X-Ray Diffraction (XRD) and Polarized-light Optical Microscopy (POM), fundamental techniques to provide details about shape, inner organization and distribution of dispersions. Before starting to examine in depth results obtained for each kind of nanomaterial tested, is necessary to give a brief overview about the theory at the base of phase identification, considering each kind of investigated systems. A brief introduction to XRD can be found in Chapter 9, section 9.3.

In our laboratory, XRD measurements have been performed without previous filtration, using a 3.5 kW Philips PW 1830 X-ray generator (Amsterdam, The Netherlands) equipped with a Guinier-type focusing camera (homemade design and construction, Ancona, Italy) operating with a bent quartz crystal monochromator (λ= 1.54Å).
Diffraction patterns are recorded on GNR Analytical Instruments Imaging Plate system (Novara, Italy). Samples were held in a tight vacuum cylindrical cell provided with thin mylar windows. Diffraction data have been collected at room temperature (25°C), using a Haake F3 thermostat (ThermoHaake, Karlsruhe, Germany) with an accuracy of 0.1°C.

Further measurements have been made at:

- Elettra Synchrotron (Basovizza, Trieste), the national synchrotron radiation facility, using a SWAXS setup, a wavelength (λ) of 1.54Å and a q range comprised between $0.01< q< 0.6Å^{-1}$;
- European Synchrotron Radiation Facility (ESRF-Grenoble, France). In this case the wavelength λ used has been of 0.99Å, using and a q range between $0.01< q< 0.5Å^{-1}$.

1.5 Phase identification of lipid-water systems

The spacing of the Bragg peaks detected in the low-angle X-ray diffraction region ($q< 0.6Å^{-1}$), being q the modulus of the scattering vector defined by $q = 4\pi \sin\theta/\lambda$, where 2θ is the scattering angle) has been measured and peak indexing performed considering different symmetries commonly observed in lipid phases. To explain how the data treatment relative to samples measured using X-ray diffraction has been made, is necessary to consider diffraction profile in two distinct regions: the *low-angle* region ($q=0.01\text{-}0.6Å^{-1}$) and the *wide-angle* region ($0.6\text{-}2.0Å^{-1}$), see Figure 1.5
Peak indexing has been made using the software IgorPRO®. Reciprocal spacing of the Braggs reflections can be calculated using different equations.
For the 1D lamellar phase only one indice, *h*, of the three Miller indices *h*, *k*, *l* can be defined. The related equation for this phase is $Q_{h00} = 2\pi\left(\frac{h}{d}\right)$ where d is the d spacing and *h*=1,2,3… and of consequence peak ratio will be 1: 2: 3: 4 … .
The relevant equation for 2D dimensional organization (hexagonal phase) is given definying the two Miller indices *h* and *k* and is $Q_{hk0} = 4\pi\frac{\sqrt{(h^2+k^2-hk)}}{(a\sqrt{3})}$ with *h,k*=1,2,3… . The ratio between peaks in this case will be $1: \sqrt{3}: \sqrt{4}: \sqrt{7}: \sqrt{9}$. Finally, for the 3D cubic mesophase, *h,k,l* can be defined. In this case the relative equation is $Q_{hkl} = 2\pi\frac{\sqrt{(h^2+k^2-l^2)}}{a}$ and of consequence peak positions $1: \sqrt{2}: \sqrt{3}: \sqrt{4}: \sqrt{5}$ … .

Using the appropriate equation, the lattice and related unit cell value can be derived and consequently phase diagram can be determined. A theoretical phase diagram has been reported in Figure 1.3.

Table 1.2 equations relative to the reciprocal spacing of Bragg's reflections for a 1D-lamellar, 2D-hexagonal and 3D-cubic phases

phase symmetry	equation	peak ratio
1D-lamellar	$Q_{h00} = 2\pi\left(\frac{h}{d}\right)$, with *h* = 1,2,3,…	1, 2, 3, 4, …
2D-hexagonal	$Q_{hk0} = 4\pi\frac{\sqrt{(h^2+k^2-hk)}}{(a\sqrt{3})}$ with *h,k* = 1,2,3,…	1, √3, √4, √7, √9, …
3D-cubic	$Q_{hkl} = 2\pi\frac{\sqrt{(h^2+k^2-l^2)}}{a}$ with *h,k,l* = 1,2,3,…	1, √2, √3, √4, √5, …

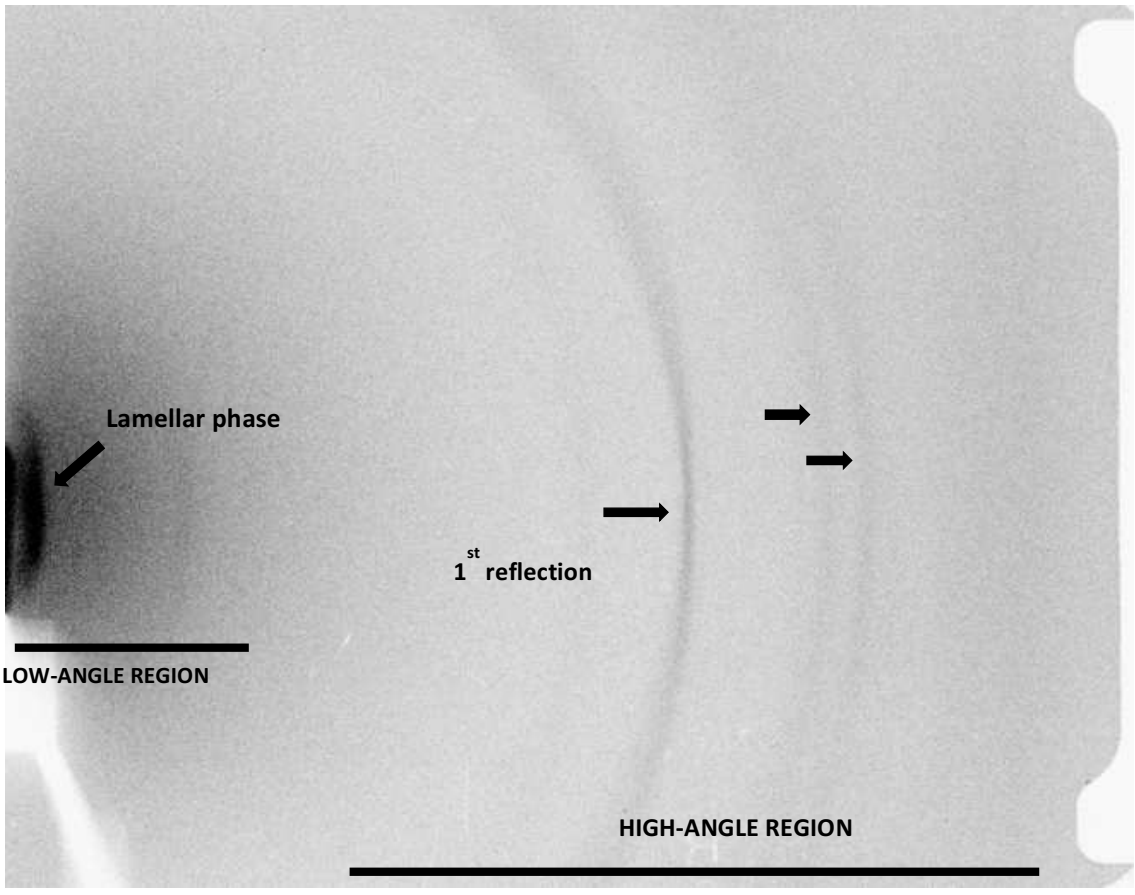

Figure 1.6 definition of the low- and the high-angle region of diffraction in a typical XRD profile obtained for nanoparticles

1.6 Determination of the subcrystalline structure of lipidic phase

Long-chain compounds, such as fatty acids and their esters, may exist in different crystals forms. Crystalllization, in the case of oil and fats, occurs in a spontaneous way, e.g. in TAGs the formation of physical or chemical links between the triacylglycerol molecules lead to a total or partial restriction of movement and of consequence to the formation of crystals, (Kawamura, 1979) characterized by the packing of molecules in a fixed pattern, defined as *lattice*. The structural complexity of these compounds justify the possibility to found different kind of molecule arrangements (polymorphism). In material science, a polymorph can be thought as a solid that can be described in more than one crystal forms (Domingues *et al.,* 2015). Morphology describes how the set of the faces determines the regular structure in which crystal is defined. In fats, crystal are solids with atoms arranged in a three-dimensional pattern.
The unit cell is the repeating unit that makes up the complete structure of a crystal. The sub-cell, in turn, is the smallest structure in the real unit of the cell, defined by the transverse packing of aliphatic chains in the long-chain compounds. The polymorphism of these compounds (and in our case of lipids used in the production of nanoparticles) is defined by the sub-cell structure (Boistelle, 1988).

Considering measurements made about nanoparticles (results will be disccused widely in the next chapter), attention has to be focused to reflections in the wide-angle region of the X-ray diffraction images acquired, that is related to atomic distance.
The analysis of the position given in q, the scattering vector, in $Å^{-1}$, enabled us to determine the sub-cellular organization of lipids in the nanoparticles.
In lipids, three are the different kinds of sub-cell structures that predominate: the α, β and the β' forms. The α is related to the metastable hexagonal chain packing, the β to the triclinic parallel organization (with the higher stability) and finally the β' to the intermediate orthorhombic perpendicular packing. The increase of stability and of consequence of melting point is in that order $\alpha \rightarrow \beta' \rightarrow \beta$ (Figure 1.7).

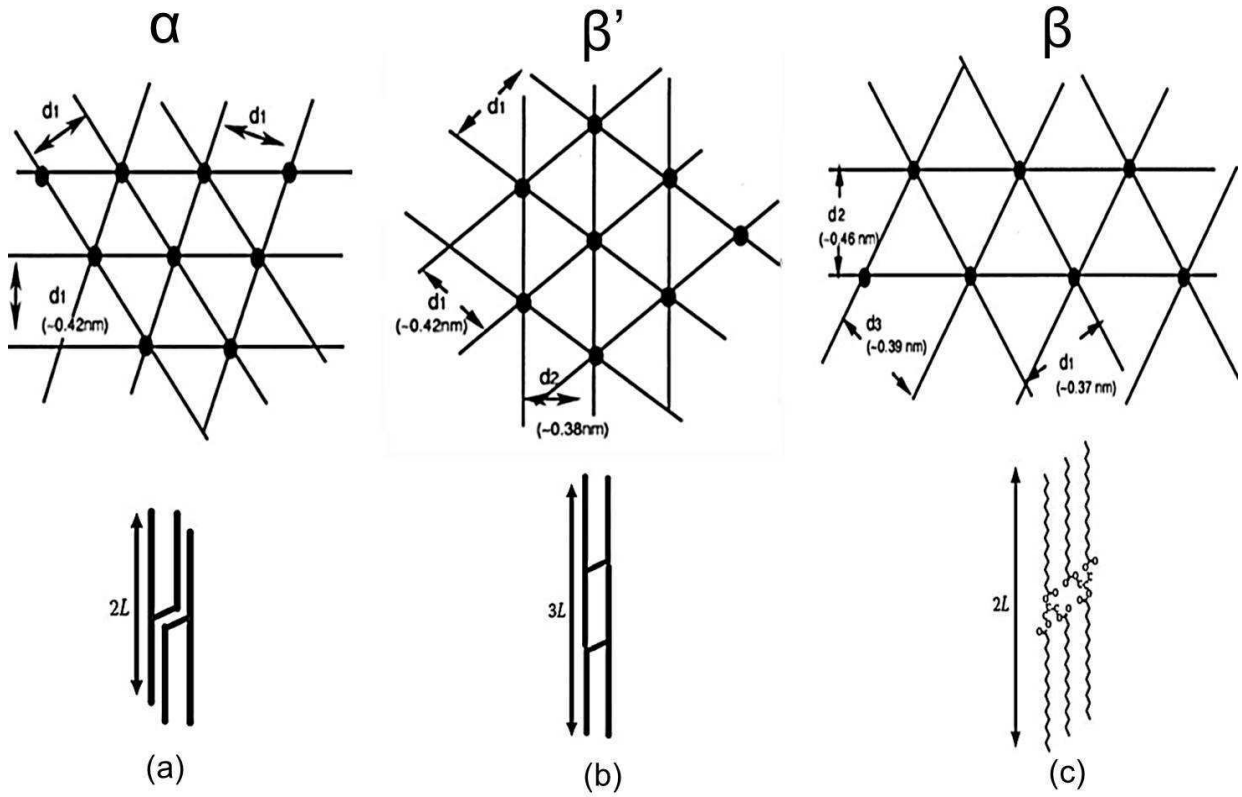

Figure 1.7 polymorphism in crystalline forms (a) α hexagonal metastable form (b) intermediate β' orthorhombic perpendicular packing (c) β triclinic parallel, the most stable form. Here is reported the spatial projections of crystalline form for long-chain compounds. The figure has been taken from the Advances in Lipids Crystallization Technology 111 http://dx.doi.org/10.5772/59767, Chapter 5, Domingues *et al.,*2015.

The determination of sub-cellular structure assumed by lipids in NPs formulations represent an additional information about the stability of nanoparticles, due to the inner organization of lipid chains.

Considering the field of industrial processing of food products, oil and fats crystallization is probably the biggest limitation that can be found. The different composition of TAGs determines the physical properties of oil and fats. The formation of crystals (also related to climatic differences between countries and long distances transport of foods) influences structure, flavor, stability, storage quality and visual characteristics of foods (O'Brien, 2008).

Thus, X-ray diffraction technique provides a unique tool to identify the polymorphism of crystals by determining the dimensions of the crystalline unit- and sub-cell, analyzing the wide-angle region of diffraction profile.

Chapter 2

Chapter 2

Structural characterization of NPs: case studies

2.1 Introduction

A very important part of the work made during my PhD thesis concerned the structural characterization of lipid nanoparticles, which are gaining an ever-growing interest as novel drug carriers. Lipid systems and dispersions have been widely studied in the last 40 years (Luzzati *et al.*,1968; Luzzati *et al.*,1997; Yeagle, 2010). The capability of lipids to organize in suprastructures is due first to their amphiphilic nature: this unique characteristics makes those biomolecules able to segregate in water their polar and paraffinic moieties into distinct regions, which they will define a periodically ordered *long-range* organization of the structural elements (in 1 dimension, up to 3) combined with an highly disordered *short-range* conformation of hydrocarbon chains; second, a key role is done by the interplay of different parameters such concentration of water and temperature, and by the nature of lipid itself in terms of molecular structure and shape (chain length, branching and unsaturation, backbone and head group structure).

Four have been the main lipid nanoparticles characterized (a brief description has been made in the previous Chapter 1, section 1.2.1-3): **SLN (**Solid Lipid Nanoparticles), a colloidal lipid emulsions and solid matrix nanoparticle, **NLC** (Nanostructured Lipid Carriers) defined as *second generation* SLN by Esposito (Esposito *et al.*, 2016), composed of a solid lipid matrix and a liquid lipid phase, **MAD** (Monoolein Aqueous Dispersions) that can be defined as dispersions of an amphiphilic lipid in water and finally **NLD** (Nanostructured Lipid Dispersions), a particular kind of dispersions made using monoolein, together with sodium cholate and caseinate as stabilizing agents. MAD can be made taking advantage of the complex and unique Lyotropic Liquid Crystalline behavior of this magic lipid.

In the following chapter, results obtained about structural characterization of nanoparticles are presented. Measurements have been made using XRD, together with POM. Results obtained using other techniques, together with details about sample preparation, have been added in the discussion of XRD/POM results to give an exhaustive comprehension of each work made. In every section is clearly declared what has been done by others.

2.2 Characterization of Nanostructured Lipid Dispersion (NLD)

2.2.1 Lipid nanoparticles for the delivery of *crocin* (*Crocus sativus L.*)

The majority of this section is published in the reference Esposito *et al.,* 2017a
(Esposito E., M. Drechsler, P. Mariani, A. M. Panico, V. Cardile, L. Crascì, F. Carducci, A. C. E. Graziano, R. Cortesi, C. Puglia*, Mater. Sci. Eng. C*, **2017a**, 669-677)

Has to be underlined that I made the structural characterization using X-ray diffraction of NLD. The preparation of samples has been made by the group of the University of Ferrara, Department of Life Sciences and Biotechnologies. Observations using Cryo-TEM has been made by Markus Drechsler of the University of Bayreuth and biological experiments by the groups of the University of Catania, Departments of Drug Sciences and Biomedical Sciences.

Crocin (CRO), in addition to *safranal*, is one of the most relevant biological constituents of saffron. These compounds show an important antioxidant and anticancer activity in vitro.
However, *crocin* is characterized by unfavorable physicochemical features that make easier its degradation. In the work presented here and published in the paper of Esposito (Esposito *et al.*, 2017a) the preparation, structural characterization and biological aspect in the use of nanostructured lipid dispersions as drug delivery systems are presented, with the aim to highlight that NLD can provide a useful system to control the rate of CRO diffusion through the skin and the photodegradation of this active principle.
In table 2.1 has been summarized the composition of NLD and structural organization obtained by X-ray diffraction experiments.

Table 2.1 composition of NLD and structural organization obtained by X-ray diffraction experiments on NLD

Sample	Composition (% w/w)					Unit Cell Value (*a*), ± 1Å	Morphology
	Monoolein	Sodium Cholate	Sodium Caseinate	Water	Crocin (CRO)		
Empty NLD-A	4.50	0.15	-	95.35	-	153.4 (Cubic 229)	Cubosome
Empty NLD-B	4.50	0.15	0.07	95.28	-	151.7 (Cubic 229)	Cubosome
NLD-A	4.50	0.15	-	95.25	0.1	148.3 (Cubic 229)	Cubosome
NLD-B	4.50	0.15	0.07	95.18	0.1	56.9 (Hexagonal)	Hexasome

NLD have been prepared by the group of Ferrara, using mixtures of monoolein with sodium cholate and sodium caseinate. To give a brief summary of results obtained, the presence of naturally derived materials as sodium cholate and caseinate lead to:

- **NLD-A**: transparent dispersions
- **NLD-B**: milky dispersions

The addition of CRO confers a characteristic yellow coloration. In both cases, the presence of CRO leads to an increase of the mean diameter. Photon Correlation Spectroscopy (PCS) enabled to check the Z average diameter of nanoparticles, which is between 150 and 250 nm. In addition:

- EE (Encapsulation Efficiency) and LC (Loading Capacity) have been evaluated.

EE value is higher in NLD-B, probably the heterogeneous inner structure of nanoparticles facilitates the encapsulation of CRO. The use of mixtures of sodium cholate and caseinate, together with monoolein, lead to the formation of a most heterogeneous system (composed of cubic phases, uni-lamellar, bi-lamellar, invaginated vesicles and sponge-like structures).

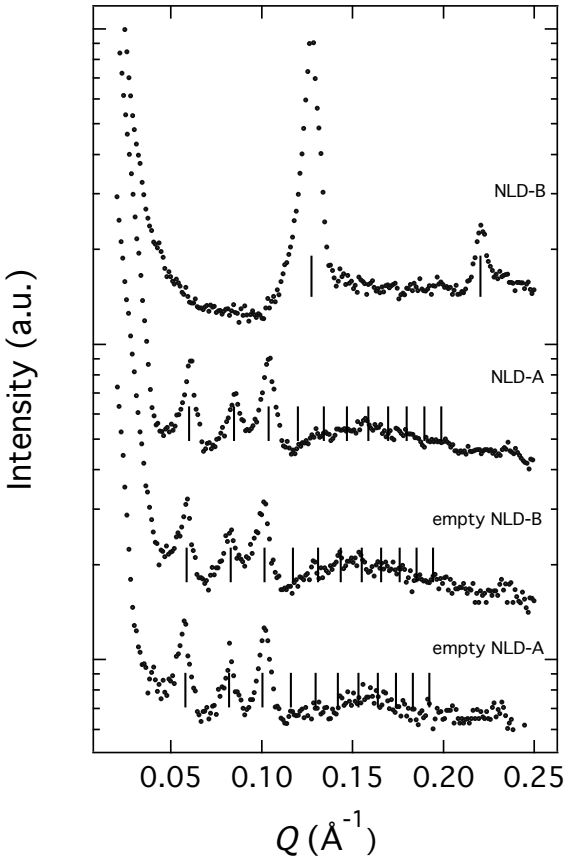

Figure 2.1 X-ray diffraction profiles observed on NLD before filtration. From the bottom: **empty NLD-A**, **empty NLD-B**, **NLD-A** and **NLD-B**. The vertical black lines indicate the expected peak positions: Im3m, spacing ratios as √2:√4:√6:√8:√10:√12…; H_{II}, spacing ratios as √1:√3:√4… q=4π sinθ/λ, where 2θ is the scattering angle

- MTT assay performed on Melanoma Human Cell line A375 cultured in DMEM (Dulbecco's Modified Eagle's Medium) shows an antiproliferative activity of this compound (respectively 86+2% in NLD-A and 90+1% in NLD-B). Empty and CRO-loaded vesicles do not interfere with cell viability in human fibroblasts, used as model of normal cells.

Using X-ray diffraction (without previous filtration) inner structural organization of NLD has been investigated, both in presence and absence of CRO. Considering NLD-A, the presence of the cubic 229 (*Im3m*) has been observed in both cases. The addition of CRO doesn't provoke modifications in terms of morphology. Different is the case of NLD-B: the presence of CRO induces a transition from cubosome to hexasome morphology of NPs. An additional confirmation of the inner phase transition has been given by the PCS (Photon Correlation Spectroscopy) measurements: in the case of NLD-B a decrease in the mean diameter of NPs has been reported, in line with the transition from cubic phase 229 to a hexagonal phase.

The use of NLD (in this case produced with naturally derived compound instead of copolymers such Pluronic 127®) represents a new strategy in the case of the delivery of *crocin*. An increase in terms of NLD lifetime stability, together with a successful prevention of degradation (which are the major limit for therapeutic application of this bioactive molecule) have been achieved.

2.3 Characterization of Solid Lipid Nanoparticles (SLN) and Nanostructured Lipid Carriers (NLC)

2.3.1 Functionalization of nanoparticles with 1,3,5-triaza-7-phosphaadamantane (PTA) platinum (II) carboxylates: a structural study

The majority of this section is published in the reference Sguizzato *et al.,* 2016
(Sguizzato M., R. Cortesi, E. Gallerani, M. Drechsler, L. Marvelli, P. Mariani, F. Carducci, R. Gavioli, E. Esposito, P. Bergamini *Mater. Sci. Eng., C*, 357-364, **2016**)

For clarity has to be remarked that I performed the structural characterization using X-ray diffraction of SLN. The preparation of samples has been made by the group of the University of Ferrara, Department of Life Sciences and Biotechnologies; the synthesis of Pt-PTA and other assays by the group of the University of Ferrara, Department of Chemical and Pharmaceutical Sciences. Observations using Cryo-TEM has been made by Markus Drechsler of the University of Bayreuth.

A new way to functionalize SLN with Pt-PTA complexes is presented in this work. Stearic acid based-SLN seems to be a promising route for the delivery of PTA, after an initial screening of several fatty acid (oleic acid, palmitic acid, castor oil, myristic acid and stearic acid) made by the group of the University of Ferrara (Department of Life Sciences and Biotechnology).
A scheme of the chemical approach used to functionalize stearic based SLN with Pt-PTA is reported here: taking advantage of the presence of carboxylic groups on the surface of SLN, these can be first deprotonated and then coordinated to Platinum-PTA complexes as carboxylates. This part has been made by the other group of Ferrara (Department of Chemical and Pharmaceutical Sciences). The formation of the complex has been proved using ^{31}P-NMR.

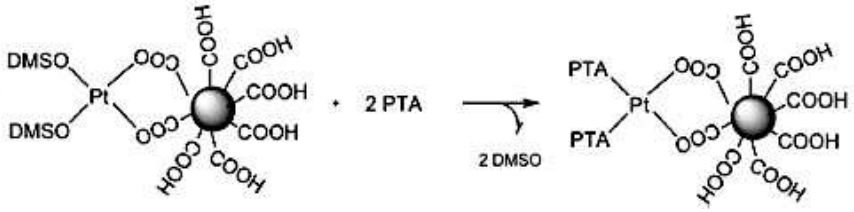

Figure 2.2 formation of Pt carboxylates on the surface of SLN. Figure has been taken from the paper *Sguizzato et al., 2016*

SLN have been produced using the emulsion-dilution method. This approach leads, in the case of stearic-acid based NPs, to the formation of a solution of vesicles characterized by great stability (up to 2 months) and homogenous aspect (in absence of aggregates and flocculates). PCS measurements show a Z-average value comprised between 600 and 800nm. The polydispersity index is between 0.21 and 0.41nm. Results obtained using X-ray diffraction are reported in the following table.

Table 2.2 composition of SLN and structural organization obtained by X-ray diffraction

Samples	Composition (%w/w)					Unit Cell Value (*a*) ± 1 Å	Morphology
	Stearic acid	Tween® 20	Tween® 80	Water	PTA		
SLN T20	2	3.34	-	94.66	-	42.7	Lamellar
SLN T80	2	-	3.34	94.66	-	41.8	Lamellar

This work provides a demonstration of the fact that the use of a different kind of polysorbate is not relevant, considering NPs morphology. In this case SLN have been produced using T20 and T80 (ST20 produced with Tween® 20 and ST80 with Tween® 80). For both SLN two low-intensity Bragg's peaks have been detected.

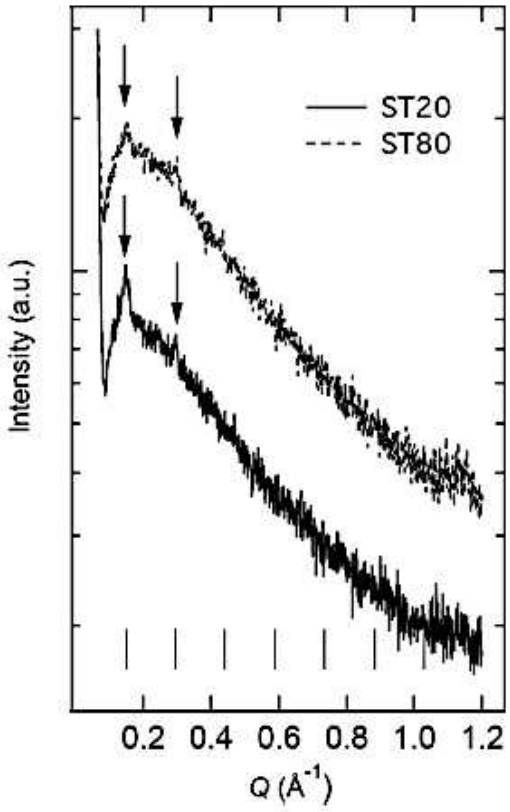

Figure 2.3 X-ray diffraction profiles of SLN T20 (ST20) and SLN T80 (ST80). $Q = 4\pi\sin\theta/\lambda$, where 2θ is the scattering angle

The determination of the inner structure of Solid Lipid Nanoparticles has been made indexing the two major peaks. Reflections have been calculated to be in a ratio 1:2 so the inner structure of nanoparticles can be attributed to a 1-dimensional lamellar phase. The distance between the mid-plane of two opposing lipid bilayers has been calculated using Bragg's Law and it's 42.7Å for ST20 and 41.8Å for ST80. The practically similar value of unit cell and X-ray profile confirm that the inner structure is lamellar for both SLN.

In addition to the structural characterization, analysis on the potential antiproliferative activity of Pt-PTA have been made by the group of Ferrara (department of Life Sciences and Biotechnology), using two different cancer cell lines: A2780 (ovarian) and K562 (erythroleukemic). ST20 and ST80 show no toxicity towards the two cell lines and considering the in vitro antiproliferative effect of ST20 and 80 containing Pt-PTA complexes cell growth inhibition is comparable of that of Cisplatin. These results confirm the promising use of Pt-PTA functionalized SLN as anticancer drugs with the advantage of reduced side-effects, very heavy in the case of Cisplatin (first generation of Pt-based anticancer drugs).

2.3.2 Nafion® containing SLN as Tool for Anticancer Pt delivery

The majority of this section is published in the reference Sguizzato *et al.,* 2017
(Sguizzato M., E. Esposito, M. Drechsler, E. Gallerani, R. Gavioli, P. Mariani, F. Carducci, R. Cortesi, P. Bergamini, *Hindawi Journal of Chemistry,* DOI 10.1155/2017/3206298, 2017)

Has to be remarked that I performed the structural characterization using X-ray diffraction of SLN. The preparation of samples has been made by the group of the University of Ferrara, Department of Life Sciences and Biotechnologies and observations using Cryo-TEM has been made by Markus Drechsler of the University of Bayreuth.

As alternative to the stearic acid based SLN for the coordination of Pt-PTA complexes, in this work has been proposed in this work the use of Nafion®, a perfluorosulfonic acid resin. In this case Nafion® has been used to establish an ionic connection with the protonable phosphine PTA (1,3,5-triaza-7-phosphaadamantane), applicable in the case of Pt coordination.
What plays an essential role is the fact that Nafion® is a strong proton donor and PTA is characterized by proton acceptor nitrogen atoms. The fact that NAF/PTAH$^+$ complexes are able to maintain the ability to coordinate Pt via phosphorus group (demonstrated using ^{31}P-NMR) makes these compounds optimal candidates for the coordination of Pt as anticancer drug.

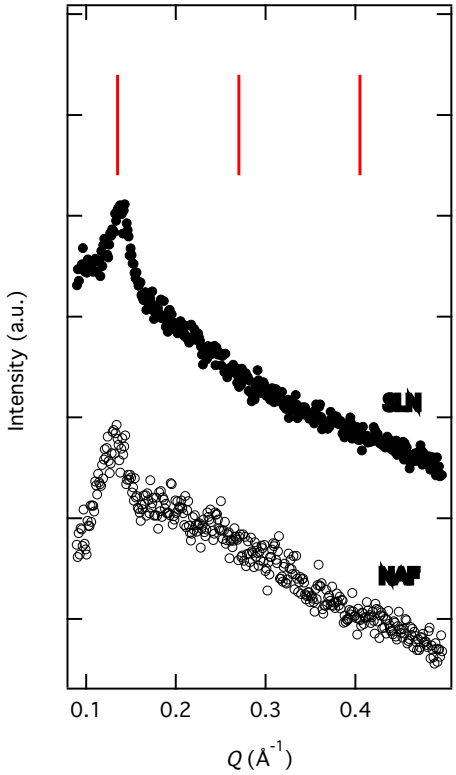

Figure 2.4 X-ray diffraction profiles observed for nanoparticles dispersions without (black dots) and with NAF (white dots) at 37°C. Red lines indicate positions of reflections expected for a 1D lamellar phase. The presence of a lamellar phase organization of nanoparticles for both samples is observable. In the case of SLN-NAF the second order of a lamellar phase can be appreciated (at very low intensity value) confirming the higher inner organization of NPs

Table 2.3 composition of SLN and structural organization obtained by X-ray diffraction

Samples	Composition (%w/w)					Unit Cell Value (*a*) ± 1Å	Morphology
	Tristearin	Poloxamer 188	Nafion®	Water	Pt		
SLN	3.35	2.50	-	94.15	-	46.0	Lamellar
SLN NAF	3.35	2.50	1.65	92.15	-	49.0	Lamellar

The production of solid lipid nanoparticles has been made by the group of Ferrara, using the method of homogenization stirring followed by ultrasonication. In table 2.3 details about the composition and structural organization have been summarized. This process leads to a white milky emulsion, with a uniform macroscopic appearance (absence of aggregates and adherence to the vial's walls). SLN-Nafion have been proved to be stable within 90 days. For the structural characterization Cryo-TEM, PCS and X-ray diffraction measurements have been performed. Electron microscopy (EM) shows a discoid shape particles; PCS gave a Z-average value of 250nm with a polydispersity index comprised between 0.202 and 0.235. Using X-Ray diffraction, characterization in terms of morphology formulations made both in the presence and absence of Nafion® has been made. Figure 2.4 shows results obtained for nanoparticles (SLN without Nafion have been used for comparison). Diffraction patterns are very similar, with only one peak resolved in the low-angle region ($q<0.6$ $Å^{-1}$) that can be attributed to an inner organization of nanoparticles into a 1-D lamellar phase. Values of unit cell parameter are reported in table x and suggest that the addition of Nafion® doesn't provoke a modification in the inner organization of NPs. Fundamental to evaluate the real possibility to use SLN-Nafion for the delivery of Pt-PTA has been evaluated performing in vitro cytotoxicity tests with two different cell lines, the same of the previous work presented in this thesis, A2780 (ovarian cancer cells) and K562 (erythroleukemic cancer cell line). No toxic effect of NAF has been reported, underlying their promising use as vehicles for the Pt-PTA complexes.

2.3.3 Characterization of SLN and NLC for the delivery of poorly water-soluble neuroactive drugs

The majority of this section is published in the reference Esposito *et al.,* 2017b

Esposito E., M. Drechsler, P. Mariani, F. Carducci, V. Trezza, M. Servadio, F. Melancia, P. Ratano, R. Cortesi, C. Nastruzzi 2017 19:44 DOI 10.1007/s10544-017-0188-x

Has to be remarked that I made the structural characterization using X-ray diffraction of SLN. Other results have been reported for clarity to give an extended comprehension of the work. When experiments have been performed by other, this is clearly indicated.

Four different neuroactive drugs have been tested with the aim to deliver Dimethyl Fumarate (DMF), Retinyl Palmitate (RP), Progesterone (PRG) and the endocannabinoid hydrolysis inhibitor URB597. It is very well

known about the low solubility level in water of these molecules and this represent the major limitation in the use of these molecules.

To give a brief overview about the spectrum of action of these drugs, DMF acts remitting multiple sclerosis. Is employed also in psoriasis treatment, early brain injury and learning deficits (Bomprezzi, 2015; Linker and Gold, 2013); RP supplementation can be considered as a new approach in the multiple sclerosis prevention and treatment and at the same time to a correct maintenance of CNS (Saboor-Yaraghi, 2015; Maden, 2007). PRG is a neurosteroid with neuroprotective effects; its action is essential during pregnancy (Webster *et al.*, 2015). Finally, URB597 in animals has potential effects against depression, anxiety and autism (Piomelli *et al.*, 2006; Servadio *et al.*, 2016).

Nanoencapsulation strategy allowed to obtain biocompatible and non-toxic vehicles. Tristearin (T) has been employed as unique component for the production of SLN and in addition of glyceril monoolein (Miglyol) for the production of NLC.

As first step, solubility of drugs has been evaluated using water, mixture of water/ethanol and pure ethanol. The higher solubility has been observed using pure ethanol. Due to the fact that this organic solvent is not appropriate for the use and toxic in human (because induces behavioral effects) and rats (due to its toxicity), has been evaluated the possibility to encapsulate drug in lipid nanoparticles, evaluating in this case drug solubility in SLN, NLC and PEG400/P80/saline 5:5:90. This part has been made by other authors.

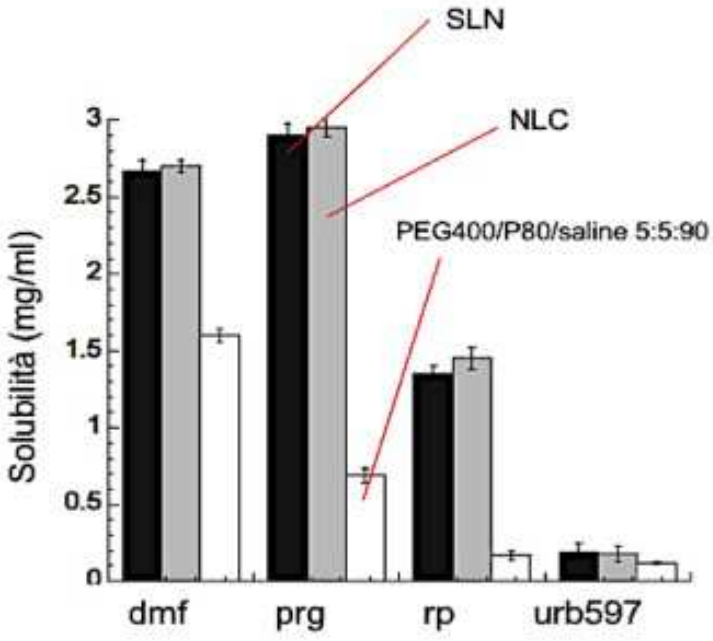

Figure 2.5 solubility level of different drugs tested using in **black**: SLN, in **grey:** NLC, in **white:** PEG400/P80/ saline 5:5:90**.** Appreciable variations can be appreciated in the case of DMF, PRG and RP. Maddalena Sguizzato et al.,2017

Figure 2.5 shows the difference in terms of solubility for PRG, RP, DMF and URB597 when incapsulated in SLN, NLC or in PEG400/P80/saline 5:5:90. The solubilization seems to be sensibly higher when drugs are encapsulated in SLN and NLC. For URB597, efficiency is low in all cases.

To improve encapsulation of URB597, the group of Ferrara tried the encapsulation of URB597 in polysorbate 80 (P80) modified nanoparticles. P80 exerts a specific role in brain targeting (Göppert and Müller, 2005). Usually unmodified NPs are captured from opsonin and eliminated from the body.
In table 2.4, results related to the structural organization of nanoparticles made with X-ray diffraction and CryoTEM have been reported.

Table 2.4 structural characterization of nanoparticles. Results obtained with X-ray diffraction and Cryo-TEM

NPs samples	X-ray diffraction Interlamellar distance (Å)	Cryo-TEM morphology
empty SLN	37.4	flat discoid
SLN/P80	45.5	bicellar
SLN-DMF	45.5	capped multilamellar
SLN-RP	38.1	bicellar
SLN-PRG	44.9	capped multilamellar
SLN-URB597	46.0	bicellar
SLN/P80-URB597	46.8	capped multilamellar
empty NLC	38.0	flat discoid
NLC-DMF	45.2	capped multilamellar
NLC-RP	45.0	flat discoid
NLC-PRG	44.8	bicellar
NLC-URB597	46.9	capped multilamellar

Graphs reported in Figure 2.6 show one major peak relative to the inner lamellar structure of nanoparticles, at low-angle value (around 0.18$Å^{-1}$) and three secondary reflections (at 1.37, 1.63 and 1.71$Å^{-1}$) relative to the subcrystalline organization of lipid chains. In this work, an evidence of a triclinic parallel organization of lipid chains (β form) is given, as reported by Sato and Ueno in *Polymorphism in Fats and Oil*, 2005 John Wiley & Sons, Inc. and by Jenning *et al.*, 2000 (Sato and Ueno, 2000). Attention has to be focused also to the fact that solubilization of lipophilic molecules into lipid nanoparticles avoiding the use of organic solvents has been achieved. For RP and PRG the solubility level has been increased respectively 4- and 8-fold using lipid nanoparticles. The use of SLN/P80 instead of PEG400/P80/saline allowed to improve the solubility level of URB597 of 1.5-fold. At the same time, they tested the intranasal administration of SLN/P80-URB597, suggesting that this can be a great alternative to the intraperitoneal administration of this drug.

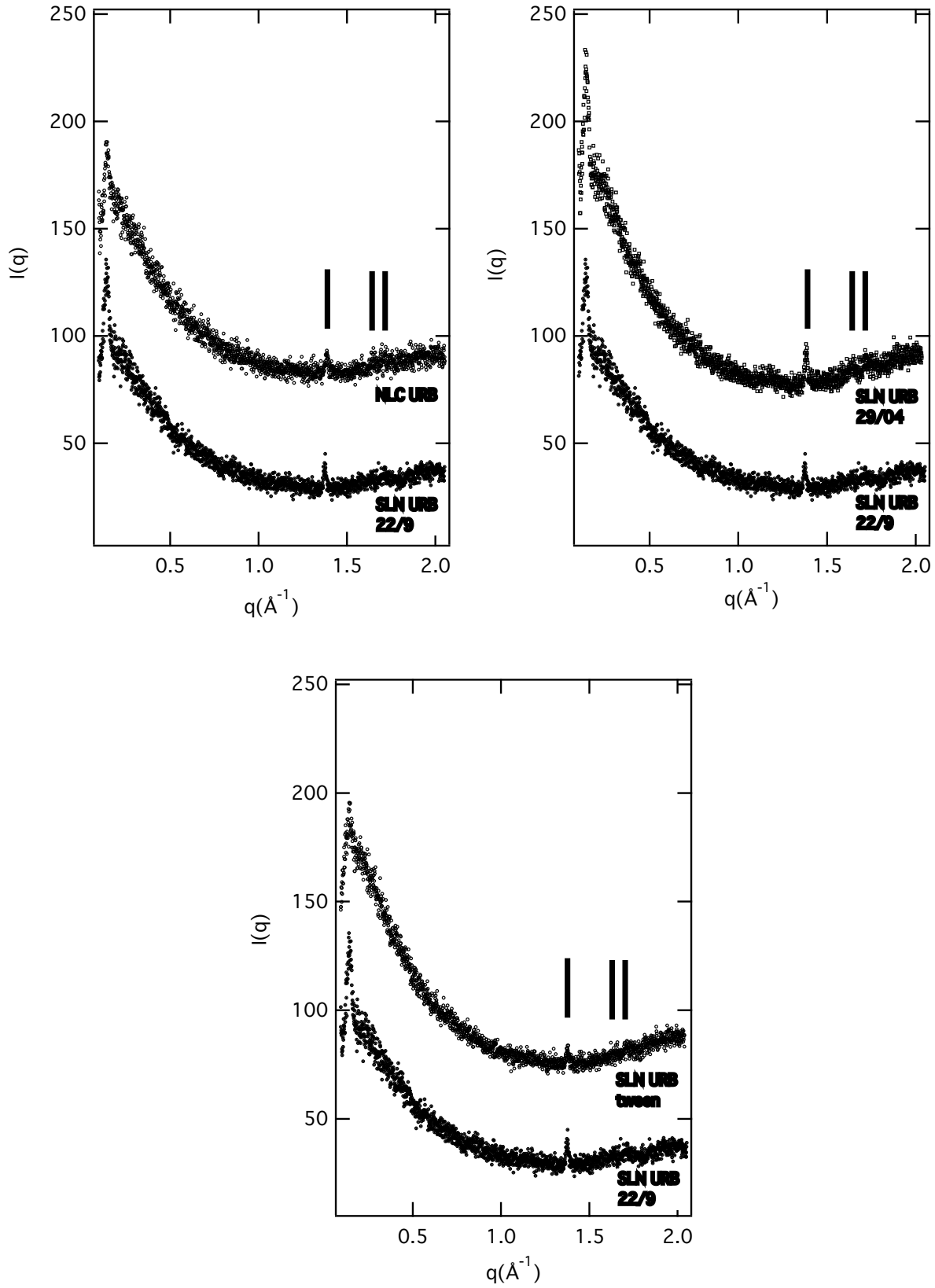

Figure 2.6 X-Ray diffraction profiles relative to A) SLN-URB compared with NLC-URB B) two different batches of SLN URB C) SLN URB made with Tween in comparison with SLN URB. Black lines indicate the position of reflections in the high-angle region relative to the subcrystalline organization of nanoparticles in a triclinic parallel geometry

2.4 Characterization of Monoolein Aqueous Dispersions (MAD)

2.4.1 Structural Characterization of MAD kept in contact with *quercetin*

The majority of this section is published in the reference Cortesi *et al.,* 2017

Cortesi R., E. Cappellozza, M. Drechsler, C. Contado, A. Baldisserotto, P. Mariani, F. Carducci, A. Pecorelli, E. Esposito, G. Valacchi *Biomed Microdevices* (2017) 19:41 DOI 10.1007/s10544-017-0185-0

Has to be remarked that I made the structural characterization using X-ray diffraction of MAD. Other results have been reported for clarity to give an extended comprehension of the work.

Quercetin (3,3',4',5-7-pentahydroxyflavone) is one the most powerful antioxidant present in nature. In addition to its key role in preventing oxidation (e.g. QT received considerable attentions regarding its activity to prevent Reactive Oxygen Species-mediated damage in skin, (Casagrande *et al.*, 2006, 2007*;* Vicentini *et al.*, 2008), it has many pharmacological potentials: decreasing lipid levels in blood, preventing anemia, as anti-platelet aggregation agent (Hollman and Katan, 1999).

Table 2.5 composition of SLN in % w/w and structural organization results obtained by X-ray diffraction

Formulation	Composition (%w/w)			Unit Cell Value (*a*) ± 1 Å	Morphology
	Monoolein	Water	Sodium Cholate		
MAD 015	4.5	94.15	0.15	153.4	Im3m
MAD 015-QT	4.5	94.15	0.15	137.9	Im3m
MAD 025	5	92.15	0.25	-	-
MAD 025- QT	5	92.15	0.25	-	-

One of the main limitations in the use of this biological compound is its low-solubility in water. Monoolein Aqueous Dispersions (MAD) represent a way to solve this problem. In this work is reported the development of MAD encapsulating QT using sodium cholate as emulsifier. Two different kind of samples have been prepared, MAD015 (with sodium cholate at 0.15% w/w, as described in table 2.5) and MAD025 (with higher concentration of sodium cholate, 0.25% w/w). Samples have been prepared using the method of emulsification of lipid and emulsifier, followed by homogenization. QT has been added to MAD before addition of water in a concentration of 0.25mg/ml (0.5% by weight with respect to the content of monoolein and 0.025% by weight with respect to the dispersing phase). Characterization has been performed using CryoEM, X-Ray Diffraction (XRD), PCS and SdFFF (Sedimentation Field Flow Fractionation) as techniques. In addition, drug content evaluation in MAD, stability studies, *In vitro* release profiles (Franz cells) studies and biological tests on antioxidant activity and cytotoxicity have been made. A brief summary of all the results obtained for this kind of dispersions of MAD-QT has to be made. Starting from some considerations of the CryoEM results, some

relevant differences have been reported relatively to the content of emulsifier used in the dispersions formulation. The 0.15% (w/w) of sodium cholate (MAD015) leads to the obtainment of a mixture of vesicles and cubic structures; in the case of 0.25% (w/w) of emulsifier (MAD025) only unilamellar invaginated vesicles have been observed. This is in line with X-ray diffraction observations, summarized in graph 2.7 and table 2.5. From diffraction profiles is clearly observable that peaks detected are related to a cubic phase inner organization of MAD-015, both in the presence and in the absence of quercetin. Experiments have been performed at 37°C, both for MAD015 and MAD025, in the presence and absence of QT.

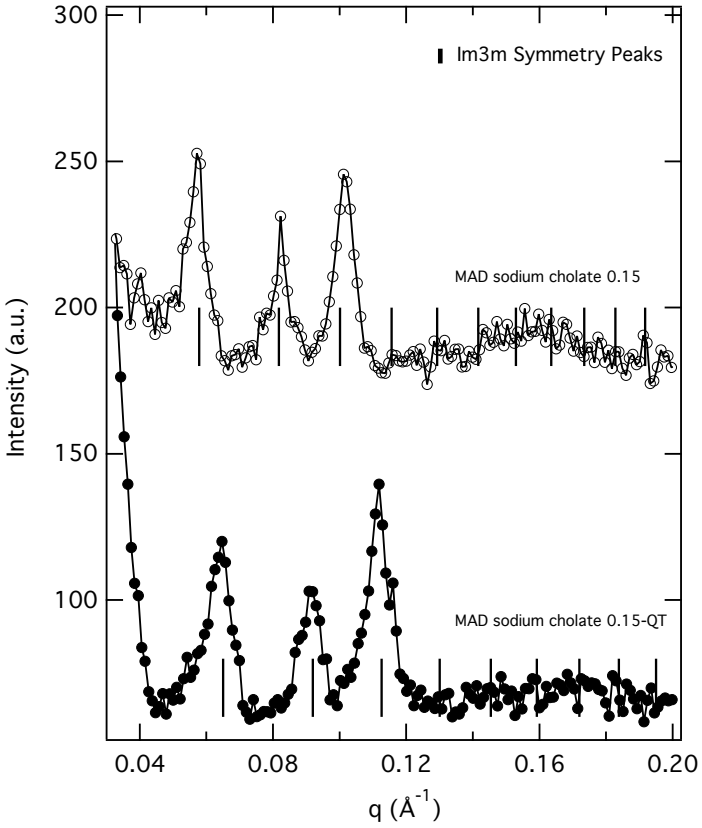

Figure 2.7 low-angle X-ray diffraction profiles of Monoolein Aqueous Dispersions, black lines indicate the expected position of Im3m cubic phase. From the diffraction profiles, it is possible to deduce that quercetin doesn't provoke changes in the nanoparticles organization

Unit cell value calculated from XRD profiles and reported in table 2.5 suggests that QT probably induces a small shrinking of water channels due to surface dehydration. No signals have been detected in the case of MAD025 and this is justifiable by the predominance of unilamellar structures observed using CryoEM, not detectable using XRD. Information about dimension have been obtained instead thanks to PCS and SdFF, performed by other groups. The addition of QT leads to a sensible increase of mean diameter of MAD015 and 025 with the respect of that one of empty MAD. For example, in the case of MAD015, the average value of empty dispersions is of 227.0nm, consequently to the addition of QT this became 402.3nm. Probably QT locates within lipids. This study let to comprise the importance of structural characterization in the development of new MAD DDS. The comprehension of lipid NPs inner organization (especially in the case of use of different emulsifiers and active principles) is a fundamental step that has to be made to obtain stable and efficient systems to be used in the delivery of drugs.

2.5 High Pressure Homogenization (HPH) vs Ultrasonication (U): characterization of NPs stability and validation of method using Small Angle X-Ray Scattering (SAXS)

Measures have been made in May 2017 at the beamline BM29 (BioSAXS)*, European Synchrotron Radiation Facility (ESRF), Grenoble (FR). Data have not yet been published.*

2.5.1 SLN and NLC

Due to the always growing interest of NPs production across industries, High Pressure Homogenization (HPH) has becoming the preferred method to be used for large-scale production of NPs.

Preliminary results are reported here, relatively to samples made by the group of Ferrara (Dept. of Life Sciences and Biotechnology) but using two different methods of production of NPs: Ultrasonication method (U) and High-Pressure Homogenization (HPH), an ongoing process widely used in pharmaceutical and food industry. This method is innovative due to its ability to lead and uniform droplets size in lipid emulsion and to avoid the presence of aggregates (Esposito *et al.*, 2017a), but the real advantage in the use of this kind of homogenization is the possibility to achieve scale-up nanoparticle volumes from lab to pilot and industrial scale. Measures have been performed in Grenoble, ESRF (European Synchrotron Radiation Facility), Beamline BM29, using small angle X-ray scattering (SAXS) technique.

Table 2.6 composition of samples related to SLN. Three columns have been reported: in the first one has been reported type of nanoparticles made, in the second one different lipid used and related concentration and finally, in the third one, method of production used

Nanoparticle	Lipid_ Concentration (% wt)	Method of production
SLN	Tristearin (T)_ 5	HPH
SLN	Suppocire (S)_5	HPH
SLN	Compritol I_5	HPH
SLN	Precirol (P)_5	HPH
SLN	Tristearin (T)_ 5	U
SLN	Suppocire (S)_5	U
SLN	Compritol I_5	U
SLN	Precirol (P)_5	U
SLN	Suppocire (S)_8	HPH
SLN	Suppocire (S)_9	HPH
SLN	Suppocire (S)_10	HPH
SLN	Suppocire (S)_8	U
SLN	Suppocire (S)_9	U
SLN	Suppocire (S)_10	U

Graphs reported in Figure 2.8 and organized in two columns indicate the two different temperatures tested (column1: 30°C, column 2: 37°C). In all graphs, black curves are related to nanoparticles produced using High Pressure Homogenization method (H). In column 1 (30°C), NPs made using the *canonical* method of Ultrasonication (U) are reported in green, in column 2 (37°C), NPs produced using ultrasonication U are showed in orange.

As it is possible to observe in Figure 2.8, lines A (Tristearin) and D (Precirol), the use of those lipids in the production of NPs does not seem to produce variations in lipid morphology, at both temperatures tested.

Layout 1:

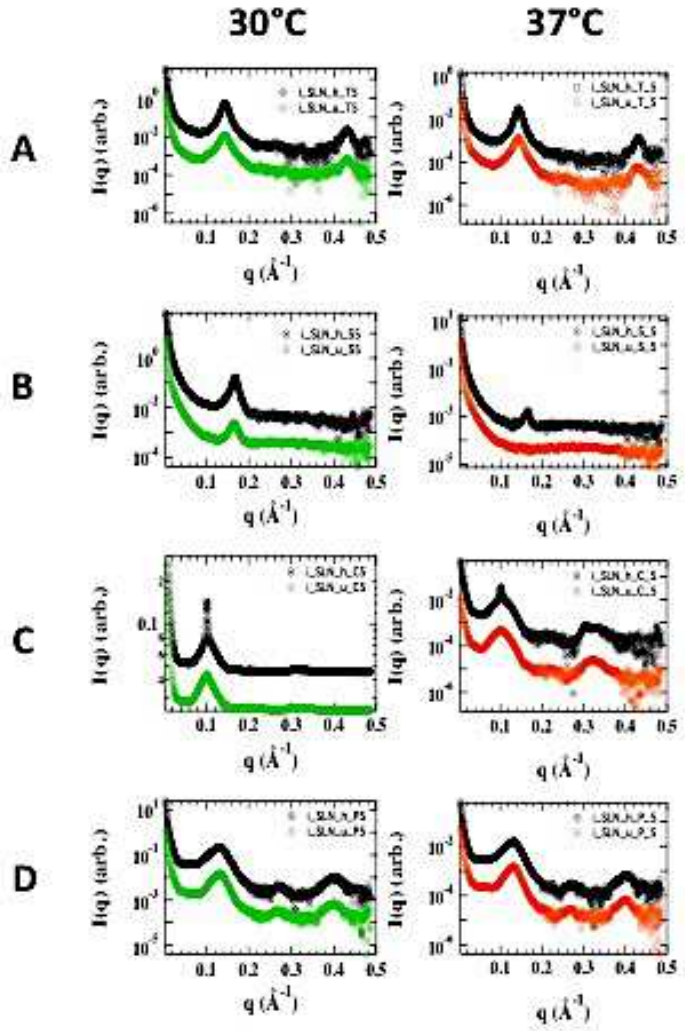

Figure 2.8 SAXS profiles related to solid lipid nanoparticles (SLN) made using different lipids (Line **A**: Tristearin (**T**), **B**: Suppocire (**S**), **C**: Compritol (**C**), **D**: Precirol (**P**)) and different method of production: High-pressure homogenization (**HPH,** in graphs indicated as **H**, **black curves**, both for 30°C (left column) and 37°C (right column)) and ultrasonication **U,** (**green curves** for the 30°C, **orange curves** in the case of 37°C)

In the case of Suppocire (line B), at 37°C, it is relevant the fact that the peak related to the lamellar phase disappears only in the case of the orange curve, that one produced using the method of Ultrasonication. Probably the High-Pressure Homogenization (HPH) is able to confer a major stability in terms of inner organization of the NPs.

General considerations about the production of NPs using H method can be made for the lipid Compritol (Line C). The characteristic morphology of the peak (large at the bottom and very narrow and defined at the top) suggest us the possibility of the presence of a double phase in the inner organization of NPs.

In addition, is very curious that the presence of higher number of peaks relative to the lamellar phase (up to the 3rd order) has been evidenced only at 37°C (Figure 2.8, column 2, line C_ in both profiles).

Table 2.7 unit cell values calculated for each lipid used in the production of NPs and temperature measured

Lipid	High Pressure Homogenization (H)		Ultrasonication (U)	
	Unit Cell (Å) @ 30°C	Unit Cell (Å) @ 37°C	Unit Cell (Å) @ 30°C	Unit Cell (Å) @ 37°C
Tristearina **T**	43.9	43.9	43.9	43.9
Suppocire **S**	37.9	37.9	37.9	-
Compritol **C**	61.6	61.6	62.2	62.2
Precirol **P**	46.9	46.9	47.6	47.6

There are no sensible variations in terms of dimension of the unit cell, considering the two different methods of production. A particular and unexpected behavior has been observed in the case of use of Compritol (Figure 2.8, Line C). At 37°C the inner organization of the lamellar phase seems to be higher than that one obtained at 30°C. A more detailed characterization must be carried out about peaks observed in the case of Compritol, black profiles.

The second group of samples investigated are related to nanoparticles produced using the same lipid, Suppocire (S) but using:

- two different methods of production (HPH and U);
- different lipid concentrations (from 8% to 10% wt).

Final graphs have been organized in Figure 2.9 in two columns, relative to temperatures measured (1st: 30°C, 2nd: 37°C). In this case lines A, B and C correspond to 8, 9 and 10% of lipid concentration (in weight). Black curves are relative to the HPH method, green and orange profile respectively to Ultrasonication method (U), at 30°C and 37°C. Suppocire (S) is not so stable to preserve the lamellar inner organization at 37°C.

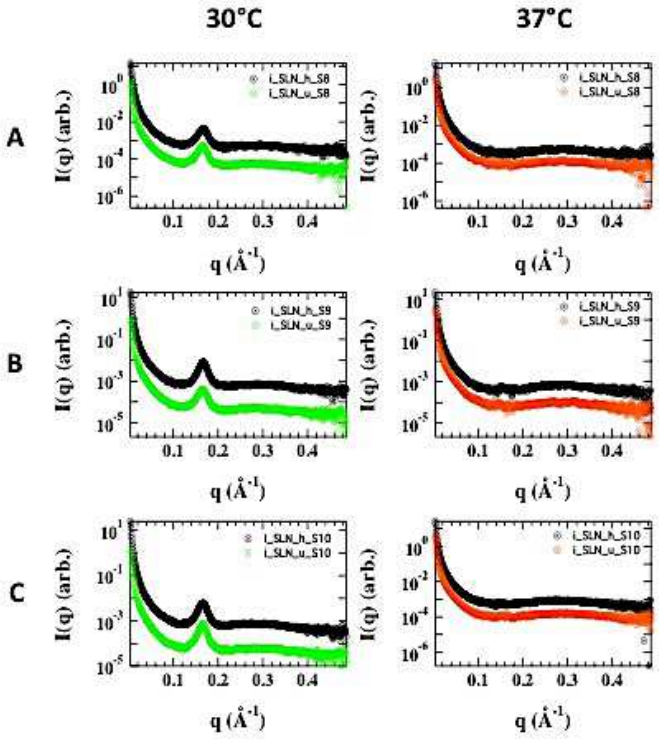

Figure 2.9 SAXS profiles related to solid lipid nanoparticles (SLN) made using the same lipid Suppocire (**S**), but at different concentration (Line **A**: **8%** wt, Line **B**: **9**% wt and Line **C**: 10% wt) and taking into account of the different method of production: High-pressure homogenization (**HPH,** in graphs indicated as **H**, **black curves**, both for 30°C (left column) and 37°C (right column)) and ultrasonication **U,** (**green curves** for the 30°C, **orange curves** in the case of 37°C)**.** Further details about the composition of samples can be found in table 2.6

A very low intensity relative to the first order peak of the lamellar phase can be observed in the case of black curves (column 2_37°C) giving a further confirmation of the fact that using High Pressure Homogenization method for the production of NPs can lead to a higher stability of the system.

In Figure 2.10 have been summarized all measurements made about NLC (Nanostructured Lipid Carriers). In table 2.8 has been reported samples measured and details about the composition, together with the method of production.

Table 2.8 composition of samples related to NLC. Three columns have been reported: in the first one has been reported type of nanoparticles made, in the second one different lipid used with the related concentration and finally, in the third one, method of production used

Nanoparticle	Lipid (% wt) lipid/mygliol ratio	Method of production
NLC	Suppocire (5%) /mygliol 1:1	U
NLC	Suppocire (10%)/mygliol 1:1	U
NLC	Suppocire (5%)/mygliol 2:1	U
NLC	Suppocire (10%)/mygliol 2:1	U
NLC	Suppocire (5%) /mygliol 1:1+ vit E 0.4%	U
NLC	Suppocire (10%)/mygliol 2:1+ vit 0.8%	U
NLC	Tristearin (5%) /mygliol 1:1 + vit E 0.4%	U
NLC	Tristearin (10%) /mygliol 1:1 + vit E 0.8%	U
NLC	Tristearin (5%) /mygliol 2:1	U

The organization of graphs in Figure 2.10 is the same of the previously reported above. In line A, B and C I compared NLC made with Suppocire and miglyol

Line A: in presence or absence of Vitamin E, at 30°C and 37°C

Line B: NLC always made with Suppocire/miglyol, but at different ratios. Line C: NLC S/m at higher ratio, in presence and absence of Vitamin E.

In all graphs reported about NLC made using Suppocire together with miglyol, there are no peaks related to the inner lamellar organization, probably due to the fact the lipid itself is not so able to provide an inner organization of lipid molecules, when kept in contact with mygliol. The presence of Vitamin E doesn't provoke changes in the NPs inner organization.

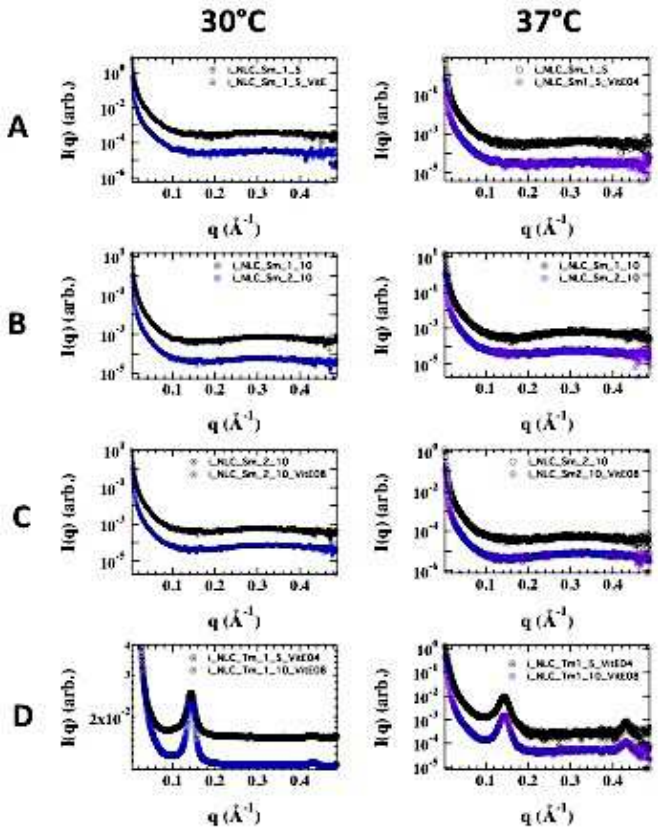

Figure 2.10 SAXS profiles related to nanostructured lipid nanoparticles (NLC) made with Suppocire (**S**), together with mygliol (**m**) (Lines **A**, **B** and **C**) or Tristearin (**T**) together with mygliol (**m**) (Line **D**). **Line A:** in presence or absence of Vitamin **E,** at 30°C (first column) and 37°C (second column). In **Line B:** NLC always made with Suppocire/miglyol, but at different ratios. **Line C**: NLC S/m at higher ratio, in presence and absence of Vitamin E. In all graphs High-pressure homogenization measures **HPH** (in graphs indicated as **H**) are showed as **black curves**, both for 30°C (left column) and 37°C (right column). Considering ultrasonication **U,** (**blue curves** for the 30°C, **violet curves** in the case of 37°C)

A completely different observation can be made for NLC made with Tristearin and miglyol. In this case the combination of these two components lead to an inner lamellar organization of NPs, probably due to the structure of the lipid itself (Suppocire chemical formula is a $OC(CH_2)_nCH_3$ where n=7-17; Tristearin a $C_{57}H_{110}O_6$) As it is possible to observe form the second graph in line D at 37°C two peaks have been detected, relative to the first and third order of the lamellar phase.

Finally, considering Figure 2.8, the use of PRECIROL leads to a higher level of inner lamellar organization of NPs (Line D). In both graphs, obtained at 30°C and 37°C it is possible to observe three peaks relative to the first, second and third order of the lamellar inner organization, suggesting a very high level of organization of lipids.

An additional consideration can be made on results of measurements obtained at 37°C in the case of COMPRITOL (Figure 2.8, Line D) In this case differences are related to temperature tested. A higher number of reflections can be observed at 37°C.
Always related to this lipid, the first order of the lamellar phase detected shows a particular morphology, probably due to the coexistence of a double phase. More detailed analysis will be carried out about this particular result.

Focusing on the graphs relative to Suppocire-based NPs (Figure 2.9, Line B), at 37°C (second graph), the first order relative to the inner lamellar organization can be detected only for the HPH method.
Probably the use of this technique leads to the obtainment of higher stability of NPs.

Always considering Figure 2.9, samples measured have been made using the same lipid, Suppocire (**S**), but exploring concentration. It is possible to observe that this lipid, at 37°C, seems to be not so stable to preserve the inner lamellar organization of NPs. At 30°C there are no variations in terms of morphology. In this case the only peak (at very low intensity) detected at 37°C is related to NPs made using the HPH process (Line B, second column)

Finally, referring to graphs reported in Figure 2.10, can be affirmed that only Tristearin, when kept in contact with Miglyol, can provide a 1D-lamellar organization of NPs, e.g. comparing graphs in **Line C** (**Suppocire/miglyol**) with those of the **Line D** (**Tristearin/miglyol**). The presence of Vitamin E in NLC made with Tristearin/miglyol doesn't modify the lamellar organization of NPs.

2.5.2 Lipid-based nanoparticles for the delivery of progesterone

The majority of this section is published in the reference Esposito et al., 2017d

- Esposito E., M. Sguizzato, M. Drechsler, P. Mariani, F. Carducci, C. Nastruzzi, R. Cortesi *Eur. J. Pharm. Biopharm.* 119 (2017) 437-446

Has to be remarked that I made the structural characterization using X-ray diffraction of SLN.

Progesterone is a steroid hormone produced in our body by the corpus luteum, by the placenta (during pregnancy), and by the adrenal glands. This can elucidate of how fundamental is its role in the regulation of monthly menstrual cycle and pregnancy. One of the most important function is to stimulate the endometrium to release special proteins during the second half of the menstrual cycle, to prepare the endometrium itself to receive and nourish implanted fertilized egg. Actually, progesterone is administered to treat habitual abortion, regulation of ovulation and menstruation (e.g. amenorrhea) etc. (Esposito *et al.*, 2017c, 2017d; Lockwood *et al.*, 2014; Tavaniotou, 2000) orally, rectally, intramuscularly, subcutaneously and intravaginal (Lockwood *et al.*, 2014; Tavaniotou, 2000). In this work, a scaling up study has been made to produce progesterone-based nanoparticles (both SLN and NLC) in a pilot scale. Lipid nanoparticles have been produced by the group of Ferrara using Ultrasound Homogenization (UH) and High-Pressure Homogenization (HPH). The production has been divided into two main steps: the first one is the emulsification of lipid using high-shear mixing, and we find it in both UH and HPH. The second step consist in the treatment of the emulsification in two different ways: in UH using a probe ultrasound generator and in HPH by high-pressure homogenizer, to reduce and uniform the droplet size.

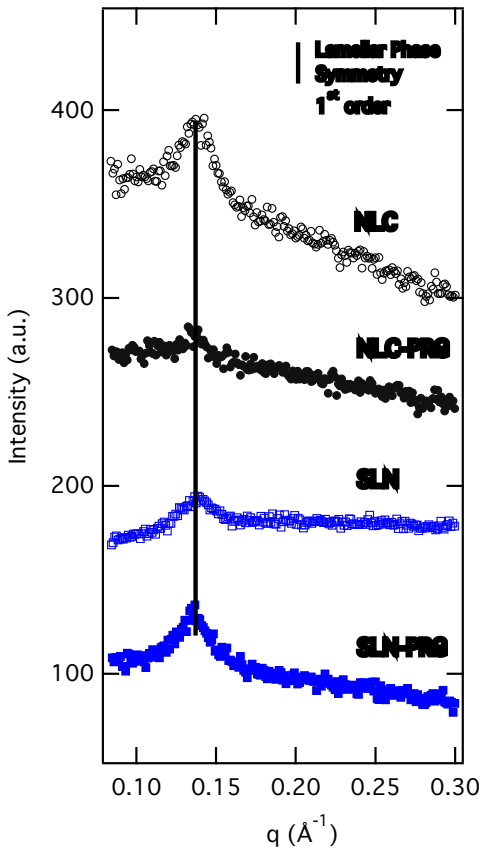

Figure 2.11 X-Ray diffraction profiles observed for SLN and NLC, in the presence and absence of PRG. From the bottom: SLN-PRG, SLN, NLC-PRG, NLC. The vertical black line in the graph indicates the peak position expected of the first order of the Lamellar Phase Symmetry. Nanoparticles have been produced using the HPH method

Table 2.9 composition of SLN/NLC progesterone-based in % w/w and structural organization results obtained by X-ray diffraction.

Sample	Composition (%w/w)					Unit Cell Value (*a*) ± 1 Å	Morphology
	Tristearin	Miglyol	Poloxamer 188	Progesterone (PRG)	Water		
SLN	5	-	2.5	0.1	92.4	46.0	Lamellar
NLC	5	2.5	2.5	0.1	89.9	49.0	Lamellar

The characterization of NPs morphology using X-Ray Diffraction has been made in our department, that one with Cryo-TEM by Markus Drechsler, of the University of Bayreuth.

Analyzing this graph is clear that the encapsulation of drug in NPs doesn't provoke variations in the morphology of the particles. In this case have been analyzed only samples relative to the second method of homogenization (HPH), confirming the good physical and chemical stability of SLN/ NLC-PRG.

2.6 An extended characterization of Monoolein/water Phase Diagram: choosing the best way to solubilize *crocetin*

Measures have been made in 2017, July at the beamline AustroSAXS, Elettra Synchrotron Basovizza, Trieste (IT). Data have not yet been published.

In this study, results relative to samples prepared exploring monoolein:water phase diagram has been reported. The aim is to find the best strategy to solubilize *crocetin*, naturally high-insoluble. Samples have been measured using Small Angle X-ray Scattering (SAXS) at the Elettra Synchrotron of Trieste, beamline Austro-SAXS.

Figure 2.12 wants to make easier the comprehension of how the macroscopic aspect changes considering different percentages of water in the case of monoolein:water system, going from a liquid-viscous solution (in the figure showed with the green bracket, mono:water 95:5-90:10) to a gel solution (red bracket, monoolein:water ratio 75:25). Each sample has been assigned to a number, the same of the list reported in Table 2.10.

Together with SAXS, observations using polarized-light optical microscopy has been made to have both a confirmation and a direct visualization of the phase assumed by different monoolein:water ratios.

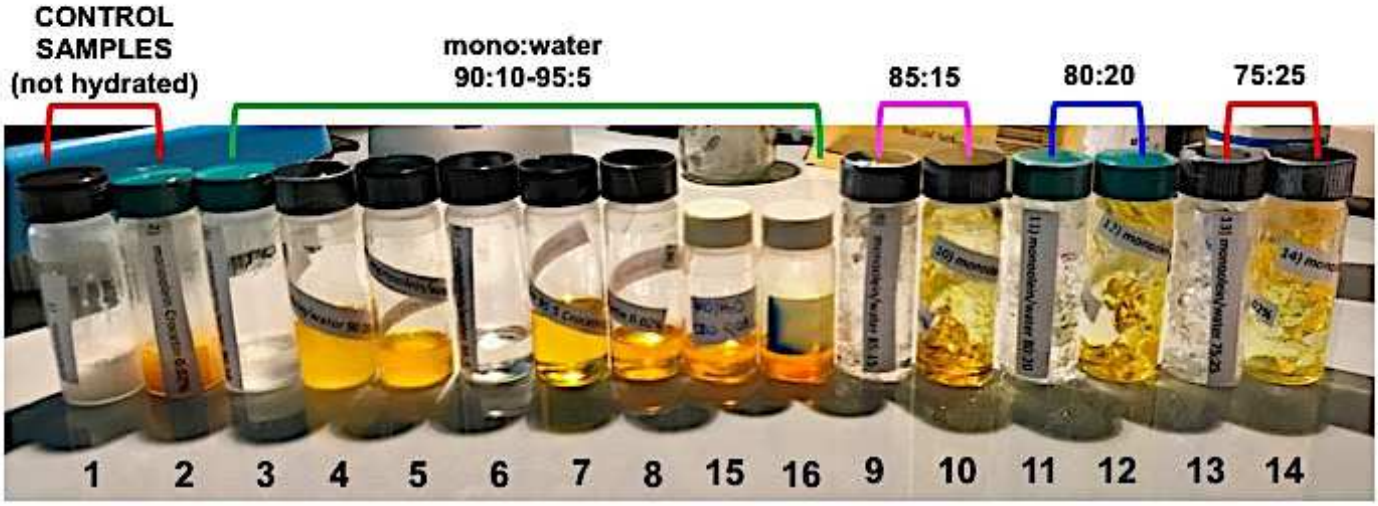

Figure 2.12 samples measured in the case of monoolein:water ratios. To have the exact composition of samples, the number reported here in the figure is the same of that one in table x. It is possible to appreciate how big is the change in terms of macroscopic aspect as function of monoolein and water content. In each graph reported in this section, curves have been separated using offset only to make more appreciable phase transitions as function of temperature variation

Table 2.10 list of samples used to screen different monoolein:water ratios, their macroscopic aspect (third column; **P** powder, **L** liquid, **V** viscous, **G** gel) and phase symmetry assumed detected using X-ray diffraction and Polarized-light Optical Microscopy (fourth column)

SAMPLE #	SAMPLE NAME	CLASSIFICATION (macroscopic)	PHASE SYMMETRY (at 20°C)
1	**monoolein (reference sample #1)**	P	not measured
2	monoolein + crocetin 0.02% **(reference sample #2)**	P	not measured
3	**monoolein/water 90:10**	L	Lamellar
4	monoolein/water 90:10 + crocetin 0.01%	L	not measured
5	monoolein/water 90:10 + crocetin 0.02%	L	Lamellar
6	**monoolein/water 95:5**	V	Lamellar
7	monoolein/water 95:5 + crocetin 0.01%	V	Lamellar
8	monoolein/water 95:5 + crocetin 0.02%	V	Lamellar
15	monoolein/water 95:5 + crocetin 0.03%	L	not measured
16	monoolein/water 95:5 + crocetin 0.04%	L	not measured
9	**monoolein/water 85:15**	G	Lamellar (L_c)/Cubic 230
10	monoolein/water 85:15 + crocetin 0.02%	G	Lamellar
11	**monoolein/water 80:20**	G	Lamellar (L_c)/Cubic 230
12	monoolein/water 80:20 + crocetin 0.02%	G	Lamellar (L_c)/Cubic 230
13	**monoolein/water 75:25**	G	Cubic 230
14	monoolein/water 75:25 + crocetin 0.02%	G	Cubic 230

To make easier the comprehension of data an almost known phase diagram of monoolein has been reported in Figure 2.13. A grid has been added to indicate the region explored with SAXS/POM measurements. Dots refer to each temperature investigated.

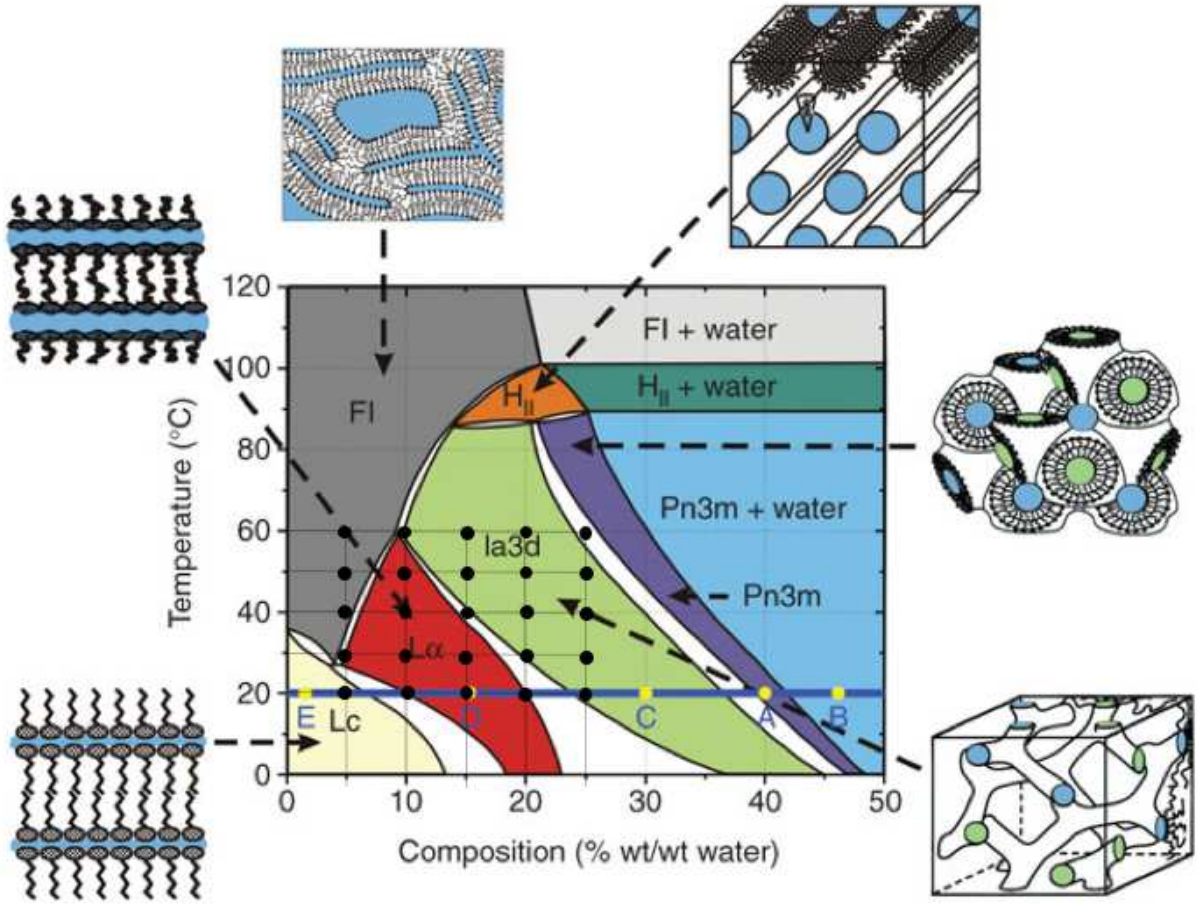

Figure 2.13 monoolein:water phase diagram, modified from the original one of Briggs and Caffrey, 1996. The grid has been added to evidence the region explored in the study presented. Dots refer to each measurement made in the study

Considering the lowest percentage of water measured of 5% (95:5 monoolein:water ratio), resulting graphs are showed in Figure 2.14. The group to be considered in this case is composed of samples #6, #7, #8, #15 and #16 (see table 2.10), in which monoolein has been kept in concact with different crocetin concentrations. Here is reported the comparison between #6 (empty monoolein:water 95:5) and #8 (monoolein:water 95:5+ crocetin 0.02%), because have been the only concentration measured for all samples using SAXS.

A phase transition can be observed at higher temperatures, both in absence (upper graph) and in presence (lower graph) of crocetin 0.02%. The transition is between a lamellar phase and an isotropic fluid phase. The first one can be defined as liquid-crystalline (L_c), observed for the lower temperatures (20 and 30°C, red and yellow curves), with Braggs' reflections up to the third order, exactly what can be expected considering the monoolein:water phase diagram that has been reported as reference above in Figure 2.13.

To better appreciate phase transition, attention can be focused to reflections evidenced at high-angles (0.36-0.54 $Å^{-1}$ in graphs reported in 2.14. Those reflections disappear at 40°C leading to a common isotropic fluid phase (FI).

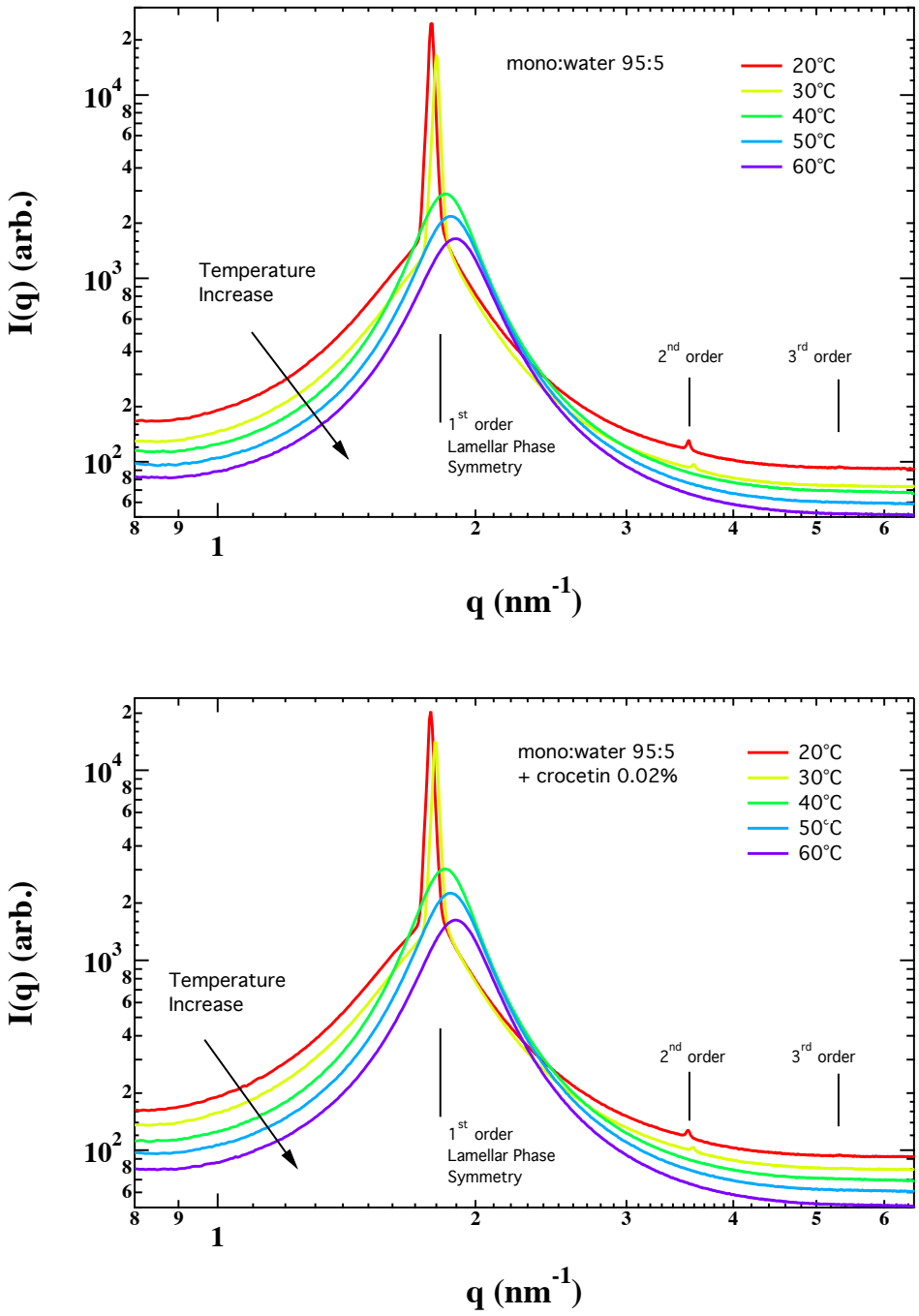

Figure 2.14 final graphs relative to measurements of monoolein:water 95:5 ratio made as function of temperature (from 20, red curve, to 60°C, purple curve); in absence (upper graph) and presence (lower graph) of crocetin at 0.02% wt. Black arrow indicates the increase of temperature (T). Black lines indicate the expected position of peaks for a Lamellar Phase Symmetry

Table 2.11 unit cell value (±1 Å) of empty monoolein:water 95:5 and of the same ratio but in the presence of crocetin 0.02%. In the last two columns have been reported phase symmetry (assumed both in presence and absence of crocetin)

Temperature (°C)	unit cell value (±1Å) mono:water 95:5	unit cell value (±1Å) mono:water 95:5 +crocetin 0.02%	phase symmetry mono:water 95:5	phase symmetry mono:water 95:5 + crocetin 0.02%
20	35.3	35.5	Lamellar (L_c)	Lamellar (L_c)
30	34.9	35.1	Lamellar(L_c)	Lamellar(L_c)
40	34.2	34.1	Isotropic fluid (FI)	Isotropic fluid (FI)
50	33.7	33.6	Isotropic fluid (FI)	Isotropic fluid (FI)
60	32.9	33.1	Isotropic fluid (FI)	Isotropic fluid (FI)

Focusing on unit cell values obtained from the analysis of X-ray diffraction profiles, there are no variation considering the presence of crocetin in the system (see Table 2.11). In addition, few examples of images obtained using POM (Figure 2.15) related to mono:water 95:5 ratio have been reported here. The presence of *flower-like* structure is typical of the lamellar phase organization (white arrows). The presence of crocetin (second column) seems to provoke the formation of a more organized network, able to solubilize completely this molecule.

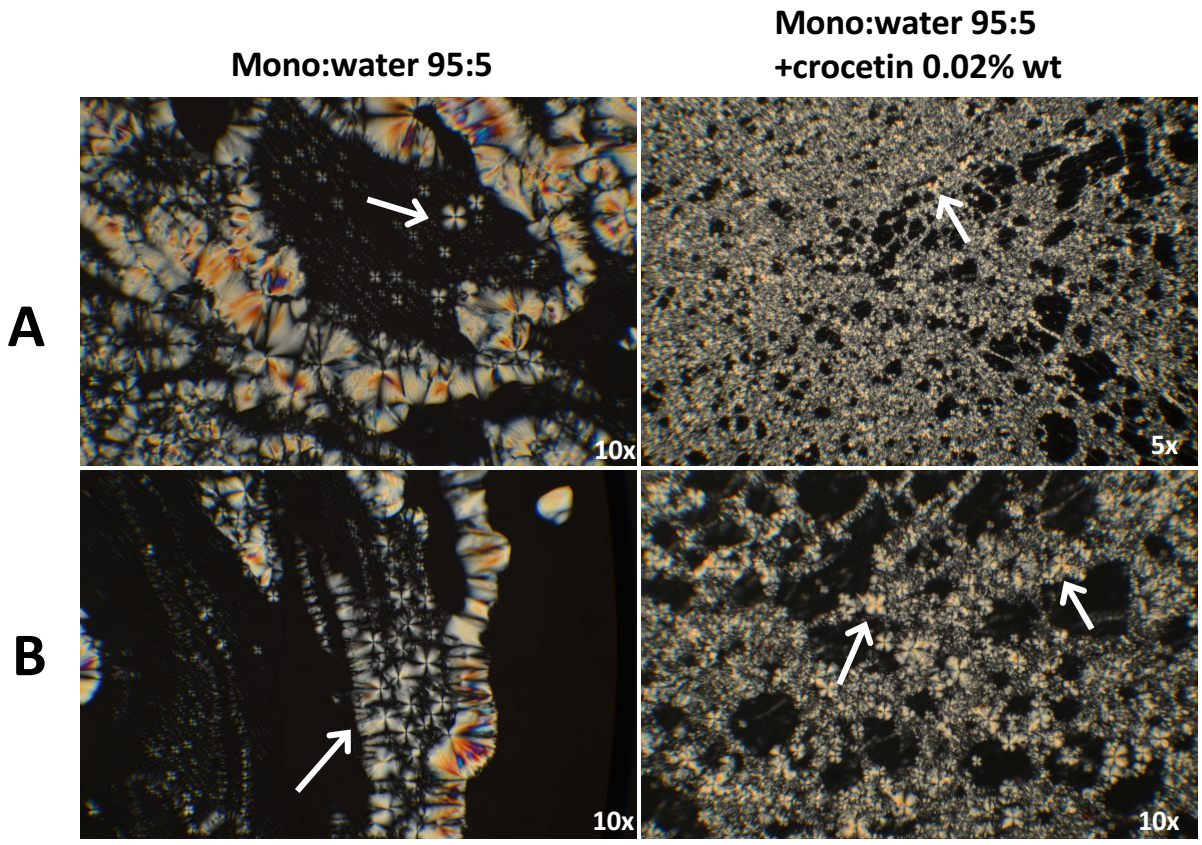

Figure 2.15 images obtained with polarized light optical microscopy (POM) at row temperature. Empty monoolein:water 95:5 (A and B, first column) and monoolein:water 95:5 in the presence of crocetin 0.02% wt (A and B, second column). White arrows indicate *flower-like* structures typical of lamellar phase

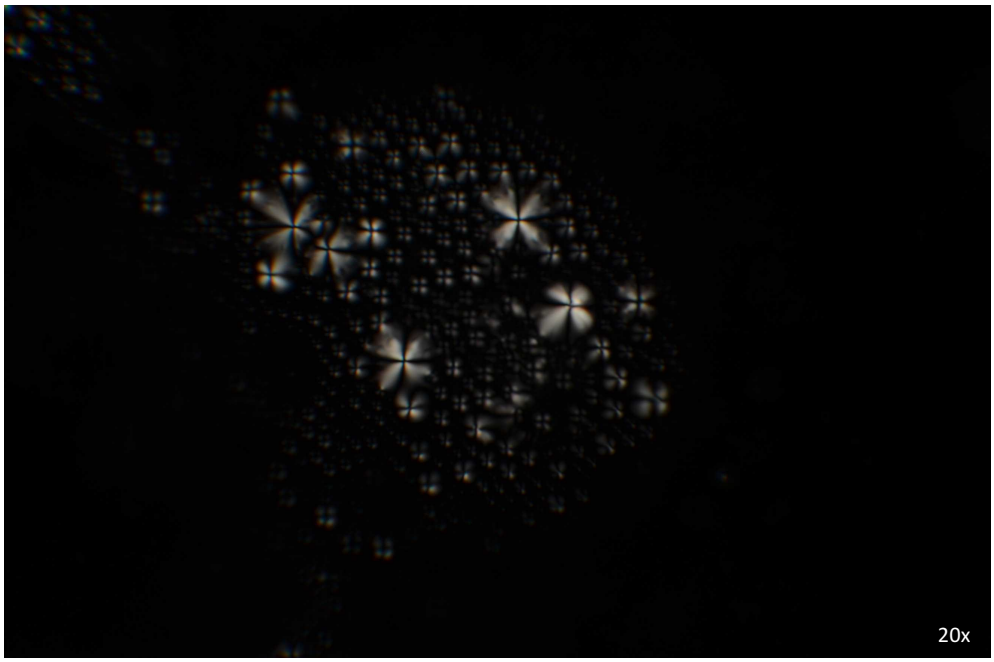

Figure 2.16 particular of the *flower-like* structure, typical of the lamellar phase organization of monoolein

Considering graphs related to mono:water 90:10 (Figure 2.17) samples #3 and #5 have been analysed and compared with the results obtained for the previous 95:5. The presence of crocetin seems to induce a conformational change at high temperatures (60°C), always between two different typologies of lamellar phase organization.
In the case of empty monoolein what happens is a decrease of the value of unit cell of the lamellar phase (from 37.7Å at 20°C, red curve to 36.7Å at 60°C, purple curve, see Table 2.12). In the presence of crocetin at 0.02% wt of concentration, not only a shift in the peak position can be observed, but also a phase transition probably from L_c (Lamellar crystalline) to an isotropic fluid (FI) phase at 60°C.

Also for this ratio, POM observations have been made to confirm the presence of the lamellar phase organization, but not reported here because very similar to that one showed for the 95:5.

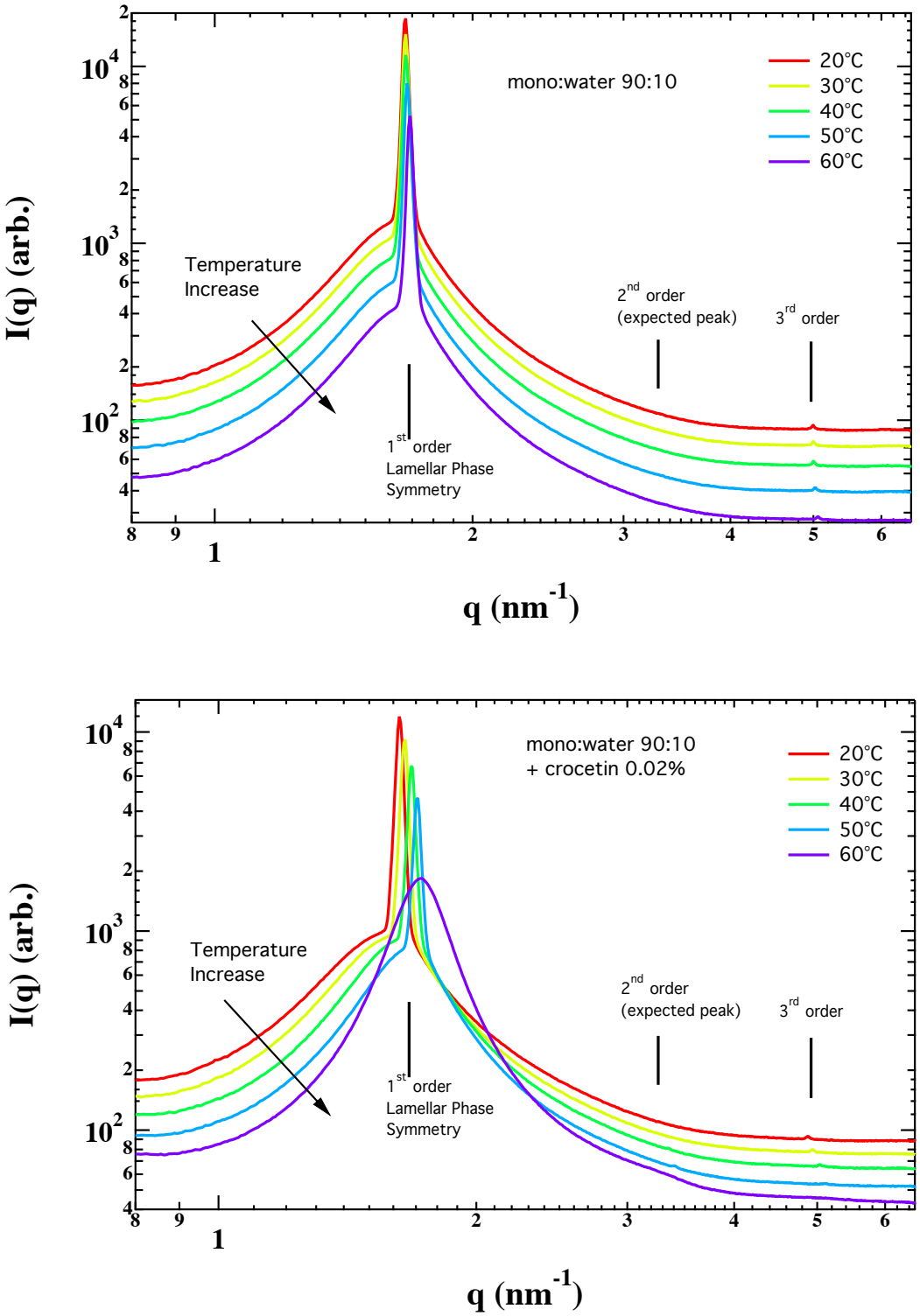

Figure 2.17 final graphs relative to measurements of monoolein:water 90:10 ratio made as function of temperature (from 20, red curve, to 60°C, purple curve); in absence (upper graph) and presence (lower graph) of crocetin at 0.02% wt. Black arrow indicates the increase of temperature (T). Black lines indicate the expected position of peaks for a lamellar phase symmetry

Table 2.12 unit cell value (Å ±1) of empty monoolein:water 90:10 and of monoolein:water 90:10 in the presence of crocetin 0.02%. In the last two columns have been reported phase symmetry (both in presence and absence of crocetin)

Temperature (°C)	unit cell value(±1Å) mono:water 90:10	unit cell value (±1Å) mono:water 90:10 +crocetin 0.02%	phase symmetry mono:water 90:10	phase symmetry mono:water 90:10 + crocetin 0.02%
20	37.6	38.7	Lamellar (L_c)	Lamellar (L_c)
30	37.6	38.2	Lamellar(L_c)	Lamellar(L_c)
40	37.6	37.4	Lamellar (L_c)	Lamellar (L_c)
50	37.4	36.8	Lamellar(L_c)	Lamellar(L_c)
60	37.1	36.6	Lamellar(L_c)	Isotropic fluid (FI)

Different is the case of monoolein:water 85:15. Considering this ratio, what it is possible to observe is the coexistence of a double phase (lamellar+ cubic phase 230) both at low and high temperatures. Starting from this ratio, a significant content in terms of water in the system probably leads monoolein to organize in a cubic bicontinuous phase.

The transition from a lamellar phase (observed for the 95:5 and 90:10 ratios) to a cubic phase organization is clearly appreciable considering variations in terms of macroscopic aspect (Figure 2.18), focus on differences between the green group 90:10; 95:5 and the pink one 85:15).
In the presence of crocetin at 0.02% wt, the diffraction profile at 20°C (red curve) is that one typical of a lamellar phase (the diffraction profile shows Bragg's reflections up to the third order of lamellar phase (red curve, Figure 2.18). Probably the presence of this molecule increases the level of organization modifying the inner organization of the lipid phase. Increasing temperature what happens is a phase transition from a lamellar to a cubic phase 230 (purple curve).

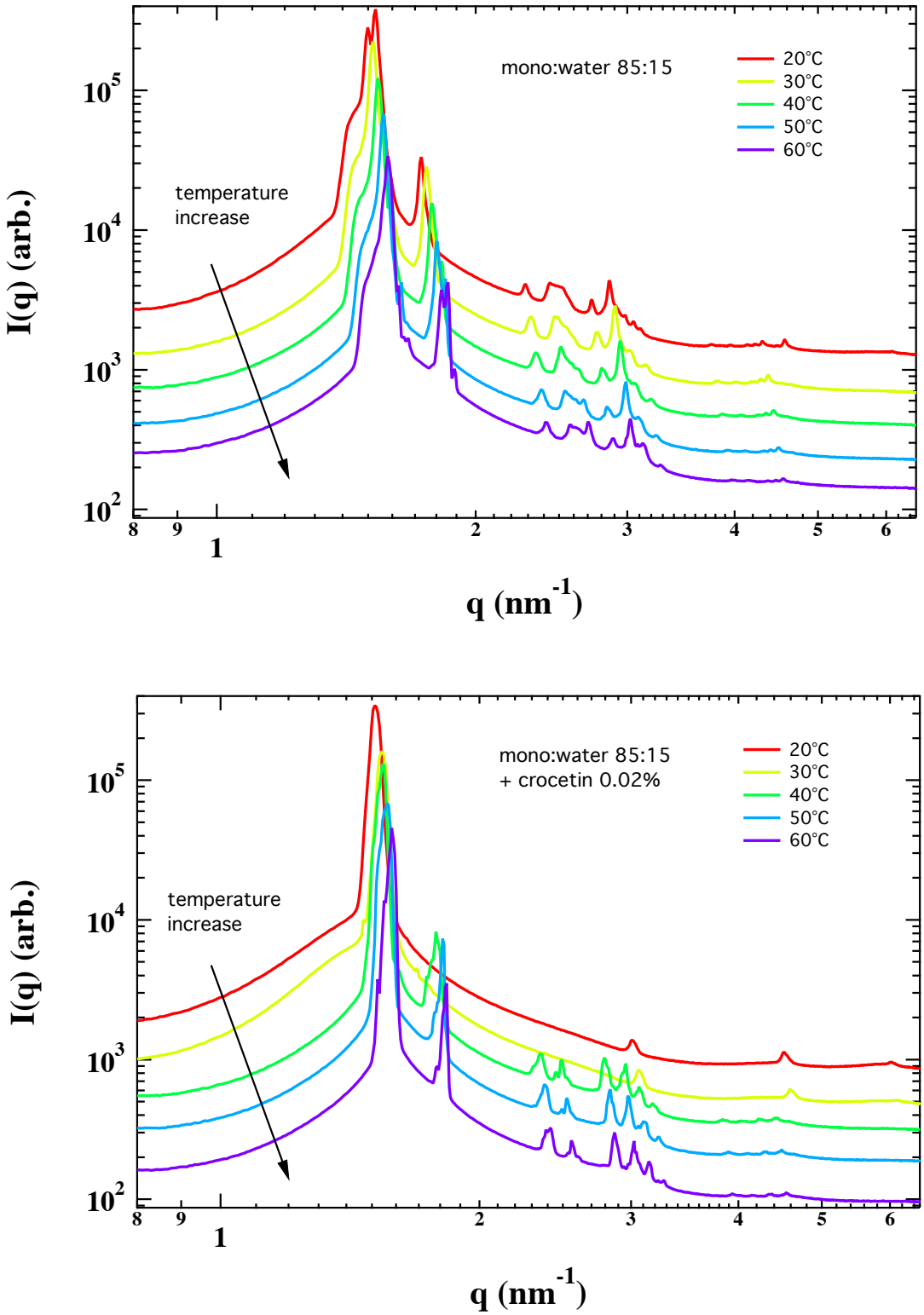

Figure 2.18 final graphs relative to measurements of monoolein:water 85:15 ratio made as function of temperature (from 20, red curve, to 60°C, purple curve); in absence (upper graph) and presence (lower graph) of crocetin at 0.02% wt. Black arrow indicates the increase of temperature (T). Black lines indicate the expected position of peaks for a lamellar phase symmetry. Also in this case, diffraction profiles of cubic phase have been shifted using offset to make easier to appreciate phase transition following temperature increase and variation of the phase symmetry, given by the exact ratio between peak position

In figure 2.19 a comparison between curves (at 20°C) of empty monoolein:water 85:15 and of the same ratio, but in the presence of (crocetin 0.02% wt), focusing on the phase symmetry peak position indexing can be showed
more in detail. Probably the presence of crocetin leads to a higher level of inner organization of lipid phase symmetry (this at 20°C).

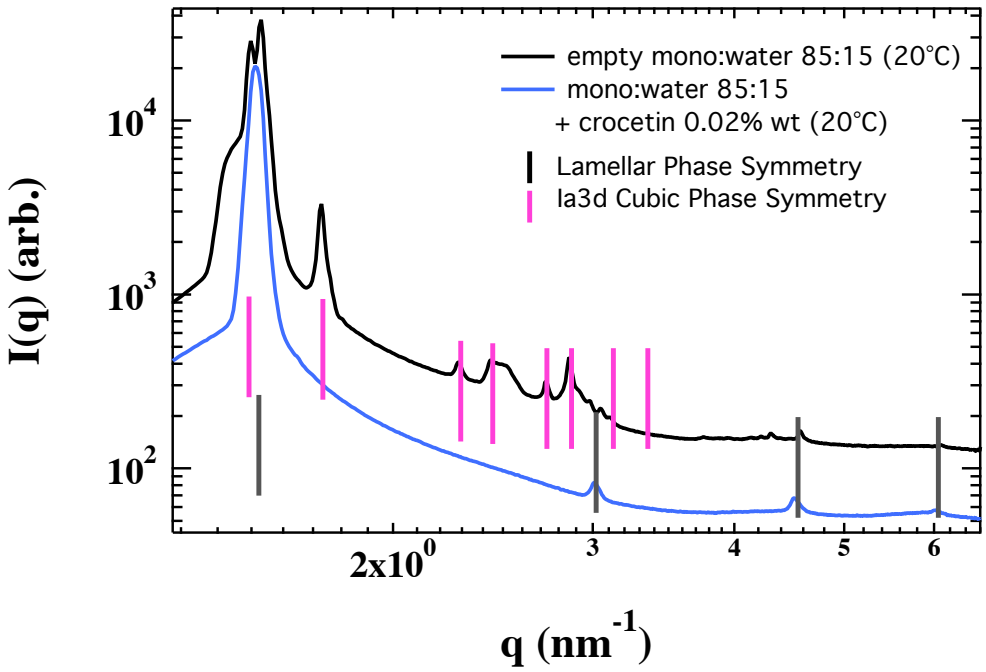

Figure 2.19 in the graph above has been reported the comparison between curves relative to the empty monoolein:water (ratio 85:15, black curve) and of the same, but in the presence of crocetin (0.02%wt, blue curve), both at 20°C. Dark grey lines in the graph represent the expected position of reflections for the Lamellar Phase symmetry; pink lines that one expected for the Cubic Ia3d Phase symmetry

Table 2.13 unit cell value (±1Å) of empty monoolein:water 85:15 and of monoolein:water 85:15 in the presence of crocetin 0.02%. In the last two columns phase symmetry has been reported, both in presence and absence of crocetin

Temperature (°C)	unit cell value (±1 Å) mono:water 85:15	unit cell value (±1Å) mono:water 85:15 +crocetin 0.02%	phase symmetry mono:water 85:15	phase symmetry mono:water 85:15 + crocetin 0.02%
20	41.2/102.6	41.6	Lamellar (L_c)/Cubic *Ia3d*	Lamellar (L_c)
30	101.3	40.8	Cubic *Ia3d*	Lamellar(L_c)
40	99.9	100.3	Cubic *Ia3d*	Cubic *Ia3d*
50	98.7	98.8	Cubic *Ia3d*	Cubic *Ia3d*
60	97.1	97.4	Cubic *Ia3d*	Cubic *Ia3d*

Few examples of images obtained with POM are reported here. Observations using polarized-light microscopy have been made at row temperature. Generally, a cubic phase is not anisotropic when observed with polarized-light. Here, anisotropic textures can be appreciated, this probably is justified by the presence of a double-phase symmetry.

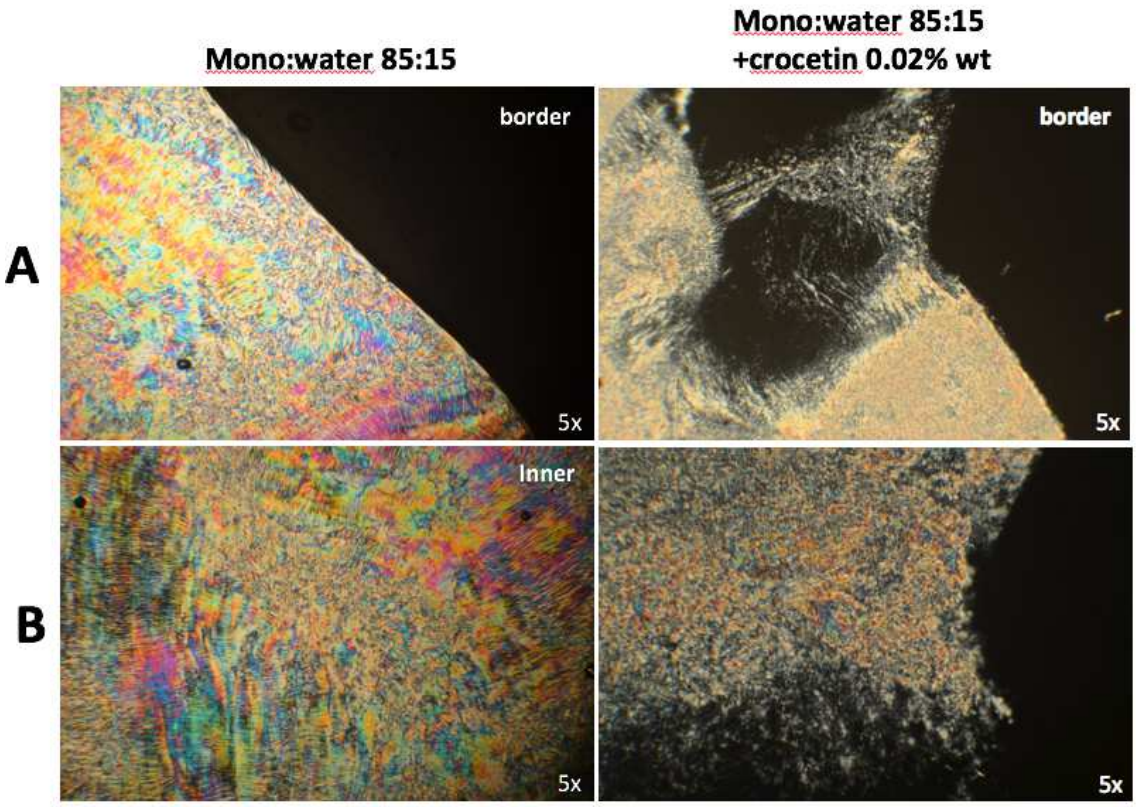

Figure 2.20 images obtained with polarized light optical microscopy (POM) at row temperature. Empty monoolein:water 85:15 (A and B, first column) and monoolein:water 85:15 in the presence of crocetin 0.02% wt (A and B, second column)

Increasing the content of water up to 20% (ratio mono:water 80:20), at low temperature it is possible to observe the presence of a double-phase symmetry (Figure 2.22), both in presence and in absence of crocetin. Increasing temperature, what happens is the presence of a single-phase symmetry, the cubic Q_{230} (*Ia3d*).

Results obtained at 20°C have been reported in red in the final graphs (Figure 2.21) and in details in Figure 2.22: black curve is relative to the empty monoolein:water, blue curve refers to the same monoolein:water ratio, but in the presence of crocetin. It is possible to affirm in general that in this case crocetin doesn't provoke any relevant changes.

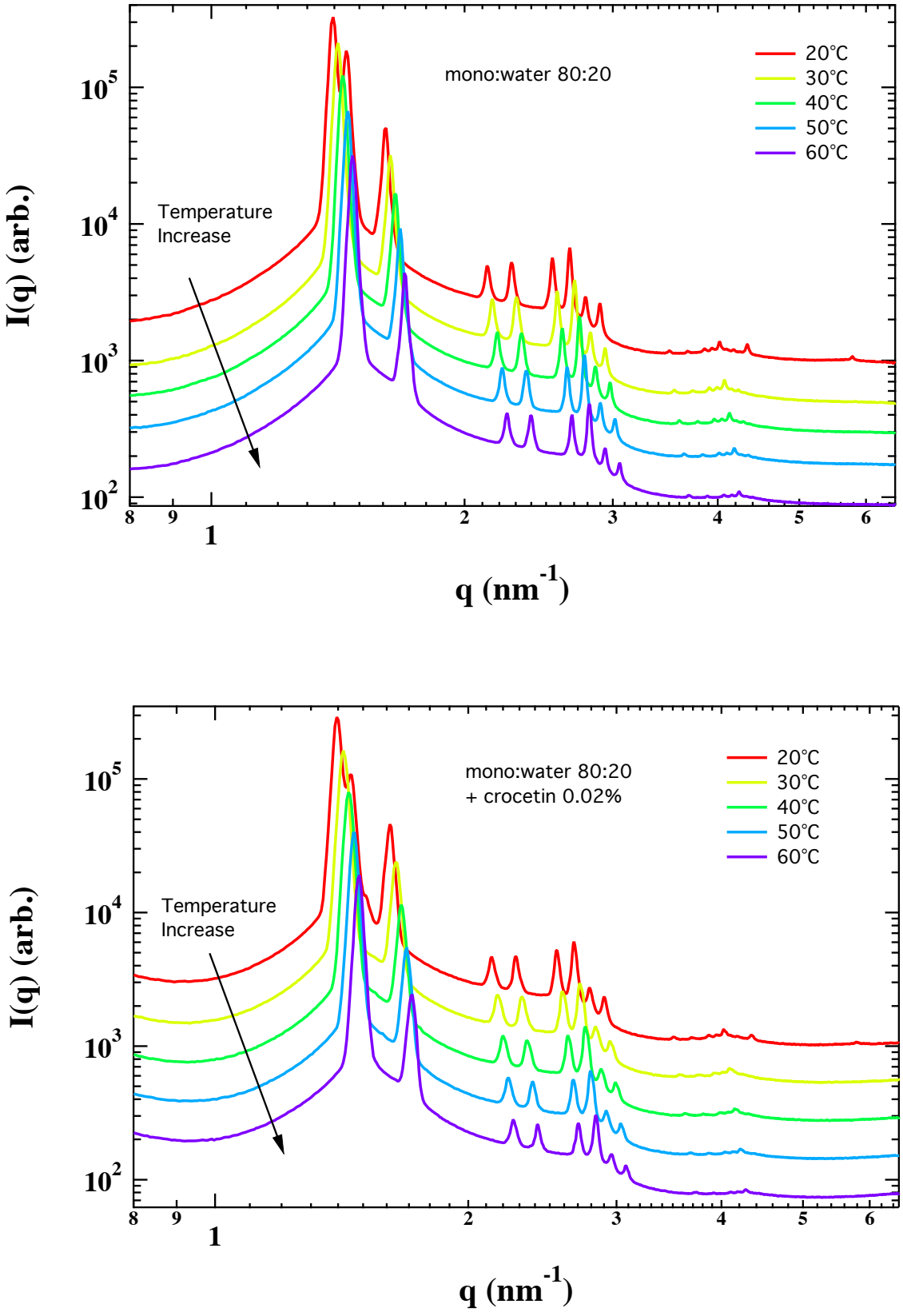

Figure 2.21 final graphs relative to measurements of monoolein:water 80:20 ratio made as function of temperature (from 20, red curve, to 60°C, purple curve); in absence (upper graph) and presence (lower graph) of crocetin at 0.02% wt. Diffraction profiles of cubic phase have been shifted using offset, to make easier to appreciate phase transition during the temperature variation and of course symmetry of the phase, given by the exact ratio between peak position.

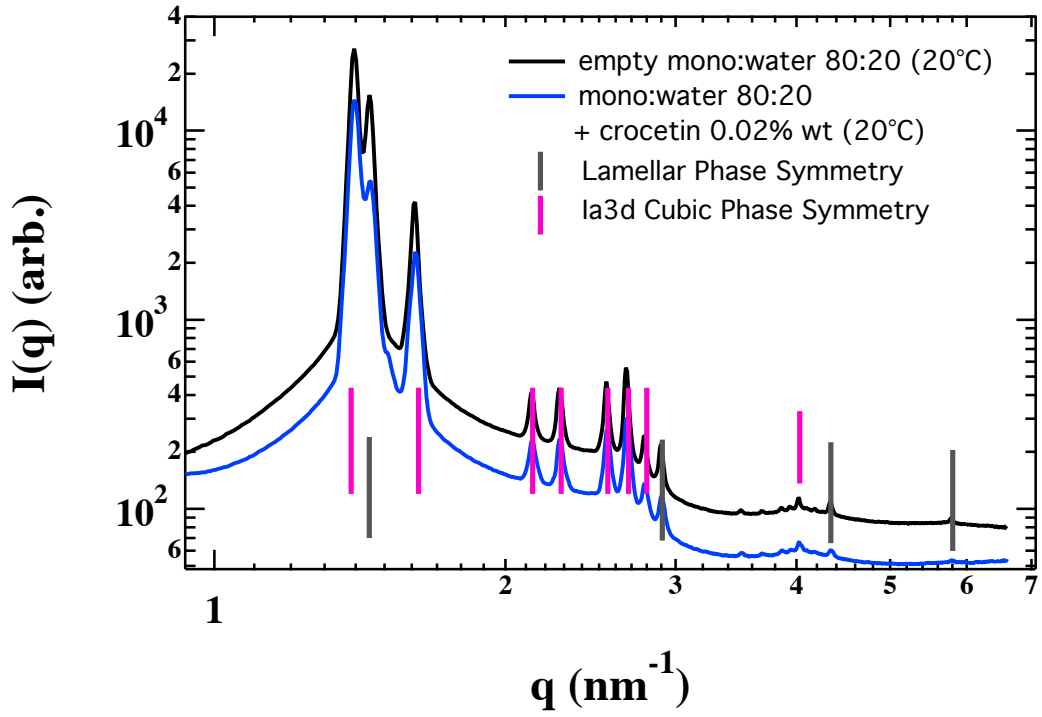

Figure 2.22 in the following graph is reported the comparison between curves relative to the empty monoolein:water (ratio 80:20, black curve) and of the same but in the presence of crocetin (0.02%wt, blue curve), both at 20°C. Black lines in the graph represent the expected position of reflections for the Lamellar Phase symmetry; pink lines that one expected for the Cubic *Ia3d* Phase symmetry

Table 2.14 unit cell value (±1Å) of empty monoolein:water 80:20 and of monoolein:water 80:20 in the presence of crocetin 0.02%. In the last two columns phase symmetry has been reported, both in presence and absence of crocetin

Temperature (°C)	unit cell value (±1 Å) mono:water 80:20	unit cell value (±1Å) mono:water 80:20 +crocetin 0.02%	phase symmetry mono:water 80:20	phase symmetry mono:water 80:20 + crocetin 0.02%
20	43.3/109.9	43.3/110.3	Lamellar (L_c)/Cubic *Ia3d*	Lamellar (L_c)/Cubic *Ia3d*
30	108.9	108.4	Cubic *Ia3d*	Cubic *Ia3d*
40	107.4	106.7	Cubic *Ia3d*	Cubic *Ia3d*
50	105.9	105.2	Cubic *Ia3d*	Cubic *Ia3d*
60	104.6	103.8	Cubic *Ia3d*	Cubic *Ia3d*

As mentioned before, cubic phase does not show any kind of anisotropic texture when observed using polarized light microscopy. No textures have been detected.

Only cubic phase symmetry has been observed in the case of monoolein:water ratio of 75:25. The two final graphs obtained both in absence (upper graph) and presence (lower graph) of crocetin can be showed in Figure 2.23. As expected, no anisotropic textures have been observed using polarized-light microscopy and of consequence not reported here.

No variations have been reported, both in presence and absence of crocetin, exception made for mono:water 75:25in presence of crocetin (lower graph, Figure 2.23) at 60°C. Probably here the presence of multiple reflections can be interpret hypothesizing a three-phase symmetry, composed of two different typologies of

cubic phase (a Pn3m and a Ia3d), together with an hexagonal phase. Probably at higher temperatures what happens is the expulsion of crocetin from the monoolein:water system that leads to a completely different inner organization of the lipid.

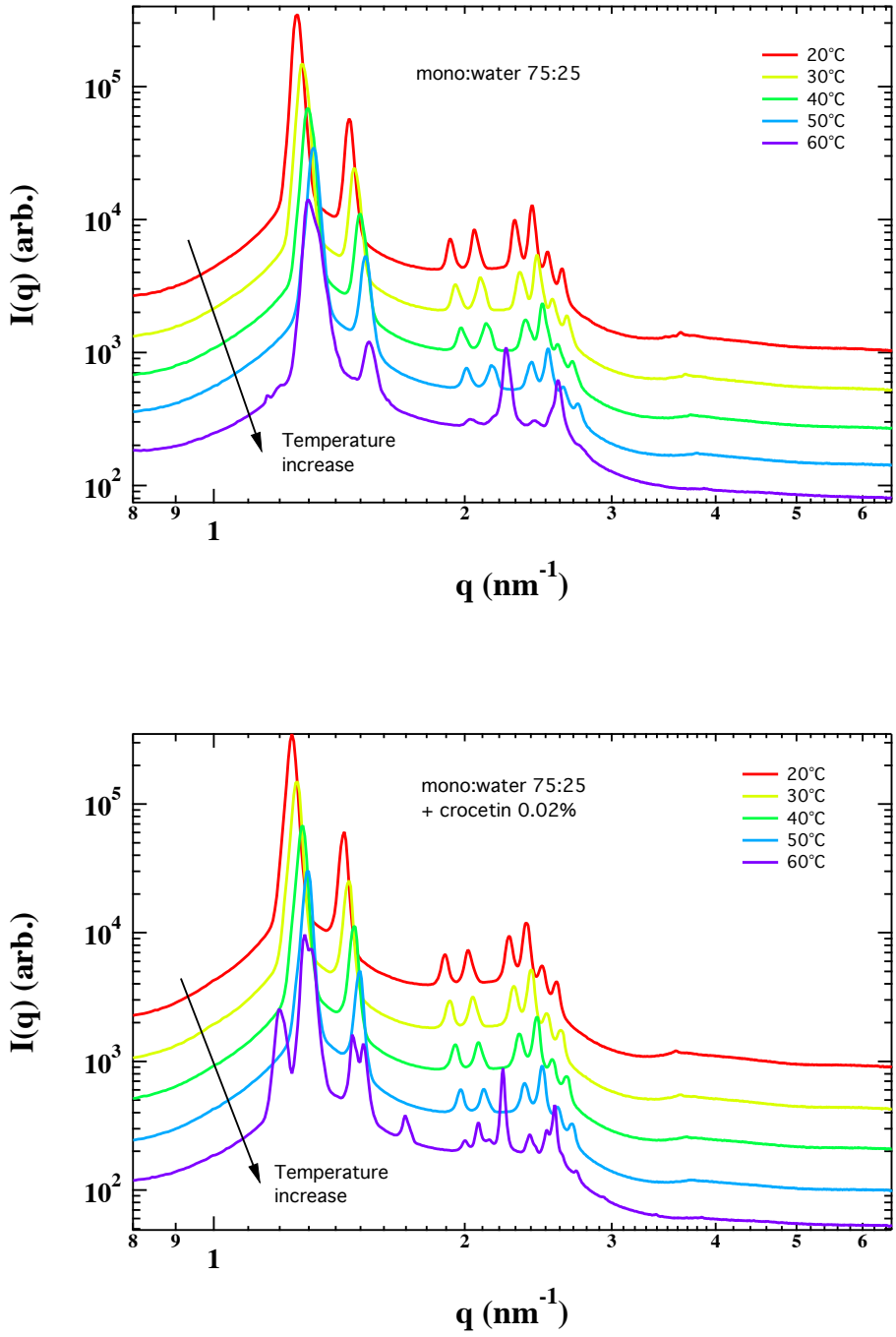

Figure 2.23 final graphs relative to measurements of monoolein:water 75:25 ratio made as function of temperature (from 20, red curve, to 60°C, purple curve); in absence (upper graph) and presence (lower graph) of crocetin at 0.02% wt. Black dashed arrows indicate the variation of the position of 1st order reflection of cubic phase symmetry. Diffraction profiles of cubic phase have been shifted using offset, to make easier to appreciate phase transition during the temperature variation and of course symmetry of the phase, given by the exact ratio between peak position

Table 17 unit cell value (±1Å) of empty monoolein:water 75:25 and of monoolein:water 75:25 in the presence of crocetin 0.02%. In the last two columns have been reported phase symmetry (both in presence and absence of crocetin)

Temperature (°C)	unit cell value (±1 Å) empty mono:water 75:25	unit cell value (±1Å) mono:water 75:25 +crocetin 0.02%	phase symmetry empty mono:water 75:25	phase symmetry mono:water 75:25 + crocetin 0.02%
20	122.2	123.6	Cubic *Ia3d*	Lamellar (L_c)/Cubic *Ia3d*
30	120.2	122.2	Cubic *Ia3d*	Cubic *Ia3d*
40	118.9	120.7	Cubic *Ia3d*	Cubic *Ia3d*
50	117.0	119.3	Cubic *Ia3d*	Cubic *Ia3d*
60	115.7/55.8	117.7/74.0/56.5	Cubic *Ia3d*/Hexagonal	Cubic *Ia3d*/cubic Pn3m/hexagonal

For this couple of samples at 75:25 mono:water a bizarre phase transition has been evidenced at higher temperature (purple curve in the previous layout), as mentioned before. To make easier the comprehension of multiple phases present at higher temperature in Figure 2.25 has been reported peak indexing made about profiles relative to 60°C, compared with that one at 20°C, both in the absence and presence of crocetin 0.02%.

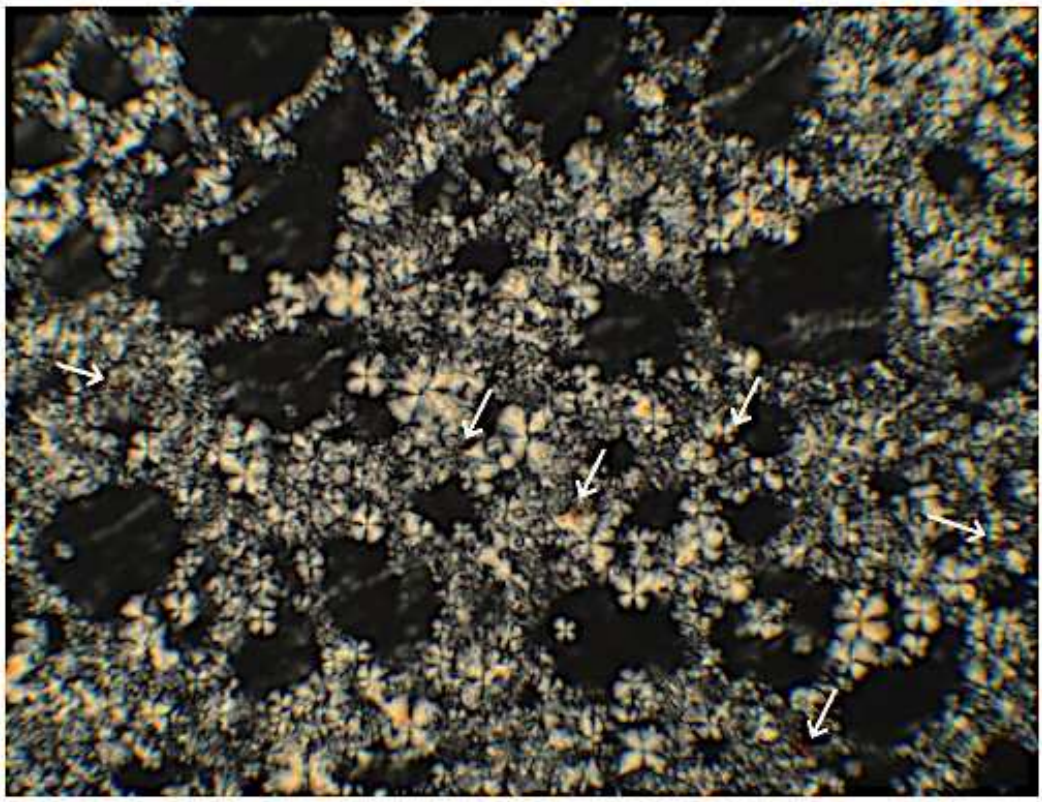

Figure 2.24 monoolein:water 95:5 in presence of crocetin in concentrations upper than 0.02% wt. Example of detection using POM of unsolubilized crocetin. White arrows indicate excess of crocetin

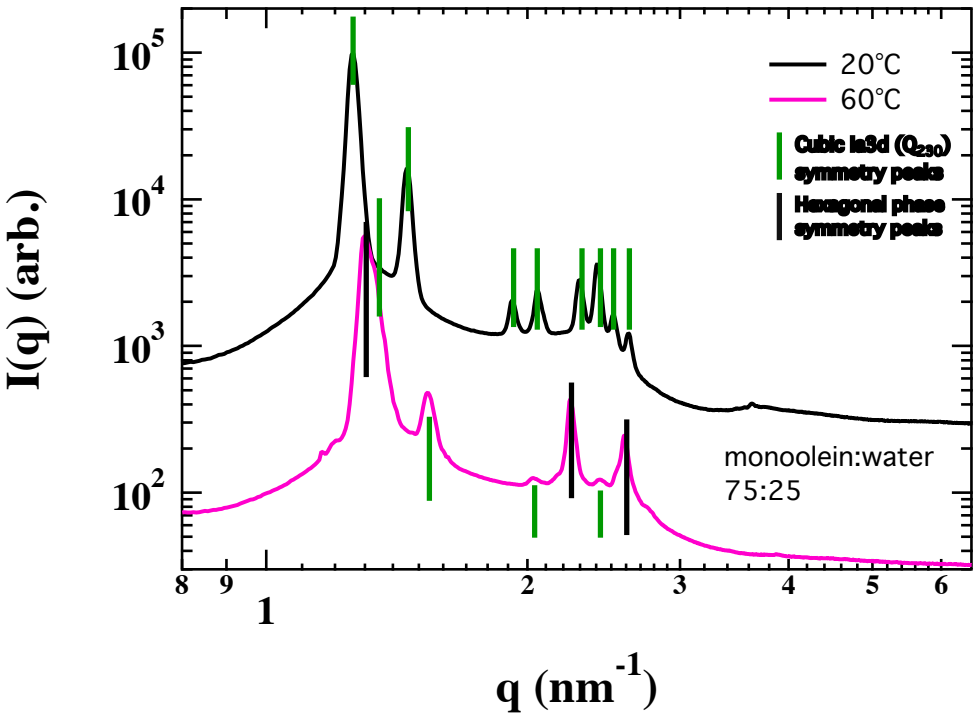

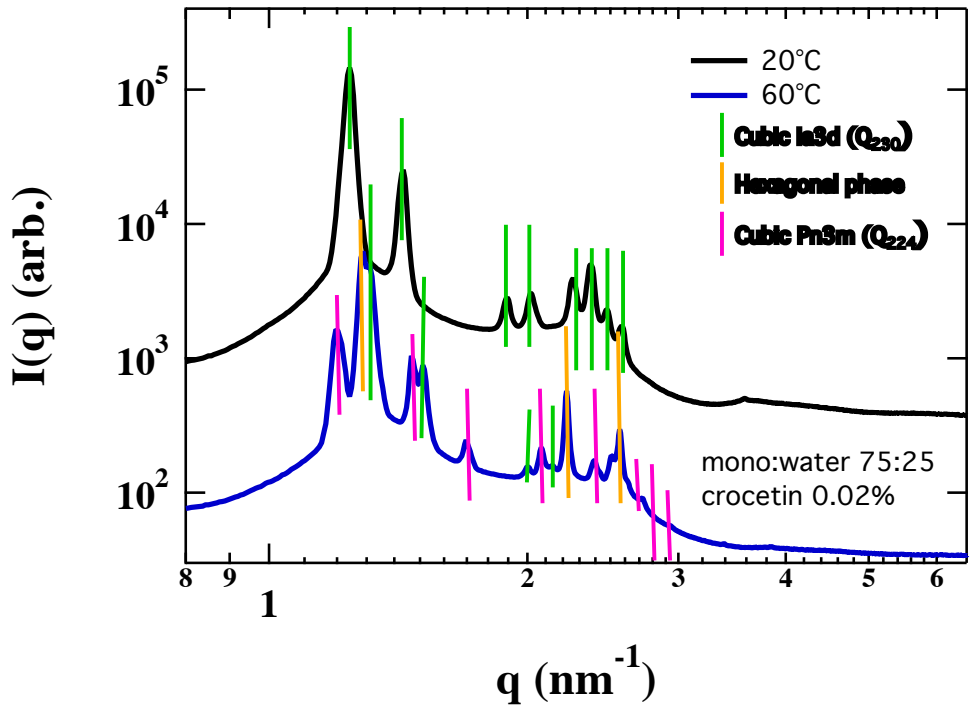

Figure 2.25 in the upper graph is reported the comparison between curves relative to the empty monoolein:water (ratio 75:25, black curve) at 20°C (black curve) and 60°C (blue curve). Green lines in the graph represent the expected position of reflections for the cubic phase symmetry *Ia3d* (Q_{230}), detected at low temperature. Pink lines indicate peak position expected for a cubic *224* (*Pn3m* phase symmetry). Finally, orange lines indicate the position of peaks in a hexagonal phase

Concluding, monoolein:water seems to be useful system in the solubilization of crocetin. Using small-angle x-ray scattering I firstly characterized monoolein:water different ratios to comprise which kind of phase symmetry characterized each ratio. To have an additional confirmation I performed POM observation of the phase assumed by the lipid:water system both in presence and absence of crocetin.
Observation using microscopy make possible to prove if the complete dissolution of crocetin inside the system has been achieved. When the molecule is not completely solubilized in the lipid:water system, this is clearly visible in the images, as reported in the image below and indicated using white arrows. (see Figure 2.24)

To summarize phase symmetry assumed by monoolein:water, both in the presence and absence of crocetin I reported in the following two graphs unit cell value (here reported in Å) as function of water content (5% means that monoolein:water ratio is 95:5).

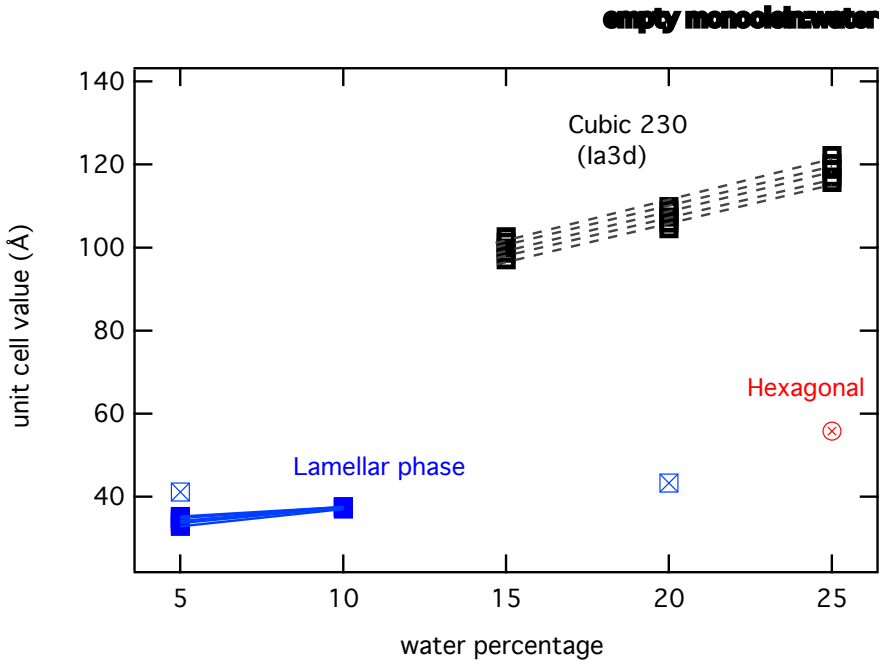

Figure 2.26 the following graph represents the unit cell value obtained for each sample as function of water percentage in monoolein: water system. Results are related to empty mono:water

Keeping in mind the monoolein: water phase diagram as reference (reported at the beginning of this paragraph), symmetries assumed from monoolein:water systems are exactly that one expected.
In the absence of crocetin (Figure 2.26, upper graph), at lower percentages of water, a lamellar phase organization can be obtained. Increasing the content of water in the system, a cubic phase is detectable, together with the phase coexistence at 20 and 25% of water.

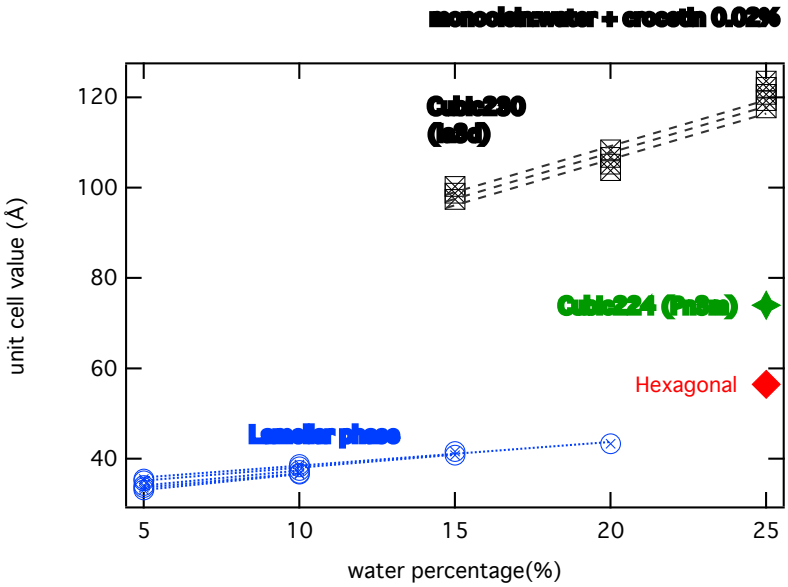

Figure 2.27 the following graph represents the unit cell value obtained for each sample as function of water percentage in monoolein: water system. Results are related to mono:water in the presence of crocetin 0.02% wt

In the presence of crocetin 0.02% (Figure 2.27) it is possible to appreciate the presence of a double-phase symmetry starting from 15 and 20% of water. At 25% of water probably there is the coexistence of three different phases, two cubic phases (Ia3d and Pn3m) and a hexagonal phase. Probably at high temperature what happens is the removal of crocetin and to a consequent re-organization of inner phase of lipid: water system.

Chapter 3

Chapter 3

DNA derivatives

3.1 Introduction

Everyone knows that DNA is the depository of genetic material of all living organism. Since the discovery and publication of the double helical structure of deoxyribonucleic acid in 1953 by Watson and Crick (thanks also to the work made by Rosalind Franklin, who collects X-ray diffraction profiles of DNA double-helix), a revolution has been started in science (Watson and Crick, 1953). The genetic information in DNA is encrypted in the sequence, which is constituted by four elements adenine A and guanosine G (purine bases); cytosine C and thymine T (pyrimidine nucleobases). These four different elements are able to bound in a complementary way (A with T, G with C). Considering thermodynamics, when A/G on one strand is bound with a T/C on the opposite, this polymer is in its most stable state, thus at the lowest free energy value (Seeman, 2015). In figure 3.1 can be showed the structure of a DNA-B molecule: is important to mention that the backbones are antiparallel, so the strands have a precise directionality. A description that I loved about the base pairing has been given by Seeman "Structural DNA Nanotechnology", Cambridge University Press (Material Research Society), 2015, and is: […] "When we are talking about A pairing with T and G pairing with C, we are talking about hydrogen bonded interactions. […] The A and G consist of a 5-membered ring fused to a 6-membered ring, and there are 4 nitrogen atoms in the nine atoms that make them up, and this group is called a *purine*. T and C consist of a 6-membered ring containing two nitrogen atoms, these are called *pyrimidines*. If we look at the hydrogen bonding pairs, we see that there are two hydrogen bonds indicated between A and T and three hydrogen bonds indicated between G and C. […]. There is something else different about the hydrogen bonding between A and T, C and G. We should recall that hydrogen bonds are directional interactions; indeed, those shown in figure 3.1 are indicated as little red arrows, to emphasize this directionality. They are said to be donated from the hydrogen atom to the electron-rich atom at which the arrow points. If we focus at the N-H→N hydrogen bond at the centre of each base pair, we see that in the A-T the donation is from a T to the A i.e., from the pyrimidine to the purine. By contrast, in G and C the donation is from the purine (G) to the pyrimidine (C). The third hydrogen bond in the G-C base pair can be thought as a bonus. Thus, we see that there is information in the structure of the bases that selects the base pairing partners […]". It is very well known that the so-called Watson-Crick base pairing is not the only way with nucleobases combine, and other phenomena will be discussed in the next paragraph.

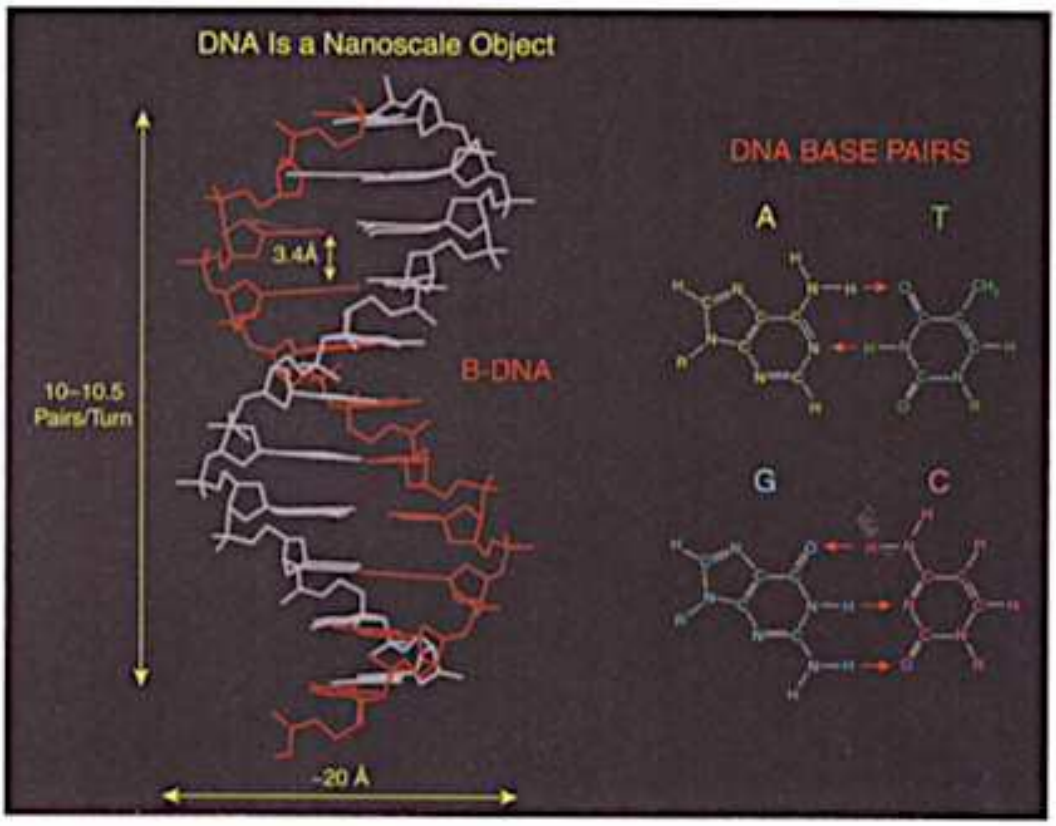

Figure 3.1 DNA-B form. In the figure are reported dimensions (left) and base pairing details (right). Image taken from the book "Structural DNA nanotechnology" by Nadrian C. Seeman, Cambridge University Press (MRS), 2015

3.2 Guanosine self-assembly

Going out of the canonical description of the DNA-B structure, there are several ways in which nucleotides can be paired, which can be grouped as "non-Watson–Crick DNA pairing". The most prominent non-canonical way to pair can be found in guanosine, which is the only DNA nucleobase to be able to pair with itself, according to the Hoogsteen scheme (Smith & Feigon, 1992). As reported in the introduction and as it is possible to observe in Figures 3.2 and 3.3, guanosine nucleosides and nucleotides are known to self-associate in water to form complex supramolecular architectures.

In diluted water solution, guanosine derivatives are able to form cyclic tetrameric units, defined as G-quartets (Figure 3.2). The formation of the tetrameric unit can be considered the initial step of a more complex supramolecular hierarchical assembly. Due to the presence of aromatic rings, the surfaces of tetramers are essentially hydrophobic. This fact leads to the stacking of G-tetrad on top of one another, up to the formation of cylindrical structures, called G-quadruplexes (Figure 3.3, A-D).

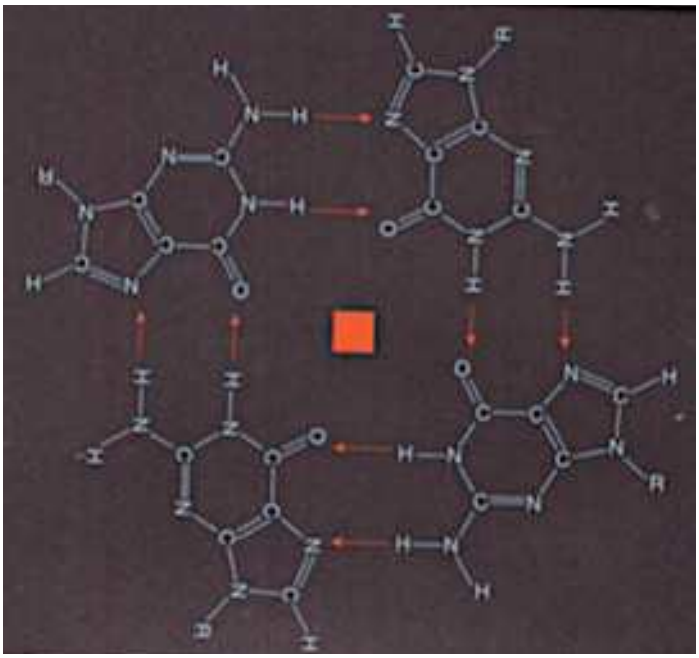

Figure 3.2 the G-tetrad structure. Four guanine molecules are connected following the Hoogsteen scheme: two donors on the Watson-Crick hydrogen-bonding surface donate two H-bonds to the two acceptors on the major groove side of the adjacent base. Image taken from the book "Structural DNA nanotechnology" by Nadrian C. Seeman, Cambridge University Press (MRS), 2015.

Who plays a key role in the stability of the whole architecture is the counterion, which must have two special features: a single positive charge (monovalent) and an appropriate size to fit in the inner cavity of a G-quartet. The stabilizing activity of cations follows this order: $K^+ \geq Na^+ \geq Rb^+ \geq NH_4^+ \geq Cs^+ \geq Li^+$. The fact that Na^+ and K^+ are characterized by the higher stabilizing activity probably is related with a regulatory process evidenced in cells, made by a switch process between two DNA forms (linear and G-quadruplex), first reported by Sen and Gilbert in 1988. (Sen and Gilbert, 1988).

So, the G-quartets associate through π−π stacking and the coordination of the centrally located metal cations with the eight oxygen atoms of two faced guanines. Depending on concentration and temperature, octamers (two G-quartets piled one on the top of the other) or longer columns, defined as G-quadruplexes, form.

Indeed, the stacked G-quartets are rotated of about 30 degrees one with respect to the next one, to minimize the hydrophobic repulsion between G-tetrads surfaces, so that a four-fold helix results (see Figure 3.3). Guanosine derivatives exhibit a further step in their hierarchical self-assembly: increasing concentration, G-quadruplexes organize in liquid-crystalline phases of cholesteric or hexagonal types (as described in section 3.3)

The formation of guanosine- and guanosine derivatives-based hydrogel has been also reported and will be widely discussed in Chapter 4.

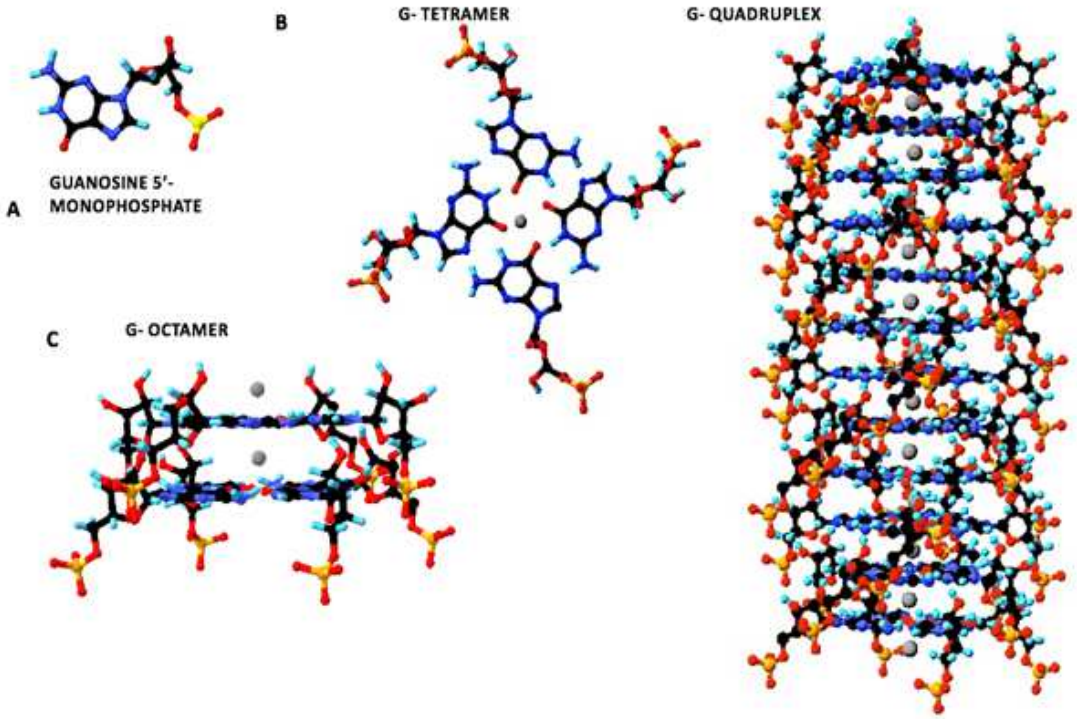

Figure 3.3 hierarchical self-assembly of guanosine 5'-monophosphate (5'-GMP). 5'-GMP monomer (A) G-tetrad (B), octamer (C) quadruplex (D). Image made using Swiss PDB viewer

3.3 Lyotropic Liquid Crystalline behaviour of DNA and DNA derivatives

DNA molecule is a right-handed double helix of 22 Å of diameter. Genetic information is encoded essentially in the DNA structure. The two strands of the helix are complementary in their nucleotide sequence with about 10 nucleotide pairs per helical turns (Livolant F. and Leforestier, 1996). In general, DNA is considered as double-stranded helices, but this polymer may exist in a wide range of conformation, depending on the DNA interhelix spacing.

In my opinion, what makes the structure of nucleic acids so extraordinary is the way with this polymer can organize its structure to "fit" in a so limited environment, the nuclear envelope. This can be appreciate considering multiple phenomena of condensation and decondensation to which DNA is subjected during cell cycle (Teif and Bohinc, 2011). When DNA molecules are confined in a restricted area, in presence of counterions, condensed phases of this polymer can be obtained. *Condensed* phases of DNA refer to liquid-crystalline mesophases.

Increasing DNA concentration of linear DNA molecules what will be enhanced is the level of organization, as showed in the following scheme reported in Figure 3.4: there are many ways to produce highly-concentrated DNA samples, such as the easiest one which consists in the dissolution of lyophilized DNA in a very small amount of buffer: using this procedure scientists reported for the first time about *cholesteric phase* (Robinson, 1961) and *columnar hexagonal phase* (Luzzati and Nicolaieff, 1959; 1963).

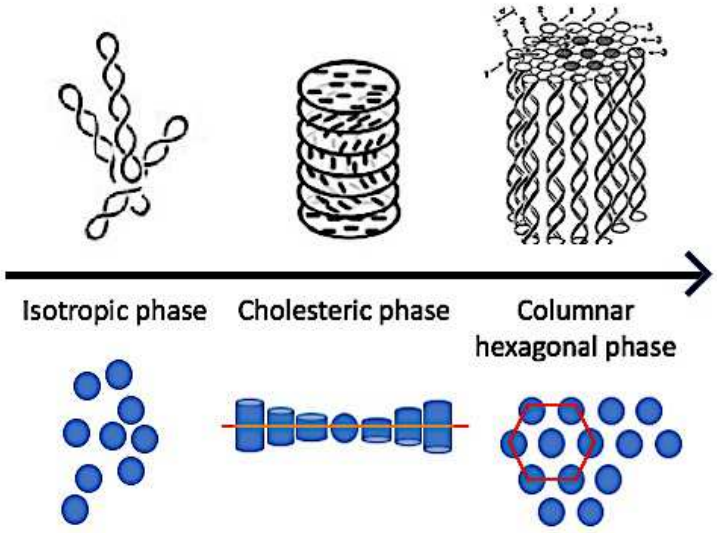

Figure 3.4 formation of liquid crystalline mesophase in DNA as function of the increasing concentration and of consequence of the level of molecular order

3.3.1 DNA derivatives: columnar mesophases

The first report that high molecular weight DNA might form liquid crystalline phases was made in 1959 by Luzzati and Nicolaieff (Luzzati and Nicolaieff, 1959). They identified two different levels of organization, including hexagonal and cholesteric phase, that one suggested by Robinson (Robinson, 1961).

When polymer (such as polynucleotide, polysaccharides and polypeptides) concentration increases, cholesteric spherulites appear within the isotropic phase and, at higher concentrations, the cholesteric regions expand to occupy the entire preparation **(**Mariani and Rustichelli, 1992**).** In the cholesteric phase, molecules are aligned in parallel along a direction, the so-called cholesteric axis, and their orientation rotates continuously. As reported by Livolant (Livolant and Leforestier, 1996) […] "The cholesteric phase can also be described as a "supramolecular" organization […], this due to the fact that the structural building units of this mesophase are the individual DNA helices that make it describable as a cholesteric superhelix.
The hexagonal phase can be imagined as a hexagonal array of more or less ordered columns, helices are at very close contact, but they maintain the capacity to freely rotate around their axis and to translate along this axis.

A more detailed description about the phase determination of columnar phases using X-ray diffraction can be found in the following paragraph**.**

3.3.2 Phase identification of Columnar mesophases of DNA derivatives

As briefly described in the previous paragraphs, DNA solutions can spontaneously undergo transition to a liquid crystalline state above a critical concentration (Livolant, 1986). To explain how has been made the comprehension of the phase behavior using X-ray diffraction, I refer to a system investigated during my PhD. In Figure 3.5 it is possible to show the main differences between an X-ray diffraction profile obtained from a cholesteric phase (upper) and a columnar hexagonal (lower). Only a very broad and weak band is present in

the low-angle region, centered around 0.12Å^{-1}, in the case of cholesteric mesophase. Different is the morphology of the reflection in the case of more concentrated samples. A narrow peak can be distinguished in the case of a hexagonal columnar hexagonal phase of binary mixtures of guanosine (G) and guanosine 5'-monophosphate (GMP), typically centered around ≅0.18Å^{-1}.

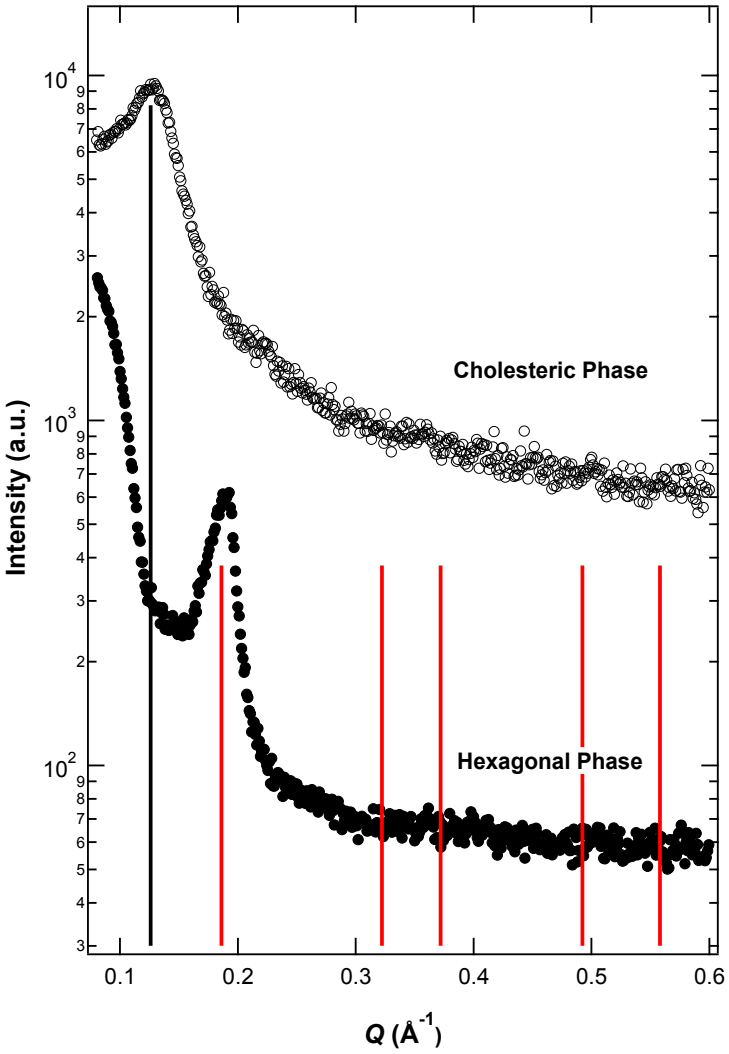

Figure 3.5 comparison between XRD profile of a cholesteric and hexagonal phase

As reported in the chapter of Mariani and Rustichelli, 1992 and as described in the section 1.5 for lipids, the ratios of the peak spacing in unit S (where S is 2sinθ/ λ; and λ is the X-ray wavelength) are $1:\sqrt{3}:\sqrt{4}:\sqrt{7}$ thereby indicating a two-dimensional hexagonal lattice. Using the convention usually adopted in lipid crystallography, the spacing of the symmetry permitted reflections in the case of a 2D-hexagonal symmetry are given by

$$S_{hk} = (1/a)(h^2 + k^2 - hk)^{1/2}$$

where h and k are the Miller indices of the reflection and a is the unit cell dimension. The position of reflections in the low-angle region changes as linear function of water content.

Different is the case of signals revealed in the high-angle region (q>0.6Å^{-1}). A brief description can be found in the next paragraph.

3.3.3 Stacking analysis

The high-angle region remains characterized by the presence of a sharp peak at 3.3Å (Mariani e Rustichelli, 1992). The presence of this reflection, in all the experiments made using X-rays about G4-based systems, represent the confirmation of the presence of G-quadruplex supramolecular assembly, in which quartets are stacked one respect to other at a distance of 3.3Å, the same of that one in DNA-B helix. No variation as function of some variables (such as temperature, water content) has been reported in the case of stacking signal.

The chiral cylinder represents the structural unit that can form either a cholesteric or a hexagonal mesophase, depending on the water content. At high dilutions, these aggregates give rise to isotropic solutions; increasing concentration, these solutions become cholesteric mesophases characterized by weak correlation between rods. Decreasing further water content, a hexagonal mesophase can be obtained. In this kind of liquid-

crystalline phase, rods are arranged in highly ordered array. As aforementioned, this model also explains the presence of the peak at 3.3Å in high-angle region, related to the distance between the planar tetramers of guanosines inside the columns. The occurrence of this peak also in the cholesteric phase indicates that the columns of stacked guanosine are already present in diluted solution (Mariani e Rustichelli, 1992).

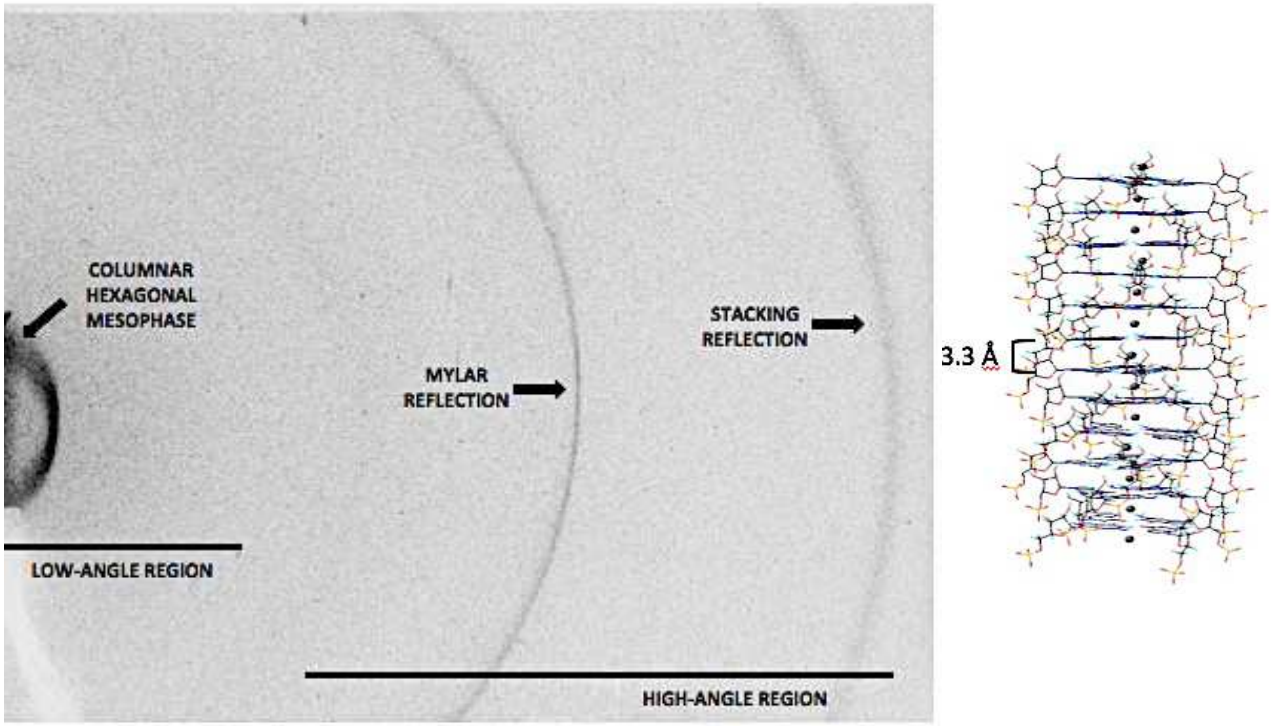

Figure 3.6 typical diffraction profile of an hexagonal phase obtained from guanosine derivative. Here is reported the distinction between low- and high-angle region

Small Angle X-Ray Scattering (SAXS) measurements have been performed using a NanoStar instrument (Bruker Corporation). The wavelength of the incident beam has been λ=1.54Å and the explored *Q*-range extended from 0.05 to 0.4Å^{-1} (q is the modulus of the scattering vector, defined as $4\pi \sin\theta/\lambda$, where 2θ is the scattering angle). Scattering data have been recorded on a 2-dimensional Bruker CCD camera of 1024 x 1024 pixels and corrected for background, detector efficiency and sample transmission. 2D data have been then radially averaged to derive *I*(q) vs q curves. Hydrogels have been measured at different temperatures (from 20 to 90 and then to 20°C, with usually 10°C of intervals) using the 1 mm sample holder provided with kapton windows. Particular attention has been paid to checking for equilibrium conditions and monitoring radiation damage. In a few tests, measurements have been repeated several times (up to 10) at the same temperature to account for a constant scattering signal.

A few high-angle X-ray diffraction experiments have been also performed. A Philips PW1830 X-ray generator equipped with a Guinier-type focusing camera operating in vacuum and a bent quartz crystal (λ = 1.54Å) has been used. Diffraction patterns have been recorded on GNR Analytical Instruments Imaging Plate system. Samples, held in a tight vacuum cylindrical cell provided with thin mylar windows, have been analyzed at room temperature.

Chapter 4

Chapter 4
G/GMP Hydrogels: macroscopical characterization, XRD analysis and Phase Diagram determination

4.1 Introduction: guanosine-based hydrogels

Guanosine nucleosides and nucleotides are known to self-associate in water to form supramolecular complex architectures (Mariani and Saturni, 1998; Mariani and Saturni, 1996; Mariani *et al.*,1989), but also hydrogel formation has been observed under certain experimental conditions and using different nucleoside and its derivatives. The state of art can be found in the most recent reviews of Peters and Dash (Peters and Davis, 2016; Dash and Saha, 2016).

The first clear observations of the ability of GMP 5'- and 3'-monophosphate to entrap large amount of water and leading to the formation of a self-standing and self-supporting hydrogels dated first to 1910 (Bang, 1910) and then to 1962, when Gellert (Gellert *et al.*,1962) evidenced (from GMP fibers) the presence of macrocyclic G-quartets as building blocks of the GMP gel phase.

The design and development of innovative supramolecular structures, based on the ability of biomolecules to self-assemble, is an extremely attractive field for nanotechnology, as suggested by the surprisingly large number of applications of biologically-inspired self-assembled nanostructures proposed in the last decade (Sangeetha and Maitra, 2005; Hirst *et al.*, 2008; Lau and Kiick, 2015; Sreenivasachary and Lehn, 2005; Sreenivasachary and Lehn, 2008; Mariani *et al.*, 1998; Yu *et al.,* 2008; Buerkle *et al.*, 2009; Adhikari *et al.*, 2014; Das *et al.*, 2012). In this context, special attention has been devoted to self-assembled material exhibiting gelation properties, as hydrogels can be used in a variety of applications, such as tissue engineering (Hunt *et al.*, 2014; Hirst *et al.*, 2008), enantiomer separation (Dowling, 2004), protein crystallization (Pietras *et al.*, 2010), drug delivery (Li and Mooney, 2016), sensor production (Dash *et al.*, 2011), and self-assembling confers promising properties.

As briefly mentioned in Chapter 1 and Figure 1.1, gels can be distinguished in *chemical*, formed by the irreversible cross-linking of polymeric material via the creation of covalent bonds and *physical* gels, characterized by the presence of non-covalent bonds (Peters and Davis, 2016). Self-assembled hydrogels can be classified as physical gels. Their formation is given by the spontaneous ordering of monomeric units into polymer-like supramolecular aggregates. When these aggregates maintain appropriate solvation in water, they can effectively entangle to immobilize the solvent and provide a 3D-network that possess similar properties to those exhibited by covalent hydrogels. However, the weak forces that stabilize the network of physical gels impart advantageous properties: softness, assembling/disassembling reversibility, adaptability to environmental changes (as pH, temperature, enzymatic activity, ionic strength...) and self-healing. Moreover, if the self-assembled hydrogels are made of biological molecules, they will also exhibit intrinsic biocompatibility and biodegradability (Peters and Davis, 2016).

In Chapter 4 and 5, attention will be focused on the extended characterization of hydrogels made using binary mixture of Guanosine (G) and Guanosine 5'-monophosphate (GMP). G/GMP mixtures ability to form in water stable and transparent gels over a temperature range that can be tuned by varying the relative proportions of the two components, has been reported for the first time in 2008 (Yu *et al.*,2008). GMP is highly soluble at neutral pH, increasing concentration what happens is a hierarchical process of self-assembling, (Figures 3.3 and 3.4) up to the formation of the columnar liquid crystalline phases (Mariani *et al.*, 2009; Mezzina *et al.*, 2001)

Guanosine is insoluble and forms a stable gel even in the presence of high salt concentrations (Dash and Saha, 2016). As a consequence, GMP helps to solubilize the insoluble G. Probably the insolubility of G, together with its key role in the decrease of the number of charges per unit length in the G-quadruplexes architecture, lead to the formation of the gel network. With the aim to investigate these fundamental roles played by G, an extended characterization is provided here.

4.2 Macroscopical characterization of guanosine-based hydrogels

4.2.1 Guanosine/Guanosine 5'-monophosphate hydrogels

As described in detail in Chapter 9, section 9.2.1, guanosine 5'-monophosphate (bought as free acid form) has been converted in potassium salt using KOH at high concentration (1M) performing chemical titration, followed by 2x washing with absolute ethanol, precipitation and lyophilizitation. The dried powder has been (re)dissolved in pure water to obtain a GMP-K^+ mother solution. The ability of this guanosine derivative to self-associate in water in presence of an appropriate counterion has been investigated focusing on the effect of lateral charges in G-quadruplexes, so reducing progressively the number of charge-per-disk adding guanosine (G). Chemical features of guanosine 5'-monophosphate provides a number of 2 negative charges for each molecule. Finding a way to insert G (chemically uncharged because not provided by the phosphate group) in the cyclic planar units of quadruplex architecture, has been calculated the exact volume of G and GMP to be inserted into a glass vial to obtain the wanted molar ratio between G and GMP in solution.

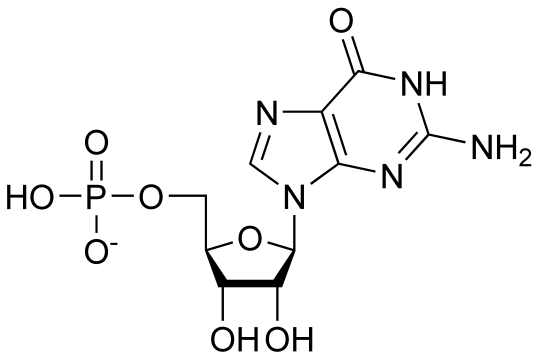

Figure 4.1 chemical structure of Guanosine 5'-monophosphate (GMP)

In the following table has been reported details about the analyzed samples. Volume fraction have been calculated using 0.651 cm^3/g as specific volume (Iball *et al.*,1963; Mariani *et al.*,1989). The number of charge-per-disk has been calculated considering the presence of 2 nominal charges provided by each GMP molecule.

Table 4.1 analyzed samples

G/GMP molar ratio	sample name	Charge-per-disk	$C_{p,\ wat}$	$C_{v,\ wat}$	flow ability (at 20°c)	macroscopic aspect at 20°c	extended $c_{v,\ wat}$ range analyzed
0	0	8	0.951	0.969	yes	transparent	-
0.067	1:15	7.50	0.951	0.969	yes	transparent	-
0.167	1:6	6.86	0.951	0.969	no	transparent	-
0.25	1:4	6.40	0.951	0.969	no	transparent	-
0.50	1:2	5.33	0.951	0.969	no	transparent	0.85-0.991
0.75	3:4	4.57	0.951	0.969	no	transparent	0.85-0.991
0.90	9:10	4.21	0.951	0.969	no	transparent	-
1.00	1:1	4.00	0.951	0.969	no	transparent	0.85-0.991
1.50	3:2	3.20	0.951	0.969	no	opalescent	-
2.00	2:1	2.67	0.951	0.969	no	opalescent	-

In this paragraph, results obtained about the macroscopical characterization, classification and consequent phase diagram determination will be presented and discussed. Second, attention will be focused on the analysis made about G/GMP swelling properties, that have been conducted both for the less hydrated systems (up to the 85% of water concentration) and for the more-hydrated systems (up to a hydration of 99.1%).

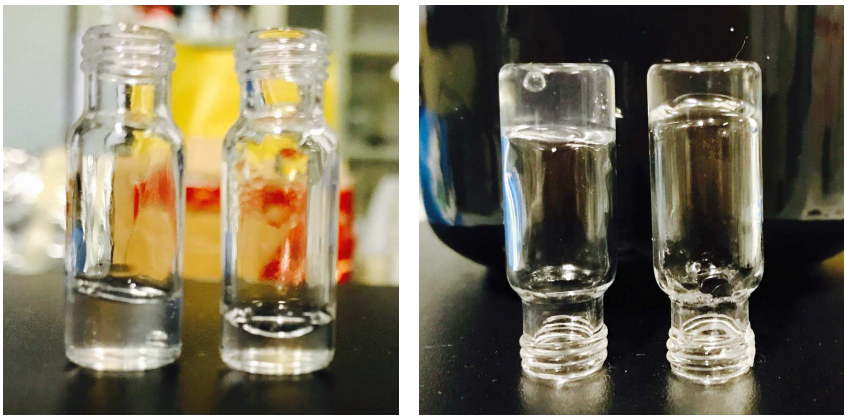

Figure 4.2 few examples of G/GMP hydrogels. On the left can be showed glass vials containing 1:1 and 1:2 G/GMP hydrogels. On the right, I reported the same samples but observed in inverted-glass vials to give a direct demonstration of the presence of gels

Hydrogel formation has been observed for all G/GMP ratios, exception made for 0.067 in which the binary mixture is in a solution state. Gel solutions have been characterized after mixing the exact volume of G/GMP and of consequence of water, to reach the final water concentration. To ensure the intimate mixing between G and GMP, the two components have been heat up to 90°C (until the formation of a liquid fluid state) and then let to equilibrate gel solutions up to room temperature. After this time of equilibration vials have been observed, inverted and consequently classified considering flow ability at 20°C (see column 5, table 4.1) and macroscopic aspect (column 6, table 4.1).

The final weight of G/GMP Hydrogels is 5% wt/vol. Who plays a key role in the formation of the 3D network is guanosine. This can explain the reason why G/GMP molar ratio 0.067 shows a flow ability at 20°C, as reported in Table 4.1**.** Probably, at this molar ratio, the number of guanosine molecules is too low and the lateral electrostatic forces even too high to allow G/GMP quadruplexes to be close.

Probably the phenomenon at the base of the formation of G/GMP hydrogel network is the minimization of lateral charges. This allows G/GMP-quadruplexes to entangle and thus to establish connections, not comparable with crosslinking points. The interweave of G/GMP cylinders leads to the entrapment of water in the 3D-network. Stable (over 1 year) and transparent hydrogels have been obtained without the addition of KCl.

Mechanical stress (e.g use of micropipettes or spatula) have been avoided to not interfere with the spontaneous orientation of molecules in the hydrogel network. Inverted-vial test has been used to macroscopically derive the gel-to-sol transition temperature and information about the reversibility of the phenomenon of gelation. Using a Lauda water thermostat, the determination of the transition temperature has been performed heating vials (starting from 20 up to 90°C, with a shift of 2 degrees). For each visualization and inspection, vials have been kept in Lauda holder for 5 minutes to let the samples equilibrate at each temperature. The gel-to-sol transition temperature has been considered as the temperature at which G/GMP solutions flow inverting tubes. Here, two distinct phases diagram have been reported: the first one (Figure 4.4, left graph) has been obtained considering a fixed water volume fraction ($C_{v,\,wat}$= 0.969). In this case transition temperatures have been reported as function of G/GMP molar ratios (Figure 4.4, left graph). The second one (figure 4.4, right graph) has been determined considering two different G/GMP ratios, 1:1 and 1:2, but exploring water concentration (from 0.85 up to 0.991). Data relative to the G/GMP 1:1 have been reported in the graph on the right usingempty rectangular. In both cases, this ratio seems to be the most stable.

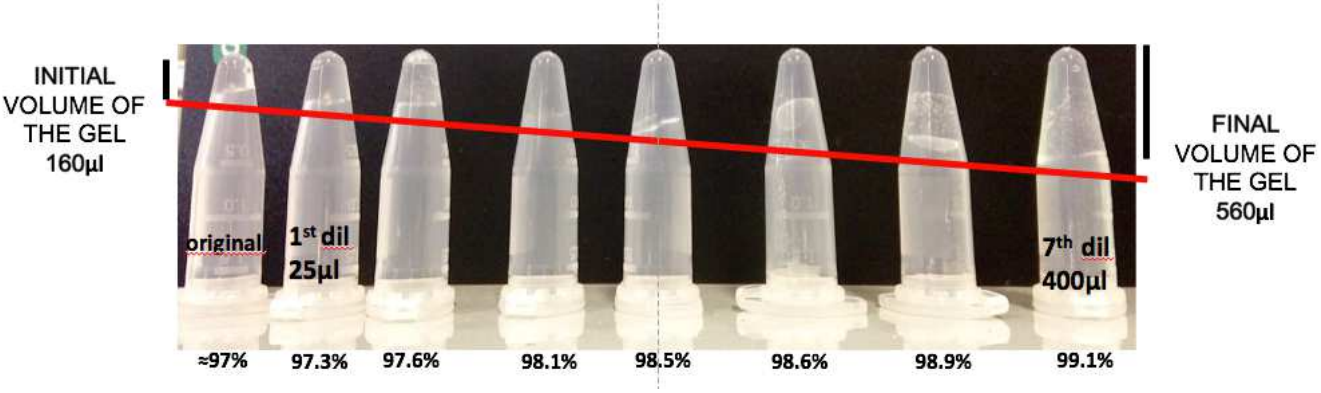

Figure 4.3 G/GMP 1:1 samples. Here is shown the progressive addition of water, starting from a $C_{v,\,wat}$ of 0.969, in the figure “original” (the first tube) up to 0.991. The volume fraction of water is indicated in the panel.

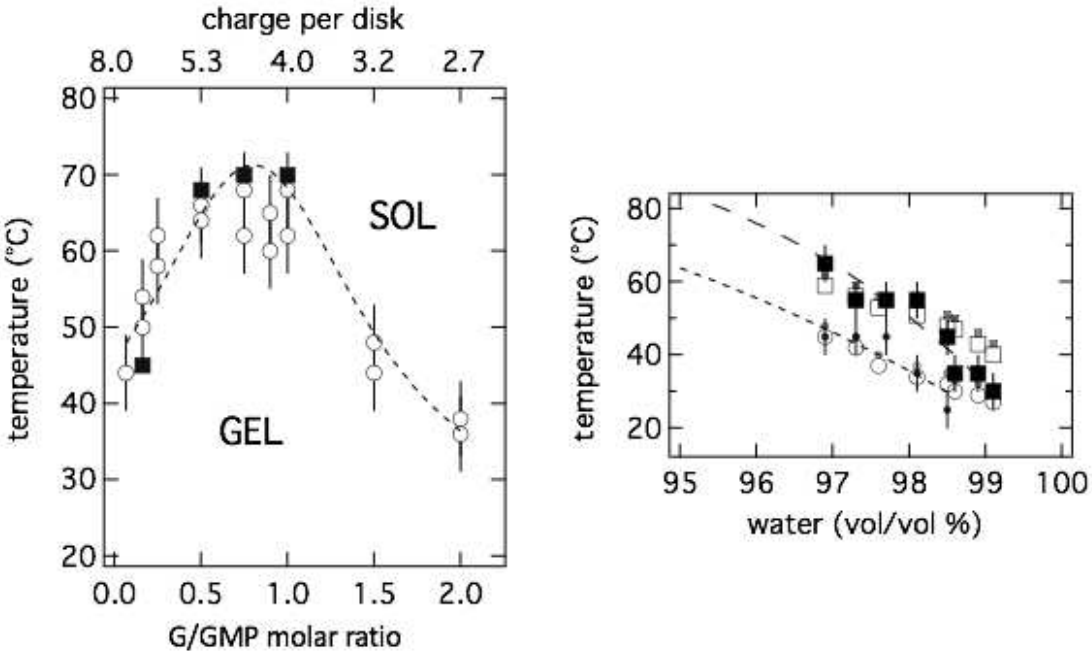

Figure 4.4 temperature-composition phase diagrams. In the left graph, can be showed that one obtained at fixed water concentration ($C_{v,wat}$= 0.969), exploring G/GMP molar ratios; the graph on the right represents the phase diagram obtained using two fixed G/GMP molar ratios 1:1 (empty rectangles) and 1:2 (empty dots). Filled dots and rectangles refer to SAXS data

Results show that the degree of entanglement of the hydrogel network and of consequence the thermal stability, depend on composition. In both phase diagrams reported here, temperature increases as function of the quantity of G added in the mixtures, but up to the 1:1 ratio. The Gaussian distribution of the temperature evidences clearly the fact that the temperature starts to decrease for further addition of G (after the 1:1 ratio). Focusing on results reported in the table x, it can be also underlined that white, opalescent samples have been obtained in the case of high amount of G, suggesting that in these conditions the nucleotide is not completely incorporated into the quadruplex structure, but they are in a gel state (e.g. 90% wt of water). On heating, clarification occurs a few ten degrees above the gel-sol transition. On the other side, pre-heated samples appear transparent and clear at all other ratios investigated, with a gel-sol transition temperature which is quite similar to the not pre-heated mixtures. Dilution effect is also very clear: as far as the water content increases, the gel-sol transition temperature decreases, conforming that guanosine hydrogel can trap a very large amount of water (up to 99% in volume), but the degree of entanglement is probably so high to ensure thermal stability.

4.2.1.1 Gel-to-sol transition temperatures determination using Polarized-light optical microscopy (POM)

Together with the determination of gel-to-sol transition temperatures performing the *canonical* inverted-vial test, the same information has been obtained using polarized-light optical microscopy in which slides have been observed using a Mettler Toledo hot-stage plate (in Chapter 9 can be found details about the preparation of samples, section 9.2.3.2; 9.5.1). Results have been coupled to compile phase-diagrams, both for the more-concentrated and the more-hydrated samples. A set of images is reported here below in Figure 4.5 to give an example of how the gel from the solution state can be distinguished using POM as technique. In addition, summarizing table (Tables 4.2-4.4) have been reported for each ratio investigated as function of water percentage (in weight, from the 85% up to the 99.1%).

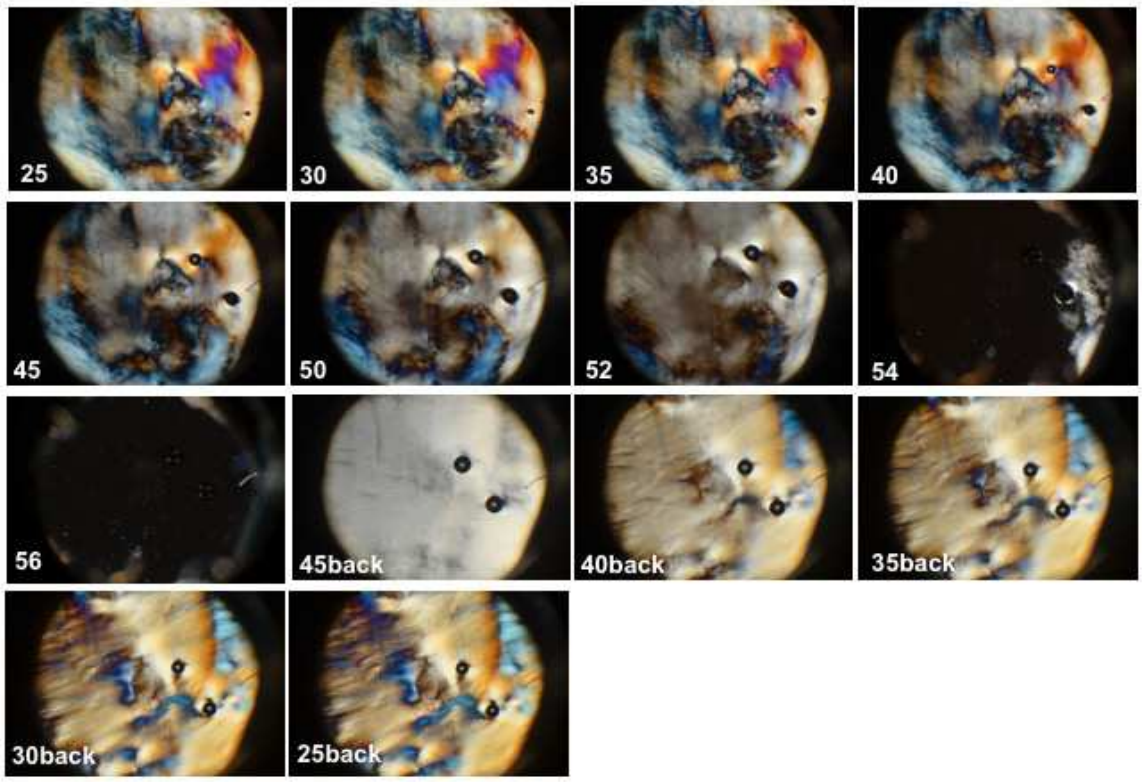

Figure 4.5a G/GMP 1:1 sample at 96.7% wt of water. Here is reported images obtained using polarized-light microscopy as function of temperature. Slide has been observed using a Mettler Toledo hot-stage plate.

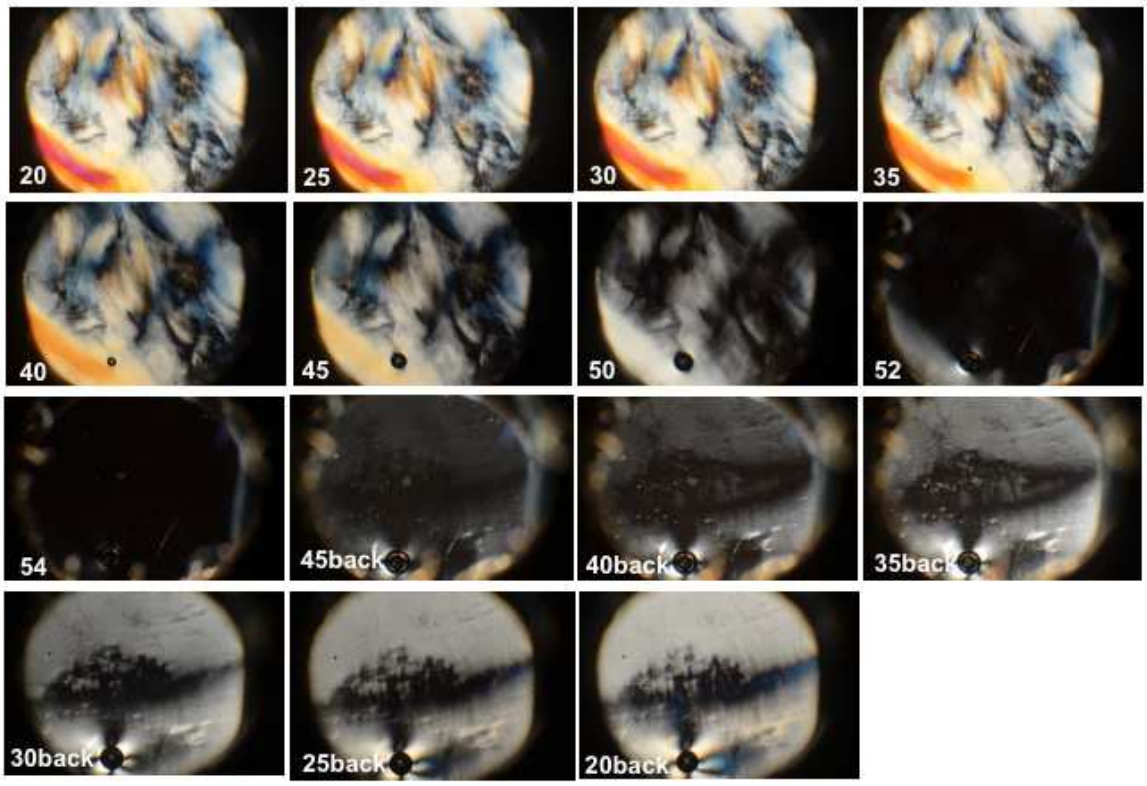

Figure 4.5b G/GMP 3:4 sample at 96.7% wt of water. Here is reported images obtained using polarized-light microscopy as function of temperature. Slide has been observed using a Mettler Toledo hot-stage plate.

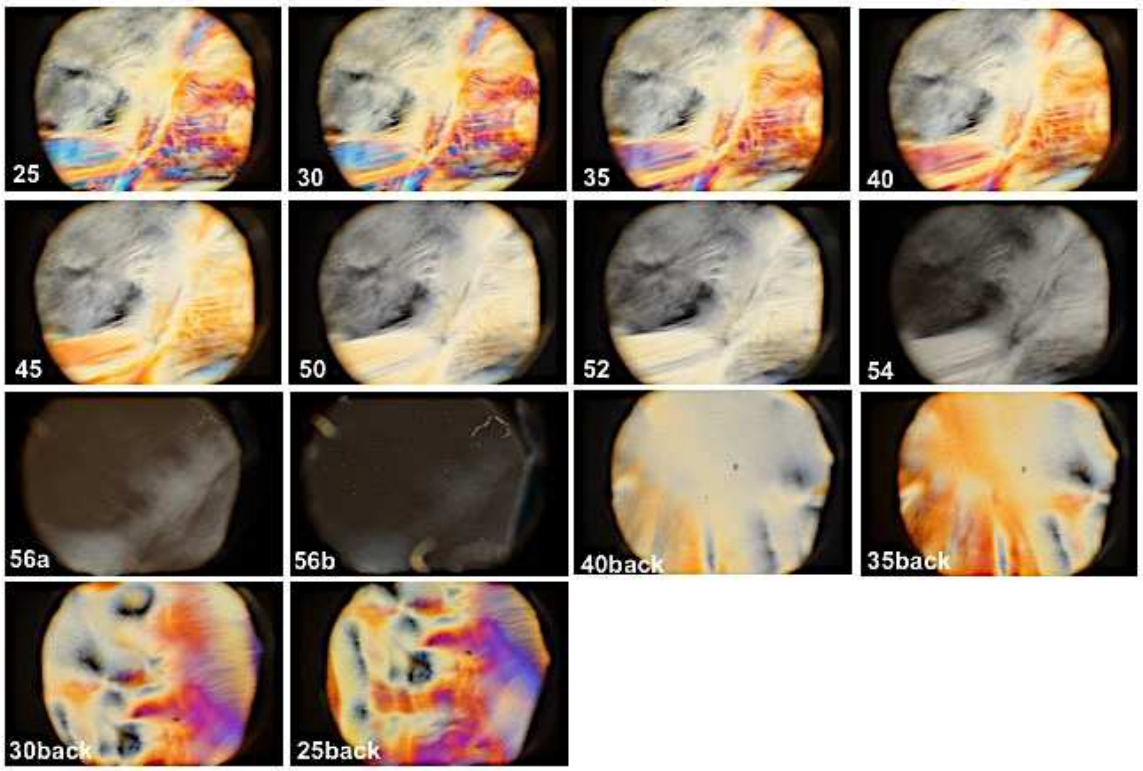

Figure 4.5c G/GMP 1:2 sample at 96.7% wt of water. Here is reported images obtained using polarized-light microscopy as function of temperature. Slide has been observed using a Mettler Toledo hot-stage plate. Increasing temperature what happens is the disappear of the texture typical of a highly concentrated G/GMP hydrogel (figure 56b), exactly when the gel to sol transition happens. The process is completely reversible (figure 25back).

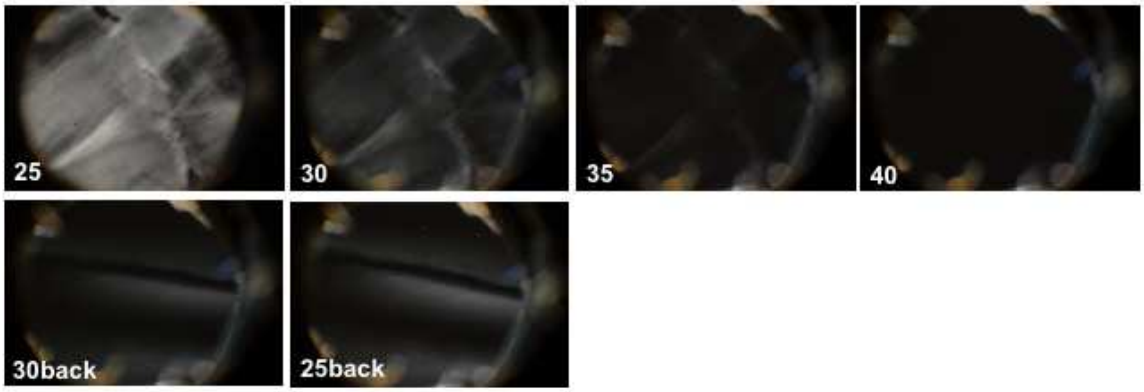

Figure 4.5d G/GMP 1:6 sample at 96.7% wt of water. Here is reported images obtained using polarized-light microscopy as function of temperature. Slide has been observed using a Mettler Toledo hot-stage plate.

At 25°C what can be observed is a colorful texture, typical of an anisotropic G/GMP hydrogel. This particular birefringence starts to disappear as function of the increase of temperature (50°C). When gel-to-solution phase transition occurs, nothing appears as birefringent (73°C). In this way, transition temperatures have been determined for 1:2, 3:4 and 1:2 G/GMP ratio, also varying water concentration in the system. In the case of 3:4 the more concentrated samples have been not measured, this due to its very similar behavior with the 1:1. Probably the highly colored profile at 25°C is due to the high quantity of G in the G/GMP solution.

Table 4.2 gel-to-sol transition temperatures evidenced using POM in the case of G/GMP 1:1

G/GMP 1:1	
water (%)	**gel-to-sol transition temp (±3°C)**
85.0	+140 (nd)
90.0	93
93.0	78
96.9	59
97.3	56
97.6	53
98.1	51
98.5	48
98.6	47
98.9	43
99.1	40

Table 4.3 gel-to-sol transition temperatures evidenced using POM in the case of G/GMP 3:4

G/GMP 3:4	
water (%)	**gel-to-sol transition temp (±3°C)**
96.9	60
97.3	55
97.6	53
98.1	51
98.5	47
98.6	47
98.9	45
99.1	43

Table 4.4 gel-to-sol transition temperatures evidenced using POM in the case of G/GMP 1:2

G/GMP 1:2	
water (%)	**gel-to-sol transition (±3°C)**
85.0	+110 (nd)
90.0	92
93.0	73
96.9	55
97.3	52
97.6	47
98.1	44
98.5	42
98.6	40
98.9	39
99.1	37

Phase diagram reported in figure 4.4 (right graph) refers to these results. For clarity, 3:4 has been not reported in the graph. Empty dots refer to 1:2 G/GMP, empty rectangles refer to 1:1 G/GMP.

What can be observed from the graph on the left, always in Figure 4.4, is that the most stable gel is the 1:1. An increase of the amount of G in the G/GMP ratio leads to the obtainment of a thicker network and consequently to a greater stability of the whole system, showed by a higher gel-to-sol transition temperature value. What is very interesting (considering the phase diagram made using the same water concentration but exploring G/GMP ratio, on the left) is the Gaussian distribution of data. This particular behavior indicates the fact that is not possible to make further additions of G in the G/GMP hydrogels going up to 1:1 ratio. The excess of G leads to an uncomplete solubilization of this compound, that is too high to be solubilized by GMP and of consequence, in this case, any transparent and stable hydrogel can be obtained.

4.2.2 Guanosine/Guanosine 2'/3'-monophosphate hydrogels

Following the same protocol used in the preparation of G/5'-GMP hydrogels, reported in Chapter 9 (section 9.2.3) mother solutions of 10% wt/v of Guanosine 2'/3'-Monophosphate have been prepared considering different salts, K^+, Na^+ and NH_4^+. This guanosine derivative is composed of a mixture of two different isomers, commercially available in the form of disodium salt and recently characterized in our laboratory.

Results obtained about phase diagrams and lateral force analysis using osmotic stress technique will be discussed in Chapter 7. Here is reported the first tentative made to obtain G/(2'/3')-GMP hydrogels.

Always with the aim to comprise both how the decrease in the number of lateral charges influences the behaviour of guanosine derivatives inducing gelation and the stability effect provided by counterion in the quadruplex architecture, initial mother solutions has been prepared considering guanosine 2'/3'-monophosphate disodium (commercially available) potassium and ammonium salt. These two latter kind of salts have been obtained chemically treating 2'/3'-GMP(Na_2) with Ion-Exchange Chromatography (Chapter 9, section 9.2.2). Mother solution have been consequently used in the G/GMP hydrogel preparation, together with Guanosine, in the same way of that one reported for 5'-GMP that can be found in Chapter 9, section 9.2.3.

Results obtained, reported in Figure 4.7, suggest that the stability effect provided by the counterions is the same considering 5'-monophosphate and 2'/3'-monophosphate of guanosine and is

$$Na^+ < NH_4^+ < K^+$$

In both cases, the hydrogel formation has been reported. That one made using potassium salt seems to be the most stable in both cases. A phase separation of G/2'/3'-GMPNa^+ hydrogel network has been reported after few hours from the hydrogel preparation. Probably the tendency of 2'/3'-GMPNa^+ to remain in the dehydrated state (evidenced also in the case of osmotic stress technique analysis, Chapter 7) leads to an uncomplete solubilisation of guanosine in the quadruplexes network that consequently starts to precipitate.

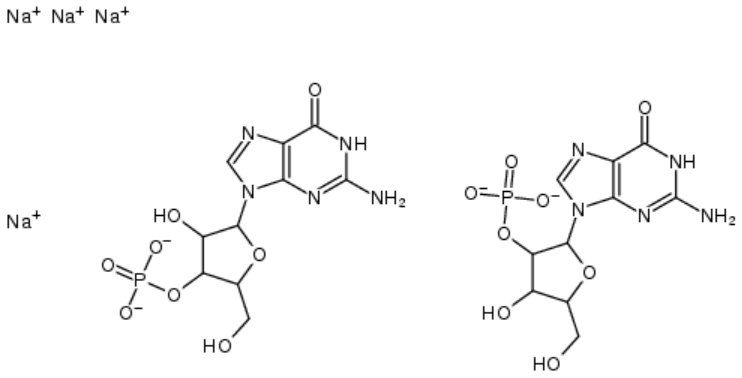

Figure 4.6 chemical structure of Guanosine 2'/3'-monophosphate (2'/3'-GMP)

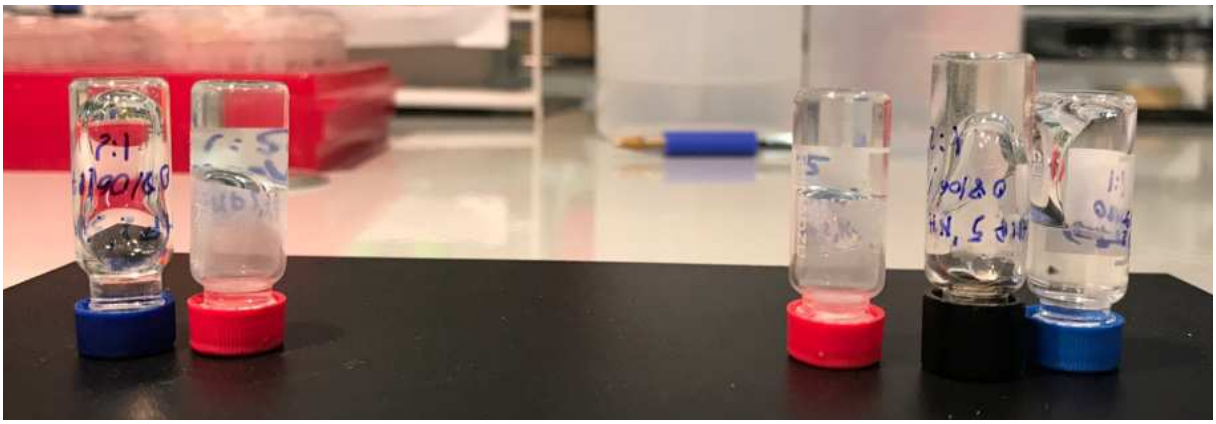

Figure 4.7a 2'/3'-GMP/G vs 5'-GMP/G hydrogels. From the left: ammonium (blue cap) and potassium (red cap) salts of the 2'/3'-GMP/G binary mixtures. On the right: potassium (red cap), ammonium (black cap) and disodium (blue cap) salts of the 5'-GMP/G binary mixtures.

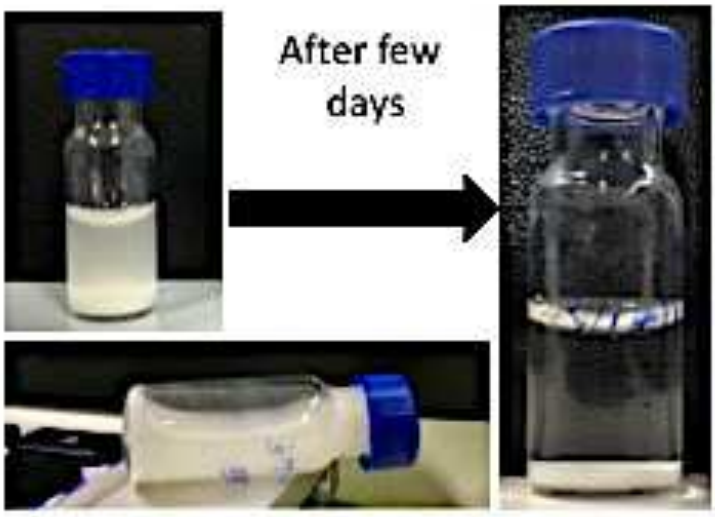

Figure 4.7b 2'/3'-GMP/G disodium salt. A very low-stable transparent gel forms after the annealing step but in few minutes a phase separation occurs and is clear visible in the left image.

4.3 Characterization of G/5'-GMP hydrogels using X-ray diffraction

4.3.1 The less-hydrated systems phase diagrams: low-angle region analysis

Phase diagrams relative to G/GMP hydrogels at water concentrations less than 96.9% have been compiled. Samples have been prepared in the following way, described also in Chapter 9, section 9.2.3.2.

An aliquot of G/GMP hydrogel has been taken and placed in a new tube, followed by the addition of absolute ethanol (in large excess) and then shaked to let the solvent being in contact with all the sample. The presence of ethanol provokes the precipitation of G/GMP. After the precipitation, a centrifugation has been made (8000 rpm for 10 minutes) and the excess of ethanol removed using a micropipette. Finally, samples have been lyophilized overnight and then re-hydrated choosing an appropriate amount of water.
An equilibration time of (at least) 24 hours is required to ensure the correct hydration of the system.
X-ray diffraction analysis have been conducted as function of temperature (from 20°C to 80°C). For example, observing the strong peak (Figure 4.9) relative to the organization of the 1:2 G/GMP in a liquid-crystalline mesophase and visible in the low-angle region, it's clear that it moves as function of the increasing content of water in the G/GMP ratio. In addition to the information relative to the mesophase organization, also a very strong reflection in the high-angle region can be observed and this will be discussed in the next paragraph.

Here I report results obtained in the case of G/GMP ratio 1, 0.5, 0.25 and 0.167. Water percentages explored have been from 50% to 80% in weight.
Information about the phase assumed by the hydrogel and ability of the G/GMP binary phase to re-hydrate have been obtained considering:
- a case in which the quantity of lateral charges is very low, the G/GMP 1:1, in which the charge per disk is 4, (see Table 4.1);
- the G/GMP1:2, in which the perfect equilibrium between components allows to obtain a transparent and stable hydrogel: in this case the charge-per-disk is 5.33, (see Table 4.1);
- a G/GMP ratio in which the quantity of lateral charges starts to be very high, this case refers to 1:6.

In general, can be affirmed that the peak related to mesophase assumed by G/GMP moves as function the increasing percentage of water and temperature investigated. Up to the 60% of water, small variations in the unit cell values have been reported. Considering the 80% of water hasn't been not possible to calculate peak position (e.g. Figure 4.9, lower graph) this for the high level of hydration of the system. In this case the setup of our instrument is not appropriate to detect signals in the small-angle region.

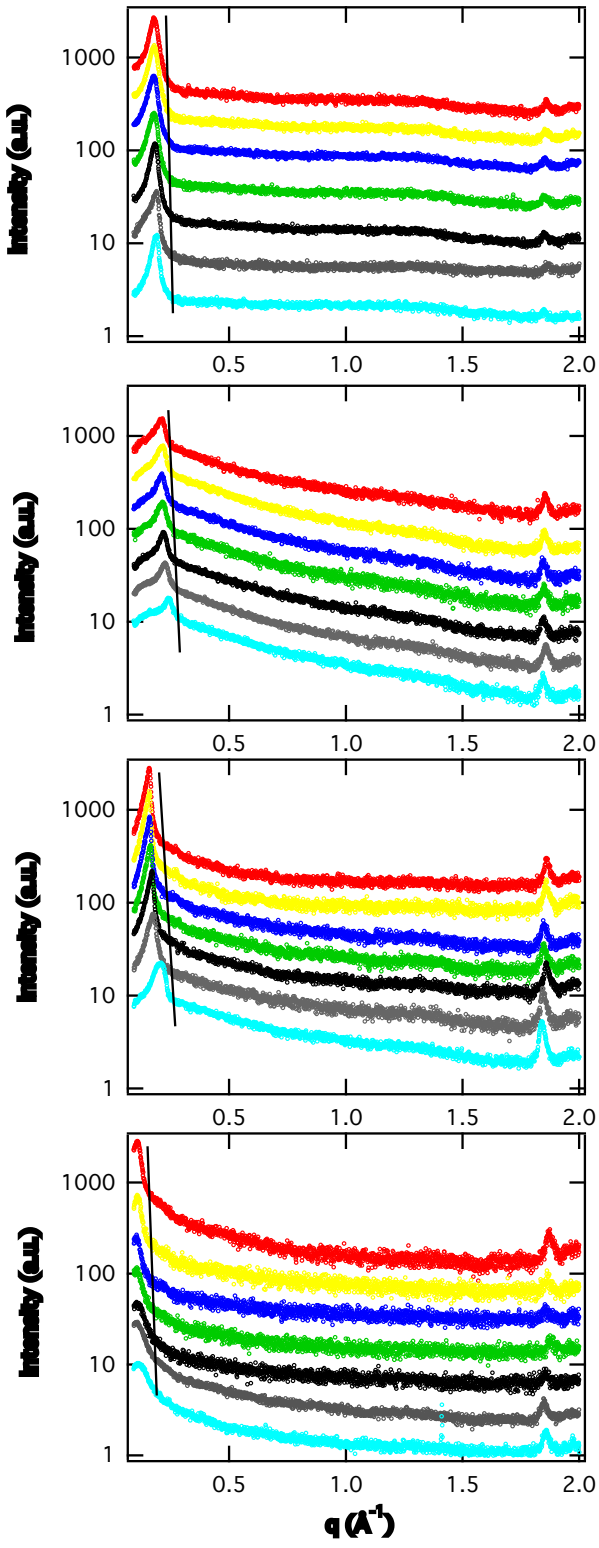

Figure 4.8 diffraction profiles relative to the low-angle region, obtained for the G/GMP ratio 1:1 reported here as function of temperature (from red 20°C to light-blue 80°C) and of the increasing percentage of water (from the upper graph, 50% wt of water, up to the lower, 80% of water). Black bar shows the trend of the peak position relative to the mesophase as function of the increase of the level of hydration. In addition, signal relative to the stacking of tetrads in the quadruplex (in the high-angle region) at 1.8Å^{-1}

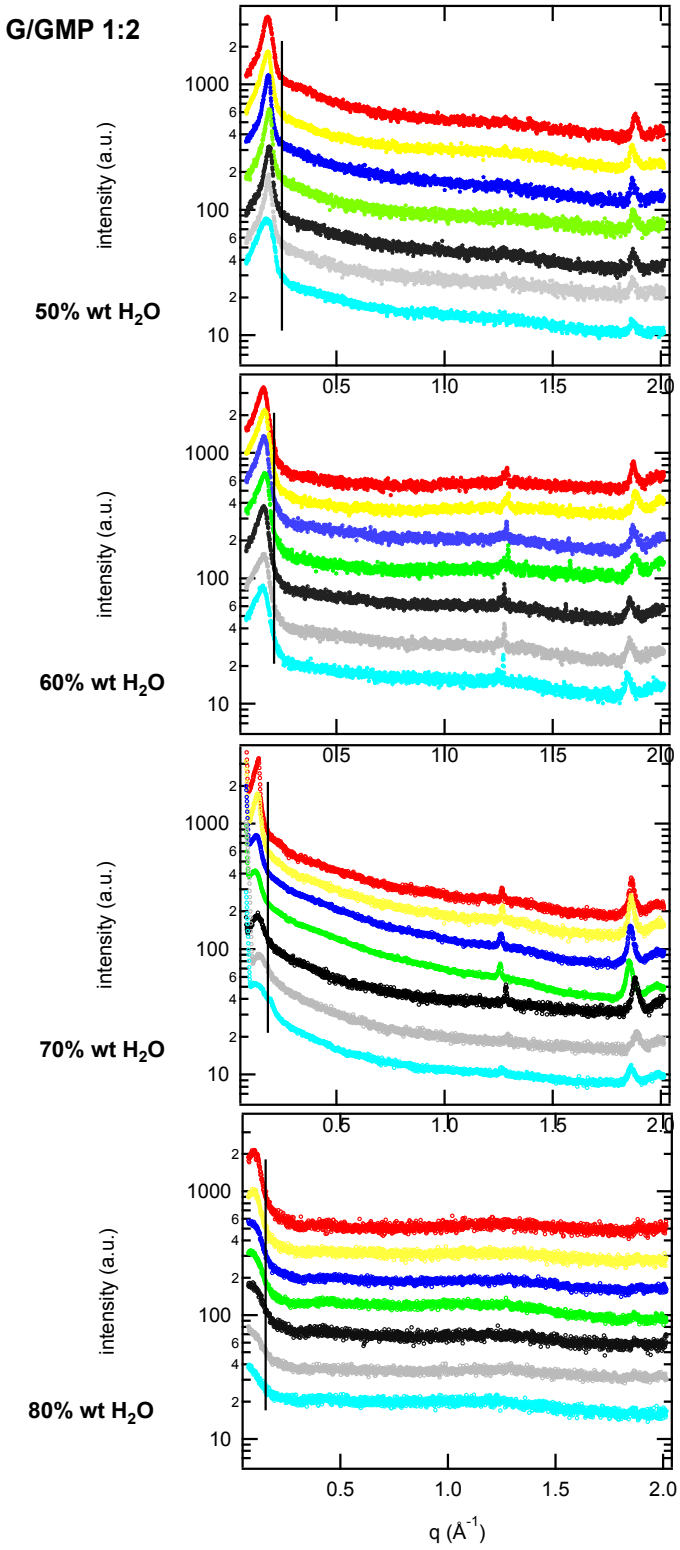

Figure 4.9 diffraction profiles relative to the low-angle region, obtained for the G/GMP ratio 1:2 as function of temperature (from red 20°C to light-blue 80°C) and of the increasing percentage of water (from the upper graph, 50% wt of water, up to the lower, 80% of water). Black bar shows the trend of the peak position relative to the mesophase as function of the increase of the level of hydration. In addition, signal relative to the stacking of tetrads in the quadruplex (in the high-angle region) at 1.8Å^{-1}

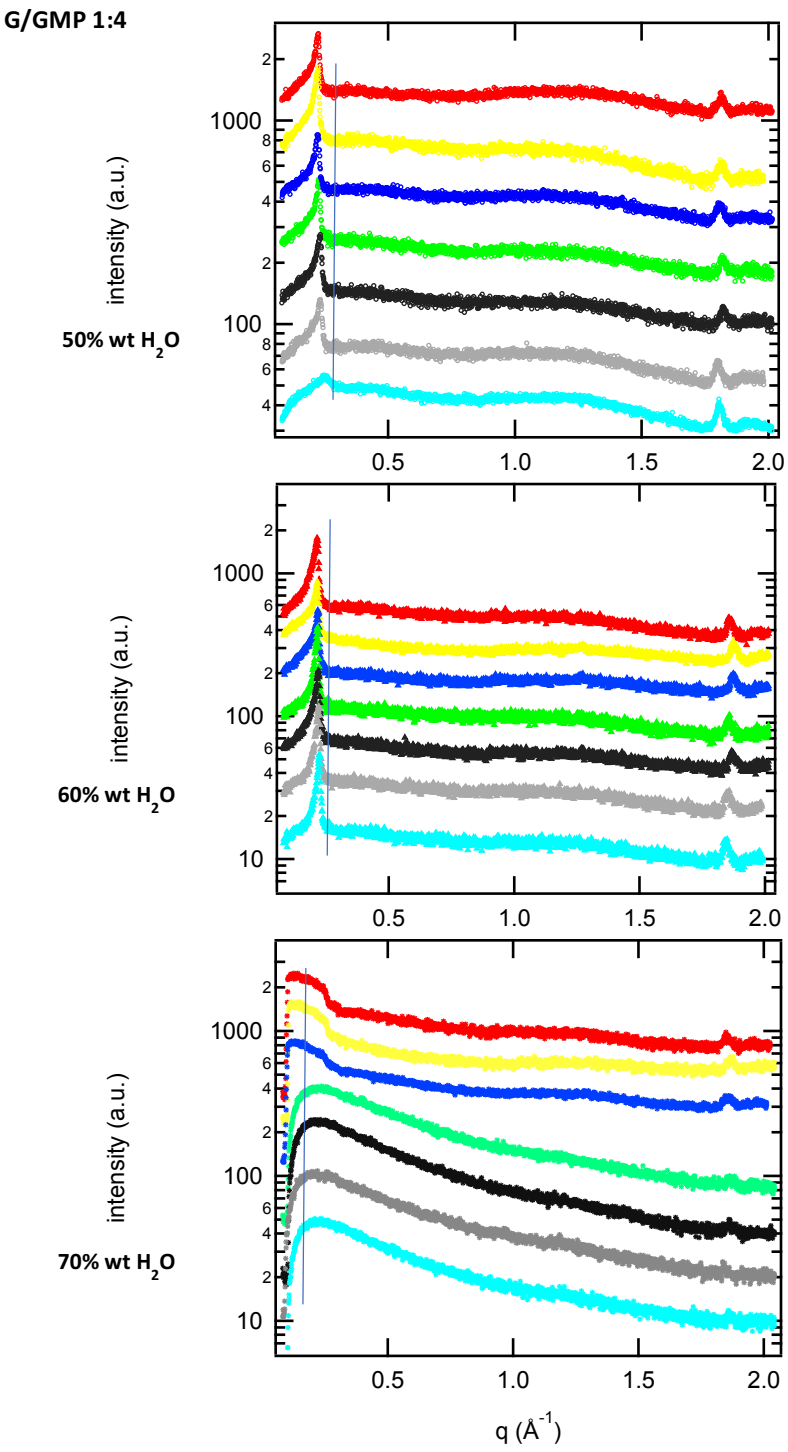

Figure 4.10 diffraction profiles relative to the low-angle region, obtained for the G/GMP ratio 1:4 as function of temperature (from red 20°C to light-blue 80°C) and of the increasing percentage of water (from the upper graph, 50% wt of water, up to the lower, 70% of water). Black bars indicate the approximate position of the peak relative to the mesophase and its movement towards low-q values as function of the increase of the level of hydration. In addition, signal relative to the stacking of tetrads in the quadruplex (in the high-angle region) at 1.8Å^{-1}

Distance between cylinders (unit cell values) has been derived from peak indexing analysis, for all measures made and reported in final graphs as function of temperature and percentages of water investigated.

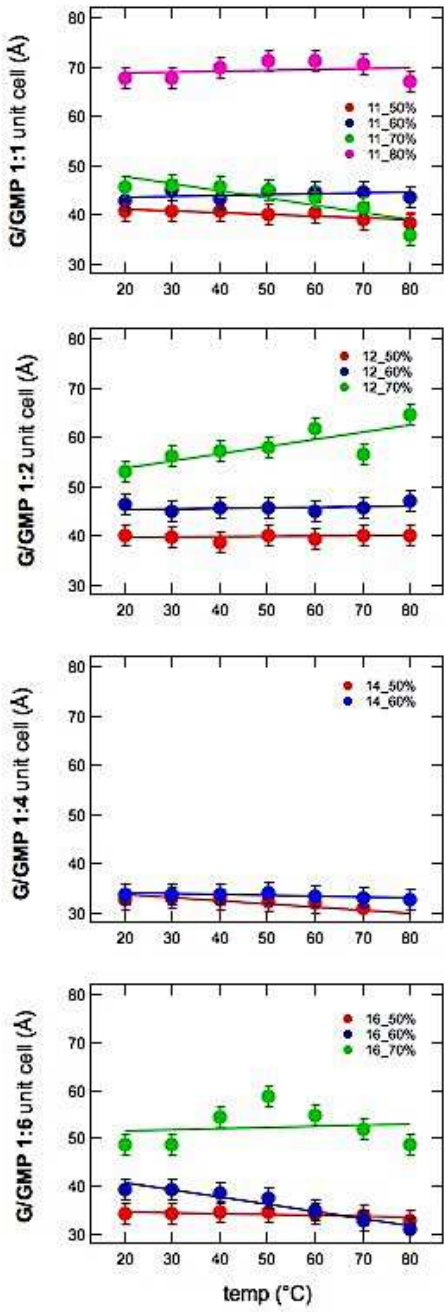

Figure 4.11 final graphs relative to the unit cell values (here reported in $Å^{-1}$) as function of temperature. Line **A**: 1:1 G/GMP; Line **B 1:2** G/GMP; Line **C** 1:4 G/GMP and Line **D** 1:6 G/GMP

Graphs relative to all G/GMP ratios show a not linear dependence of the unit cell values as function of the increasing concentration of water in the system, exception made for the 1:2. Values relative to the 80% of water have been not reported because of the impossibility to index peaks from XRD profiles (e.g. lower graph, Figure 4.9). Nevertheless, the morphology of the peak suggests the presence in the system of a highly hydrated mesophase and this justify our association of 80% broad peaks to the presence of a cholesteric phase, as reported below in phase diagram relative to the 1:2.

Going towards to the higher GMP content in the system, for the 1:6 no considerably variations in the unit cell values (up to 60% of water) have been reported. At 70% of water a not linear variation of the unit cell value as function of the increasing temperature can be observed. Is important to remark that this specific ratio can be

considered as a critical sample, in which probably the strength of the hydrogel starts to be very weak and thus not able to confer an high stability to the whole system. Data relative to the 80% of water shows clearly that at this level of hydration the system is in a solution state.

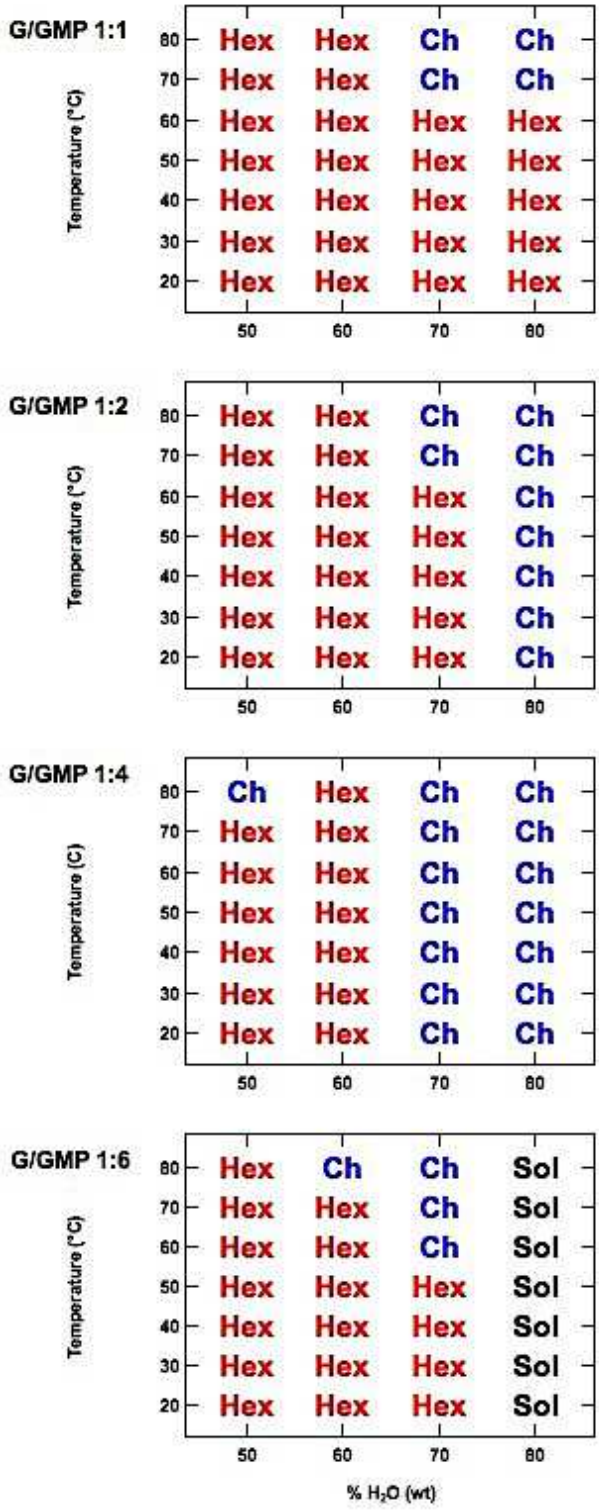

Figure 4.12 phase diagrams relative to each G/GMP ratio, as indicates in the graphs. **Hex** means hexagonal Phase, **Ch** cholesteric phase and finally **Sol** for the solution state, as function of temperature (°C) and level of hydration (% of water in the system)

4.3.2 Stacking of quartets in the quadruplex architecture: high-angle region analysis

To get information about the structural properties of G/GMP hydrogels, X-ray diffraction experiments have been made. In addition to signals relative to the macroscopical mesophase organization, the high-angle region can provide an unequivocal confirmation about the presence of quadruplex architecture in the system. A reflection can be found at 3.35Å (in the graph reported below at 1.87Å^{-1}) and is the Braggs' reflection related to the stacking of cyclic planar quartets in the quadruplex supramolecular assembly.

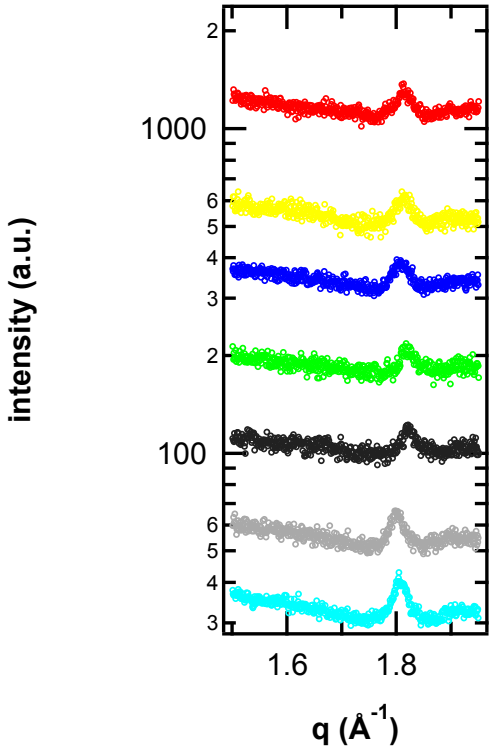

Figure 4.13 diffraction profile relative to the wide-angle region in which is possible to appreciate peak relative to the stacking of quartets in the G-quadruplex. The position of peak in the figure is around 1.87Å^{-1} and this correspond to 3.35Å

Chapter 5

Chapter 5

G/GMP Hydrogels: analysis of anisotropicity and SAXS results

5.1 The more-hydrated systems: Small-angle X-ray Scattering (SAXS) analysis

SAXS analysis using Nanostar® (Bruker) have been made at the Applied Physics Institut of Sao Paulo, Brazil, from March to the end of May 2016, in collaboration with the Prof. Rosangela Itri and PhD Juliana Sakamoto Yoneda. Samples measured have been reported in the table below. All measurements have been conducted as function of temperature and testing and extended $C_{v,wat}$.

Table 5.1 samples analyzed using small-angle X-ray scattering. Measurements have been conducted as function of temperature and of the water concentration

G/GMP molar ratio	sample name	water concentration analyzed	T-range analyzed (°C)
0.167	**1:6**	0.97	25to70
0.50	**1:2**	0.969-0.985	10to70
0.75	**3:4**	0.969-0.991	10to70
1.00	**1:1**	0.969-0.991	10to70

In the following panels, relative to the 1:1, 1:2 and 3:4, I reported 2D-images obtained using Nanostar® (small-angle scattering setup). Any mechanical stress (such as the use of micropipettes) has been avoided to not interfere with the spontaneous orientation of components in the sample. All samples have been placed in the holder using a spatula. A flat holder provided by a Teflon spacer (sealed with silicon and kapton windows) has been used.

Relatively to the 96.9% of water, considered as the starting point, this has been measured in two different conditions (pre-heated and not pre-heated).

Not pre-heated refers to the absence of the annealing step at 90°C made before the measurement. *Pre-heated* means that the hydrogel has been kept at 90°C before being charged in the sample holder, this to ensure the complete solubilization of components and the obtainment of a stable, transparent gel. Considering the two different conditions in which the 96.9% has been measured (this referring to all three ratios showed below), is clearly deducible that the pre-heating is a fundamental step to achieve the higher thermal stability of the gel. In Figure 5.1 (line 1) attention has to be focused on the last 2D-image (70°C), the scattering is associable with that one of a liquid solution, contrary in line 2 (at the same temperature), the scattering is relative to a gel state (not-oriented, but still in a gel state). Always considering the 96.9%, for the lower temperatures, the small-angle scattering profiles are typical of an anisotropic sample.

Information that can be derived from 2D-images are strictly related to the inner organization of particles in the hydrogel network and thermal stability of the gel itself. First, a discrimination between an oriented and a not-oriented sample can be made. In G/GMP 1:1, the shape of anisotropic profiles is *bullet-like* for the not pre-heated and as a simply elongated in the case of the pre-heated. More detailed analysis about the anisotropicity will be showed in the next section 5.2. When a sample is not oriented, the scattering profile appears as a circle (e.g. pre-heated, 70°C).

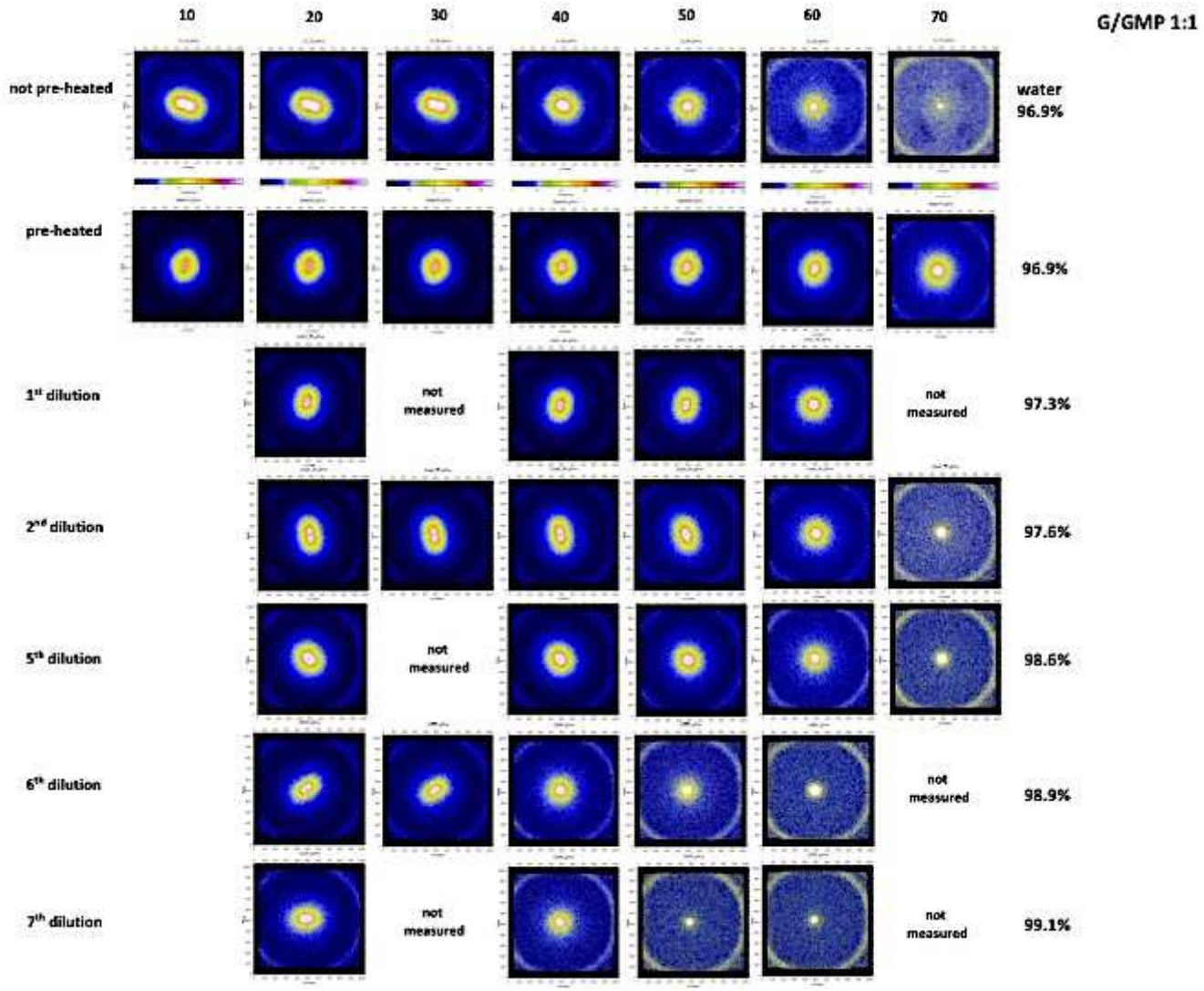

Figure 5.1 summary of the SAXS 2D-images obtained for the hydrogel G/GMP 1:1. Measures have been made starting from the 96.9% (rows 1 and 2), these are relative to two different conditions (pre-heated and not pre-heated). From the 3rd row can be showed results relative to dilutions made starting from aliquot of 96.9% of pre-heated gel. Not all the dilutions 2D-images have been reported here in the panel for clarity

Second, two different phase transition temperatures can be derived: the first one related to the transition from gel oriented to gel not-oriented (e.g 2nd dilution, from 50 to 60°C) and the second one to gel not-oriented to solution (e.g. 2nd dilution, from 60 to 70°C). These temperatures have been inserted in the phase diagram reported in the previous section 4.2.1 (see Figure 4.4, left graph) as filled dots and rectangles**.** Results obtained using SAXS are in line with that one obtained using POM and inverted-vial test.

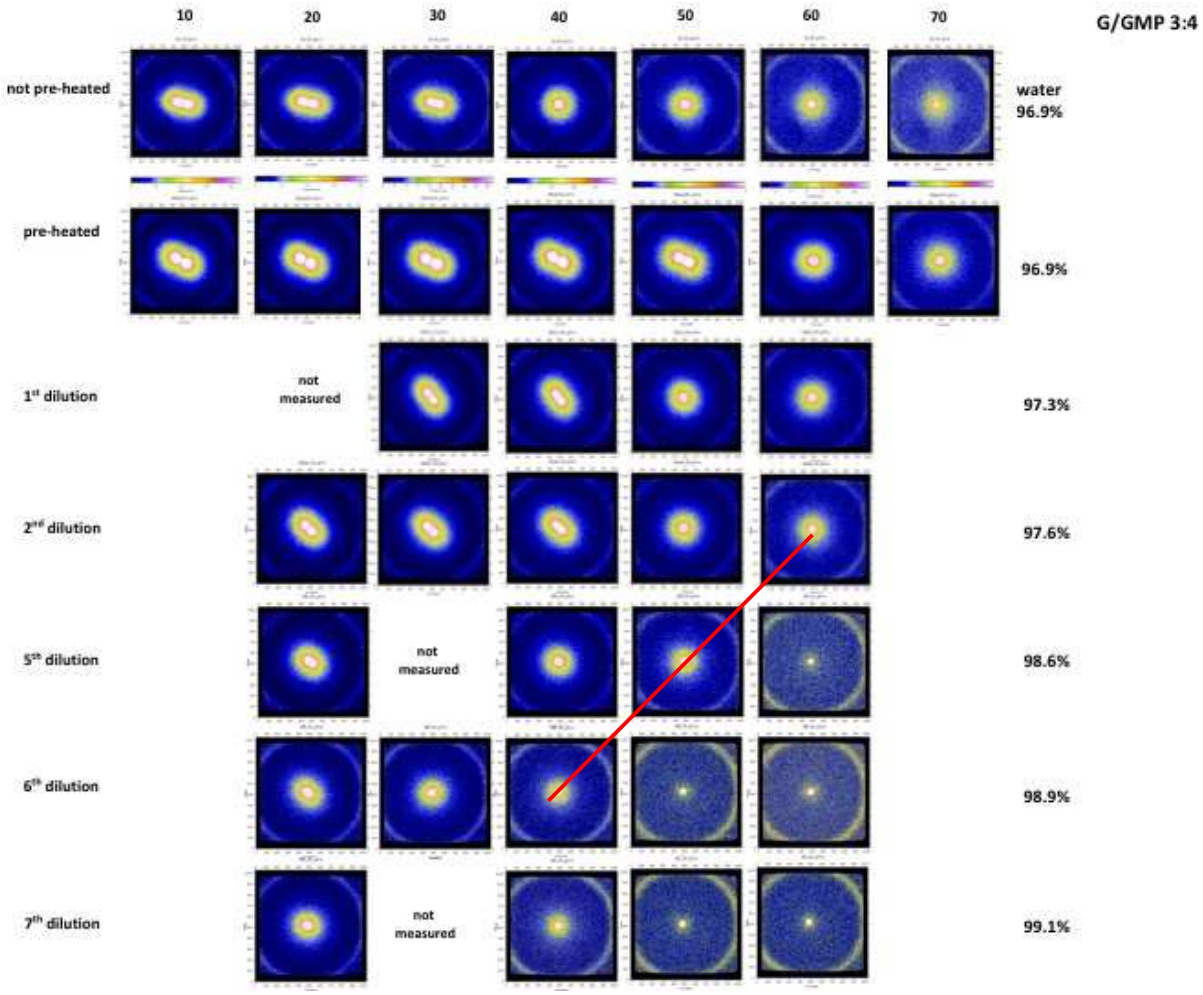

Figure 5.2 summary of the SAXS 2D-images obtained for the hydrogel G/GMP 3:4. Measures have been made starting from the 96.9% (rows 1 and 2), these are relative to two different conditions (pre-heated and not pre-heated). From the 3rd row can be showed images relative to dilutions made starting from aliquot of 96.9% of pre-heated gel. Not all the dilutions 2D-images have been reported here in the panel for clarity

The same considerations can be made considering the panel of 2D-images relative to the G/GMP 3:4, reported in Figure 5.2. Also in this case the annealing phase at 90°C is an essential condition to obtain the higher stability of the system, here showed by the presence of the scattering intensity associable to the presence of a gel until 70°C. Considering the 2D-image obtained at the same temperature in the case of the not pre-heated (first line, not pre-heated), probably here the gel starts to become solution.

Interesting is the fact that the temperature at which the gel-to-sol transition occurs decreases as function of the increase of quantity of water in the system: this can be appreciate considering circular intensities of gels evidenced in the image with a red oblique line (97.6, 98.6 and 98.9% of water).

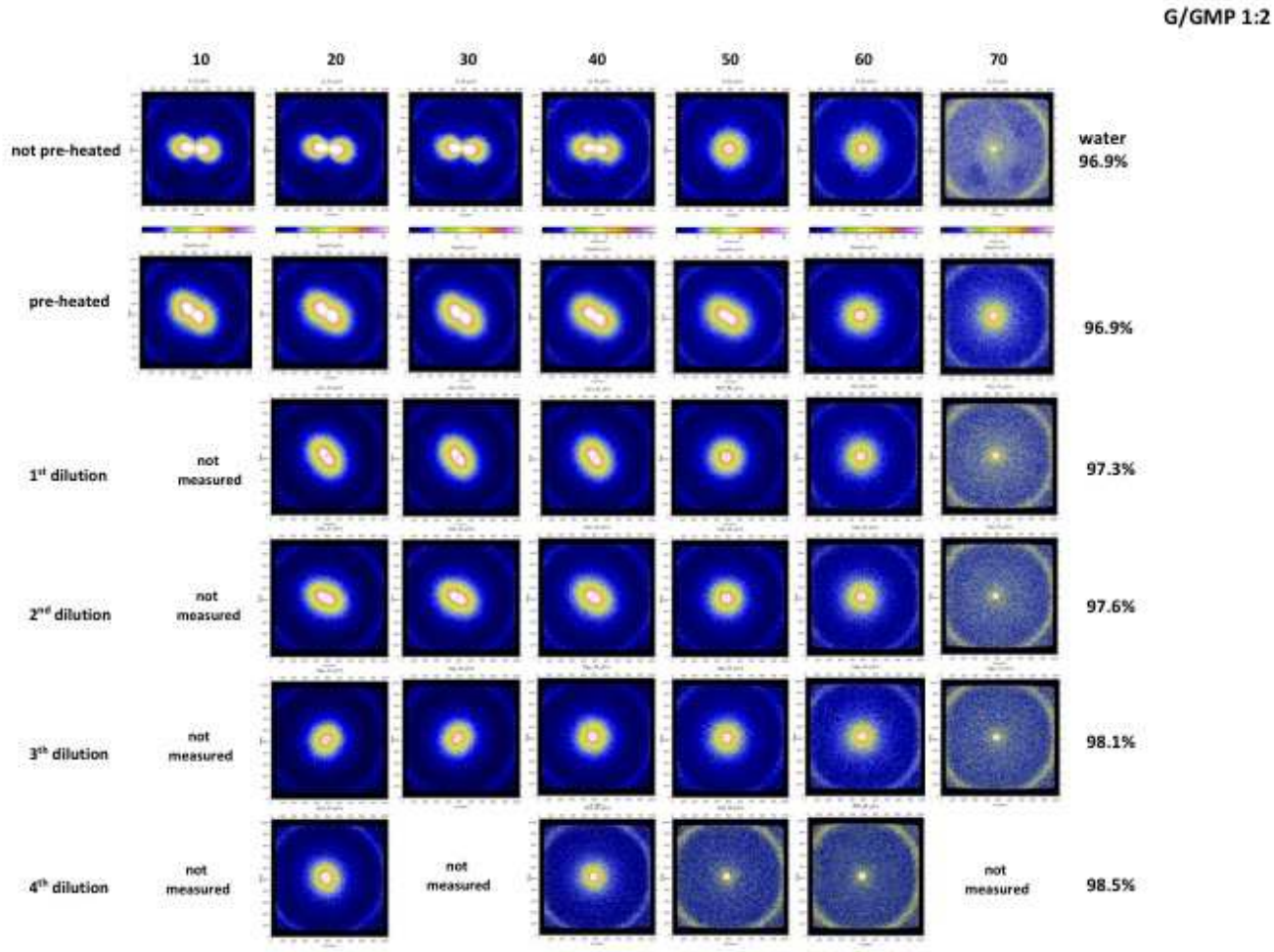

Figure 5.3 summary of the SAXS 2D-images collected for the hydrogel G/GMP 1:2. Measures have been made starting from the 96.9% (rows 1 and 2), these relative to two different conditions (pre-heated and not pre-heated). From the 3rd row can be showed images relative to dilutions made starting from aliquot of 96.9% of pre-heated gel. Not all the dilutions 2D-images have been reported here in the panel for clarity

In the case of the G/GMP 1:2, SAXS analysis performed about 1:2 dilutions have been made up to the fourth (98.5%), this due to the transition from gel not-oriented to solution that occurs at low temperature (40°C). Instead, preparation of sample has been made up to the 7th dilution (details about the procedure can be found in Chapter 9, section 9.2.3.3). At 20°C the presence of the gel has been reported also at 99.1% of water (see Figure 5.4).

5.2 Analysis of anisotropicity

To give a first evidence of the anisotropicity of G/GMP hydrogels, calculations on 2D-scattering profiles have been made using Fit2D software (http://www.esrf.eu/computing/scientific/FIT2D). Simply, uploading the anisotropic 2D-SAXS profile relative to the sample and then using the function *exchange* to load and keep in memory the profile relative to the background (kapton windows), a scaled subtraction has been made. An example of the procedure made has been reported here below in Figure 5.4.

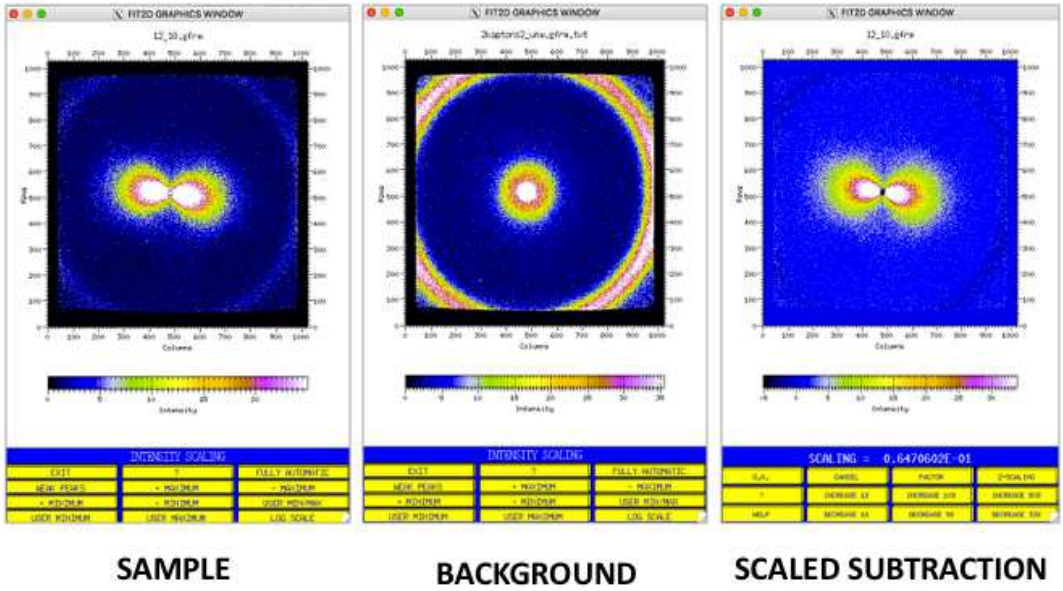

Figure 5.4 example of subtraction made about 2D-SAXS profiles. All procedures have been made using Fit2D software. On the left, 2D-SAXS intensity relative to an oriented sample (without subtraction); in the center: 2D-SAXS image relative to the background (kapton windows) that has been consequently subtracted to the initial 2D-SAXS profile using a scaled factor and showed on the right.

after this initial step, intensity has been acquired manually in the two directions of the orientation, defined here as *weak* and *strong* and showed in the following image.

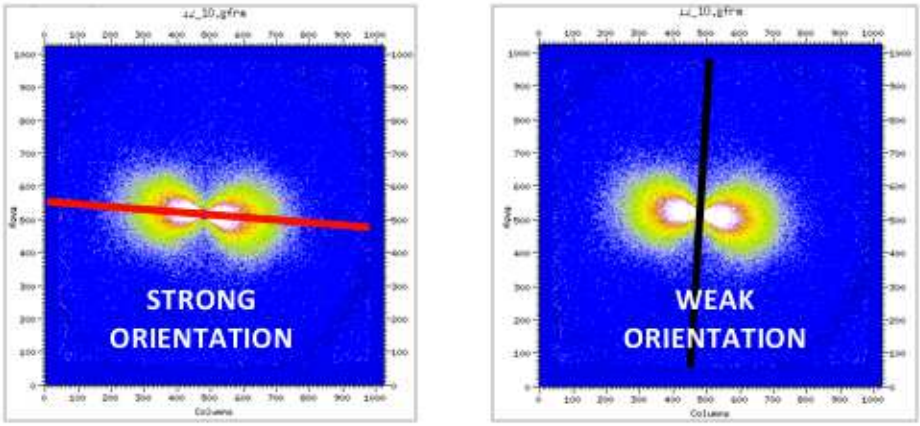

Figure 5.5 definition of the *strong* and *weak* orientation of the 2D-scattering profile

Values relative to the intensities acquired in the two directions can be saved and exported as .chi files and consequently managed with a common data analysis program (e.g. IgorPRO, Matlab, SasView).

1D-plot has been consequently obtained converting pixels in scattering vector q, here reported in $Å^{-1}$. In graph reported in Figure 5.6 intensities relative to the strong and weak orientations of the anisotropic 2D-profile have been plotted as function of the scattering vector q. The same procedure has been made considering all temperatures investigated for a given G/GMP ratios and final graphs obtained (see Figures 5.7 and 5.9).

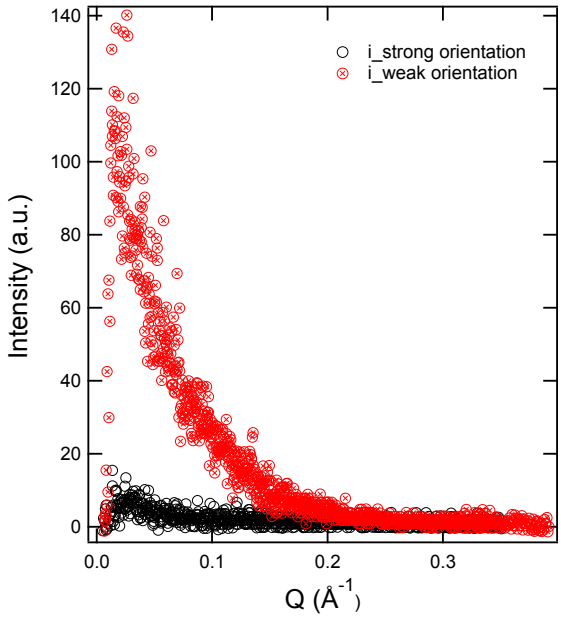

Figure 5.6 1D-plot derived from the manual acquisition made from the 2D-SAXS anisotropic profiles.

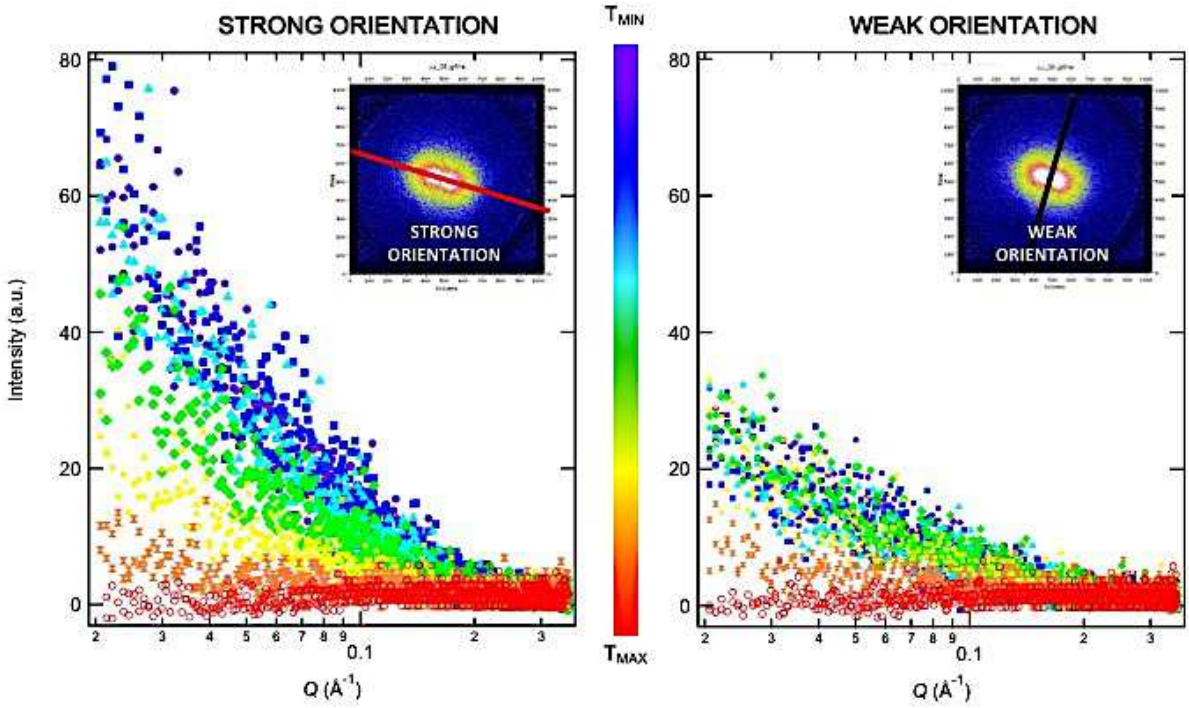

Figure 5.7 final graphs obtained for the G/GMP ratio 1:1. In the left graph, intensities relative to the strong orientation of the anisotropic 2D-profiles have been reported as function of the scattering vector q ($Å^{-1}$) for all temperatures investigated; in the right graph those relative to the weak orientation.

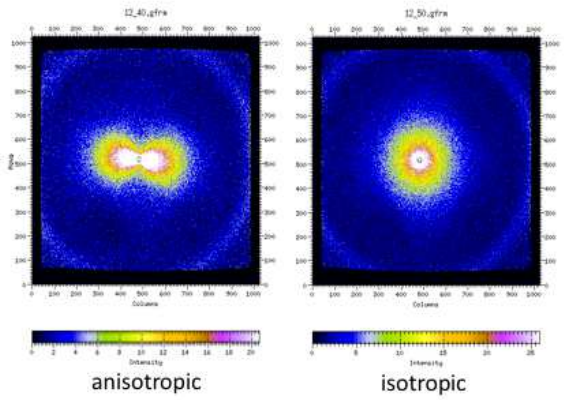

Figure 5.8 distinctive morphology of the SAXS 2D-profile related to an oriented on the left) and a not-oriented sample (on the right)

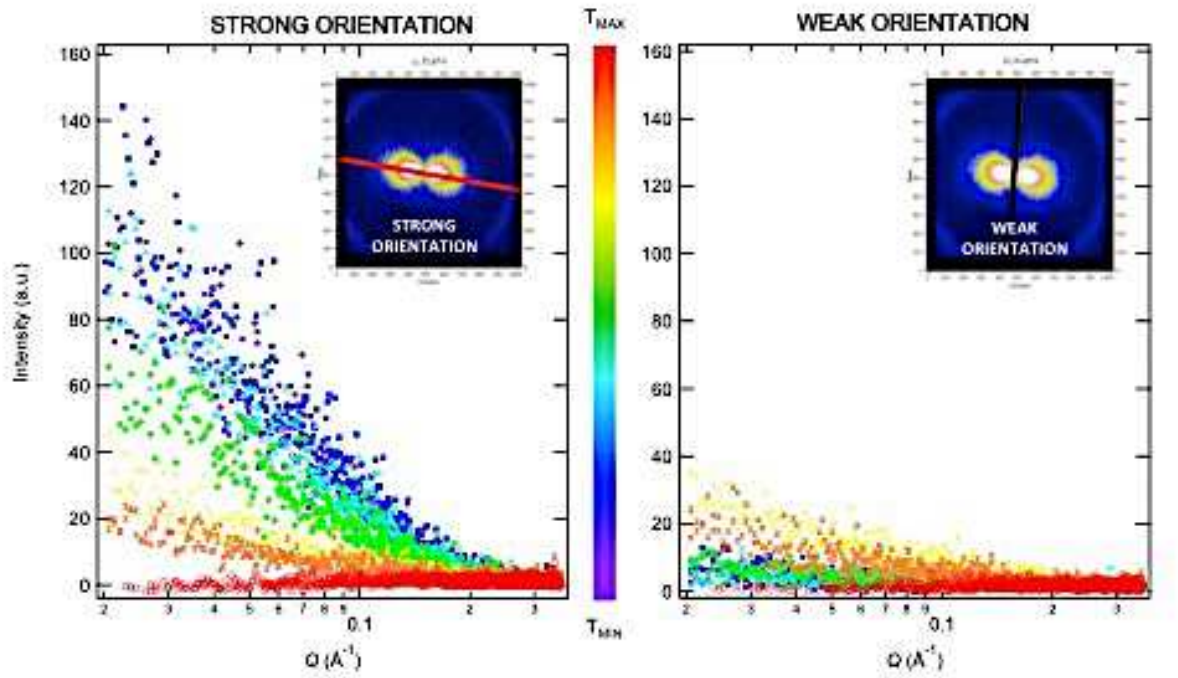

Figure 5.9 final graphs obtained for the G/GMP ratio 1:2. In the left graph, intensities relative to the strong orientation of the anisotropic 2D-profiles have been reported as function of the scattering vector q ($Å^{-1}$) for all temperatures investigated; in the right graph those relative to the weak orientation

From the final graphs (reported for the G/GMP 1:1 in Figure 5.7 and for the 1:2 in Figure 5.8) is clearly visible how the intensity relative to the strong orientation decreases as function of the increase of temperature, contrarily that one related to the weak orientation increases (very little) as function of the decrease of temperature.

The transition between the oriented (*butterfly-like*) and a not oriented profile (*circle*) justify the increase in terms of intensity evidenced in the scattering related to the weak orientation (see Figure 5.8).

Additional analysis has been made taking into account the possibility to manually trace circular intensities, always considering anisotropic SAXS profiles. In this case, analysis of the intensities has been made using a macro developed by the Prof. Paolo Mariani for the software Image J.

In this case diameter values have been changed for each manual acquisition of intensities, as showed in Figure 5.10. Global fitting analysis have been performed considering the Maier-Saupe theory of liquid crystals. Has to be underlined for this kind of analysis intensities have been not converted in q.

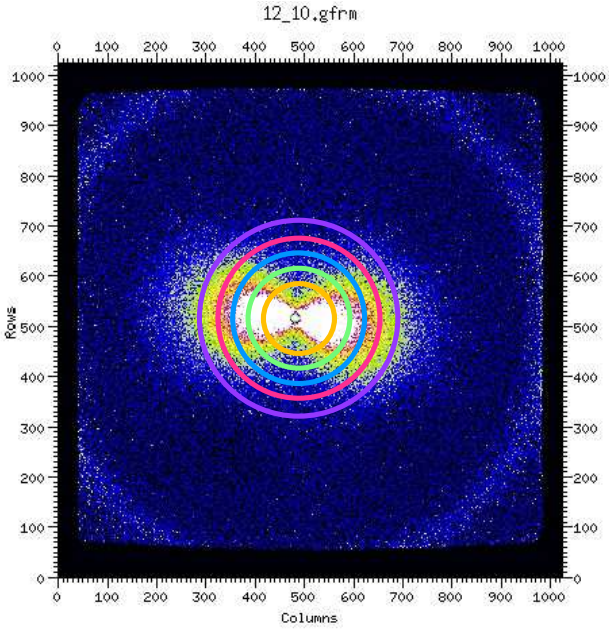

Figure 5.10 different diameter widths (manually acquired using a macro in ImageJ) that have been considered in the analysis of anisotropicity.

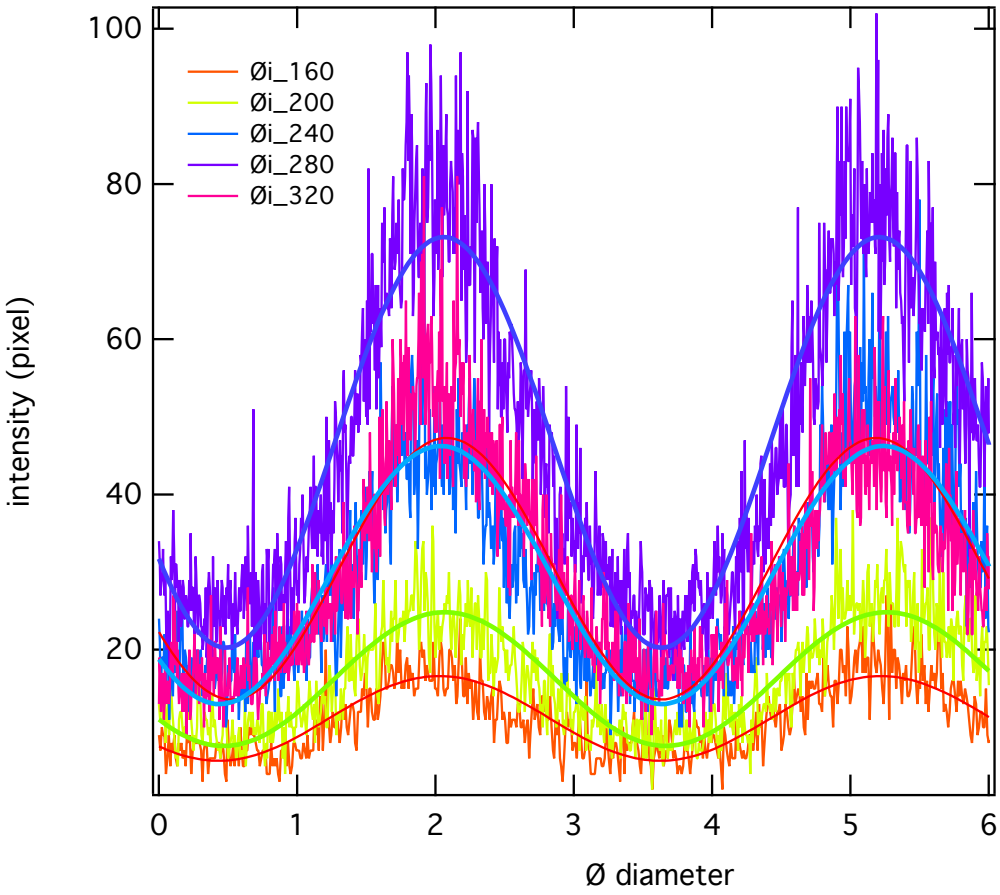

Figure 5.11 final graph relative to the G/GMP ratio 1:2 in which intensities have been analyzed considering each time different diameter values. Continuous line represents curve fitting made using the equation relative to the Maier-Saupe theory of liquid crystals

5.2.1 Structure factor calculation: circularly averaged 1D-profiles analysis

2D-SAXS anisotropic profiles suggest the presence of a complex structural behavior, characterized by a partially disordered network. Samples are intrinsically oriented and maintain oriented for a quite large degree of swelling (the order degree decreases with dilution, as it is possible to observe from the final layout) and temperature. The ordering of molecules in the samples has been investigated focusing on the 1D-scattering curves, calculated by circular average of 2D-data. Here, results obtained in the case of 1:1 and 1:2 G/GMP ratios have been reported. Focusing on 1D-scattering curves related to the 1:1 G/GMP (Figure 5.12), these clearly show the presence of a broad correlation peak, whose intensity and position depends on hydrogel hydration level and temperature (Graph 5.15).

Correlation peaks have been highly evidenced in the less-hydrated systems and this is in agreement with the hypothesis of the possible formation of a liquid-crystalline phase that disappear on heating, exactly in correspondence with the gel-to-sol transition temperature detected using inverted-vial test and polarized-light optical microscopy observation in the macroscopical characterization of hydrogels. At higher temperatures, the total scattering becomes very low, indicating the complete disassembling of quadruplexes (e.g. yellow curves in the graphs related to the G/GMP 1:1 85% and 89% of water). A detailed definition of the scattering intensity I(q) has been given in Chapter 9, section 9.4, but here the equation has to be reported again to explain how structure factor can be calculated.

Equation 5.1:

$$I(q) = kN_pP(q)S_{meas}(q)$$

where N_p is the number of density of the scattering particles, k the correlation factor, $P(q)$ is the particle effective form factor and $S_{meas}(q)$ the measured structure factor.

The $S_{meas}(q)$ has been calculated as follow: first, a screening of higher-temperature curves has been made to choose the appropriate value of $P(q)$. Second, the estimated pure *P*(*q*) profiles have been fitted using the form factor of long, straight cylinders with section of radius R and composite cross-sectional scattering length density profile (core-shell cylinder model, see section 9.4.2); third, in the case of good *global fitting* analysis, the appropriate value of *P*(*q*) has been used to calculate the $S_{meas}(q)$ using the following equation:

Equation 5.2:

$$S_{meas}(q) = I(q)/bP(q)$$

where *b* is the normalization coefficient.

5.2.1.1 G/GMP 1:1

Here can be showed results obtained in the case of circularly averaged 1D-scattering profiles relative to the G/GMP ratio 1:1. Percentages of water from the 85% to the 98.5% have been considered in the determination of the structure factor *S*(q). SAXS measurements have been made up to the 99.1% of water (2D-profiles have been reported at the beginning of this chapter).

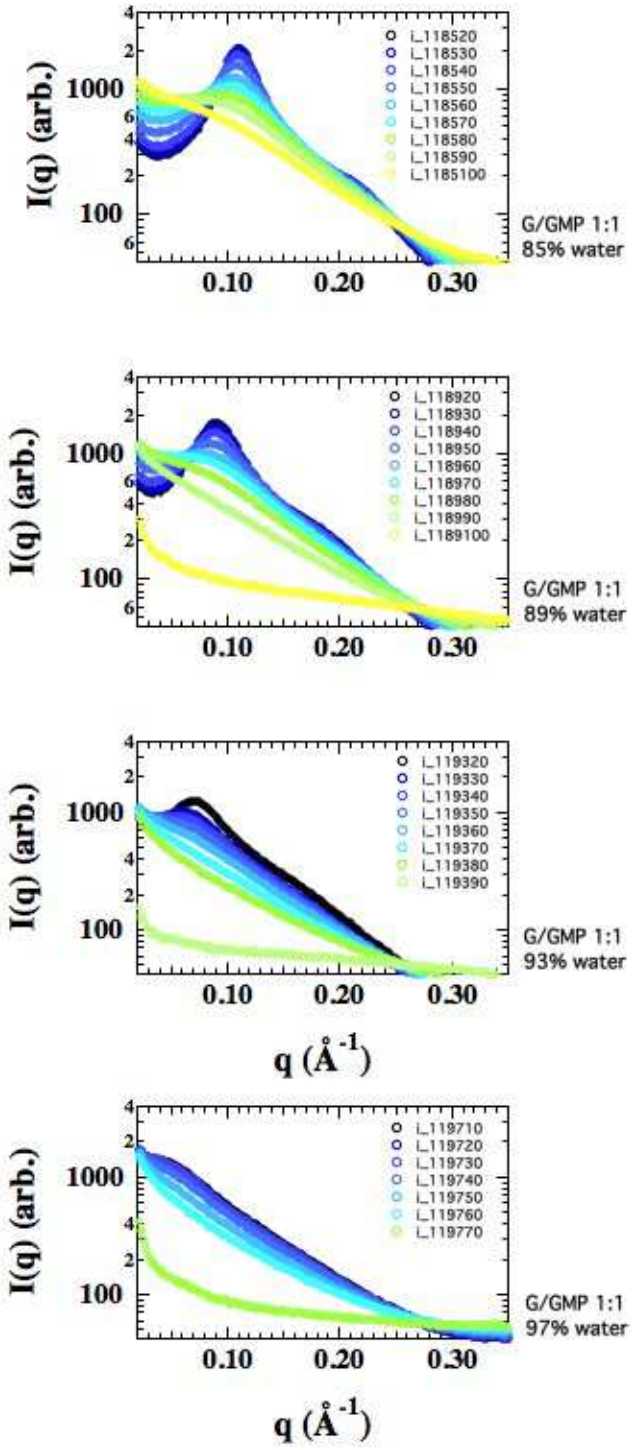

Figure 5.12 circularly averaged 1D-scattering curves relative to the G/GMP ratio 1:1 (from 85% to 97% of water). The percentage of water has been indicated on the right side. In each graph can be showed all the intensities relative to all temperatures investigated at a given percentage of water. For the more concentrated samples, temperature range investigated has been from 20 to 100 (both for the 85% and 89% of water) up to 90°C (for the 93% of water) and from 10°C to 70°C (in the case of 97% of water)

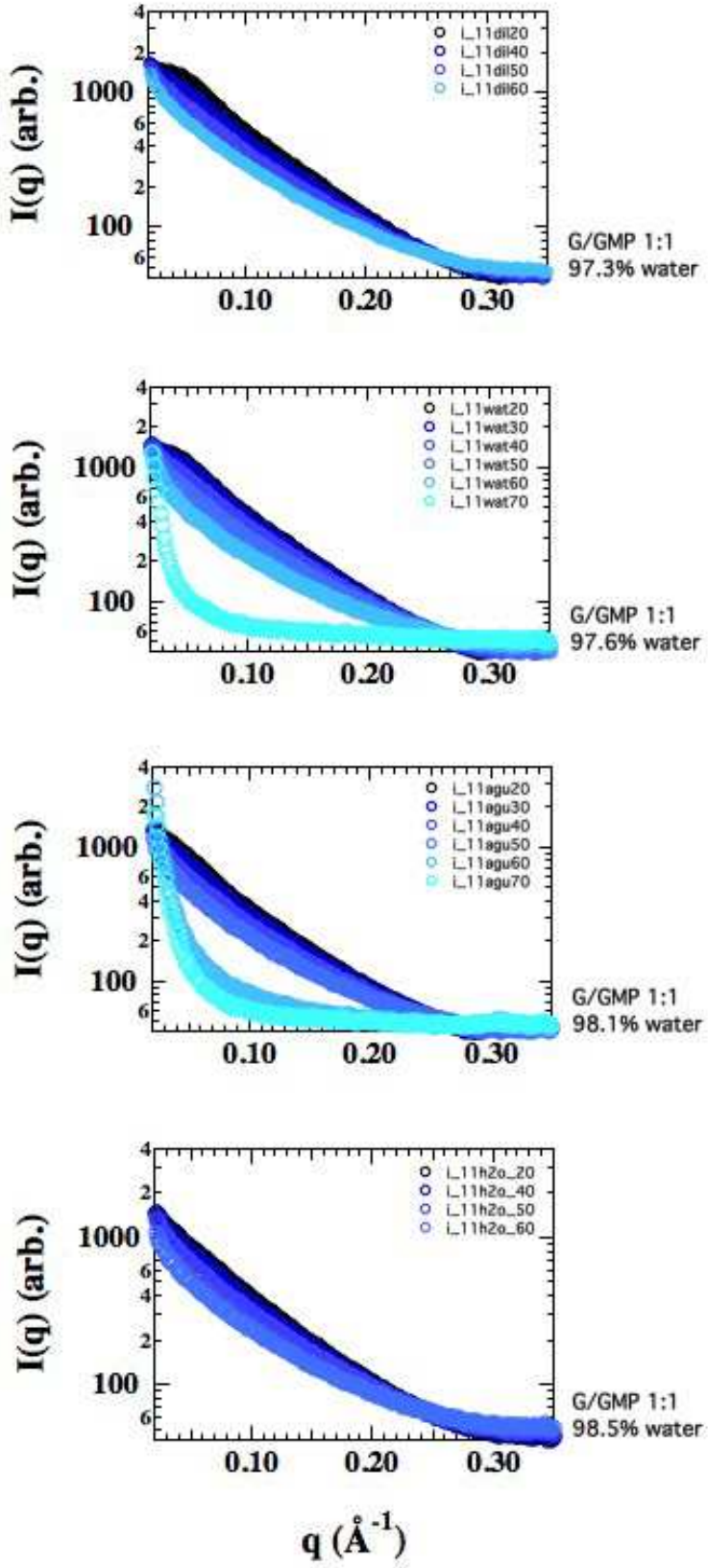

Figure 5.13 circularly averaged 1D-scattering curves relative to progressive dilutions of G/GMP ratio 1:1 (from 97.3% to 98.5% of water). The percentage of water has been indicated on the right side. In each graph can be showed intensities relative to all temperatures investigated at a given percentage of water.

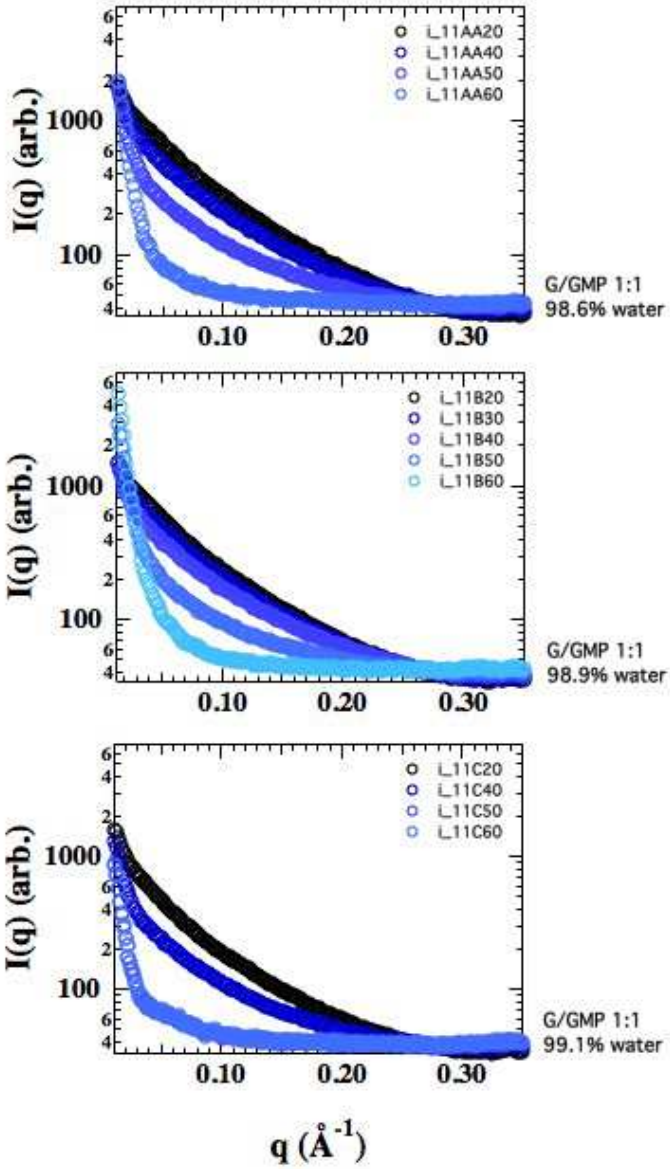

Figure 5.14 circularly averaged 1D-scattering curves relative to the G/GMP ratio 1:1 (from 98.6% to 99.1% of water). The percentage of water has been indicated on the right side. In each graph can be showed intensities relative to all temperatures investigated at a given percentage of water.

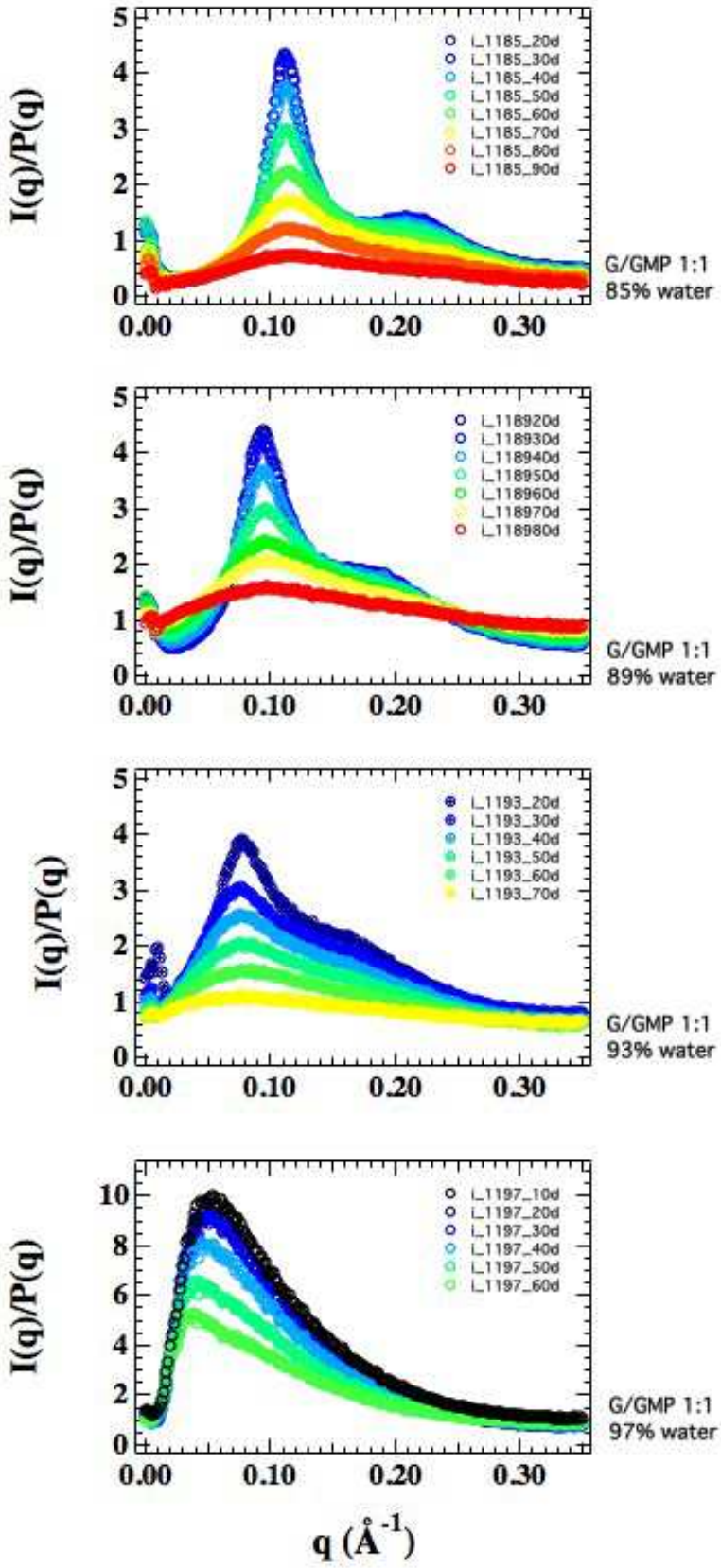

Figure 5.15 relatively to the G/GMP 1:1, structure factors S(q) are showed here as function of the scattering vector *q* (reported in $Å^{-1}$), from 85 to 97% of water.

Peak position has been determined for each G/GMP ratio investigated (considering temperature and water percentage) and reported in the following tables. Consequently, graphs relative to peak position (both in *q* and *d*) plotted as function of temperature range explored have been made.

In the case of the more concentrated samples (from 85% to the 93% of water), the position relative to two peaks have been calculated and thus, two different graphs have been reported.
Relatively to the G/GMP 1:1, the trend of the peak is completely unique. Considering the less hydrated samples, an increase in terms of q values relative to the first peak position can be coupled with a decrease of the second one detected (Figure 5.16). No significant variation of the peak position has been reported for the 93% of water. The position of the peak starts to decrease significantly as function of the increase of temperature in the case of 97% of water, in which a single peak has been detected. Has to be underlined that for us the 97% is considered as the starting point.

Table 5.2 and 5.3 summarize peak positions determined consequently to the structure factor S(q) determination. In the upper table values are reported in q ($Å^{-1}$), in the lower table in d (Å) where d is the d spacing between cylinders in the G/GMP hydrogel network. Peak position has been calculated using a LogNormal fit.

values reported in q ($Å^{-1}$)

T (°C) range	1:1 85% 1st peak	1:1 85% 2nd peak	1:1 89% 1st peak	1:1 89% 2nd peak	1:1 93% 1st peak	1:1 93% 2nd peak	1:1 97% 1st peak
10	-	-	-	-	-	-	0.0538
20	0.1123	0.2066	0.0939	0.1636	0.0783	0.1209	0.0532
30	0.1125	0.2061	0.0940	0.1636	0.0754	-	0.0528
40	0.1126	0.2009	0.0946	0.1558	0.0771	-	0.0504
50	0.1131	0.1974	0.0961	-	0.0777	-	0.0469
60	0.1147	0.1648	0.0982	-	0.0779	-	0.0407
70	0.1158	-	0.0983	-	-	-	-
80	0.1163	-	-	-	-	-	-
90	0.1168	-	-	-	-	-	-

values reported in d (Å)

T (°C) range	1:1 85% 1st peak	1:1 85% 2nd peak	1:1 89% 1st peak	1:1 89% 2nd peak	1:1 93% 1st peak	1:1 93% 2nd peak	1:1 97% 1st peak
10	-	-	-	-	-	-	116.7
20	55.9	30.4	66.8	38.4	80.3	52.0	117.9
30	55.8	30.5	66.8	38.4	83.2	-	118.9
40	55.8	31.3	66.4	40.3	81.5	-	124.7
50	55.5	31.8	65.4	-	80.8	-	133.7
60	54.8	38.1	64.0	-	80.6	-	154.4
70	54.3	-	63.9	-	-	-	-
80	54.0	-	-	-	-	-	-
90	53.8	-	-	-	-	-	-

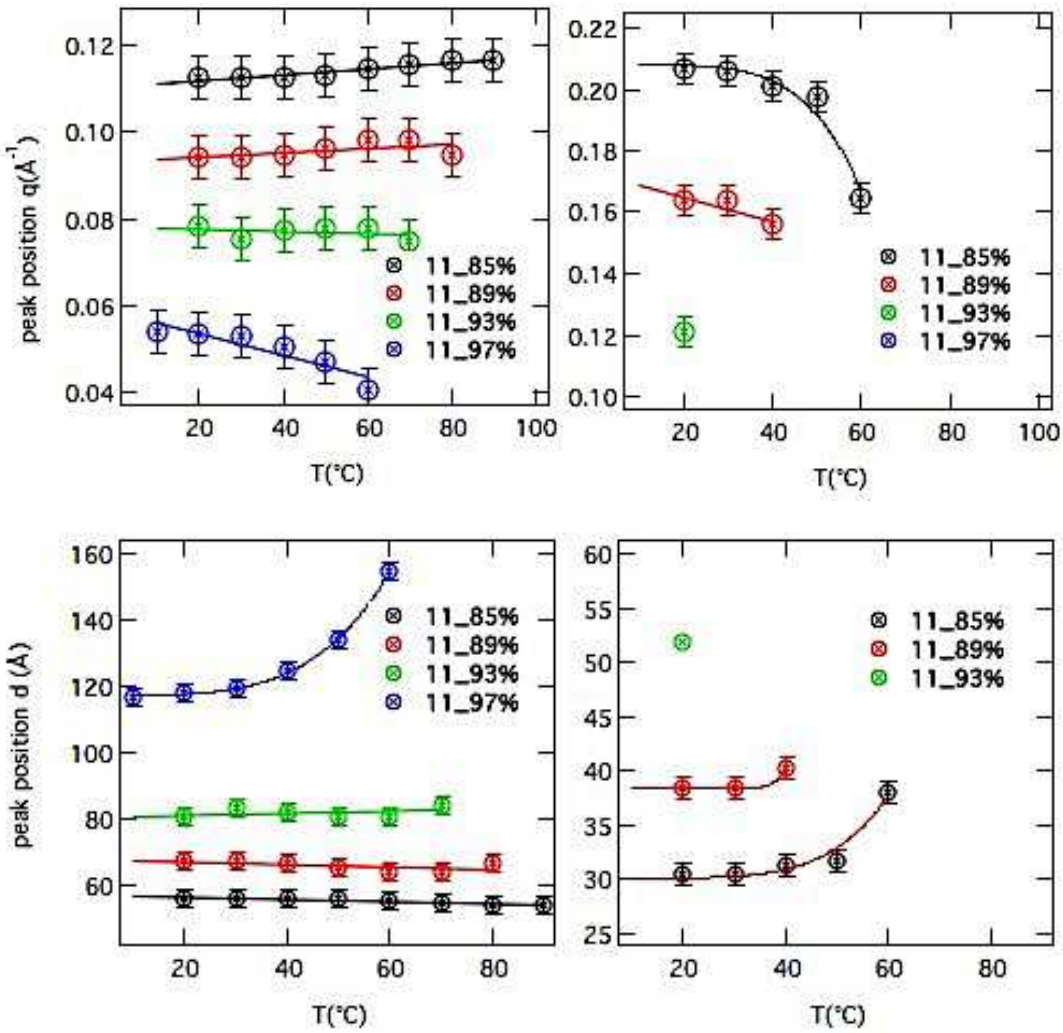

Figure 5.16 G/GMP 1:1 final (upper) graphs relative to the peak position (in q, reported in Å^{-1}) showed here as function of temperature range explored. Up to the 93% of water two different peaks have been detected and thus two graphs have been reported. The left graph is relative to the first peak detected, the right graph to the second one. Error bars correspond to 0.005
In lower graphs can be observed the same results, but reported in *d* (Å), where *d* is the d spacing between cylinders in the hydrogel network. Error bars correspond to 2.

Before starting to present results obtained in the case of hydrogel G/GMP 1:2, here can be found circularly average 1D-scattering profiles relative to the more hydrated samples (from 98.6% to 99.1% of water)**.** Determination of the structure factor S(q) has been made for the lower temperature (20°C) because is the only case of the presence of anisotropic 2D-profile (showed at the beginning of this chapter, section 5.2) and thus of correlation between cylinders in the hydrogel network.

5.2.1.1 G/GMP 1:2

The same calculations have been made taking into account circularly averaged 1D-scattering profiles relative to the hydrogel G/GMP 1:2. Here SAXS 1D-profiles relative to percentages of water from the 85% to the 98.5% has been reported. These have been furthermore considered in the case of structure factor determination.

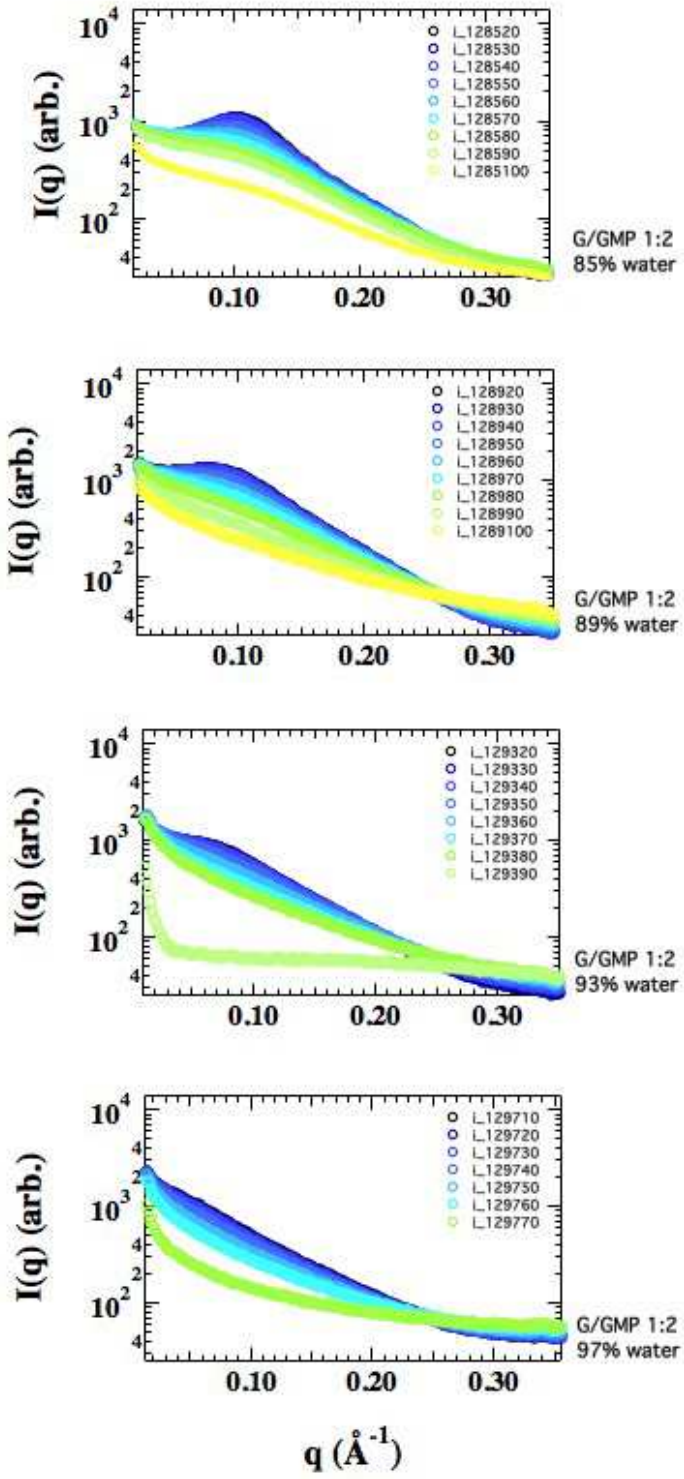

Figure 5.17 circularly averaged 1D-scattering curves relative to the G/GMP ratio 1:2 (from 97.3% to 98.5% of water). The percentage of water has been indicated on the right side. In each graph can be showed all the intensities relative to all temperatures investigated at a given percentage of water

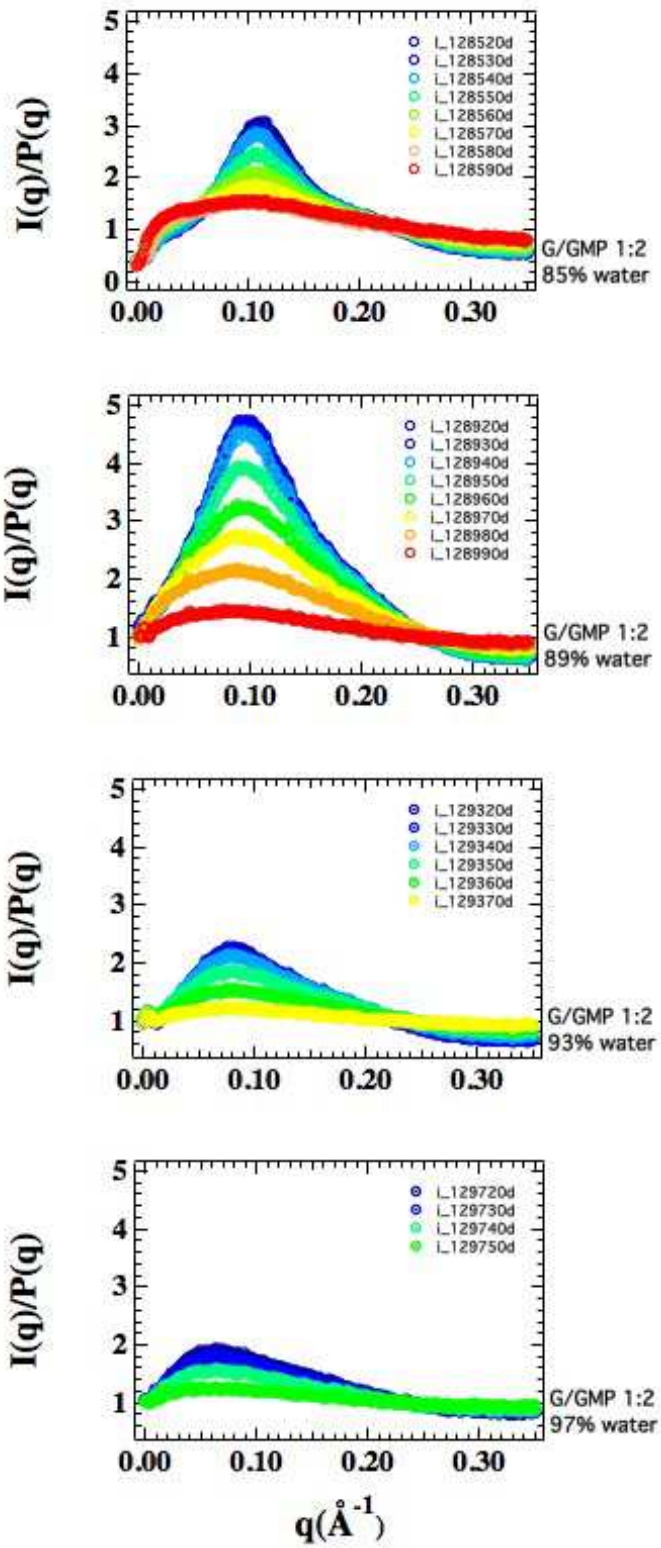

Figure 5.18 relatively to the G/GMP 1:2, structure factors S(q) are showed here as function of the scattering vector *q* ($Å^{-1}$), from 85 to 97% of water.

As for the hydrogel G/GMP 1:1, peak position has been derived and reported in the following tables and graphs as function of temperature range explored. In this case, only one peak has been observed.

Table 5.4 and 5.5 summarize peak positions determined consequently to the structure factor S(q) calculations. In the upper table values are reported in q ($Å^{-1}$), in the lower table in d (Å) where d is the d spacing between cylinders in the G/GMP hydrogel network.

values reported in q ($Å^{-1}$)

T (°C) range	1:2 85% 1st peak	1:2 89% 1st peak	1:2 93% 1st peak	1:2 97% 1st peak
20	0.1085	0.0944	0.0788	0.0608
30	0.1067	0.0939	0.0784	0.0596
40	0.1062	0.0933	0.0777	0.0584
50	0.1052	0.0928	0.0770	0.0469
60	0.1042	0.0905	0.0758	0.0569
70	0.1003	0.0868	0.0735	-
80	0.0955	0.0835	-	-
90	0.0903	0.0749	-	-

values reported in d (Å)

T (°C) range	1:2 85% 1st peak	1:2 89% 1st peak	1:2 93% 1st peak	1:2 97% 1st peak
20	57.9	66.6	79.7	103.3
30	58.9	66.9	80.1	105.3
40	59.2	67.3	80.8	107.6
50	59.7	67.7	81.6	110.3
60	60.3	69.4	82.9	-
70	62.6	72.4	85.5	-
80	65.8	75.3	-	-
90	69.5	83.9	-	-

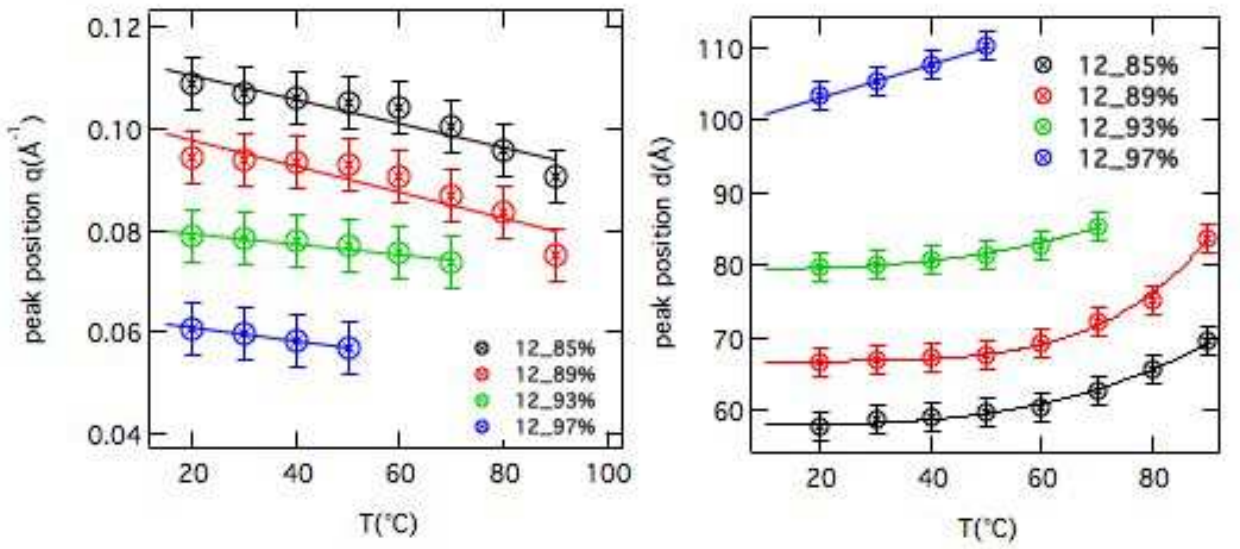

Figure 5.19 G/GMP 1:2 final graphs relative to the peak positions of S(q). The left graph is relative to the position reported in q ($Å^{-1}$), where q is the scattering vector. Error bars correspond to 0.005. In the right graph can be observed the same results, but reported in *d* (Å), where *d* is the d spacing between cylinders in the hydrogel network. Error bars correspond to 2.

In general, can be affirmed that the peak position (in q values) decreases as function of temperature and water concentration. More significant variations of q values have been evidenced for the less-hydrated samples, especially for the 85 and 89% of water), in which the correlation between cylinders in the hydrogel network is higher.

Thus, a model is reported here for the G/GMP network formation. Cylinders, characterized by a high flexibility (Increasing the concentration of G and thus reducing the charge per disk, what happens is the increase in terms of quadruplex flexibility and lateral, side by side aggregation, becomes more and more evident), entangle to generate a network able to entrap water. An intrinsic anisotropicity has been reported for these binary mixtures. Probably, a key role is played by the annealing step that ensure the complete solubilization of G by GMP.

This step determines stacking stabilization and as consequence elongation of quadruplexes which induces the strongest anisotropicity. Presumably, in the consequent re-equilibration at room temperature cylinders organize maintaining a certain degree of orientation and flexibility, this latter depending on G content in G/GMP binary hydrogel.

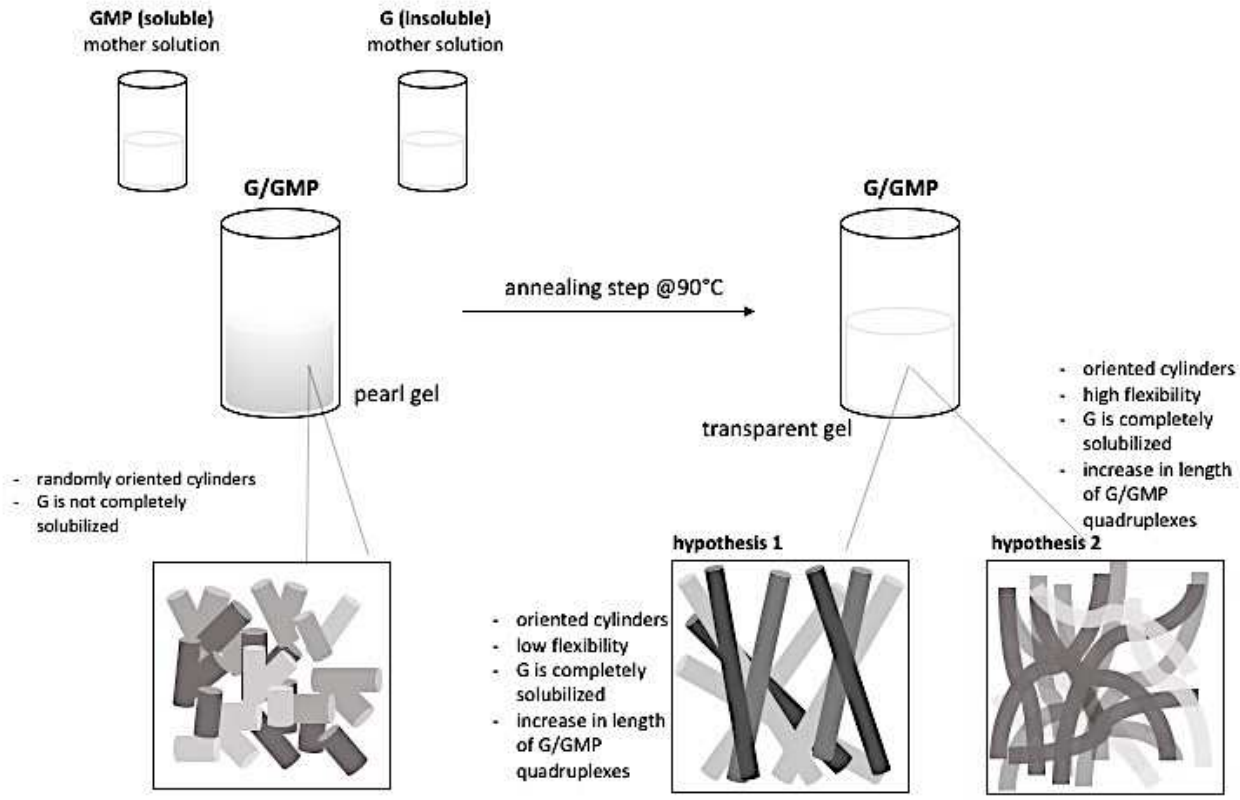

Figure 5.20 proposed mechanism at the base of the formation of G/GMP network. The figure wants to show the fundamental role played by the annealing step, necessary to have all the G in solution. Other key role is played by the content of G, that determines the degree of flexibility of entangled cylinders in the G/GMP network

Chapter 6

Chapter 6

Possible applications of G/GMP hydrogels

6.1 Introduction

in Chapter 3 has been reported a brief introduction about the unique property that guanine has to assemble in complex suprastructures. Guanosine derivatives, such as 5'-GMP, have long been known to be characterized from gelation properties, involving G-quartet as structural basic unit (Bang, 1910; Gellert, 1962). The first report on gel obtained starting from binary mixtures of guanosine (G) and Guanosine 5'-monophosphate (5'-GMP) has been made in 2008 by McGown and coworker (Yu *et al.,*2008). Authors provided an explanation of the reason why 5'-GMP is able to undergo gelation when kept in contact with G. The insolubility of G is balanced out from GMP high solubility, that is able to bring G in solution. Phase diagram reported in Chapter 4 for G/5'-GMP mixtures and the particular Gaussian distribution evidenced in the case of gel-to-sol transition temperatures of G/5'-GMP hydrogels confirms that is fundamental to maintain an exact ratio between components. It is not possible to make further addition of G in the binary mixtures if stable and transparent hydrogels have to be obtained.

A detailed comparison between G and 2'-deoxyguanosine (2'-dG) ability to form stable gels has been made by Kraatz and coworkers (Adhikari *et al.,* 2014) in which gels characterized by an excellent lifetime stability have been obtained. In the last years, many works have been published on the developing of guanosine derivatives able to form gels, e.g. binary mixtures of G and 2',3',5'-tri-O-acetylguanosine (TAcG) reported by Rowan and coworkers (Buerkle *et al.,* 2009; Li *et al.,* 2010); guanosine-borate (GB) hydrogels (Peters *et al.,* 2015a; Peters *et al.,* 2015b). Here has been reported a starting point in one of the possible applications in which binary mixtures of G/5'-GMP can be used. The dynamic and reversible nature that characterize these hydrogels, together with the high stimuli-responsiveness when exposed to external stimuli, give us hope in the involvement of G/GMP hydrogels in the biological field.

6.2 G/GMP inner structural organization: AFM observations

The presence of a cylindrical arrangement in the G/GMP network has been showed and widely discussed in Chapter 4 and 5. Before moving towards the field of possible application using G/GMP hydrogels, observations using Atomic Force Microscopy (AFM) as technique have been made to provide additional details about the inner organization of cylinders in the hydrogel network. Measurements have been performed in collaboration with Juliana Sakamoto Yoneda of the University of Sao Paulo in the laboratory of Prof. Pietro Ciancaglini (USP-Ribeirao Preto). In the following table can be found the complete list relative to samples investigated with the related concentrations considered. Further details about the sample preparation for AFM observations can be found in Chapter 9, section 9.2.3.4**.**

Table 6.1 Complete list of samples measured using AFM. Further details about the preparation can be found in Chapter 9, section 9.2.3.4

G/GMP	sample concentration
1:1	97% 6x dilution 11x dilution 26x dilution
1:2	97% 6x dilution 11x dilution 26x dilution
1:4	97% 6x dilution 11x dilution 26x dilution
1:6	97% 6x dilution 11x dilution 26x dilution
1:15	97% 6x dilution 11x dilution 26x dilution

For clarity, results are reported here only for the 1:2 G/GMP hydrogel, because this G/GMP ratio has been chosen for experiments related to possible applications of G/GMP hydrogel (reported in the next section) and because of the perfect proportion between components that leads to the obtainment not only of a perfectly transparent and homogeneous hydrogel, but also of the most interesting results, in the case of AFM observations.

Figure 6.1 clearly shows the presence of entangled fibers and confirms the model proposed for the formation of G/GMP network. Increasing the rate of dilution, what happens is that the unravelling of fibers in the G/GMP network. Attention has to be focused in the case of higher dilution rate (26x), in which is possible to observe a kind of point of interconnection, a kind of tangle, composed of intertwined wires. Particular about this extremely attractive structure are showed in Figure 6.1.

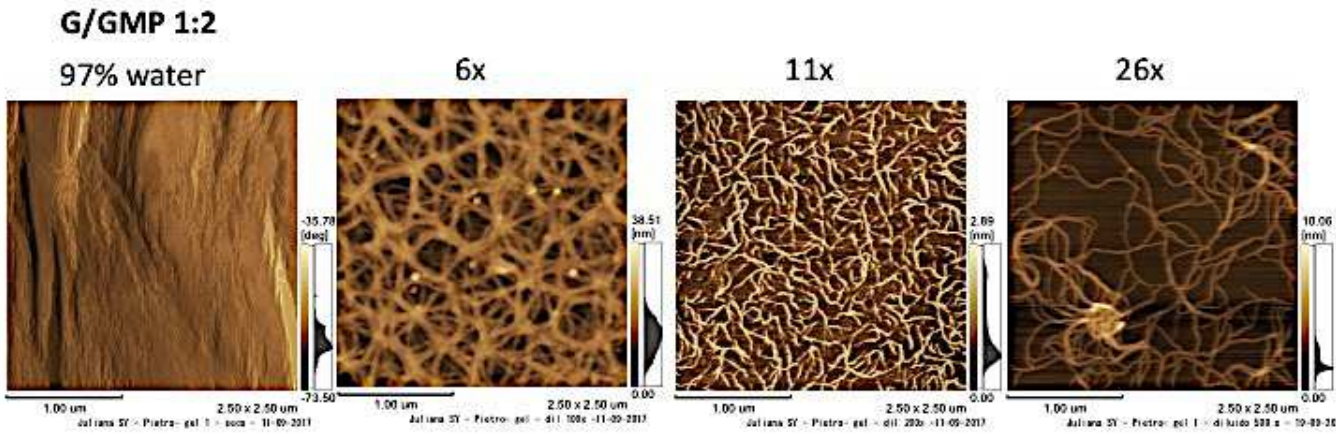

Figure 6.1 AFM observations relatively to the G/GMP 1:2. From the left: 97% of water, 6x, 11x and 26x dilution of the 97%. Bars correspond to 1.00 μm

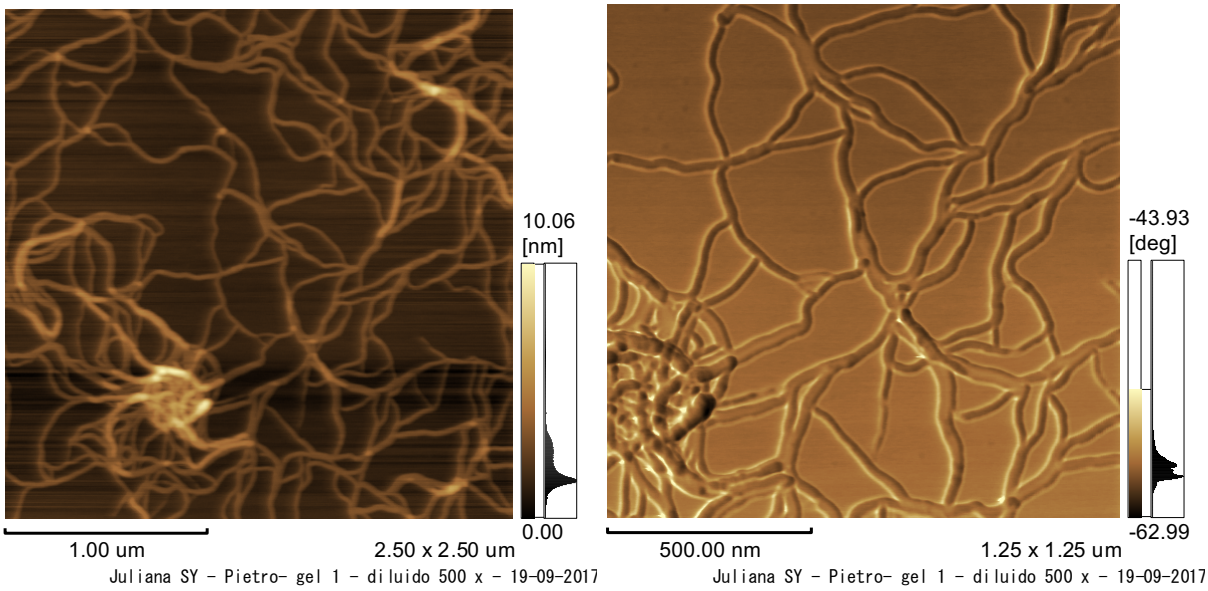

Figure 6.2 particular of AFM observations relatively to the G/GMP 1:2 26x dilution of the 97%. Bars correspond to 1.00 Å (left) 500.00 nm (right)

Has to be underlined that the dimension of wires in the network corresponds to that one observed using XRD and is around 28Å (height of the bar, Figure 6.3), exactly the value of diameter for a GMP cylinder. The average value of distance detected between stripes (observable in red, blue and green in Figure 6.3), is around 100Å, exactly the same distance between cylinders calculated from SAXS profiles (see section 5.2.1.1, Table 5.5, column #4).

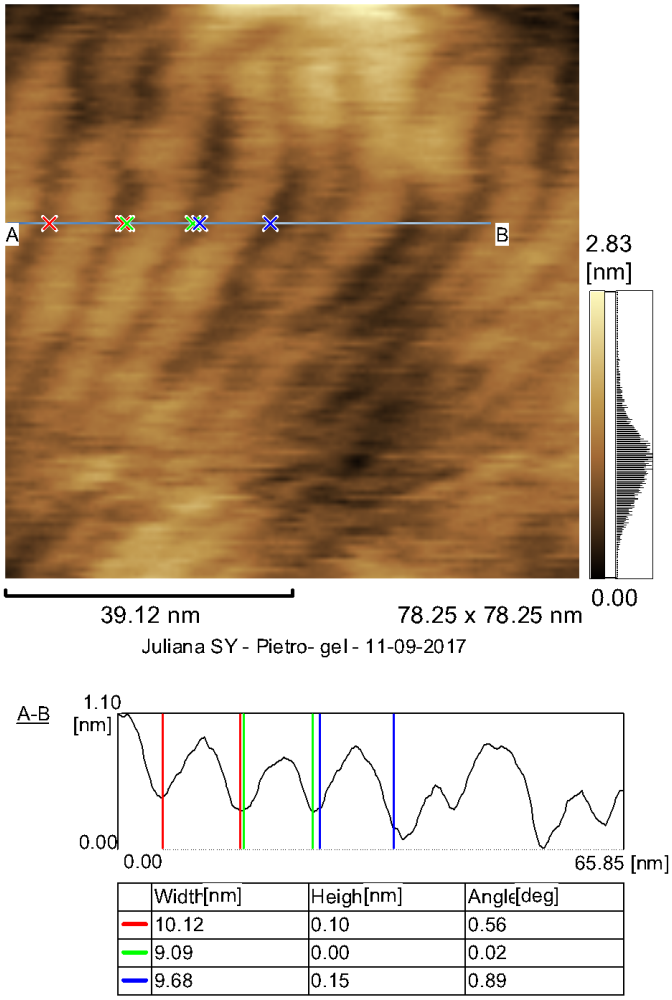

Figure 6.3 particular of AFM observations relatively to the G/GMP 1:2 97% (not diluted). Bars correspond to 39.12 nm

6.3 Interaction of G/GMP hydrogel and model proteins

Based on these results obtained using atomic force microscopy (AFM), a question arises spontaneously about what is the behavior of different model proteins, once they have been kept in contact with the G/GMP hydrogel 1:2. The pH value of the hydrogel has been measured and is around 7.86.

The choice of proteins to be tested has been made focusing on different parameters, such as:

- pH of the gel;
- dimension;
- isoelectric point;
- list of charges over pH range.

Information relative to each protein has been taken using Protein Calculator (http://protcalc.sourceforge.net).

Table 6.2 list of protein examined with G/GMP with related characteristics. Dimension, isoelectric point and charge value at 7.86 (the pH of the G/GMP hydrogel) has been calculated using Protein Calculator (http://protcalc.sourceforge.net/cgi-bin/protcalc)

protein	dimension (kDa)	Isoelectric point (pI)	charge @ pH 7.86	PDB file
BSA (Bovine Serum Albumin)	66.4	5.86	-23.8	4F5S
Cyt-C Cytochrome C	12.4	9.57	8.2	1HRC
HEWL (Hen-Egg White Lysozyme)	14.4	9.04	6.1	1LYS

6.3.1 Macroscopical observations

6.3.1.1 BSA

Probably the high molecular weight of BSA and highly negative charge value at pH 7.86 (the pH value of the 1:2 G/GMP hydrogel 97% of water) confers to this protein the ability to diffuse into the G/GMP network. After 15 days, the gel appears to be completely destroyed. The choice of this protein has been made to try to understand the behaviour of the G/GMP hydrogel when kept in contact with a high molecular weight molecule.

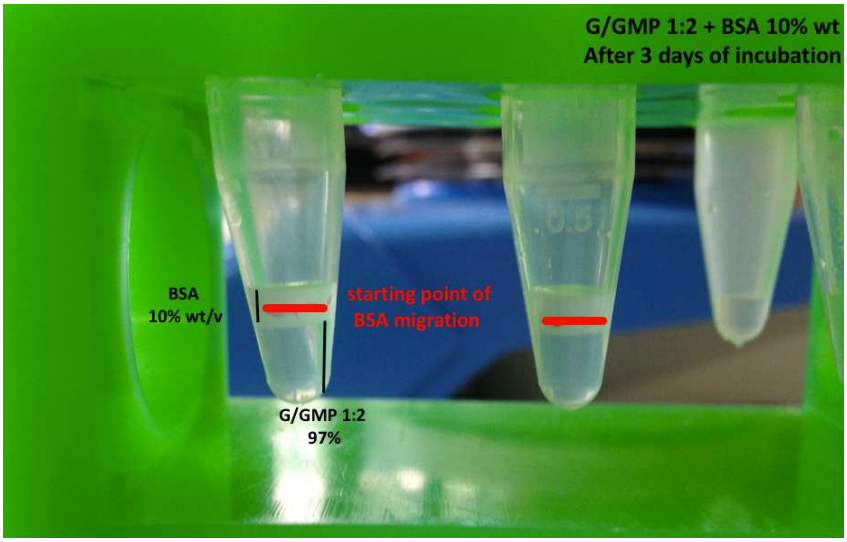

Figure 6.4 G/GMP hydrogel 1:2 after 3 days of incubation with a BSA solution of 10% w/v

X-ray diffraction measurements have been made taking an aliquot of the BSA at the interface gel-protein solution after 1, 3 and 15 days of equilibration. The confirmation that probably the high dimension of BSA leads to the damage of the G/GMP fibers organization and consequently to the disruption of the gel comes from the XRD profile obtained measuring protein after 15 days of equilibration, in addition to the macroscopical observation. No more signals relative to the building block (G-tetrads) have been revealed. Of course, the fact that has been collected every time the same aliquot cannot be ensured, but this can represent the starting point to understand how the charge, together with the molecular weight, influence the behaviour of macromolecule when kept in contact with the G/GMP hydrogel.

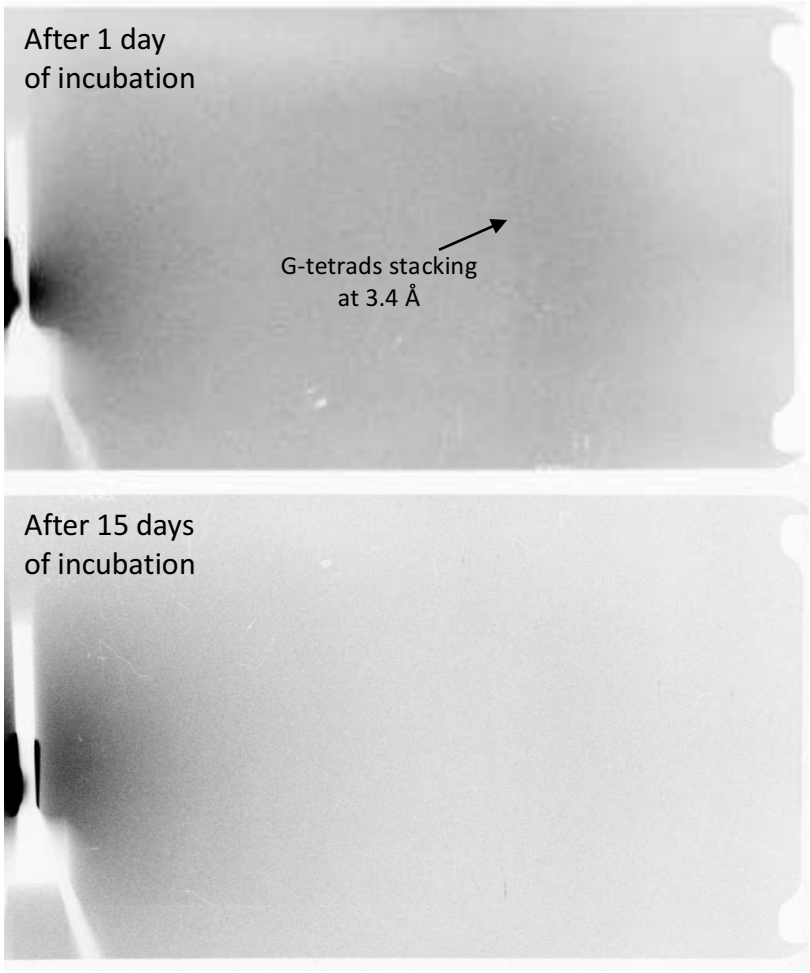

Figure 6.5 G/GMP hydrogel 1:2 after 1 and 15 days of incubation with a BSA solution of 10% w/v. After 1 day of equilibration it is possible to observe a weak signal relative to the stacking of G-quartets. The signal seems to be completely disappeared after 15 days of equilibration of BSA with G/GMP 1:2.

6.3.1.2 Cytochrome C

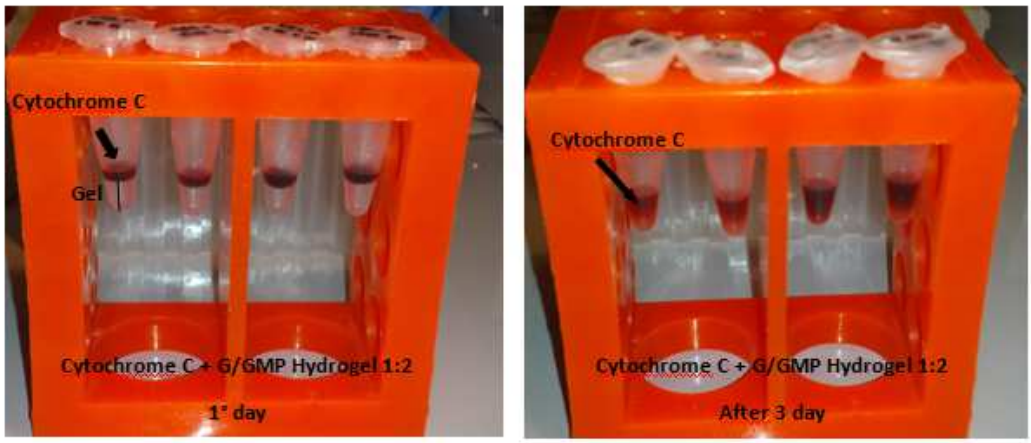

Figure 6.6 G/GMP hydrogel 1:2 after 1 and 3 days of incubation with a solution of 10% w/v of Cytochrome C

Cytochrome C is small protein of 12.4 kDa, characterized from a positive charge at the value of pH measured for the G/GMP hydrogel 1:2. Also in this case an aliquot of cytochrome c at 10% w/v (50 microliters) has been left to equilibrate upon a hydrogel G/GMP 1:2 (200 microliters). What happens after 3 days of equilibration is that the protein solution diffuses into the G/GMP hydrogel network. Probably the small dimension of this

peptide confers to cyt c the ability to locate between G/GMP quadruplexes, without provoking the disruption of the hydrogel. Has to be underlined that the rate of diffusion of the cytochrome c into the hydrogel is very slow, especially this can be observed testing a lower concentration of protein solution. A test has been made using a 4% wt/v protein solution to make a comparison with the 10% wt/v. In all cases, the disruption of the gel has been not evidenced.

6.3.1.2 Lysozyme

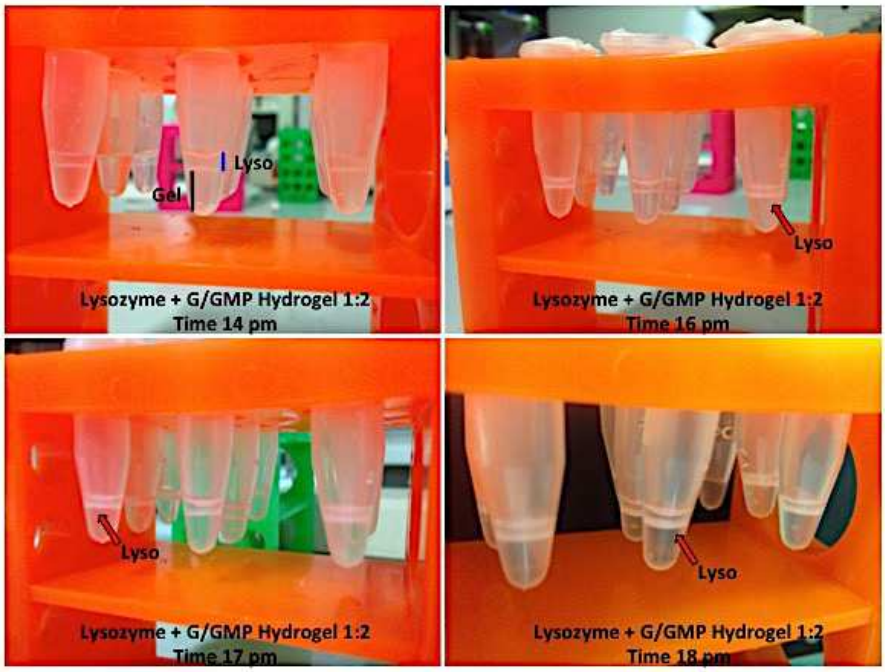

Figure 6.7 G/GMP hydrogel 1:2 incubation with a solution of 10% w/v of HEWL, monitored up to 3 days.

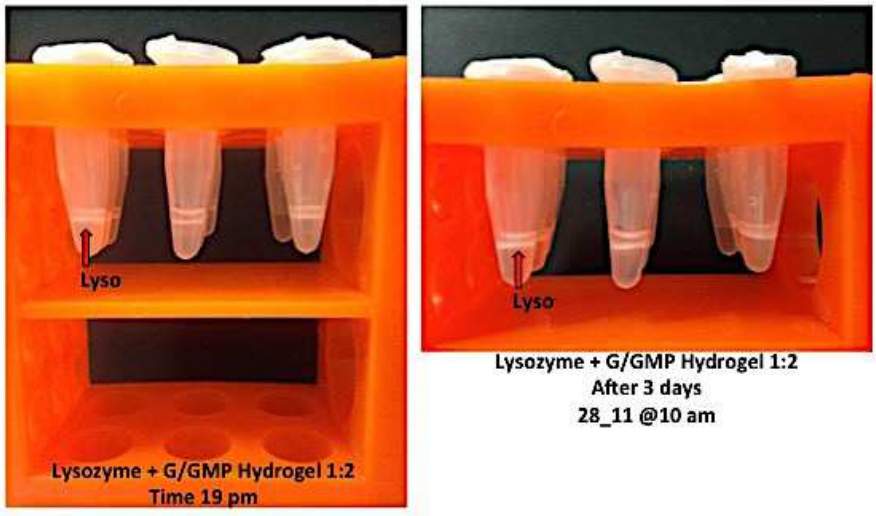

Hen-Egg White Lysozyme (HEWL) has a positive charge at pH of the hydrogel. The choice of this protein can be justified considering the isoelectric point. This is practically the same of that one reported for Cytochrome c, but what happens in the case of HEWL is extremely unexpected.

Leaving HEWL (protein concentration of 10 wt/v) to equilibrate upon the gel, what happens is that immediately, the lysozyme solution starts to become white. Considering Figure 6.7 (time 14 pm), here the interface protein-

gel can be observed. After few minutes, the protein starts to become white and trackable, and no diffusion occurs.

Based on these results, ten samples have been prepared exactly in the same way, leaving HEWL to equilibrate upon the gel. Measurements have been made each day taking a small quantity of the protein localized at the interface gel-protein solution. Also in this case, cannot be ensured that every time protein had been taken from the same position, but results obtained are very interesting.

After 15 days, HEWL seems to crystallize. HEWL powder used to prepare protein mother solution has been analysed using XRD to verify the nature of the protein commercially available. An XRD profile typical of that one of an amorphous solid has been obtained, characterized by a very broad peak in the low-angle region. Thus, probably HEWL undergo a transition from amorphous to crystalline state thanks to the incubation with the G/GMP hydrogel. When signals are referable to the presence of crystals in the samples, G/GMP hydrogel located below protein solution (white and highly concentrated) at the interface appears to be completely disrupted. Thank to these observation, the HEWL crystallization has been associated to a possible effect due to the presence of counterions, provided by the G/GMP quadruplexes architecture. Additional experiments have been planned in the following way. G/GMP hydrogels have been prepared at three different conditions:
(a) G/GMP 1:2 prepared at 98.9% of water (6^{th} dilution, see Section 9.2.3.3) in KCl 0M;
(b) G/GMP 1:2 prepared at 97% of water, KCl 0M;
(c) G/GMP 1:2 prepared at 97% of water, in KCl 1M

The idea has been to prepare a hydrogel in which the high concentration of water cannot provide enough K^+ counterions to provoke the phase transition of lysozyme, and this is the case (a). The concentration of K^+ starts to be higher in the case of sample (b) and finally, as control, counterions have been provided in vast excess in the sample (c). What happened has been exactly what can be expected: HEWL crystallizes only after an incubation of 15 days in the case of G/GMP (b) and after 7 days upon (c).
A theory of the reason why HEWL crystallizes has been formulated and reported in Figure 6.8. Probably the protein concentrates at the interface, due to the swelling property of the gel, able to receive the water of the protein solution. This leads to an increased flexibility of the structural elements of the gel and thus to a major availability of K^+ counterions. Thanks to the augmented hydration level of the G/GMP hydrogel, HEWL probably become able to remove K^+ from the quadruplex architecture. This can justify the disruption of the gel after the lysozyme incubation. Experiments have been performed maintaining the same approach but using glass capillaries, filled with the same amounts of gel and protein and let to incubate. In this case, the interface gel-protein has been monitored using POM and the formation of protein crystals reported.

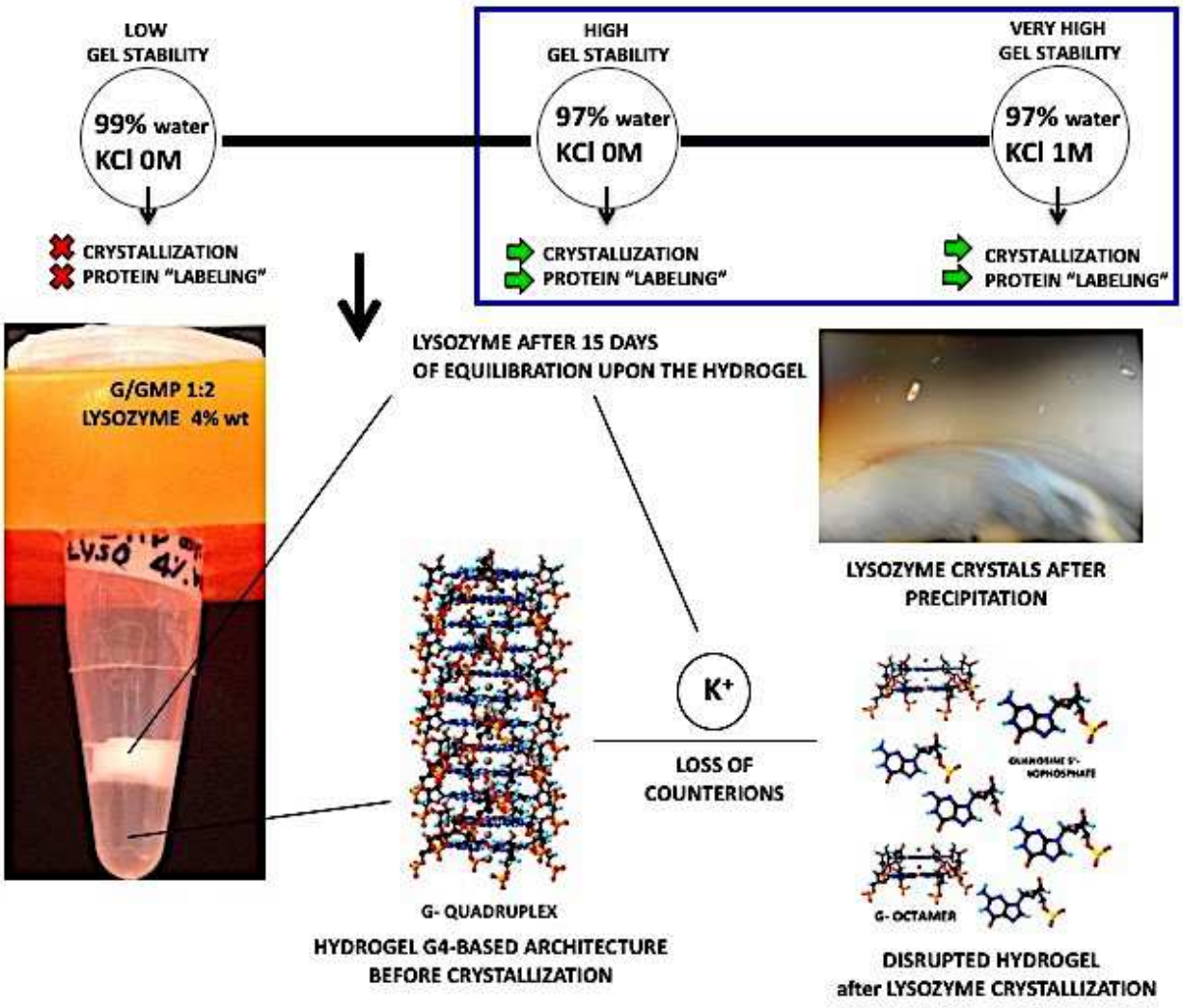

Figure 6.8 possible mechanism at the base of HEWL crystallization after the incubation with G/GMP 1:2 hydrogel

Chapter 7

Chapter 7

Guanosine derivatives: Osmotic Stress Technique

7.1 Introduction

It is well known that guanosine shows a unique polymorphism, determined by its ability to assemble in a spontaneous way. A hierarchical mechanism can be found at the base of the formation of guanosine tetramers, in which four guanine molecules are able to establish connections thanks to their non-canonical way to bind, that is represented by the Hoogsteen scheme, first evidenced by Gellert in 1962 (Gellert *et al.*, 1962). Starting from the structural tetrameric unit, in the presence of an appropriate counterion, what happens increasing concentration is the formation of octamers. If other tetramer units pile above the already stacked tetrameric units, this lead to the obtainment of a very complex chiral suprastructure, the so-called *G-quadruplex*. In this latter, G-quartets are stacked one with the respect to each other, with a tilt angle of 30 degrees to minimize repulsion effect due to external phosphate groups. In aqueous solution, G-quadruplexes show a lyotropic polymorphism, with the formation of columnar Liquid Crystalline cholesteric and hexagonal mesophases (Mariani *et al.*, 2009; Mezzina *et al.*, 2001). Has to be underlined that guanosine self-assembling properties have been evidenced also in DNA, in particular in gene promoters and in G-rich sequences of telomeric tails of chromosomes (Rhodes and Lipps, 2015; Murat and Balasubramianan, 2014). The study of structural properties, quadrihelices stability and the consequent determination of interactions at the base of the formation of columnar phases is of extreme importance, especially if attention is focused to the crucial role played in biology by telomeres and gene promoters. The always growing number of synthesized and patented G-quadruplexes ligands represents the new frontier in the development of potential anticancer drugs (Hansel-Hertsch *et al.*, 2017. It is therefore evident how different applications in medicine and nanotechnology require a complete explanation of the mechanisms at the base of the G-quadruplexes formation and a comprehension of their stability, in particular in the presence of different counterions. In this Chapter can be found a detailed characterization made about a mixture of Guanosine 2'/3'-Monophosphate isomers (Santa Cruz Biotechnology) first determining phase diagram as function of temperature and concentration and then using the osmotic stress technique. Three different counterions have been tested, Na^+, K^+ and NH_4^+, trying to comprise if the degree of stability conferred from the monovalent cation to the GMP 2'/3'-quadruplex architecture is the same of that one evidenced for other G-derivatives, such as for 5'-GMP (Ausili *et al.* 2004), 5'-dGMP (Mariani and Saturni, 1996; Mariani *et al.*, 1998). X-ray diffraction experiments have been conducted under different osmotic pressure conditions and ionic strength. This enable to characterize electrostatic and hydration repulsion contributions, at the base of intercolumnar interactions for a polyelectrolyte in solution and thus to find a relationship with the structure of polyelectrolyte itself.

7.2 The osmotic stress technique: a brief introduction

Many works have been published in the last 40 years on different macromolecules such as phospholipid membranes (LeNeveu, 1976); muscles filaments or tobacco virus particles (Millman and Nickel, 1984); 5'-dGMP (Mariani and Saturni, 1996; Mariani et al.,1998) and DNA (DeRouchey et al.,2010), but the comprehension of the physical phenomena at the base of nucleic acids condensation is still an open challenge. DNA in solution, when exposed to a polymer such as polyethylenglycol (PEG), condenses into a phase (DNA pellet) separated from the polymer. Highly concentrated phases of DNA can be obtained inducing precipitation with (1) a high-MW polymer or (2) ethanol.

As reported in the work of Rau *et al.*,1984, these two methods are independent in the determination of interaxial spacing between molecules, even if different behaviors have been evidenced in the following step of controlled dehydration. For example, in the case of ethanol-induced precipitation of DNA, swelling in PEG solution has been described; different is the case of PEG induced-precipitation of DNA, that lose water and contract. In both cases, the obtained pellets can be used in osmotic stress method, leaving pellet to equilibrate against a polymer solution (such as PEG) provided in vast excess. In the case of guanosine derivatives, such as for Guanosine 2'/3'-Monophosphate, condensation using high-molecular weight polymer (PEG 20000-40000) ensures the obtainment of hexagonal lattice, in which G-quadruplexes are localized at the vertex and the center of a hexagon (See Chapter3, section 3.3).

Thus, the osmotic stress technique can be described as the controlled removal of water from a system, allowed to come at the equilibrium state with a polymer solution of known osmotic pressure. PEG is excluded from the packed DNA, applying a direct force on the condensate. Water, salt and small molecules are free to exchange between PEG and DNA phase. At the equilibrium state, osmotic pressure will be the same in both phases. Thus, osmotic pressure can be considered in terms of energy per unit length (G) per column in the hexagonal lattice and is (Rau *et al.*,1984)

Equation 7.1

$$\pi_{osm} = \frac{dG}{d\sigma} = \left(\frac{dG}{da} \Big/ a\sqrt{3} \right)$$

where σ is the area of the 2D-unit cell and is

Equation 7.2

$$\sigma = a^2\sqrt{3}/2$$

where a is the interaxial distance between 2'/3'-GMP, detectable using X-ray diffraction.

Consequently, the force per unit length $\mathrm{f}(a)$ can be derived:

Equation 7.3

$$\mathrm{f}(a) = \pi a/\sqrt{3}$$

As reported in the work of Mariani and Saturni published in 1996 (Mariani and Saturni, 1996) made using 5'-deoxyGMP, two main contributions can be evidenced in the measurement of intercolumnar forces between parallel guanosine four-stranded helices: one is purely electrostatic, effective at large distances, considerably as the long-range contribution. This one shows a strong dependence on the salt concentration of the solution. The second one is the short-range contribution, that dominates at interaxial distances less than 30-32 Å and

rises steeply as the column approach each other, preventing coalescence of the helices. This latter contribution has an exponential nature and is insensitive to ionic strength of the medium.

Equation 7.4

$$\mathrm{f}(a) = f_{hyd}(a) + F_{el}(a)$$

The equation relative to the hydration repulsion (short-range contribution) has been first described by Israelachvili, (Isarelachvili, 1994) and has the following form

Equation 7.5

$$f_{hyd}(a) = f_0\, e^{-a/\lambda}$$

The hydration force is characterized by the hydration coefficient f_0 , which reflects the degree to which the surface orders the boundary water and by the decay distance λ, which is a property of the water itself and reflects the way that ordering is propagated through water.

The long-range contribution has been described by Parsegian, 1973 and Israelachvili, 1994 and is given by the following equation

Equation 7.6

$$F_{el}(a) = F_0\, \frac{e^{-ka}}{\sqrt{ka}}$$

where F_0 is the force coefficient, independent of the interaxial distance a; k is the inverse of Debye length. Coefficients F_0, f_0, 1/k and λ have been calculated performing curve fitting on curves obtained about force per-unit-length f(a) and will be discussed in the next chapter.

7.3 Guanosine 2'/3'-monophosphate

Phase diagrams have been obtained considering three different salts of the 2'/3'-GMP, K^+, Na^+, NH_4^+ in 0.5M salt solution, as function of concentration (from 10 to 80% in weight of GMP) and temperature (from 20 to 80°C). No relevant variations have been evidenced. In the case of disodium salt, an isotropic phase has been observed at lower concentrations (10-20%) and a hexagonal phase from 30% to 80% wt of GMP. The potassium salt of 2'/3'-GMP shows a cholesteric phase at lower percentages and a hexagonal mesophase up to 80%, for all temperatures explored. Finally, no transitions have been observed in the case of ammonium salt, in which a XRD profile relative to a hexagonal array has been reported for all concentrations and temperatures investigated.

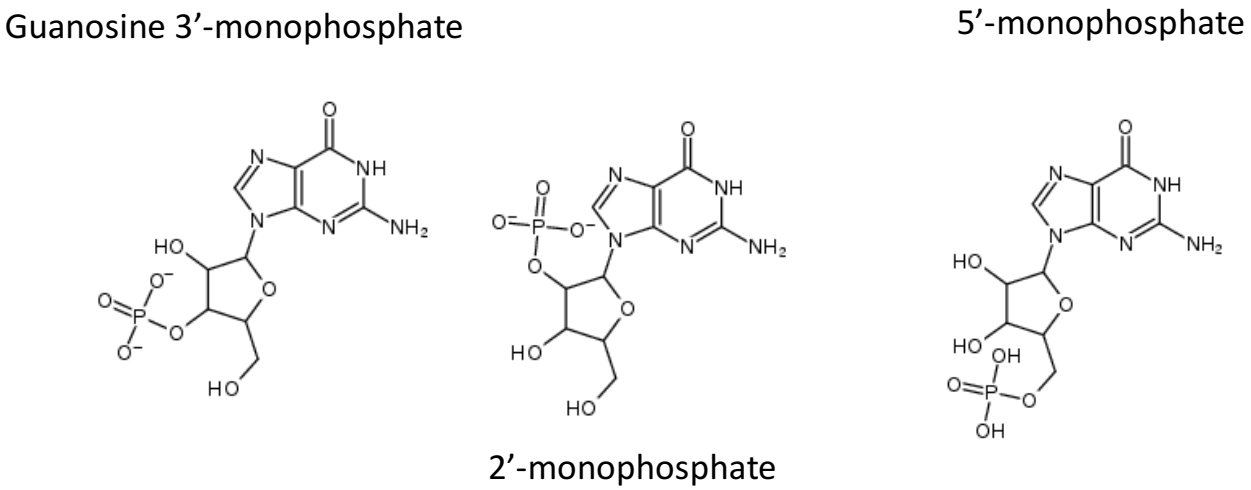

Figure 7.1 chemical structure of guanosine 2'/3'- vs 5'-monophosphate

7.3.1 Analysis of lateral forces using osmotic stress technique: PEG and salt concentration

The complete list of samples measured and the detailed protocol used in the preparation have been described in section 9.2.4. In the following paragraphs can be found results obtained for each salt, starting from the determination of interaxial distance using XRD up to the graphs relative to the force per unit length as function of the axis-to-axis distance, in which global fitting analysis have been performed to extrapolate coefficients relative to the two force contributions, widely described in the previous section.

7.3.1.1 (2'/3')-GMP disodium salt

The following graph shows an example of diffraction profiles obtained from the analysis of 2'/3'-GMP using the osmotic stress technique, prepared at a final concentration of 5% weight/volume and left to equilibrate with PEG of 20% of weight, this latter dissolved first in water and then using different salt concentrations.

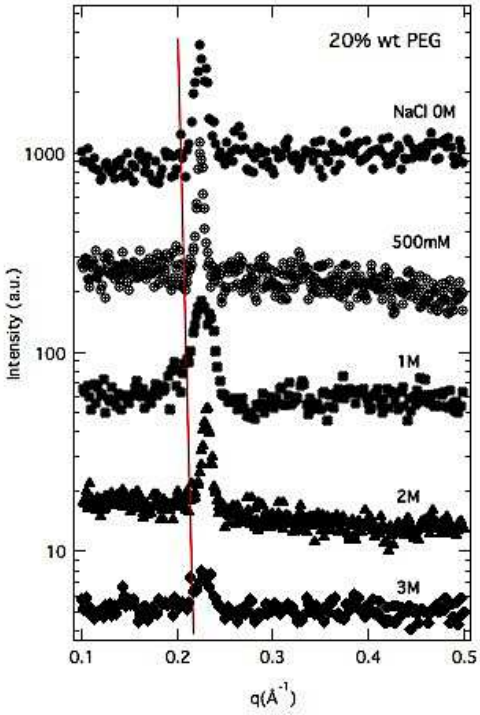

Figure 7.2 XRD profiles have been reported here considering the same polymer concentration (20% PEG) but dissolved first in water (upper profile) and then at different salt molarity. Red line evidences the trend of peak position and clearly shows that no relevant variations in the interaxial distance have been evidenced

From XRD profiles showed in the figure above, what it is possible to observe is a main peak at q value of $\cong 0.22 Å^{-1}$, where q is the scattering vector, reported in $Å^{-1}$. The reflection is narrow and well-defined, thus associable to a hexagonal mesophase. The peak position varies as function of the polymer concentration and of the salt concentration used to dissolve PEG. Considering the q value related to the peak position detected from the XRD analysis, unit cell values have been consequently derived and reported in the following table.

Table 7.1 unit cell values obtained for 2'/3'-GMP disodium salt as function of the different PEG concentration (% in weight)

%PEG(wt)	unit cell NaCl 0M (Å±0.5)	500mM NaCl (Å±0.5)	1M NaCl (Å±0.5)	2M NaCl (Å±0.5)	3M NaCl (Å±0.5)
10	33.0	32.3	32.0	31.4	31.3
20	32.5	32.2	31.7	31.3	31.3
30	32.2	31.8	31.0	30.7	30.6
40	31.3	31.3	30.6	30.5	30.1
50	31.1	31	30.2	30.0	29.8

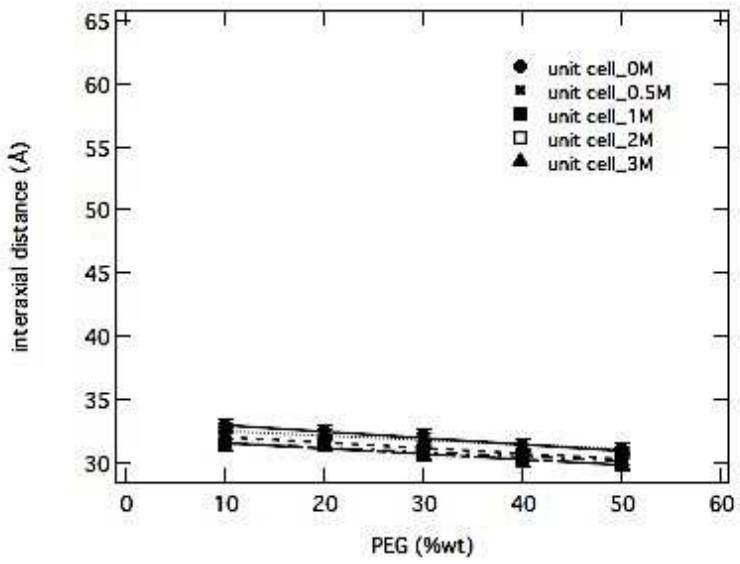

Figure 7.3 unit cell obtained at different salt molarity, reported as function of PEG concentration. Error bars correspond to ±0.5

Focusing attention on unit cells values reported in Table 7.1 and on relative graph showed in Figure 7.3, in which has been reported interaxial distances as function of the PEG concentration investigated, no relevant variations have been observed (considering value obtained in the case of 10% of PEG in water and that one obtained in the case of 50% of PEG in NaCl 3M, the difference is approximately of 3Å) and this allow us to affirm in general that 2'/3'-GMP disodium salt prefers to remain in the dehydrated state. The same behavior has been described for the same compound, when this has been used together with G in the preparation of 2'/3'-GMP(Na_2)/G hydrogels, in which a phase separation (together with a very low stability of the gel) between components has been reported (Chapter 4, section 4.2.2).

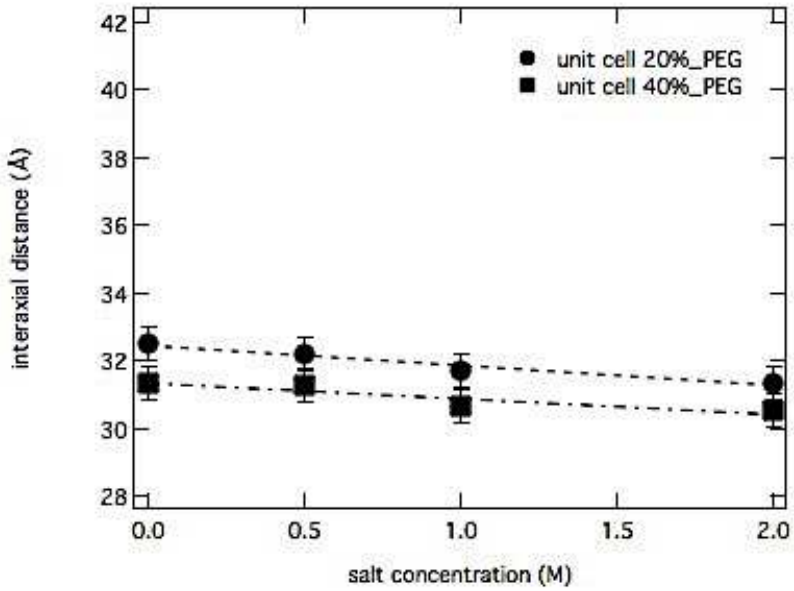

Figure 7.4 unit cell values relative to 20 and 40% of PEG and reported as function of salt molarity. Error bars correspond to ±0.5

The successive step after the comprehension of how unit cell varies as function of polymer and salt concentration, the osmotic pressure values have been calculating using the equation

Equation 7.7

$$\text{Log}\prod = a + b(\text{polymer wt\%})^{c}$$

where a=1.57, b=2.75 and c=0.21.

Table 7.2 osmotic pressure values calculated using the equation $\text{Log}\prod = a + b(\text{polymer wt\%})^{c}$ where a=1.57, b=2.75 and c=0.21

%PEG(wt)	Log∏ (dyne/cm^2)	∏ (dyne/ cm^2)	∏ (dyne/Å)
10	6.03	1.07e06	0.01
20	6.63	4.25e06	0.04
30	7.19	1.54e07	0.15
40	7.54	3.45e07	0.34
50	7.82	6.66e07	0.66

The equation can be found in the web page of the Laboratory of Physical and Structural Biology Eunice Kennedy Shriver of the National Institute of Health and also in that one relative to the Professor Peter R. Rand of the Brock University https://brocku.ca/researchers/peter_rand/osmotic/data/peg20000.

The osmotic pressure values obtained have been then used in the calculation of force per unit length f(a), following the equation 7.3 reported in section 7.2.

Table 7.3 force per unit length values relative to the 2'/3'-GMP disodium salt

%PEG (wt)	f(a) 0M NaCl (dyne/Å)	f(a) 500mM NaCl (dyne/Å)	f(a) 1M NaCl (dyne/Å)	f(a) 2M NaCl (dyne/Å)	f(a) 3M NaCl (dyne/Å)
10	0.20	0.20	0.20	0.19	0.19
20	0.79	0.79	0.78	0.77	0.77
30	2.86	2.83	2.75	2.73	2.72
40	6.23	6.22	6.08	6.06	5.98
50	11.9	11.9	11.6	11.5	11.4

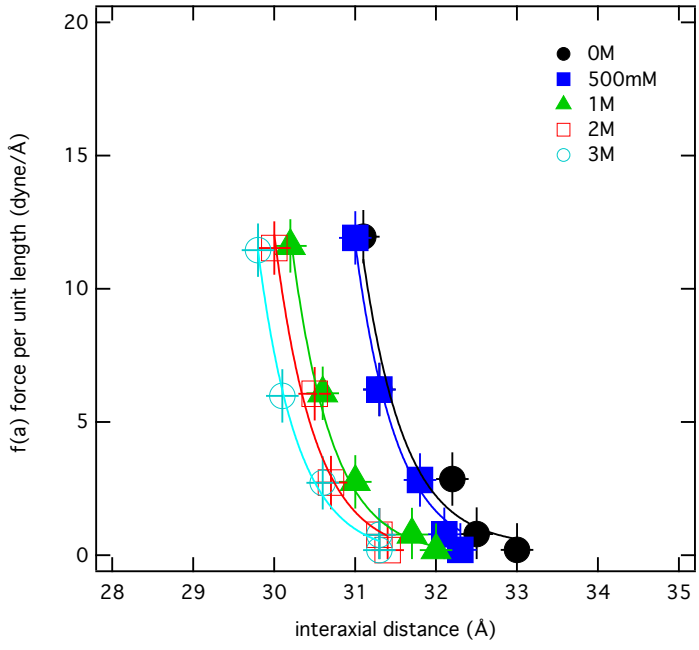

Figure 7.5 force per unit length f(a) calculated in the case of GMP 2'/3' disodium salt and reported as function of the interaxial distance. Global fitting analysis have been made considering equation x and x. Error bars correspond to ±1 and ±0.2 respectively in y and x axis.

In the following graph (Figure 7.5), f(a) have been plotted as function of interaxial distance between cylinders. The graph reported in Figure 7.3 shows that considering the same percentage of PEG, small variations can be appreciated between different salt concentrations. The sodium counterion seems to confer a high stability to the system and this is in line with the fact that hexagonal symmetries have been detected also at low concentrations of polymer.

7.3.1.2 (2'/3')-GMP potassium salt

The same characterization has been made considering 2'/3'-GMP(K^+). An example of the diffraction profiles obtained using XRD has been reported. Compared with that one reported for the disodium salt (Figure 7.2), at low concentrations of salt (curves relative to KCl 0M and 20mM in the graph below), a broad peak can be appreciated, due to a high level of hydration and probably at 0M KCl to the presence of a double-phase. Increasing salt molarity, the peak is instead narrow and well-defined.

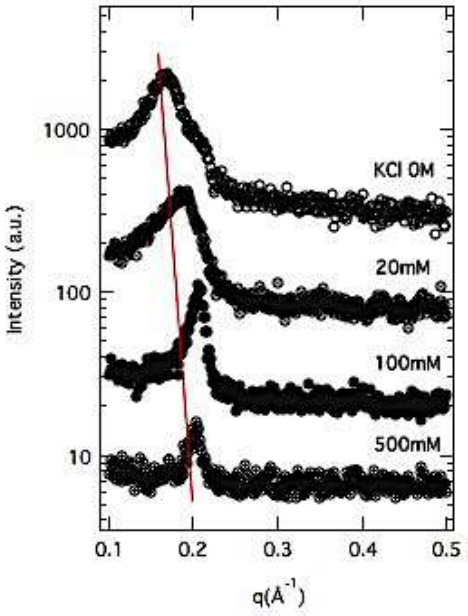

Figure 7.6 XRD profiles relative to 20% PEG reported here considering different salt concentrations investigated. Red line evidences peak position and clearly shows that no relevant variations in the interaxial distance have been evidenced

Relevant variations in terms of unit cell values have been reported in the case of potassium salt. More or less 30Å of difference can be calculated considering 10% of PEG in water with 50% of PEG dissolved in KCl 500mM, this because potassium salt of 2'/3'-GMP is more susceptible to PEG and salt concentrations used in the dissolution of polymer. Considering both Table 7.4 and graphs 7.7 and 7.8 it is possible to observe how unit cell dimension decreases as function of the increasing concentration of PEG and salt.

Table 7.4 unit cell values obtained for 2'/3'-GMP disodium salt as function of the different PEG concentration (% in weight)

%PEG(wt)	unit cell 0M KCl (Å±0.5)	20mM KCl (Å±0.5)	100mM KCl (Å±0.5)	500mM KCl (Å±0.5)
10	62.6	54.9	50.4	35.4
20	42.7	39.5	35.7	35.3
30	34.6	34.5	34.2	34.1
40	33.1	32.9	33.2	33.0
50	32.4	31.6	31.9	32.0

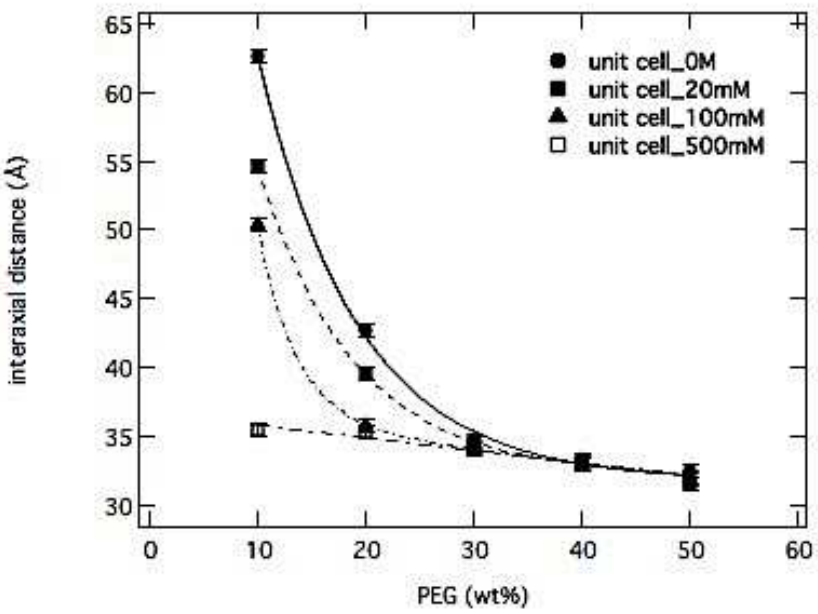

Figure 7.7 unit cell obtained at different salt molarity, reported as function of PEG concentration (% weight). Error bars correspond to ±0.5

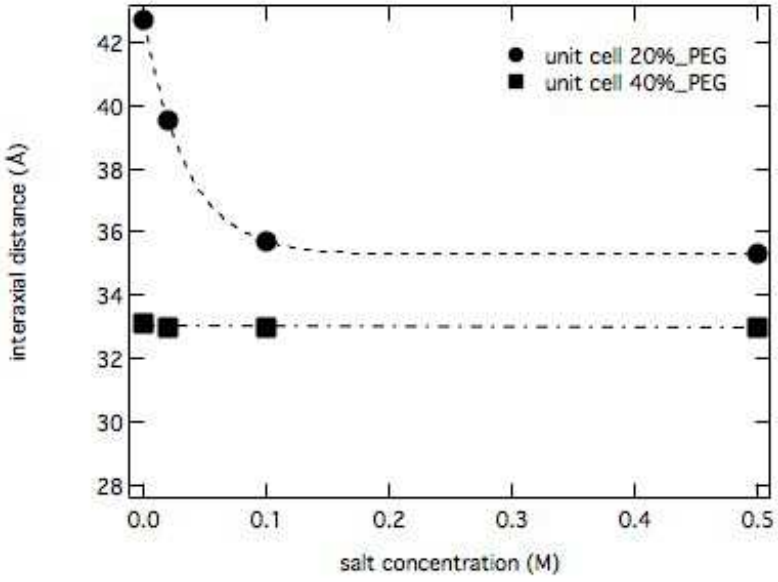

Figure 7.8 unit cell values relative to 20 and 40% of PEG and reported as function of salt molarity.

Unit cell values (Table 7.4), together with osmotic pressure calculated for each PEG concentration (Table 7.2), have been used in the calculation of force per-unit-length f(a). It is clearly observable how f(a) varies as function of PEG and salt concentration. At low-osmotic pressure and f(a) values a strong dependence on ionic strength has been evidenced. Different is the case of higher-pressure values in which data appear to be independent of salt concentration (curves converge to a common point).

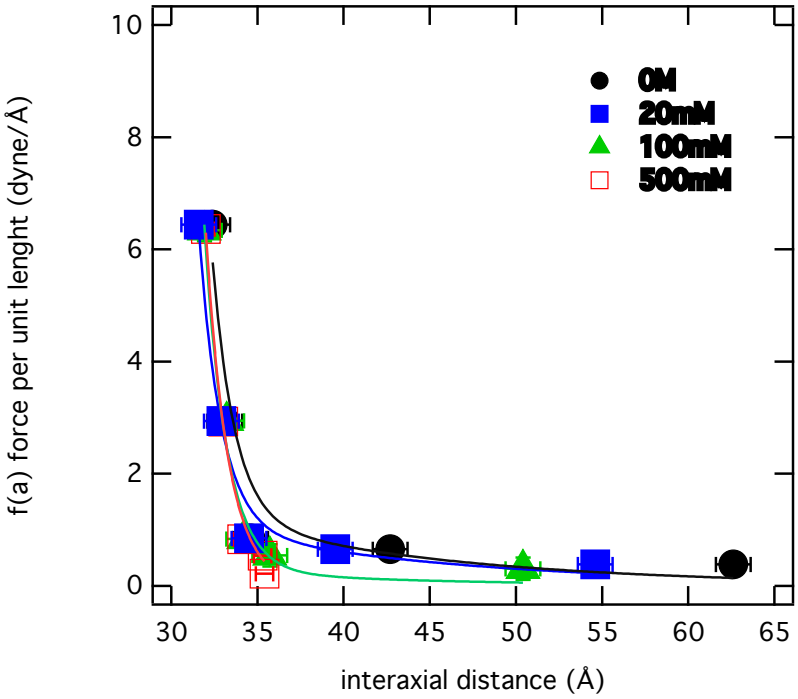

Figure 7.9 force per unit length f(a) calculated in the case of GMP 2'/3' potassium salt and reported as function of the interaxial distance. Global fitting analysis have been made considering equation x and x. Error bars correspond to ±1.

Table 7.5 unit cell values obtained for 2'/3'-GMP disodium salt as function of the different PEG concentration (% in weight)

% PEG(wt)	f(a) 0M KCl (dyne/ Å)	f(a) 20mM KCl (dyne/ Å)	f(a) 100mM KCl (dyne/ Å)	f(a) 500mM KCl (dyne/ Å)
10	0.39	0.39	0.31	0.22
20	0.66	0.66	0.55	0.54
30	0.85	0.85	0.84	0.84
40	2.94	2.94	2.95	2.93
50	6.44	6.44	6.34	6.36

7.3.1.3 (2'/3')-GMP ammonium salt

Finally, the ammonium salt of GMP 2'/3' has been characterized. The same scheme in the presentation of results has been followed, to provide a direct comparison with other two counterions tested (previous paragraphs 7.3.1.1 and 7.3.1.2). Also in this case, such as for potassium, relevant variations in terms of unit cell values have been reported using XRD, after the equilibration of GMP 2'/3' pellet with high molecular weight polymer (PEG) dissolved first in water and then using different salt concentrations. An example of XRD profiles has been reported in Figure 7.10, considering the same PEG concentration, in water and different salt molarities.

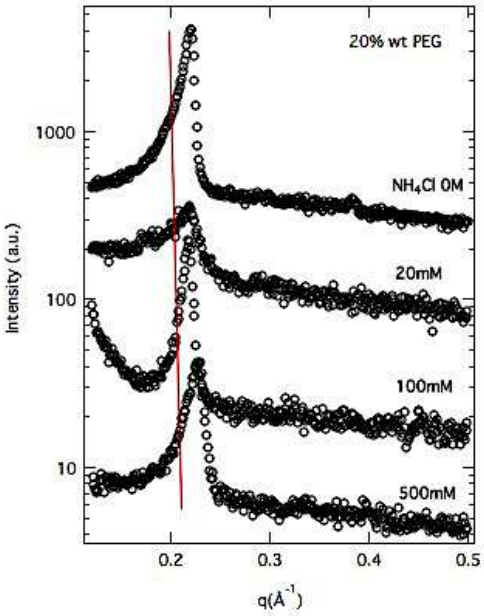

Figure 7.10 XRD profiles relative to 20% PEG reported here considering different salt concentrations investigated. Red line evidences peak position and clearly shows that no relevant variations in the interaxial distance have been evidenced

Unit cell values have been calculated for each sample measured and reported in the following table. A variation of ≅25Å have been reported comparing 10% of PEG in water with 50% of PEG dissolved in 500mM of KCl, showing the ammonium, such as potassium, is sensible to different PEG and salt concentrations used.

Table 7.6 unit cell values obtained for 2'/3'-GMP disodium salt as function of the different PEG concentration (% in weight)

%PEG(wt)	unit cell 0M KCl (Å±0.5)	20mM KCl (Å±0.5)	100mM KCl (Å±0.5)	500mM KCl (Å±0.5)
10	56.2	51.6	53.8	32.2
20	33.1	33.4	33.3	31.7
30	32.4	32.5	32.5	31.7
40	31.8	31.4	31.6	31.3
50	31.1	31.2	31.2	30.4

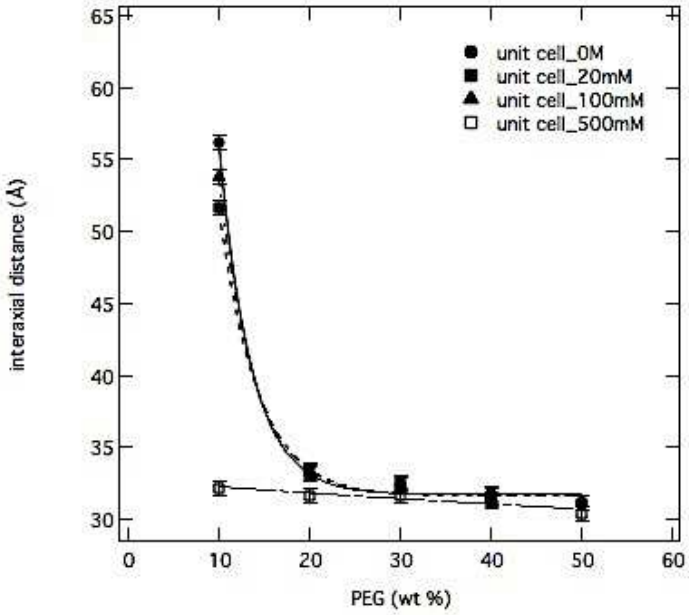

Figure 7.11 unit cell obtained at different salt molarity, reported as function of PEG concentration (% weight). Error bars correspond to ±0.5

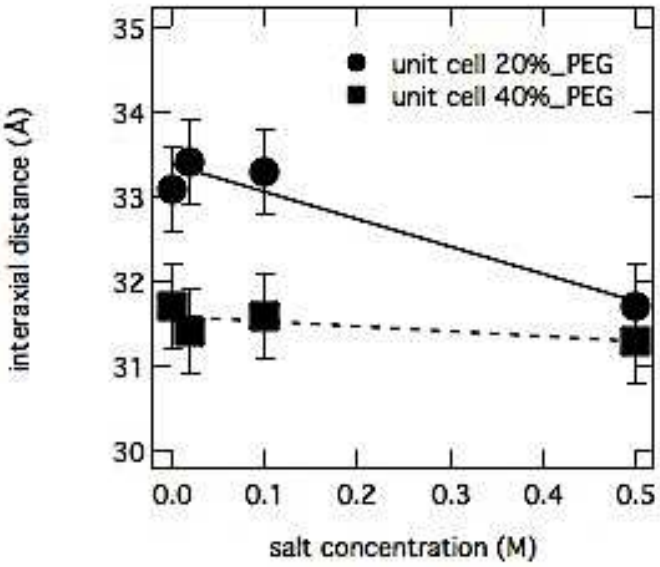

Figure 7.12 unit cell values relative to 20 and 40% of PEG and reported as function of salt molarity. Error bars correspond to ±0.5.

Unit cell values (Table 7.6), together with osmotic pressure calculated for each PEG concentration (Table7.7), have been used in the calculation of force per-unit-length f(a). It is clearly observable in Figure 7.13 how f(a) varies as function of PEG and salt concentration. At low-osmotic pressure and f(a) values a strong dependence on ionic strength has been evidenced. Different is the case of higher-pressure values in which data appear to be independent of salt concentration (curves converge to a common point).

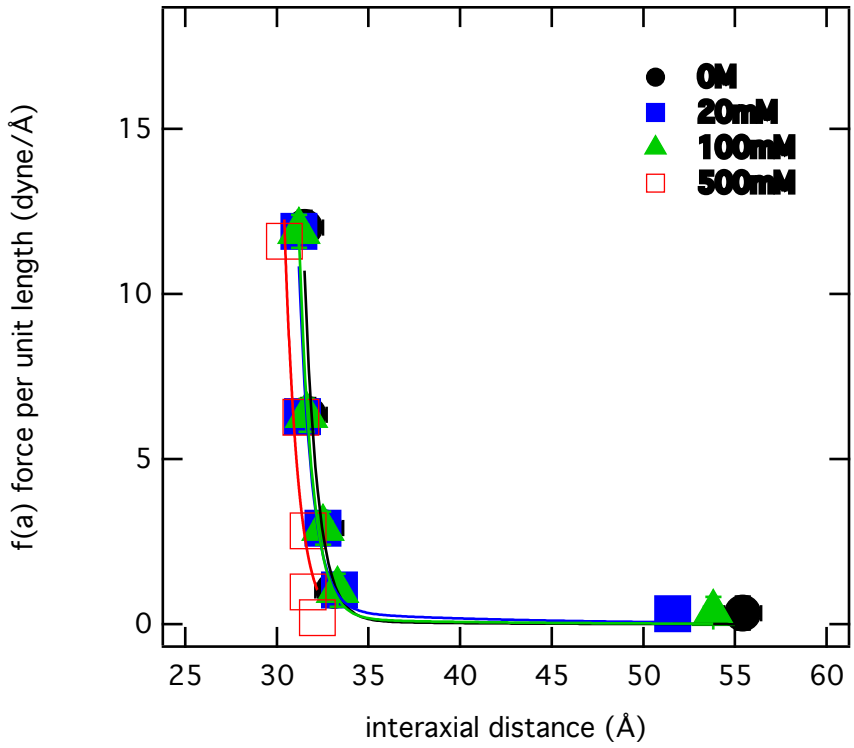

Figure 7.13 force per unit length f(a) calculated in the case of GMP 2'/3' potassium salt and reported as function of the interaxial distance. Global fitting analysis have been made considering equation x and x. Error bars correspond to ±0.5

Table 7.7 unit cell values obtained for 2'/3'-GMP disodium salt as function of the different PEG concentration (% in weight)

%PEG(wt)	f(a) 0M KCl (dyne/ Å)	f(a) 20mM KCl (dyne/ Å)	f(a) 100mM KCl (dyne/ Å)	f(a) 500mM KCl (dyne/ Å)
10	0.32	0.30	0.31	0.19
20	0.76	0.77	0.77	0.73
30	2.82	2.81	2.81	2.74
40	6.22	6.16	6.20	6.14
50	12	11.9	11.9	11.6

In the next paragraph an extended discussion about curve fitting performed of f(a) as function of axis-to-axis distance will be presented.

7.3.2 Analysis of lateral forces using osmotic stress technique: curve fitting

Results have been presented and widely discussed in the previous paragraphs allowing to make some general considerations about these only recently characterized GMP isomers. The first one is related to unit cell values, in which small variations have been reported in the case of disodium salt. Completely different is the case of potassium and ammonium, that show a strong dependency on PEG and salt concentrations. Probably the higher stability level conferred by potassium and ammonium to the GMP 2'/3' suprastructures leads to a 2D hydration of the G-quadruplexes. Values of about 60 and 56 Å observed respectively in the case of 10%PEG in water of 2'/3'-GMP(K) and 2'/3'-GMP(NH_4), suggests the presence of a high content of water in the system. In addition, has to be underlined that measurements using the OST have been performed also in the presence of 5% PEG, but results have been not reported here only because of the difficulty found in the correct attribution of value of zero in the calculation of the scattering vector. The second consideration refers to the use of curves related to f(a) as function of the interaxial distance, reported in Figures 7.14. These curves, obtained as function of ionic strength, allow to derive important information about the quadrihelices organization and the condensation of these suprastructures. Attention has to be focused to the key role played by water in the stability of quadruplexes and to the effect that chirality of these objects has on forces entailed in their interaction.

Performing *global fitting* on these curves using equations 7.5 and 7.6 reported in the section 7.2 best fit curves have been obtained and reported again here below. Fit parameters, both for the hydration and electrostatic repulsion have been consequently derived and reported here in Table 7.8.

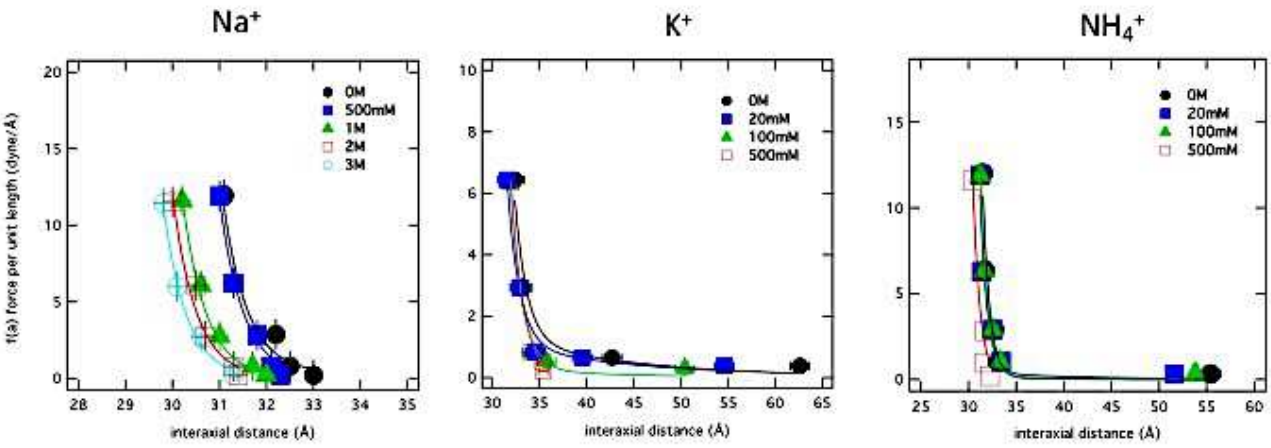

Figure 7.14 summary of curve fitting performed in the case of the three different salts of 2'/3'-GMP analyzed

Table 7.8 fit parameters obtained performing curve fitting on f(a) vs interaxial distance profiles.

salt molarity (M)	f_0(dyne/Å)	λ (Å)	F_0 (dyne/Å)	κ (Å)
NaCl				
0	3.80e27	0.51	17	0.1
0.5	2.90e27	0.51	4	0.23
1	2.00e27	0.50	1	0.33
2	1.37e27	0.50	0.1	0.47
3	2.95e27	0.50	0.01	0.57
KCl				
0	4.58e11	1.28	12	0.06
0.02	2.95e11	1.28	8	0.055
0.1	3.99e11	1.28	4	0.07
0.5	4.19e11	1.28	0.5	0.23
NH_4Cl				
0	5.80e19	0.73	12	0.085
0.02	3.90e19	0.73	8	0.08
0.1	4.20e19	0.73	5	0.09
0.5	1.50e19	0.73	0.5	0.209

No significant variations have been reported in the case of disodium salt of GMP 2'/3'-monophosphate. Thus, a detailed analysis about fit parameters and different contributions in terms of forces will be discussed about potassium and ammonium as counterions.

A clear dependency on ionic strength have been evidenced only in the case of parameters related to long-range electrostatic repulsion contribution F_0 and k (Figure 7.15 and 7.17, lower graphs). The analysis of the short-range contribution (section 7.2, equation 7.5) provide useful information. Considering differences in terms of force intensity for each GMP salt used in osmotic stress experiments, this can suggest a different correlation pattern between hydrophilic and charged surfaces and counterions, possibly linked to the surface itself. Different decay distance λ (Table 7.8, column #3) detected for each counterion is probably related to the difference periodicity of the helix, due to variations in helix pitch.

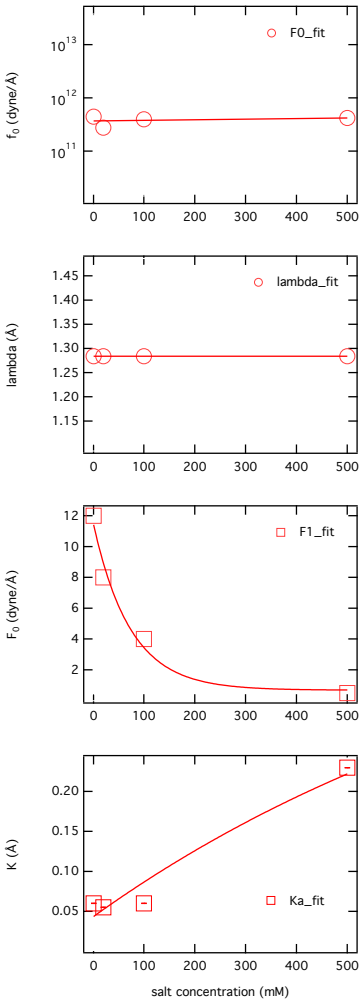

Figure 7.15 fit parameters obtained in case of 2'/3'-GMP potassium salt

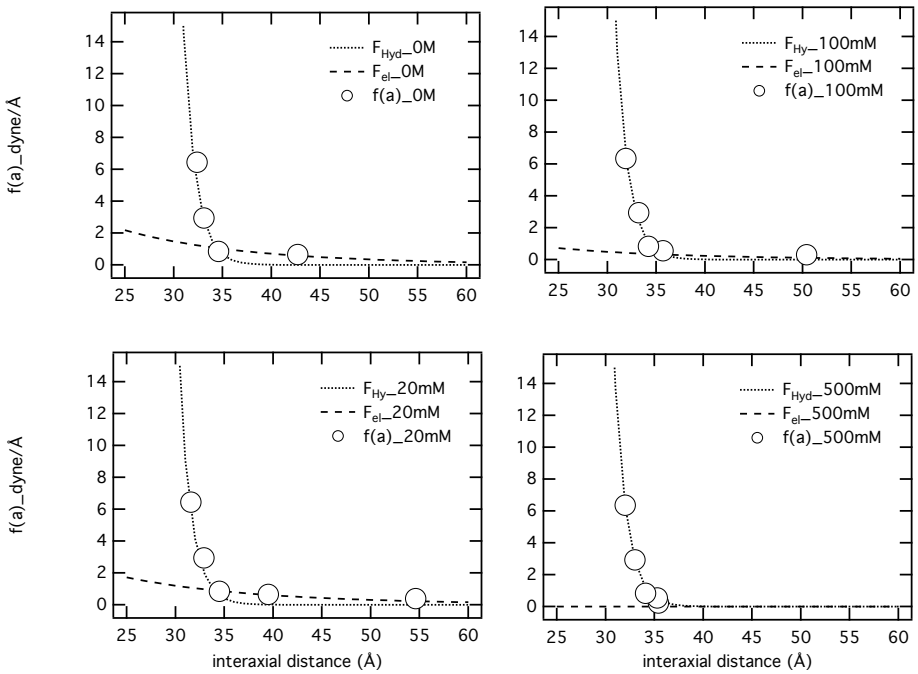

Figure 7.16 fit results related to the 2'/3'-GMP potassium salt with related analysis of the two contributions of the lateral force

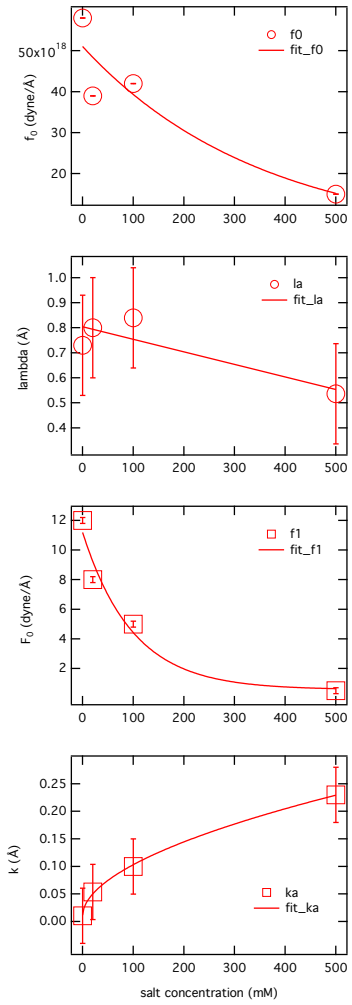

Figure 7.17 fit parameters calculated in case of 2'/3'-GMP ammonium salt

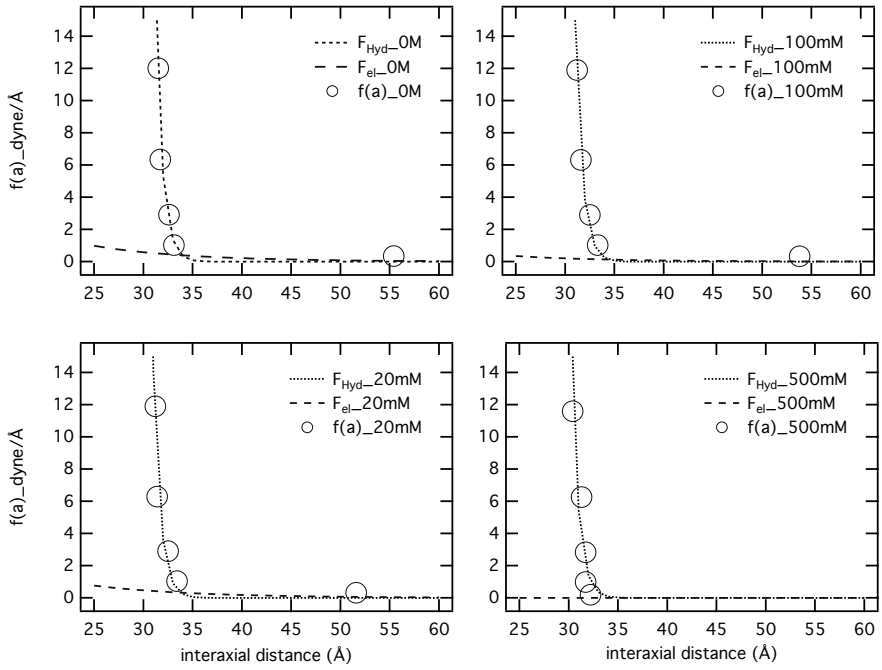

Figure 7.18 fit results obtained for the 2'/3'-GMP ammonium salt with related analysis of the two contributions of the lateral force

Applying theories formulated by Leikin and Parsegian (Leikin and Parsegian, 1994) about interactions between helices of the following kind, can be demonstrated that the hydration force decay length (λ) is directly related to the that one of water (3Å) and to the helix pitch *p*. This can be calculated using the following equation (Leikin and Parsegian, 1994):

Equation 7.8

$$\lambda^* = \frac{1}{2[(1+\lambda_w)^2 + (2\pi/p)^2]^{0.5}}$$

Considering fit parameters obtained for each counterion tested, results have been reported in the following table.

Table 7.9 Results of the calculation made about helix pitch following the equation 7.8

2'/3'-GMP salt	λ* (Å)	p (Å)	number of disk piled
Na^+ in NaCl	0.51	6.8	2
K^+ in KCl	1.28	30.6	9
NH_4^+ in NH_4Cl	0.71	10.2	3

A very high repulsion between phosphate groups can be associate to the case of 2'/3'-GMP disodium salt. This is consistent with the high value of F_0 obtained in the global fitting analysis (Table 7.8). Thus, the helix pitch for the disodium salt is very short. Considering symmetry between tetramers piled, the rotation angle can be easily derived, and is of 45 degrees.

Different is the case of potassium salt, in which the number of tetramers piled is very high, 9. The twist angle in this case is of 10 degrees and of consequence the helix pitch is very long. An intermediate value between sodium and potassium has been calculated for ammonium salt, consistent with results obtained from Mariani and Saturni (Mariani and Saturni, 1998). A simple model can be made:

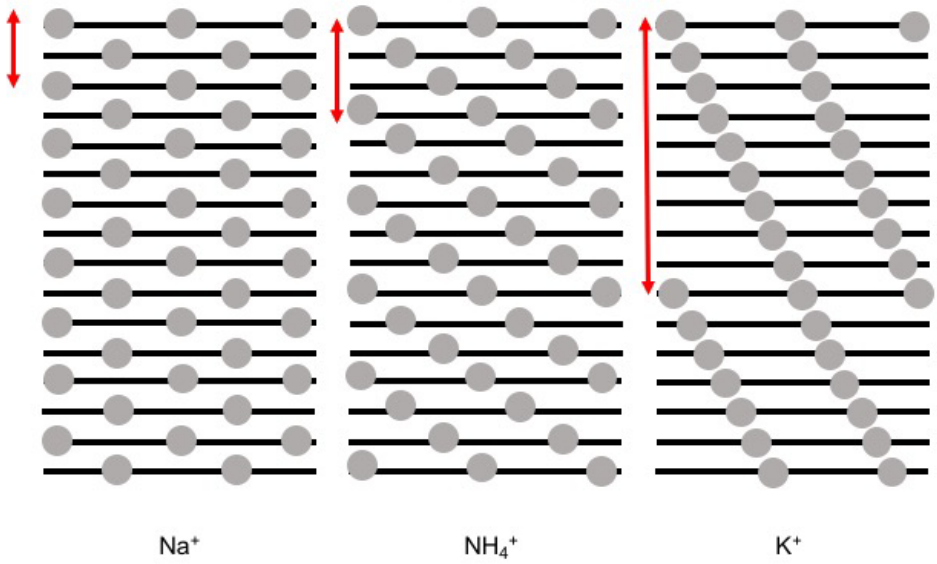

Figure 7.19 schematic representation of different quadrihelices structures. Quartets are reported as black bars, phosphate groups with grey circles. The red arrow indicates helix pitch proposed for each different counterion.

7.4 Guanosine/Guanosine 5'-Monophosphate Hydrogels

Measurements of lateral forces using the osmotic stress technique has been made also in the case of binary mixtures of G/GMP(K^+). Results reported here represent the initial effort to achieve an extended comprehension of forces contributions on the complex of G/GMP hydrogels network, when exposed to a high molecular weight polymer. The same approach of that one used in the case of Guanosine 2'/3'-monophosphate has been adopted. Thus, the protocol used for the preparation of samples can be considered the same and can be found in section 9.2.4. The unique difference is in the obtainment of DNA derivatives pellet: in this case precipitation using absolute ethanol has been made starting from small amounts of G/GMP hydrogels at a given ratio, prepared at 97% of water (in weight), as reported in detail in section 9.2.3.

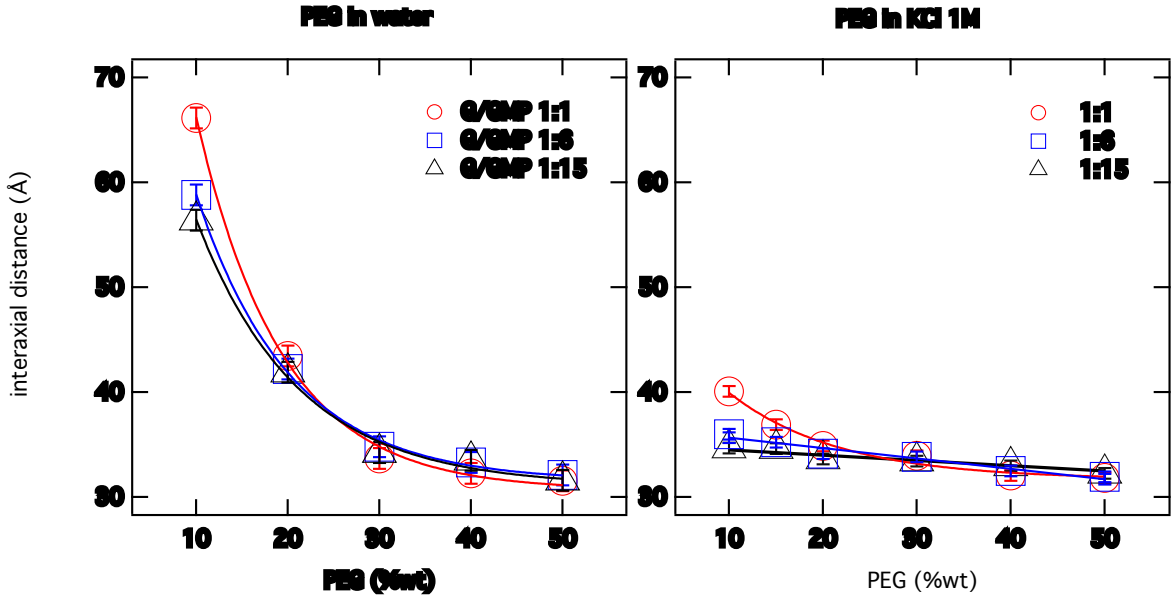

Figure 7.20 fit parameters calculated in case of 2'/3'-GMP ammonium salt

PEG has been tested at different concentrations, from 10 to 50% wt/v. In the following tables have been reported unit cell values obtained from X-ray diffraction profiles, both for PEG dissolved in water and KCl 1M.

Table 7.10 unit cell values obtained for G/5'-GMP(K^+) as function of the different PEG concentration (% in weight) dissolved in water

PEG (% wt) in water	unit cell (Å) G/GMP 1:1	unit cell (Å) G/GMP 1:6	unit cell (Å) G/GMP 1:15
10	66.1	58.8	56.4
20	43.5	42.2	41.9
30	33.7	34.8	34.3
40	32.3	33.3	33.5
50	31.6	32.1	31.6

Table 7.11 unit cell values obtained for G/5'-GMP(K^+) as function of the different PEG concentration (% in weight) dissolved in KCl 1M

PEG (% wt) in salt	unit cell (Å) G/GMP 1:1	unit cell (Å) G/GMP 1:6	unit cell (Å) G/GMP 1:15
10	40.1	36.0	34.7
15	36.9	35.2	34.6
20	34.9	34.1	33.6
30	33.9	33.8	33.4
40	32.1	32.5	33.0
50	31.8	31.9	32.3

Graphs reported in figure 7.19 clearly show the high level of hydration achieved at lower percentage of PEG dissolved in water (10% wt) with the respect of that one dissolved in KCl 1M. Focusing on charge-per-disk, a correlation with the different ability of G/GMP to hydrate can be found: in G/GMP 1:1, in which is higher the amount of G, a major hydration level can be observed. This is probably due to the lower inter-helix electrostatic contribution that makes easier the control of the level of hydration. Different is the case of G/GMP hydrogels 1:6 and 1:15 in which unit cell values seems to be very similar at all PEG concentrations tested.

A possible mechanism to explain this different behavior has been proposed and resumed in the following image.

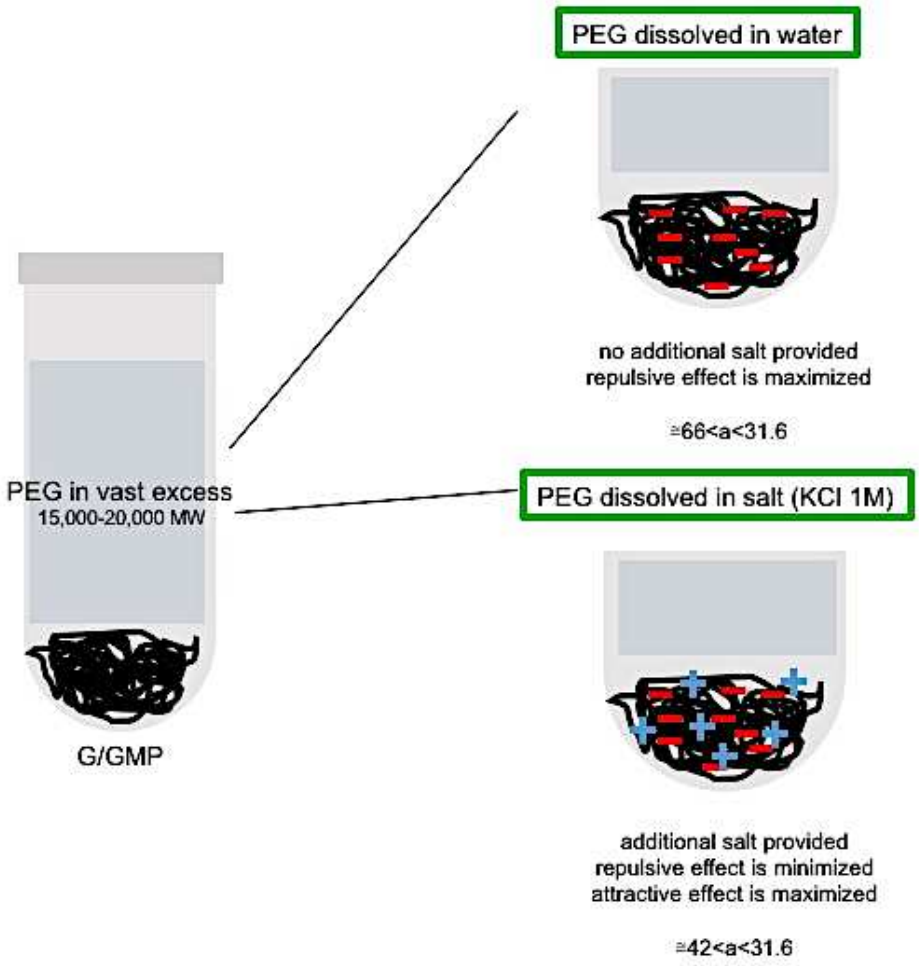

Figure 7.21 proposed theory of different behavior of G/GMP tested using PEG dissolved in water and in salt

Salt used to dissolve PEG seems to be the responsible of the minimization of electrostatic repulsion between cylinders in the G/GMP sample. The higher values obtained in the case of 5% of PEG dissolved in water can be related to the presence of a strong electrostatic repulsion that let G/GMP to hydrate.

Chapter 8

Chapter 8

Conclusions and future insights

The ability of biomolecules to organize spontaneously in supramolecular structures led to the obtainment of versatile molecular architectures, with diverse and important functions in living systems (Dash and Saha, 2016).

An intense collaboration with Profs. Rita Cortesi and Elisabetta Esposito has been pursued concerning the structural organization of lipid-based nanoparticles. Many different kinds of NPs and active principles have been measured (without previous filtration) using both X-Ray Diffraction (XRD) and Small Angle X-Ray Scattering (SAXS).

Many works have been published concerning the characterization of solid lipid nanoparticles (SLN) with *crocin* (Esposito *et al.*, 2017a), one of the most powerful natural antioxidant that can be found in *Crocus sativus* sp.; Pt-PTA, a phosphinic platinum complex (Sguizzato *et al.*, 2017a); Nafion (Sguizzato *et al.*, 2017b).

Progesterone, dimethylfumarate and retynil palmitate (Esposito *et al.*, 2017c) have been tested both with SLN and Nanostructured Lipid Carriers (NLC) to find a reproducible production protocol for the development and analysis of NLC/SLN in pilot scale batches. Finally, in the case of Monoolein Aqueous Dispersions (MAD) *quercetin* (Cortesi *et al.*, 2017) and most recently, another natural antioxidant isolated from *Crocus sativus* sp., *crocetin*, have been tested.

In all cases reported here, characterization made using XRD represented a very useful tool to comprise how the presence of the active principle can lead to structural modifications of the inner organization of lipid molecules in nanoparticles. For example, in few cases, also phase transitions have been reported consequently to the addition of drug in the formulation (e.g. a transition from cubosome to hexasome in the case of NLD-B when kept in contact with *crocin*, reported in the work of Esposito et al.,2017a).

XRD and POM play a fundamental role not only in the determination of the phase assumed by lipid, but also in the comprehension of differences in terms of structure and degree of stability of lipid phase induced by the use of different additives (emulsifier, stabilizing agents) and protocol of production (the *canonical* Ultrasonication vs the most recent High-Pressure Homogenization). An extended work of characterization has been made both for SLN/NLC taking into account different lipids (Tristearin, Suppocire, Precirol and Compritol) and concentrations to try to comprise which differences occurs when NPs formulations have to be produced in a pilot scale.

In parallel to the extended structural characterization made about lipidic nanoparticles, a completely different self-assembling system has been considered in my PhD project, the G4-based hydrogels.

Thanks to the intrinsic ability that guanine has to bind in a non-canonical way, following the so-called Hoogsteen scheme, G-quadruplexes can be obtained *in vitro* using different DNA/RNA derivatives, in the presence of an appropriate counterion. These unique suprastructures can be found also *in vivo* in regions characterized by a high biological relevance, such as human telomeres and oncogene promoters (K-RAS, c-MYC, BCL-2) (Murat and Balasubramianan, 2014). This makes intuitive the perception of how fundamental is the role played by quadruplexes in telomerase activity.

However, the role of G-quadruplexes as anticancer targets is only one of the numerous applications in which these complex molecular assemblies are involved, for example as basic structural units in the formation of

gels for (e.g. enantiomeric separation (Dowling, 2004); environmental remediation (Plank *et al.*, 2017); cell media (Buerkle *et al.*, 2012); controlled incorporation of dyes (Das *et al.*, 2016)).
Gelation ability of guanosine and its derivatives has been reported for the first time about 70 years ago, from Ivar Bang in 1910 and then from Gellert in 1962 (Bang, 1910; Gellert *et al.*, 1962).
Guanosine-based hydrogels can be defined as supramolecular non-covalent (physical) gels, due to the key role played by molecular self-assembly that drives gelation in a hierarchical, stepwise arrangement of components (Peters and Davis, 2016). An extended characterization has been presented here in the case of binary mixtures of Guanosine/Guanosine 5'-monophosphate hydrogels.

At the beginning of the PhD project an initial comprehension of the stabilizing effect provided by the counterion in the G/GMP network has been made testing 5'-GMPNa^+, NH_4^+ and K^+, together with guanosine. The decision to examine in depth hydrogels made combining G/5'-GMP(K^+) has been taken, because of the high stability provided by potassium to the whole G/5'-GMP architecture. The use of potassium as counterion is fundamental in the obtainment of highly-stable and transparent hydrogels.
Results obtained classifying them macroscopically (Chapter 4) with that one obtained in the case of SAXS measurements (Chapter 5) have been combined in the determination of phase diagrams, see Chapter 4, Figure 4.4. Inverted-vial tests and POM observations have been made to derive gel-to-sol transition temperatures. Data are completely in agreement with information derived form 2D-SAXS profiles about aniso-to-isotropic phase transitions, starting from the 97% of water in weight, up to the more-hydrated samples (97.3-99.1% of water, Chapter 5, Figures 5.12-5.14). In the case of phase diagram reported for the 97%, this is characterized by a unique Gaussian distribution. That one brings to mind the immediate comprehension of how further additions of guanosine (above the 1:1 ratio) lead to a decrease in terms of stability of these binary mixtures. A precise equilibrium between components has to be maintained to ensure the complete solubilization of naturally insoluble G, made by GMP and followed by an annealing step at 90°C.
The presence of guanosine can be related to the unique anisotropic nature of G/5'-GMP hydrogels, evidenced both by SAXS and POM measures. A detailed analysis of the anisotropic profiles of G/GMP hydrogels has been made to provide an evidence of the precise way with molecules organize in the G/GMP network.

Completely in agreement with the theory reported by Peters and Davis in the last review published in 2016 about Guanosine-based hydrogels (Peters and Davis, 2016) about SAFiN formation (Self-Assembled Fibrillary Network), probably what happen in the formation of G/5'-GMP(K^+) 3D-architecture is exactly what they hypothesized in the case of low-molecular weight gelators (LMWG). All starts from a basic building block (represented by G-quartet) that is able to organize in our case in short cylinders (as reported in Chapter 5, Figure 5.20). The formation of fibers starts form these short cylinders, thanks to the solubilization of G, provoked by the annealing step. Thanks to this step what happens is the stacking stabilization that lead to the growth in length of cylinders, that now are able to entangle in bundles of fibers and of consequence to entrap water. We argue that the degree of flexibility of cylinders depends on the G content in the G/GMP binary mixture, as showed in Figure 5.20, in which two distinct hypotheses have been reported. The intrinsic anisotropicity of these binary mixtures is probably due to the increasing in length of cylinders, that entangle maintaining a certain degree of orientation.

Diluting Guanosine/Guanosine 5'-monophosphate binary mixtures and performing Atomic Force Microscopy (AFM) observations in collaboration with Prof. Rosangela Itri and PhD Juliana Sakamoto Yoneda, a clear evidence of the presence of entangled G/GMP fibers has been provided (see Chapter 6, Figures 6.1 and 6.2). The dimensions detected in the case of AFM observations (more or less 28Å, confirm the presence of G/GMP quadruplexes). The average value reported in the case of G-quartet radius is of 13Å (Zimmerman *et al.*, 1975).

In addition, the presence of an interference peak due to the correlation between G/GMP cylinders can be clearly appreciated analyzing 1D-SAXS circularly averaged profiles. Structure factors S(q) calculations have been made and reported in Chapter 5. S(q) peak positions seems to move as function of temperature range explored, in all water concentrations investigated.
No less attractive is the strict connection between the comprehension of the phenomena at the base of the formation of supramolecular architectures (originated from Guanosine derivatives) and the RNA World hypothesis. G-quadruplexes can be found widely in RNA and chemists have not yet found a plausible prebiotic synthesis for RNA (Li *et al.*, 2013). As affirmed in the work published in PCCP from Hud and co-workers (Li *et al.*, 2013)., "(…) These assemblies and the propensity of these compounds to form liquid crystals suggest a possible means by which non-covalent structures might have originally selected the shape of the Watson-Crick base pairs (…)". Exactly what can be affirmed from SAXS measurements obtained from G/GMP hydrogels. The very strong peak evidenced in the less hydrated conditions suggests the possible formation of a liquid-crystalline phase that disappears on heating at the temperature which correspond to the gel-to-sol transition detected by inverted-vial test.

These results enabled us to move in the direction of possible applications using G/GMP hydrogels. The decision to test model proteins to try to understand how different protein structural parameters (e.g. molecular weight, isoelectric point and net charge at G/GMP hydrogel pH) can influence the protein behavior when let to equilibrate upon the gel has been made. BSA, Beta-lactoglobulin, HEWL and cytochrome C have been examined.
The most curious results can be attributed to lysozyme, in which crystallization of protein has been observed. HEWL has been measured using X-ray diffraction before its equilibration upon the 1:2 G/GMP hydrogel, in which a typical XRD profile of an amorphous solid has been reported. Thus, a phase transition consequent to the equilibration of protein upon the gel occurs.
Further experiments have been conducted varying water and salt concentration of G/GMP hydrogel. Crystallization occurs when this latter is characterized by a certain degree of fibers flexibility. Probably this characteristic influences the G/GMP hydrogel network ability to swell and consequently to acquire water from the protein solution network, increasing protein concentration at gel-protein interface. Another essential condition is that G/GMP hydrogel has to provide enough potassium counterion to guarantee protein crystallization. The proposed mechanism at the base of amorphous-to-crystal state transition has been summarized in Chapter, Figure 6.8. This represent only a starting point but highlights clearly how the unique stimuli-responsiveness of G/GMP physical hydrogels provides infinite possibilities in finding some biological applications.

Chapter 9

Chapter 9

Materials and Methods

9.1 Lipid nanoparticles

Has to be underlined that the preparation of nanoparticles samples, for all the results reported here, has been made by the group of University of Ferrara (Department of Life Sciences and Biotechnology). Different types of NPs have been analyzed. In the section of Results, for each kind of nanoparticles, has been reported the related method of production. The main lipids that have been used for the preparation of nanoparticles are:

- Tristearin ($C_{57}H_{110}O_6$);
- Monoolein ($C_{21}H_{40}O_4$);
- Suppocire (C_{10}-C_{18} triglycerides);
- Precirol ($C_{37}H_{50}O_4$);
- Compritol ($C_{25}H_{50}O_4$);

In addition to lipids, surfactant and oils have been added, such as:

- Sodium cholate
- Sodium caseinate
- Tween® 20
- Tween® 80
- Miglyol
- Nafion®

the role played by those compounds (e.g. Tween 80 is necessary to confer brain-target specificity to nanoparticles) in each formulation has been specified in each paragraph related to NPs results.

Finally, a monoolein:water phase diagram is reported here to have a better comprehension of results presented in the section 2.6.

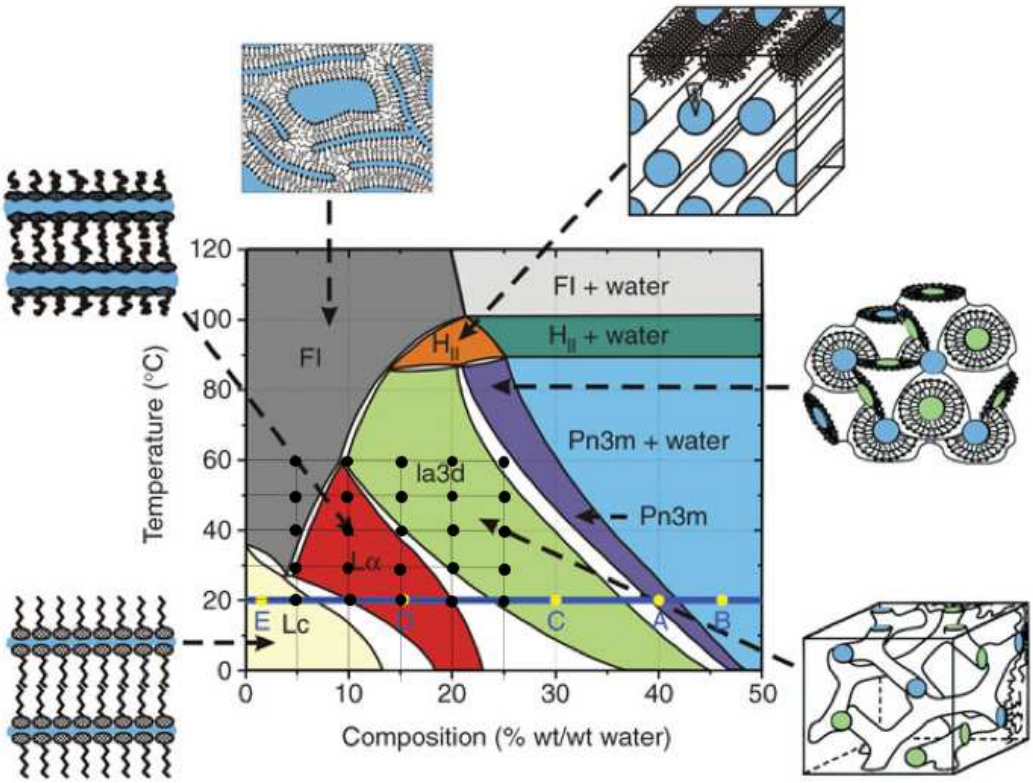

Figure 9.1 phase diagram of monoolein:water system. Modified from the original one of Briggs and Caffrey, 1996. The grid wants to evidence the region explored in the study presented in the section 2.6. Dots refer to measurements made in the study

9.2 Guanosine derivatives

Guanosine hydrogels have been prepared starting from mother solutions of guanosine and guanosine derivatives.

Guanosine 5'-monophosphate (GMP) is commercially available as free acid form (Santa Cruz Biotechnology) or disodium salt (Santa Cruz Biotechnology, Sigma Aldrich).
Chemical formula: $\mathbf{C_{10}H_{14}N_5O_8P}$
Molecular weight: 363.22 g/mol

The fundamental role played by the counterion in the quadruplex architecture has been explained in Chapter 3. To obtain GMP linked with the desired counterion has been necessary to treat chemically guanosine: in the case of disodium salt is necessary to make ion exchange chromatography; if you are managing free acid form, chemical titration is the more practice and easy way to treat guanosine.

9.2.1 Acid-base titration of 5'-GMP free acid form

The acid-base titration of GMP free acid form requires:

- an appropriate hydroxide solution (XOH, where X is the desired counterion (K, Na, NH_4) at 1M concentration;
- 5'-GMP dissolved in bidistilled water as starting solution.

The process of solubilisation of GMP in water is long, because you are forcing an acid to come in solution. The heating of GMP aqueous solution to increasing the solubility level has to be avoided. One time obtained the complete solubilisation of 5'-GMP(H^+), the pH of the starting solution of GMP can be measured and small quantities of KOH 1M progressively added to the GMP aqueous solution.

The addition of the appropriate hydroxide solution has to be made monitoring continuously the pH value until 9. The progressive addition of XOH solution is characterized by absence of colour switch of the solution, thus the pH value is the only way to monitoring the exchange of counterion.
The obtained salt (in this case 5'-GMP(K^+) is now completely soluble in water.
The titration is followed by two cycles of:

- precipitation using 1:3 ratio of GMP/absolute ethanol (two times);
- centrifugation at 4000 rpm/15 minutes after each washing.

The collected GMP can be placed in tubes and then in a ThermoSavant SPD 111V SpeedVac. GMP can be now lyophilized overnight and then stored at -20°C.

Guanosine (G) (Sigma Aldrich) has been used without additional treatments. It is characterized to be insoluble in water.
Chemical formula: **$C_{10}H_{14}N_5O_8P$**
Molecular weight: 283.24 g/mol.

9.2.2 Ion-exchange chromatography of GMP disodium salt

This chemical procedure can be applied in the case of GMP salts (in this case e.g. 5'-GMP disodium salt; 2'/3'-GMP disodium salt and so on) to obtain the exchange of a desired counterion. The whole process is more complex with the respect of chemical titration and requires:

- 150ml (for 15g of resin) of hydroxide solution (XOH, where X is the desired counterion (K, Na, NH_4) at 2M concentration;
- 5'-GMP(Na_2) or 2'/3'-GMP(Na_2) aqueous solution as starting solution
- 15g of resin DOWEX 50WX8
- a falcon syringe (20ml of volume)
- MilliQ water

The first step requires the equilibration of DOWEX ion-exchange resin with KOH 2M. For 15g of resin, 150ml of hydroxide solution has to be used.
Hydroxide solution can be added to the resin and let to equilibrate using a magnetic stirrer (very slowly).
At the end of the resin equilibration, this can be placed in a Gooch filter and washed with MilliQ water up to pH 7. Now the resin is ready to be placed in a falcon syringe (a small amount of cotton is required at the top of the syringe to avoid the leakage of the resin).

The GMP dissolved in MilliQ water (10 ml of water/500mg of GMP) can be collected with a falcon glass syringe and placed in the ion exchange column. At least 10 times washing are required to ensure the complete exchange between counterions.

After the 10 washes, GMP is now providing the desired counterion. An additional washing of the column with milliQ water (5ml) is necessary to recover the remaining GMP entrapped in the resin.

These steps are followed by 2 times precipitation using absolute ethanol (1:3 ratio GMP aqueous solution/ethanol) and centrifugation at 4000 rpm for 15 minutes.
The washed and precipitated GMP is now ready to be placed in cleaned tubes, lyophilized overnight and then stored at -20°C.
I chemically treated GMP using ion exchange chromatography in the case of 2'/3'-GMP, where the free acid form is not commercially available.

9.2.3 Guanosine Hydrogels

Hydrogels have been prepared combining together into a glass vial the exact volume of G and GMP solutions and then adding pure water to reach the final water concentration. Mixtures were allowed to stand for ca. 15 min without disturbance and then classified at room temperature according to flow ability (by tube inversion test, see below) and transparency. In particular, analyzed samples resulted unable to flow, but those prepared at high guanosine content appeared opalescent and macroscopically not homogeneous. Mixtures were then heated up to 90°C (i.e., till the formation of a liquid fluid state), fundamental step to ensure the complete dissolution of two components (guanosine is white and become transparent when is completely solubilized, thanks to GMP) then left to cool down at room temperature. After 30 min equilibration at 20°C, the pre-heated mixtures resulted transparent and clear and were finally classified for flow ability. Mechanical stresses have been avoided, as the gel eventually forms immediately after the mix of the two components.
Here I report a table in which I summarized volumes necessary to obtain different molar ratios of G/GMP.

Table 9.1 in the following table can be found values (in microliters) relative to the GMP and G solutions that has to be used to obtain a wanted G/GMP ratio. Volumes have been calculated considering mother solutions of GMP of 10% w/v and G 6% w/v; final volume 1ml

G/GMP	fGMP	fG	GMP (mol)	G (mol)	vol GMP (μl)	vol G (μl)
1:15	0.95	0.05	0.131	0.009	475.29	41.18
1:6	0.88	0.12	0.122	0.020	442.49	95.85
1:4	0.84	0.16	0.115	0.029	418.43	135.95
1:2	0.72	0.28	0.099	0.050	359.74	233.77
3:4	0.63	0.37	0.087	0.065	315.49	307.52
1:1	0.56	0.44	0.077	0.077	280.93	365.12

9.2.3.1 G/GMP less-hydrated samples (XRD)

With the aim to determine phase diagrams for the less-hydrated G/GMP hydrogels, samples have been prepared in the following way: an aliquot of pre-heated G/GMP hydrogel, prepared as described in the previous paragraph, has been taken and placed in a new tube and then precipitated thanks to the addition of absolute ethanol in vast excess. Precipitation of G/GMP is followed by a centrifugation at 8000rpm/10min and a lyophilization. At this point sample is ready to be weighted and re-hydrated with the desired percentage of water, simply calculating the amount of water to be added using a proportion.

9.2.3.2 G/GMP less-hydrated samples (SAXS-POM)

The preparation of more-concentrated G/GMP samples for SAXS measures and POM observations has been different from that one made for the determination of phase diagrams using XRD and briefly explained in the previous paragraph. In the case of XRD an aliquot of G/GMP hydrogel prepared at 96.9% of water (in weight) has been lyophilized and then re-hydrated at a given % of water. In this case, samples have been prepared starting from more-concentrated mother solutions of 5'-GMP and G. An example is given, considering GMP mother solution at 40% and G at 11% wt/v.

Table 9.2 in the following table can be found values (in microliters) relative to the GMP and G solutions used to obtain more concentrated samples. Volumes have been calculated considering mother solutions of GMP of 40% w/v and G 11% w/v

G/GMP 1:2			
% water	**GMP (μl)**	**G (μl)**	water **(μl)**
85	89.93	127.55	-
89	89.93	127.55	79.0
93	89.93	127.55	250.0

9.2.3.3 G/GMP more-hydrated samples (SAXS-POM)

For the preparation of diluted samples, an aliquot of the G/GMP hydrogel at 96.9% of water (see section 8.2.3) has been taken and placed in a new tube. Depending on the increasing level of hydration, a specific volume of water has been added to the starting solution of hydrogel.
Here in the table I summarized values relative to each more-hydrated sample prepared.

Table 9.3 in the following table can be found details about the content of diluted samples

dilutions	% of water	composition
1st	97.3	80 μl G/GMP + 12.5 μl water
2nd	97.6	80 μl G/GMP + 25 μl water
3rd	98.1	80 μl G/GMP + 50 μl water
4th	98.5	80 μl G/GMP + 80 μl water
5th	98.6	80 μl G/GMP + 100 μl water
6th	98.9	80 μl G/GMP + 150 μl water
7th	99.1	80 μl G/GMP + 200 μl water

9.2.3.4 G/GMP hydrogels (AFM observations)

As initial step, G/GMP hydrogels have been prepared at 97% of water (wt) and then heated up to 80°C to achieve the complete dissolution of components, transparency and homogeneity. At this point, approximately 20 microliters of gel have been deposited on a mica surface and let dry in air. An additional step using argon flux has been made to form a slim layer of the gel.

Using not-diluted gels is practically impossible to investigate the inner organization of elements in the hydrogel network. Thus, dilutions have been made with the aim to reduce the crowded network of the G/GMP hydrogel. In the following table, has been reported dilutions and related amounts of gel/water for each sample. In the case of 97% of water G/GMP hydrogels, (that has been always considered as starting point), volumes have been reported considering mother solutions of GMP at 10% wt/v and G at 6% wt/v for a final volume of 0.5ml.

Table 9.4 in the following table can be found details about the composition of sample investigated using Atomic Force Microscopy. Note that for G/GMP hydrogels at 97% in weight of water, volumes are given considering concentrations of mother solution of GMP 10% w/v and G 6% w/v. Final volumes considered is of 0.5 ml

G/GMP	sample concentration	specification
1:1	97%	140.5μl (GMP) + 365.12μl (G)
	6x dilution	20μl (G/GMP) + 100μl (water)
	11x dilution	20μl (G/GMP) + 200μl (water)
	26x dilution	20μl (G/GMP) + 500μl (water)
1:2	97%	179.9μl (GMP) + 116.9μl (G)
	6x dilution	20μl (G/GMP) + 100μl (water)
	11x dilution	20μl (G/GMP) + 200μl (water)
	26x dilution	20μl (G/GMP) + 500μl (water)
1:4	97%	209.2μl (GMP) +67.9μl (G)
	6x dilution	20μl (G/GMP) + 100μl (water)
	11x dilution	20μl (G/GMP) + 200μl (water)
	26x dilution	20μl (G/GMP) + 500μl (water)
1:6	97%	221.3μl (GMP) + 47.9μl (G)
	6x dilution	20μl (G/GMP) + 100μl (water)
	11x dilution	20μl (G/GMP) + 200μl (water)
	26x dilution	20μl (G/GMP) + 500μl (water)
1:15	97%	237.7μl (GMP) + 20.6μl (G)
	6x dilution	20μl (G/GMP) + 100μl (water)
	11x dilution	20μl (G/GMP) + 200μl (water)
	26x dilution	20μl (G/GMP) + 500μl (water)

9.2.4 Osmotic Stress Technique: 2'/3'-GMP sample preparation

Guanosine 2'/3'-monophosphate (Santa Cruz Biotechnology) is characterized by a mixture of two different isomers: the 2'-monophosphate and 3'-monophosphate. The 2'-monophosphate is present in the formulation at 65% more or less. This mixture of isomers Is commercially available in the form of disodium salt and thus has to be treated using Ion-exchange chromatography (IEC) to test different counterions.

IEC method has been described in detail in section 8.2.2. Depending on hydroxide solution (XOH, where X is the desired counterion (K^+, Na^+, NH_4^+) at 2M concentration) used in the equilibration of DOWEX 50WX8 resin, the starting counterion provided by the 2'/3'-GMP can be exchanged.

For the preparation of samples, a final weight of 5% wt/v has been considered. GMP has been first weighted in tube and dissolved in MilliQ water. Absolute ethanol has been added to precipitate 2'/3'-GMP in vast excess. The following steps are of centrifugation (8000 rpm for 10 minutes) and then lyophilized. At this point, the 2'/3'-

GMP has the ideal texture and softness to act as a permeable membrane. The obtainment of DNA pellet represents the first step in the preparation of samples for the osmotic stress technique. Thus, the preparation of GMP pellets at 5% wt/v and of PEG solutions has to made separately. At this point, what has to be made is to add PEG solution in vast excess above the 2'/3'-GMP and let to equilibrate at least for 24 hours.
PEG solutions have been prepared in small glass vials considering a final volume of 6ml. Percentages considered have been 5-10-20-30-40-50% wt/v. High molecular weight polymer (Poly-Ethylene Glycol 15000-20000 MW, Sigma Aldrich) has been used. In the case of analysis made using salt, PEG has to be dissolved using salt solution.

In the following table have been reported details about PEG concentration and ionic strength used for each 2'/3'-GMP salt.

Table 9.5 reported PEG and salt concentration used in the osmotic stress analysis performed using 2'/3'-monophosphate

2'/3'-GMP	PEG (15,000-20,000 MW)	salt	salt molarity
Na^+	5-50% wt/v	NaCl	0-3M
K^+	5-50% wt/v	KCl	0-0.5M
NH_4^+	5-50% wt/v	NH_4Cl	0-0.5M

9.3 X-Ray Diffraction (XRD)

To give a brief overview of X-ray diffraction I chose a chapter that in my opinion is one of the most complete and easily written of Van Holde *et al.*, 1998
Actually, the primary technique used to make the determination of structure of biomolecule, powder and crystal remains the X-Ray diffraction. Steps required to gain a structure is:

i) grow a crystal
ii) collect X-ray diffraction profile
iii) find an appropriate model to fit data

no one step is any more important than other. The closest distance between two atoms correspond to 0.12 nm (Glasel and Deutscher, 1995), the covalent bond distance between two atoms. If we have to find a radiation source that allows us to determine that distance, we have to start from the definition of limit resolution of an incident radiation (LR) defined as

$$LR \cong \frac{\lambda}{2}$$

consequence of the wave properties of light. To gain a resolution of the technique to about 0.12 nm to resolve the atomic structure of a biomolecule, the wavelength of light must be < 0.24 nm, the X-ray range of electromagnetic spectrum.

9.3.1 Huygens' Principle

X-rays are electromagnetic radiation with a wavelength in the range of 0.1-100 Å, with an energy between 100 eV and 1 MeV; the wavelengths frequently used for diffraction experiments can vary from 0.5 Å to 2.5 Å. The first intuition of the ability of X-rays to be diffracted or scattered can be find in the Huygens' principle which

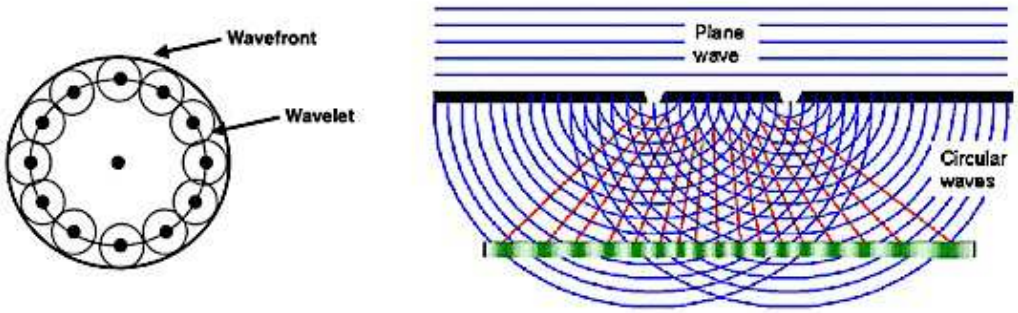

states that each point in front on a wavefront acts as a point of propagation for a new wavelet which sum to form a new wavefront. Each point in front of the incident wavefront generates a wavelet having the same velocity as the wavefront, represented as a set of concentric circles emitted from the point. (Van Holde *et al.*, 1998) The new wavefront is formed by connecting the tangents of the wavelets from all point of propagation. Making several observations of the amplitude of the new wavefront can be extrapolated information to determine the relative position of the diffracting objects related to the origin of the initial wavefront.

Figure 9.6 on the left can be observed the explanation of the difference between wavefront and wavelet; on the right, a schematic representation of the Huygens' principle: each point in front on a wavefront acts as a point of propagation for a new wavelet which sum to form a new wavefront

9.3.2 Braggs' Law and Lattice Theory

The law which defines the correlation between diffraction and the relative position of point object in the space is the Bragg's Law (William and Lawrence Bragg, Nobel Prize 1912). Crystal can be imagined as a repetition of structural unit called "elementary cell", whose symmetry and repetition rules define the crystalline lattice. Lattice points in the crystal can be imagined as parallel planes, equidistant and separated by the same distance *d*. When a wave of X-rays of a given wavelength λ is incident on the reflecting planes at an angle θ, this will be scattered. In this case constructive interference can be observed only when the reflected waves are perfectly in phase (nodes aligned with nodes). This only occurs when the difference in length of the path of the incident and the reflected waves of each plane is equal to some integer *n* of the wavelength of the incident X-rays.

Equation 9.1

$$PD=n\lambda$$

This path difference is related to the distance separating the reflecting planes by the simple trigonometric relationship

Equation 9.2

$$1/2PD = d\sin\theta$$

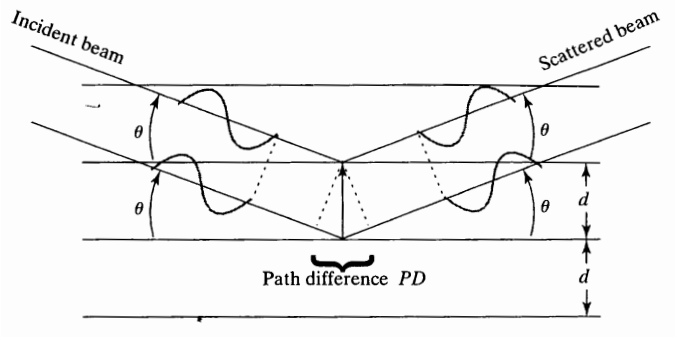

Figure 9.6 the Braggs' Law

making a substitution the Bragg's Law can be derived.

Equation 9.3

$$2d\sin\theta = n\lambda$$

As mentioned before, Bragg's Law correctly describes the case of constructive interference. When this condition occurs, what can be observed in X-ray diffraction experiment is a series of reflections or *Bragg's peaks* related to the position of atoms in the crystalline lattice and of consequence to the distance between planes (*d* spacing).

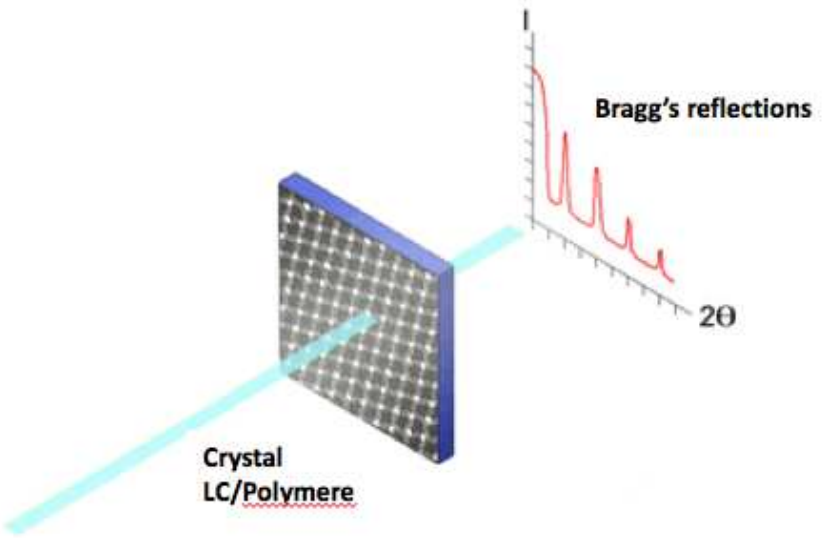

Figure 9.7 Example of X-ray diffraction profile obtained from a high-ordered system (Crystal, Liquid Crystal (LC) or a polymere)

9.4 Small Angle X-Ray Scattering (SAXS)

The use of Small Angle X-Ray Scattering technique is a powerful tool for determining structural information about biological macromolecules in solution, defined as particles that have a linear dimension comprised between 10 and 10000 Å, in particular focusing about size, shape, compactness degree and state of aggregation, which can be explored varying experimental conditions such as pH (Barbosa *et al.*, 2010), temperature or pressure (Ortore *et al.*, 2009), salt concentration (Zhang *et al.*, 2007) etc.

In this PhD thesis experiments using SAXS have been made:

- for the structural characterization of aqueous solution of nanoparticles, at the beamline BM29 (European Synchrotron Radiation Facility, Grenoble (France)),
- for guanosine-based hydrogels analysis of swelling behavior, temperature stability and structural properties, at the beamline AustroSAXS (Elettra Synchrotron, Basovizza (Italy)) and at the Institute of Physics (department of Applied Physics) of the University of Sao Paulo, Brasil

The high intensity flux of beam radiation which can be obtained using synchrotron radiation sources made possible, for example, time-resolved SAXS experiments, with 50-100 msec resolution (Perkins and Weiss, 1983).

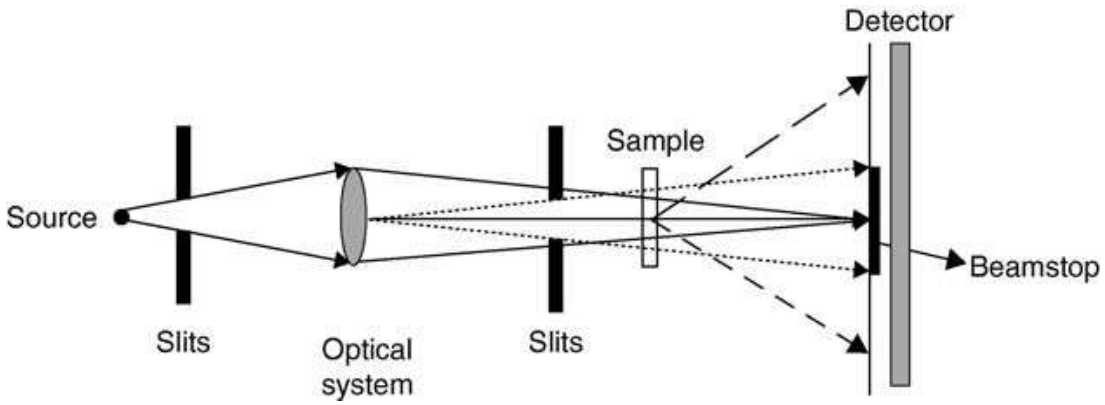

Figure 9.8 schematic representation of a typical small-angle X-ray scattering setup. Image taken from the chapter "Structural Studies of Proteins and Nucleic Acids in Solution Using Small Angle X-ray Scattering (SAXS)", Das and Doniach, Springer-Verlag Berlin Heidelberg, 2008

Considering a general Small Angle X-ray experiment, a polychromatric X-ray beam, coming from a conventional or not (e.g. synchrotron storage ring) X-ray generator, passes through a monochromator to selects a wavelength (typically around 0.1nm). The monochromatic incoming beam now can go through the collimation system up to the sample holder, in which hits the sample. Only few components of the instrumentation or the whole system can be under vacuum (to avoid the non-negligible SAS scattering of air). Is important to underline that each setup can be different considering the different *q*-range (where *q* is the scattering vector, defined as difference between the transmitted and incident X-Ray beam), sample compositions and detector type (Barbosa *et al.*, 2013).

When the transmitted beam reaches the sample holder stage, it scatters at a defined 2θ angle (comprised between 0.1° and 10°, at very low angles). The signal of the scattered X-ray beam will be reached by the detector. The measured data comprises the variation of X-ray scattered intensity as a function of the scattering angle 2θ and of the scattering vector $\vec{q}$ (Barbosa *et al.*, 2013). The reconstruction of the structure of a particle

from the experimental SAS curve is usually difficult, due to the loss of information (e.g. usual case of proteins in solution) caused from averaging the scattering intensity over all particle orientations. Different procedures are then used: some are direct (such as the well-established methods based on the multipole expansion of the excess scattering length density), in the other case *data fitting* procedures are required to a form factor calculated from a model shape, which can range from a simple geometrical structure to a complex heterogeneous particle or directly evaluated from the crystallographic coordinates (Barbosa *et al.*, 2013). An additional scattering signal can be detected, called the *structure factor,* related to the spatial distribution of the particles, when the particle-particle interactions cannot be neglected.

9.4.1 General Equations of SAXS

The most general equation of Small Angle Scattering is (Guinier and Fournet, 1955)

Equation 9.4

$$I(q) = V^{-1}\langle | \int_V \delta\rho(\vec{r}) d\vec{r} e^{i\vec{q}\vec{r}} |^2 \rangle$$

where I(q) is the scattering intensity as a function of the exchanged wave vector $\vec{q}$. The modulus of q is defined as

Equation 9.5

$$q = \frac{4\pi}{\lambda} \sin\theta$$

In Equation 9.4 the integral is extended over the total sample volume *V* and and $\vec{r}$ the position vector; the angular brackets $\langle \dots \rangle$ indicate the ensemble over all positions, orientations and microstates of the particles in the systems. Finally, $\rho(\overrightarrow{r})$ is the electron density multiplied for the electron radius (for X-rays its value is $r_e = 2.8\times10^{-13}$ cm).

In absence of long range order, the scattering density can be thought as having a uniform value ρ_0 on which fluctuations $\delta\rho(\overrightarrow{r})$ are superimposed. The amplitude factor $F(\vec{q})$ is defined as the normalized Fourier Transform of $\delta\rho(\overrightarrow{r})$ function

Equation 9.6

$$F(\overrightarrow{q}) = \frac{1}{f}\int_{Vp} d\vec{r}\, \delta\rho(\vec{r}) e^{i\vec{q}\vec{r}},$$

where f is the scattering amplitude at *q*=0 and V_p is the volume of the scattering particles.

Equation 9.7

$$f = \int_{Vp} d\vec{r}\, \delta\rho(\vec{r})$$

If we are considering a polydisperse system given by a mixture of *p* components the effective form factor has to be defined:

Equation 9.8

$$P_{eff}(\vec{q}) = \sum_{i=1}^{p} n_i f_{i^2} |F_i^2(\vec{q})|,$$

where n_i is the number density of species *i* . At this point, the scattering intensity $\mathrm{I}(\vec{q})$ can be written as

Equation 9.9

$$\mathrm{I}(\vec{q}) = P_{eff}(\vec{q})\, S_{eff}(\vec{q}).$$

The form factor P_{eff} refers to the distribution of the scattering matter inside the particles, the structure factor S_{eff} is related to the particle-particle (or the protein-protein) interactions.

9.4.2 Cylinder Model

As mentioned in the previous section, guanosine derivatives are able to organize in quadruplex structure, in which tetrads are stacked one with respect to the other at a given distance, the practically the same of DNA (3.3 Å), generating a cylindrical structure. Thus, is necessary to give a brief overview of those two fundamental models used in the Small Angle X-Ray Scattering data treatment.

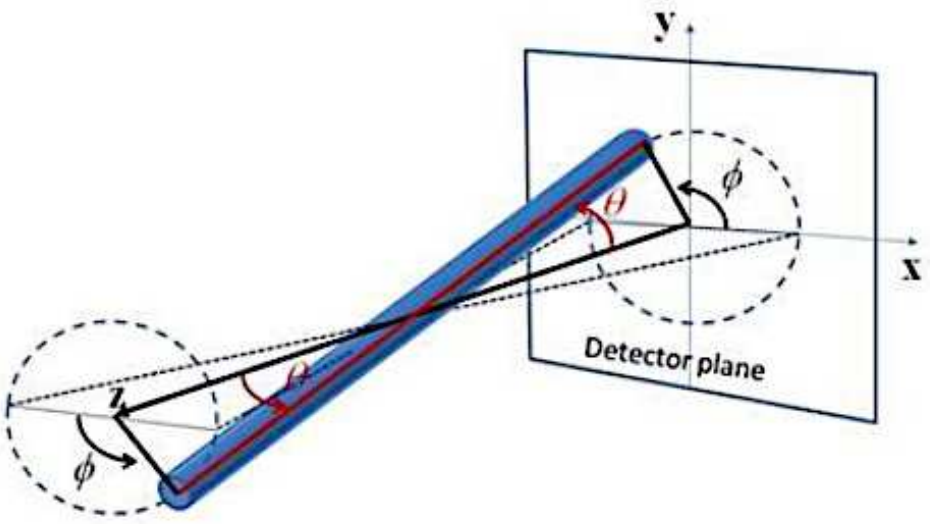

Figure 9.9 definition of the angles θ and ϕ for oriented cylinders

As reported in the http://danse.chem.utk.edu/downloads/ModelfuncDocs.pdf (which refers to a c-library provided by the NIST Center for Neutron Research), the cylinder form factor

refers to a right circular cylinder. In this case the form factor has been normalized by the particle volume. As

described by Guinier (Guinier, 1955), the 2D scattering intensity function for oriented cylinders is given by

Equation 9.10

$$P(q,\alpha) = \frac{scale}{V}\sin(\Delta\rho)V\ \ \sin q\ L\cos\alpha\ /2)\ \frac{J_1\ (qr\sin\alpha)}{(qr\sin\alpha)}$$

where α is the angle between the axis of cylinder and the q-vector volume; V is the volume of the cylinder, $\Delta\rho$ is the contrast scattering length density different between scatterer and solvent and J_1 is the first order of the Bessel function.

The definition of the axis of the cylinder can be made using two angles, theta and phi as indicated in Figure 9.10).

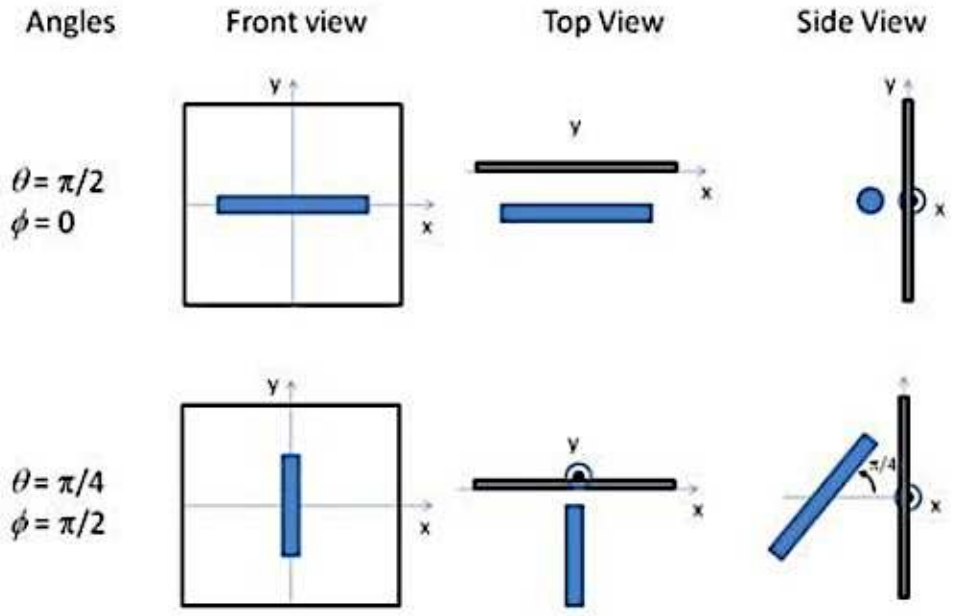

Figure 9.10 Examples of θ and ϕ angles for oriented cylinders, here reported against the detector plane

A series of parameters can be obtained by the curve fitting using Cylinder Model, and these are reported below in Table 9.6.

Table 9.6 Parameters related to the cylinder model and relative units

Parameter Name	Units
scale	none
radius	Å
length	Å
contrast	$Å^{-2}$
background	cm^{-1}
cyl_theta	degree
cyl_phi	degree

The output of 1D scattering intensity function for randomly oriented cylinders is given by all the parameters except for cyl_theta and cyl_phi, and is:

Equation 9.11

$$P(q) = \frac{scale}{V} \int_0^{\frac{\pi}{2}} f^2(q, \alpha) \sin \alpha \; d\alpha + bkg$$

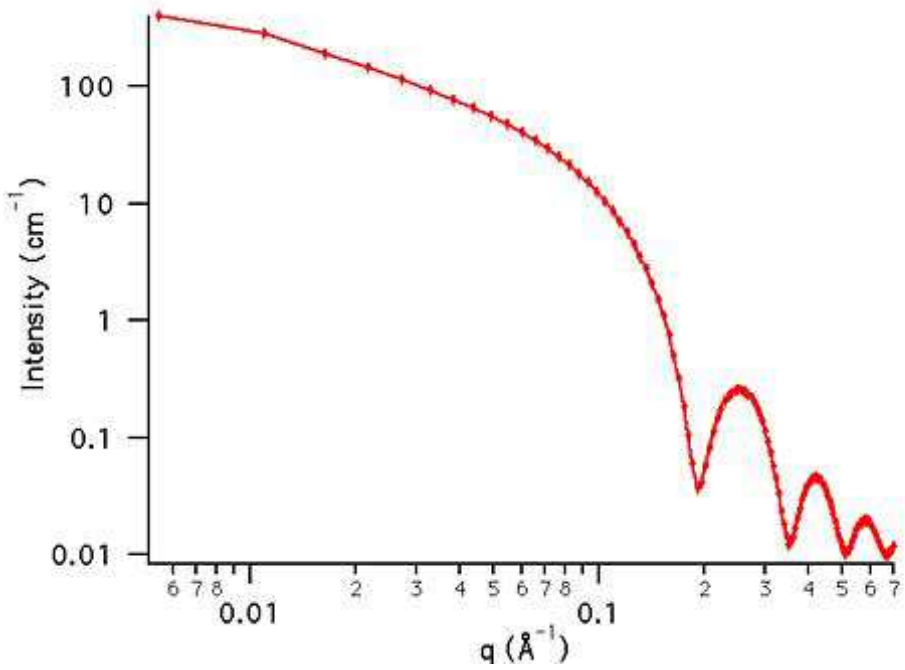

Figure 9.11 scattering intensity for a cylinder. Here is reported the 1D plot of the form factor

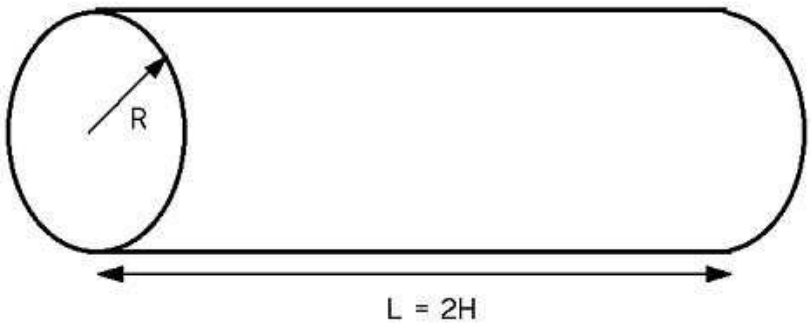

Figure 9.12 schematic representation of a cylinder

9.4.3 Core shell cylinder Model

In this case the model provides the form factor of a cylinder with a core-shell scattering length density profile. Also in this case the form factor is normalized by the particle volume.

The output of the 2D scattering intensity function has given by Kline (Kline, 2006) and is:

Equation 9.12

$$P(q,\alpha) = \frac{scale}{V_s} f^2(q) + bkg$$

where *f*(q) is

Equation 9.13

$$f(q) = 2(\rho_c - \rho_s)V_s \sin[qL\cos\alpha\,/2]/\,[qL\cos\alpha\,/2]\,\frac{J_1[qr\sin\alpha]}{[qr\sin\alpha]} + 2(\rho_s - \rho_{solv})V_s \sin[q(L+t)\cos\alpha\,/2]/[q(L+t)\cos\alpha/2]\frac{J_1[q\,(r+t)\sin\alpha]}{[q(r+t)\sin\alpha]}$$

where α is the angle defined between the axis of the cylinder and the q-vector, V_s is the volume of the outer shell, V_c is the volume of the core, L and r are the length and radius of the core, t is thickness of the shell and ρ_c, ρ_s and ρ_{solv} are respectively the scattering length density of core, shell and solvent. Finally, bkg is the background level.

The term r+t indicates the outer radius of the shell, whereas the total length of the shell is given by L+2t. J_1 is the first order Bessel function.

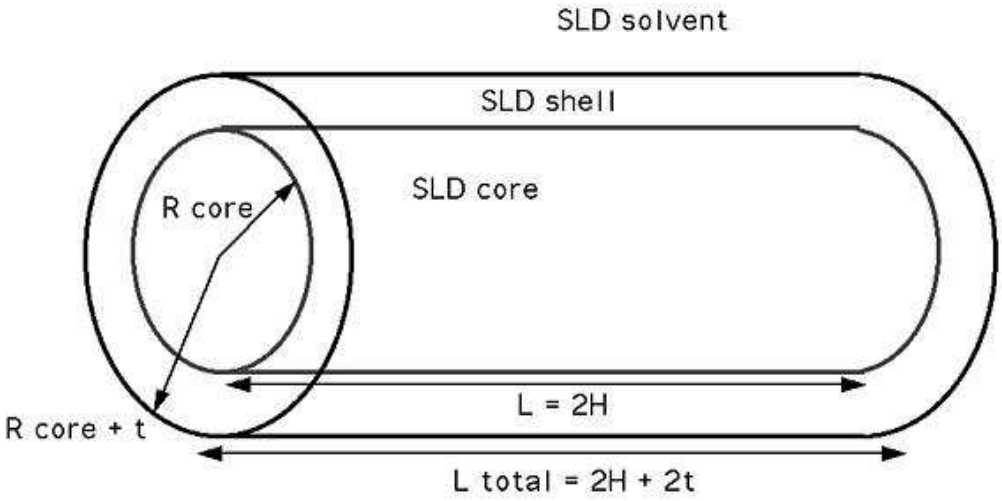

Figure 9.13 schematic representation of a core-shell cylinder

For this model, parameters derived from the curve fitting will be:

Table 9.7 parameters related to the cylinder model and relative units

Parameter Name	Units
scale	None
radius	Å
thickness	Å
length	Å
core_sld	$Å^{-2}$
shell_sld	$Å^{-2}$
solvent_sld	$Å^{-2}$
background	cm^{-1}
axis-theta	degree

9.5 Polarized Light Optical Microscopy (POM)

Polarized light optical microscopy (POM) is the most useful technique for the observation of samples characterized by *chirality*. Chirality in our case refers to the anisotropic nature of Lyotropic Liquid Crystals (LLCs) such as lipid and guanosine derivatives mesophases.

The polarized light differs from sunlight and almost every other form of artificial illuminations. Natural unpolarized light transmits light waves whose electric field vector vibrate in all perpendicular planes with respect to the direction of the propagation. The phenomenon of polarization occurs when electric field vectors are restricted to a single plane

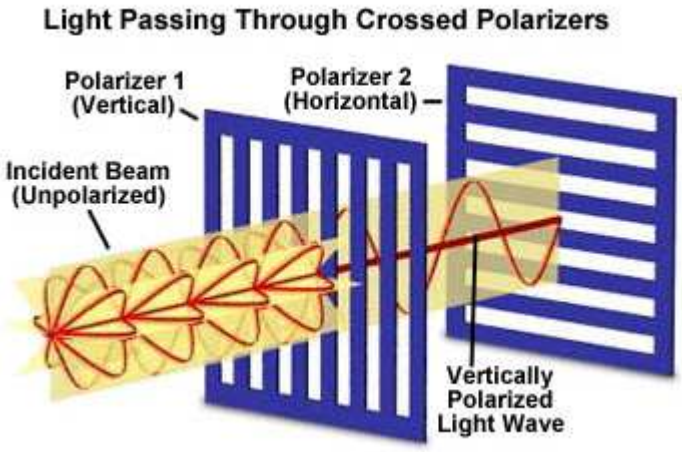

Figure 9.14 scheme of the polarization of light

by filtration and thus *polarized* with respect to the direction of propagation. In the case of polarization all waves vibrate in the same plane.

The figure shows the concept of light polarization: the unpolarized incoming light passes through the first polarizer, in which only the waves that are vertical in the incident beam will pass. Waves passed through polarizer 1 will blocked by polarizer 2. The use of two polarizers is fundamental for the practice of polarized light microscopy. And is called crossed polarization. The microscope configuration uses crossed polarizers where the first polarizer (polarizer) is placed below the sample in the light path and the second polarizer (analyzer) is placed above the sample, between the objective and the eyepieces. With no sample on the microscope stage, the light polarized by the polarizer is blocked by the analyzer and no light will be visible. When samples that are *birefringent* are viewed on the stage between crossed polarizers, the microscopist can visualize aspects of the samples through light rotated by the sample and then able to pass through the analyzer (https://www.olympus -life science.com/en/microscope-resource/primer/lightandcolor/polarization). The observation of anisotropic sample can be made both for qualitative and quantitative analysis. The qualitative analysis is the most common practice in the case of POM but quantitative is not less important, especially in the case of crystallography (especially for mineralogists, geologists and chemists). Here I report two images for lipid phases observed both at light and dark fields.

9.5.1 POM observations using hot-stage plate (Mettler Toledo®)

The use of a hot stage plate (available in our laboratory) has been fundamental in the case of the determination of the gel-to-sol temperatures of G/GMP hydrogels.

In this case slides have been modified: an area has been delimitated using silicone: this avoids the dehydration of samples and to block samples using cover slides. An aliquot of G/GMP hydrogel has been placed in the modified slide and let to equilibrate to a desired temperature, set in the main control of the instrumentation.

Slide, one time inserted in the hot-stage plate instrumentation, can be observed continuously using POM, as function of temperature.

Ringraziamenti

Bibliography

Bibliography

Adhikari B., A. Shah, H.B. Kraatz Self-assembly of guanosine and deoxy-guanosine into hydrogels: monovalent cation guided modulation of gelation, morphology and self-healing properties. *J Mater Chem B* (2) 4802, **2014**

Attama A.A and C.C. Müller-Goymann Effect of beeswax modification on the lipid matrix and solid lipid nanoparticle Crystallinity. *Colloids Surf A: Physicochem Eng Aspects* 2008 (315) 189-195, **2008**

Attama A.A., M.A. Momoh, P.F. Builders Lipid Nanoparticulate Drug Delivery Systems: A revolution in Dosage Form Design and Development. Recent Advances in Novel Drug Carrier Systems, *InTech*, **2012**

Ausili P., M. Pisani, S. Finet, H. Amenitsch, C. Ferrero, P. Mariani Pressure Effects Columnar Lyotropics: Anisotropic Compressibilities in Guanosine Monophosphate Four-Stranded Helices. *J Phys Chem B* (108), 1783-1789, **2004**

Bang I. Untersuchungen über die Guanylsäure *Biochem Ztschr* (26), 293, **1910**

Barbosa L.R.S., M.G. Ortore, F. Spinozzi, P. Mariani, S. Bernstoff, R. Itri The importance of Protein-Protein Interactions on the pH-Induced Conformational Changes of Bovine Serum Albumin: A Small-Angle X-Ray Scattering Study. *Biophys J* (98), 147-157, **2010**

Barbosa L.R.S., F. Spinozzi, P. Mariani, R. Itri Small-Angle X-Ray Scattering Applied to Proteins in Solution. Proteins in Solution and at Interfaces: Methods and Applications in Biotechnology and Materials Science, First Edition, John Wiley & Sons, Inc., **2013**

Boistelle R. Fundamentals of nucleation and crystal growth. In: Crystallization and Polymorphism of Fats and Fatty Acids. Ed. Garti N., Sato K. Marcel Dekker: New York, 189-226, **1988**

Bomboi F., F. Romano, M. Leo, J. Fernandez-Castanon, R. Cerbino, T. Bellini, F. Bordi, P. Filetici, F. Sciortino Re-entrant DNA gels. *Nat Commun* (7), 13191 doi: 10.1038/ncomms13191, **2016**

Buerkle L.E., Z. Li, A.M. Jamieson and S.R. Rowan Tailoring the properties of Guanosine-based supramolecular hydrogels. *Langmuir* (25), 8833-8840, **2009**

Bomprezzi R., Dimethyl fumarate in the treatment of relapsing–remitting multiple sclerosis: An overview. *Ther Adv Neurol Disord* (8), 20–30, **2015**

Cafferty B.J., I. Gallego, M.C. Chen, K.I. Farley R. Eritja, N. Hud, Efficient Self-Assembly in Water of Long Noncovalent Polymers by Nucleobase Analogues. *J Am Chem Soc* (135), 2447-2450, **2013**

Casagrande R., S.R. Georgetti, W.A. Verir Jr., M.F. Borin, R.F. Lopez, M.J. Fonseca, In vitro evaluation of

quercetin cutaneous absorption from topical formulations and its functional stability by antioxidant activity. *Int J Pharm (*328), 183-190, **2007**

Casagrande R., S.R. Georgetti, W.A. Verir Jr., D.J. Dorta, A.C. dos Santos, M.J. Fonseca, Protective effect of topical formulations containing quercetin against UVB-induced oxidative stress in hairless mice. *J. Photochem Photobiol B* (84), 21-27, **2006**

Chen H.R. Maier-Saupe theory in Liquid Crystal Displays. (First Edition) John Wiley & Sons Inc., **2011**

Cortesi R., E. Cappellozza, M. Drechsler, C. Contado, A. Baldisserotto, P. Mariani, F. Carducci, A. Pecorelli, E. Esposito, G. Valacchi Monoolein aqueous dispersions as delivery systems for quercetin. *Biomed Microdevices*, 19:41 doi 10.1007/s10544-017-0185-0, **2017**

Cullis P.R. *et al.* Structural properties of lipids and their functional role in biological membranes. In Membrane Fluidity in Biology. (ed. R.C. Aloia) Vol. 1, *Acad Press, NY*, p. 39, **1983**

Das R.N., Y.P. Kumar, S. Pagoti, A.J. Patil and J. Dash Diffusion and Birefringence of Bioactive Dyes in Supramolecular Guanosine Hydrogels, *Chem Eur J* **(**18), 6008-6014**, 2012**

Dash J. and P. Saha Functional architectures derived from guanine quartets. *Org Biomol Chem* (14), 2157-2163, **2016**

Dash J., A.J. Patil, R.N. Das, F.L. Dowdall, S. Mann Supramolecular hydrogels derived from silver ion-mediated self-assembly of 5'-guanosine monophosphate. *Soft Matter* (7), 8120-8126, **2011**

DeRouchey J., V.A. Parsegian, D.C. Rau Cation charge dependence of the forces driving DNA assembly, *Biophys J* (99), 2608-2615, **2010**

Domingues M.A.F, Ribeiro A.P.B., Kieckbusch T.G., Gioielli L.A, Grimaldi R., Cardoso L.P. and Lireny A.G.G. Advances in Lipids Crystallization Technology. *Advanced Topics in Crystallization*, Prof. Yitzhak Mastai (Ed.), InTech, DOI: 10.5772/59767. Available from: https://www.intechopen.com/books/advanced-topics-in-crystallization/advances-in-lipids-crystallization-technology, **2015**

Dowling V.A., J.A.M. Charles, E. Nwakpuds, L.B. McGown A Reversible Gel for Chiral Separations. *Anal Chem* (76), 4558-4563, **2004**

Esposito E., M. Sguizzato, M. Drechsler, P. Mariani, F. Carducci, C. Nastruzzi, R. Cortesi Data on Scaling up and in vivo human study of progesterone lipid nanoparticles. *Data in Brief* (14) 639-642, **2017d**

Esposito E., M, Sguizzato, M. Drechsler, P. Mariani, F. Carducci, C. Nastruzzi, R. Cortesi Progesterone lipid nanoparticles: Scaling up and in vivo human study**.** *Eur J Pharm Biopharm* (119), 437-446, **2017c**

Esposito E., M. Drechsler, P. Mariani, F. Carducci, M. Servadio, F. Melancia, P. Ratano, P. Campolongo, V. Trezza, R. Cortesi, C. Nastruzzi Lipid nanoparticles for administration of poorly water soluble neuroactive

drugs. *Biomed Microdevices*, 19:44 DOI 10.1007/s10544-017-0188-x **2017b**

Esposito E., M. Drechsler, P. Mariani, A. M. Panico, V. Cardile, L. Crascì, F. Carducci, A.C.E. Graziano, R. Cortesi, C. Puglia Nanostructured lipid dispersions for topical administration of crocin, a potent antioxidant from saffron (Crocus sativus L.). *Mater Sci Eng C* 669-677, **2017a**

Esposito E., P. Mariani, M. Dechsler and R. Cortesi Structural Studies of Lipid-Based Nanosystems for Drug Delivery: X-ray Diffraction (XRD) and Cryogenic Transmission Electron Microscopy (Cryo-TEM). Handbook of Nanoparticles, *Springer International Publishing Switzerland* DOI 10.1007/978-3-319-15338-4_39, M. Aliofkhazraei (ed.), **2016**

Esposito E., M. Fantin, M. Marti, M. Drechsler, L. Paccamiccio, P. Mariani, E. Sivieri, F. Lain, E. Menegatti, M. Morari, R. Cortesi Solid Lipid Nanoparticles as Delivery Systems for Bromocriptine. *Pharm Res* (25), 7, **2008**

Gellert M., M.N. Lipsett D.R. Davies Helix Formation by guanylic acid. *Proc Natl Acad Sci* (48), 2013-2018, **1962**

Glasel J.A. and M.P. Deutscher Introduction to Biophysical Methods for protein and Nucleic Acid Research. *Academic Press*, **1995**

Glatter O. and O. Kratky Small Angle X-ray Scattering. Academic New York, **1982**

Göppert T.M. and R.H. Müller Polysorbate-stabilized solid lipid nanoparticles as colloidal carriers for intravenous targeting of drugs to the brain: Comparison of plasma protein adsorption patterns. *J Drug Target* (13), 179–187, **2005**

Guinier A. and G. Fournet Small Angle Scattering of X-Rays, Wiley, New York, **1955**

Gustafsson J., H. Ljusberg-Wahren, M. Almgren, K. Larsson Cubic Lipid-Water Phase Dispersed into Submicron Particles. *Langmuir* (12), 4611-4613, **1996**

Hansel-Hertsch R., M. Di Antonio and S. Balasubramianan DNA G-quadruplexes in the human genome: detection, functions and therapeutic potential. *Nat Rev Mol Cell Biol*, (18), 279-284, **2017**

Hollman P.C.H. and M.B. Katan Dietary flavonoids: Intake, health effects and bioavailability. *Food Chem Toxicol* (37), 937-942, **1999**

Hirst A.R., B. Escuder, J. F. Miravet and D.K. Smith High-Tech Applications of Self-assembling Supramolecular Nanostructured gel-phase materials: From Regenerative medicine to Electronic devices. Angew Chem Int Ed (47), 8002-8018, **2008**

Hunt J.A., R. Chen, T. van Veen and N. Bryan Hydrogels for tissue engineering and regenerative medicine. *J Mater Chem B* (2), 5319-5338, **2014**

Israelachvili J.N., Measurement of Hydration Forces Between Macroscopic Surfaces. *Chemica Scripta* (25), 7-14, **1985**

Jenning V., A.F. Thunemann, S.H. Gohla Characterisation of a novel solid lipid nanoparticle carrier system based on binary mixtures of liquid and solid lipids. *Int J Pharm* (199), 167-177, **2000**

Jeong J.H., S.H. Kang, J.H. Kim, K.S. Yu, I.H. Lee, Y.J. Lee, N.S. Lee, Y.G. Jeong, D.K. Kim, S.H. Lee, S.K. Hong, S.Y. Han, B.S. Kang Protective effects of poly(lactic-co-glycolic acid) nanoparticles loaded with erythropoietin stabilized by sodium cholate against glutamate-induced neurotoxicity. *J Nanosci Nanotechnol* (14), 8365-8371, **2014**

Kahn J.S., Y. Hu, I. Willner Stimuli-Responsive DNA-Based Hydrogels: From Basic Principles to Applications. *Acc Chem Res* (50), 680-690, **2017**

Kawamura K. The DSC thermal analysis of crystalline behavior in palm oil. *J Amer Oil Chem Soc*, (56), 753, **1979**

Kline S.R. Reduction and analysis of SANS and USANS data using IGOR Pro. *J Appl Cryst* (39), 895-900, **2006**

Koynova R. and B.Tenchov, Lipids, Phase Transitions of. *Wiley Encyclopedia of Chemical Biology*, doi: 10.1002/9780470048672.wecb287, **2008**

Kreuter J. Drug Targeting with nanoparticles. *Eur J Drug Metab Pharmacokinetics* (19), 253-256, **1994**

Larsson K Aqueous dispersion of cubic lipid-water phases. *Curr Opin Colloid Interface Sci* (5), 64-69, **2000**

Lau H.K. and K.L. Kiick Opportunities for multicomponent hybrid hydrogels in biomedical applications *Biomolecules* (16), 28-42, **2015**

Leikin S., D. Rau, V.A. Parsegian Direct measurement of forces between self-assembled proteins: Temperature-dependent exponential forces between collagen triple helices. *Proc Natl Acad Sci* (91), 276-280, **1994**

LeNeveu D.M., R.P. Rand, V.A. Parsegian Measurement of forces between lecithin bilayers. *Nature* (259), 601-603, **1976**

Li J. and D.J. Mooney Designing hydrogels for controlled drug delivery. *Nat Rev Mater* (1), 16071, **2016**

Li Z., L.E. Buerkle, M.R. Orsero, K.A. Streletzky, S. Seifert, A. Jamieson, S.J. Rowan Structure and gelation mechanism of tunable guanosine-based supramolecular hydrogels. *Langmuir* (25), 10093-10101, **2009**

Linker R.A. and R. Gold, Dimethyl fumarate for treatment of multiple sclerosis: Mechanism of action, effectiveness and side effects. *Curr Neurol Neurosci Rep* (13), 394, **2013**

Lippacher A., R.H. Müller, K. Mäder Preparation of semisolid drug carriers for topical application based on

solid lipid nanoparticles. *Int J Pharm* (214), 9-12, **2001**

Livolant F. and A. Leforestier Condensed phase of DNA: Structures and phase transitions. *Prog Polym Sci* (21), 1115-1164, **1996**

Livolant F. Cholesteric liquid crystalline phases given by three helical biological polymers: DNA, PBLG and xanthan. A comparative analysis of their textures. *J Physique* (47), 1605-1616, **1986**

Lockwood G., G. Griesinger, B. Cometti, Subcutaneous progesterone versus vaginal progesterone gel for luteal phase support in in vitro fertilization: a noninferiority randomized controlled study. *Fertil Steril* (101) 112–119, **2014**

Luzzati V. H. Delacroix, A. Gulik et al. The cubic phases of lipids, in Lipid Polymorphism and Membrane Properties. ed. by R.M. Epand. *Current topics in membrane*, vol. 44 Academic, San Diego, 3–24, **1997**

Luzzati V. X-ray diffraction studies of lipid-water systems, in Biological Membranes. *Academic*, New York, **1968**

Luzzati V. and F. Husson The structure of the liquid-crystalline phases of lipid-water systems. *J Cell Biol* (12) 207-219, **1962**

Luzzati V. and A. Nicolaieff Etude par diffusion des rayons X aux petits angles des gels d'acide désoxyribonucléique et de nucléoprotéines: (note preliminaire) *J Mol Biol* (1) 127-133, **1959**

Maden M. Retinoic acid in the development, regeneration and maintenance of the nervous system. *Nat Rev Neurosci* (8), 755–765, **2007**

Mariani P., V. Luzzati and H. Delacroix Cubic phases of lipid-containing systems. Structure analysis and biological implications. J Mol Biol, 204 (1), 165-189, **1988**

Mariani P., C. Mazabard, Garbesi A., Spada G.P. A study of the structure of the Lyomesophases Formed by the Dinucleoside Phosphate d(GpG). An Approach by X-ray Diffraction and Optical Microscopy. *J Am Chem Soc* (111), 6369-6373, **1989**

Mariani P. and F. Rustichelli Phase Transition in some biomolecules, Chapter 29 in *Phase Transition in Liquid Crystals,* Edited by S. Martellucci and A.N. Chester, Plenum Press, New York, **1992**

Mariani P. and L. Saturni Measurement of intercolumnar Forces between Parallel Guanosine Four-Stranded Helices. *Biophys J* (70), 2867-2874, **1996**

Mariani P, F. Ciuchi, L. Saturni "Helix-Specific Interactions Induce Condensation of Guanosine Four-Stranded Helices in Concentrated Salt Solutions" *Biophys J* (74), 430-435, **1998**

Mariani P., F. Spinozzi, F. Federiconi, H. Amenitsch, L. Spindler and I. Devrensek-Olenik Small Angle X-Ray Scattering Analysis of Deoxyguanosine 5'- Monophosphate Self-Assembling in Solution: Nucleation and Growth of G-Quadruplexes. *J Phys Chem B* (113), 7934-7944, **2009**

Mezzina E., P. Mariani, R. Itri, S. Masiero, S. Pieraccini, G.P. Spada, F. Spinozzi, J.T. Davis and G. Gottarelli The Self-Assembly of a Lipophilic Guanosine Nucleoside into Polymeric Columnar Aggregates: The Nucleoside Structure Contains Sufficient Information To Drive the Process towards a Strikingly Regular Polymer. *Chem Eur J* (7), 388-395, **2001**

Millman B.M., T.C. Irving, B.G. Nickel, M.E. Loosley-Millman Interrod forces in aqueous gels of tobacco mosaic virus. *Biophys J* (45), 551-556, **1984**

Mody V.V., R. Siwale, A. Singh, H.R. Mody. Introduction to metallic nanoparticles. *J Pharm Bioallied Sci* (2), 282-289, **2010**

Müller R.H, M. Radtke, S.A. Wissing Solid Lipid Nanoparticles (SLN) and nanostructured lipid carriers (NLC) in cosmetic and dermatological preparations. *Adv Drug Deliv Rev* (54) *Suppl* (1), S131-S155, **2002**

Müller R.H., K. Mäder S. Gohla Solid Lipid Nanoparticles (SLN) for the controlled drug delivery - a review of the state of art. *Eur J Pharm Biopharm* (50), 161-177, **2000**

Murat P. and S. Balasubramanian Existence and consequence of G-quadruplex structure in DNA, *Curr Opin Genet Dev* (25), 22-29, **2014**

Navarra MA, C. Dal Bosco, J.S. Moreno, F.M. Vitucci, A. Paolone, S. Panero Synthesis and Characterization of Cellulose-based Hydrogels to Be Used as Gel Electrolytes. *Membranes* (5), 810-823**, 2015**

O'Brien R.D. Fats and Oils Analysis. In: Fats and Oils- Formulating and Processing for Applications. Ed. Hasenhuettl G.L., Hartel R.W., Springer: New York, 1-7, **2008**

Ortore M.G, F. Spinozzi, P. Mariani, A. Paciaroni, L.R.S Barbosa, H. Amenitsch, M. Steinhart, J. Ollivier, D. Russo Combining structure and dynamics: non-denaturing high-pressure effect on lysozyme in solution. *J R Soc Interface* (6), S619-S634, doi: 10.1098/rsif.2009.0163.focus, **2009**

Pardeike J., A. Hommoss, R.H. Müller Lipid nanoparticles (SLN, NLC) in cosmetic and pharmaceutical dermal products, *Int J Pharm* (366), 170-184, **2009**

Parsegian V.A. Long-range physical forces in the biological milieu *Annu Rev Biophys Bioeng***, (**2), 221-255, **1973**

Park K., Controlled drug delivery systems: Past forward and future back. *J Control Release* (190), 3-8, **2014**

Perkins S.J., H. Weiss Low-resolution structural studies of mitochondrial ubiquinol: Cytochrome c reductase in detergent solutions by neutron scattering. *J Mol Biol*, (168), 847-866, **1983**

Peters G.M. and J.T. Davis Supramolecular gels made from nucleobase, nucleoside and nucleotide analogs. *Chem Soc Rev* (45), 3188-3206, **2016**

Peters G.M., L.P. Skala, T.N. Plank, H. Oh, G.N.M Reddy, A. Marsh, S. P. Brown, SR. Raghavan, J.T. Davis

G4-Quartet•M^+ Borate Hydrogels. *J Am Chem Soc* (138), 134-139, **2015b**

Peters G.M., L.P. Skala, J.T. Davis A Molecular Chaperone for G4-Quartet Hydrogels. *J Am Chem Soc* (138), 134-139, **2015a**

Peters G.M., L.P. Skala, T.N. Plank, B.J. Hyman, G.N.M. Reddy, A. Marsh, S.P. Brown, J.T. Davis A G4•K^+ Hydrogel Stabilized by an Anion, *J Am Chem Soc* (136), 12596-12599, **2014**

Pietras Z., H.-T. Lin, S. Surade, B. Luisi, O. Slattery, K.M. Pos and A. Moreno The use of novel organic gels and hydrogels in protein crystallization. *J Appl Cryst* (43), 58-63, **2010**

Piomelli D., G. Tarzia, A. Duranti, A. Tontini, M. Mor, T.R. Compton, O. Dasse, E.P. Monaghan, J.A. Parrott, D. Putman Pharmacological profile of the selective FAAH inhibitor KDS-4103 (URB597). *CNS Drug Rev* (12), 21–38, **2006**

Plank T.N., L.P. Skala, J.T. Davis Supramolecular hydrogels for environmental remediation: G_4-quartet gels that selectively absorb anionic dyes from water. *Chem Comm* (53), 6235-6238, **2017**

Rau D.C., B. Lee, V.A. Parsegian Measurement of the repulsive force between polyelectrolyte molecules in ionic solution: hydration forces between parallel DNA double helices. *Proc Natl Acad Sci*, (81), 2621-2625, **1984**

Reis R.L., J.F. Neves, M.E. Gomes, A.P. Marques, H.S. Azevedo Natural-based Polymers for Biomedical Applications. Woodhead Publishing in Materials, CRC Press, **2008**

Robinson C. Liquid-crystalline structures in polypeptide solutions. *Tetrahedron* (13), 219-234, **1961**

Rhodes D. and H.J. Lipps G-quadruplexes and their regulatory roles in biology. *Nucleic Acid Res,* **2015**, (43), 8627-8637

Saboor-Yaraghi A.A., M.H. Harirchian, N. Mohammadzadeh Honarvar, S. Bitarafan, M. Abdolahi, F. Siassi, E. Salehi, M.A. Sahraian, M.R. Eshraghian, T. Roostaei, F. Koohdani The effect of vitamin a supplementation on FoxP3 and TGF-β Gene expression in Avonex-treated multiple sclerosis patients. *J Mol Neurosci* (56), 608–612, **2015**

Sangeetha N.M. and U. Maitra Supramolecular gels: function and uses. *Chem Soc Rev* (34), 821-836, **2005**

Sato K. and S. Ueno Polymorphism in Fats and Oils. *Bailey's Industrial Oil and Fat Products, Sixth Edition*, Six Volume Set. Edited by Fereidoon Shahidi, John Wiley and Sons, Inc **2005**

Seeman N. Structural DNA Nanotechnology. Cambridge University Press (Material Research Society), **2015**

Sen D. and W. Gilbert Formation of parallel four-stranded complexes by guanine-rich motifs in DNA and its implication for meiosis. *Nature* (334), 364-366, **1988**

Servadio M., F. Melancia, A. Manduca, A. di Masi, S. Schiavi, V. Cartocci, V. Pallottini, P. Campolongo, P.

Ascenzi, V. Trezza. Targeting anandamide metabolism rescues core and associated autistic-like symptoms in rats prenatally exposed to valproic acid. *Transl. Psychiatry* 6 (e902) **2016**

Smith F.W. and J. Feigon. Quadruplex structure of Oxytricha telomeric DNA oligonucleotides. *Nature* 356(6365), 164-168, **1992**

Sguizzato M., E. Esposito, M. Drechsler, E. Gallerani, R. Gavioli, P. Mariani, F. Carducci, R. Cortesi, P. Bergamini. Nafion®-Containing Solid Lipid Nanoparticles as a Tool for Anticancer Pt Delivery: Preliminary Studies. *Hindawi Journal of Chemistry,* DOI 10.1155/2017/3206298, **2017**

Sguizzato M., R. Cortesi, E. Gallerani, M. Drechsler, L. Marvelli, P. Mariani, F. Carducci, R. Gavioli, E. Esposito, P. Bergamini. Solid lipid nanoparticles for the delivery of 1,3,5-triaza-7-phosphaadamantane (PTA) platinum (II) carboxylates. *Mater Sci Eng C* 357-364, **2016**

Siekmann B., H. Bunjes, M. Koch, K. Westesen. Preparation and structural investigations of colloidal dispersions prepared from cubic monoglycerides-water phases. *Int J Pharm* (244), 33-43, **2002**

Siekmann B, and K. Westesen Submicron-sized parenteral carrier systems based on solid lipids. Pharm Pharmacol Lett (1), 123-126, **1992**

Singh R. and J.W. Jr Lillard. Nanoparticle-based targeted drug delivery. Exp Mol Pathol. 86(3), 215-223, **2009**

Sreenivasachary N. and J.M. Lehn Gelation-driven component selection in the generation of constitutional dynamic hydrogels based on guanine-quartet formation *Proc Natl Acad Sci*, (102), 5938-5943, **2005**

Sreenivasachary N. and J.M. Lehn Structural selection in G-quartet-based Hydrogels and controlled release of bioactive molecules *Chem Asian J* (3), 134-139, **2008**

Srinivasan M, H. Singh, P.A. Mueno Sodium caseinate stabilized emulsions. Factors affecting coverage and composition of surface protein. *J Agric Food Chem* (44), 3807-3811, **1996**

Tavaniotou A., J. Smitz, C. Bourgain, P. Devroey, Comparison between different routes of progesterone administration as luteal phase support in infertility treatments, *European Centers, Hum. Reprod*. Update (6) 139–148, **2000**

Teif V.B. and K. Bohinc. Condensed DNA: condensing the concepts. *Prog Biophys Mol Biol* (105), 208-222, **2011**

Vicentini F.T., T.R. Simi, J.O. del Ciampo, N.O. Wolga, D.L. Pitol, M.M. Iyomasa, M.V. Bentley, M.J. Fonseca Quercetin in w/o microemulsion: in vitro and in vivo skin penetration and efficacy against UVB-induced skin damages evaluated in vivo. *Eur J Pharm Biopharm* (69), 948-957, **2008**

Van Holde K.E. W.C. Johnson and P.S. Ho Principles of Physical Biochemistry. Prentice Hall, Upper Saddle River, N.J. ,**1998**

Zhang F., M.W.A. Skoda, R.M.J. Jacobs, R.A. Martin, C.M. Martin, F. Schreiber. Effect of Ionic strength and protein concentration for BSA in aqueous solution (111), 251-259, **2007**

Zimmermann S.B., G.H. Cohen, D.R. Davis Thestructure of helical 5'-guanosine monophosphate. *J Mol Biol* (92), 171-179, **1976**

Watson J.D. and F.H. Crick. A structure for Deoxyribose Nucleic Acids. *Nature*, **(**4056), 737-738, **1953**

Webster K.M., D.K. Wright, M. Sun, B.D. Semple, E. Ozturk, D.G. Stein, T.J. O'Brien, S.R. Shultz Progesterone treatment reduces neuroin-flammation, oxidative stress and brain damage and improves long-term outcomes in a rat model of repeated mild traumatic brain injury. *J Neuroinflamm* (12), 238, **2015**

Wichterle O and D. Lim Hydrophilic Gels for Biological Use. *Nature*, (4706), 117-118, **1960**

Whitesides G.M., J.K. Kriebel, B.T. Mayers Self-Assembly and Nanostructured Materials. In: Huck W.T.S. (eds) Nanoscale Assembly Nanostructured Science and Technology. Springer, Boston (MA) **2005**

Yeagle P.L., The structure of Biological Membranes. 2nd edition (CRC Press, Boca Raton), **2010**

Yoshimura T., K. Sengoku, R. Fujioka Pectin-based superabsorbent hydrogels crosslinked by some chemicals: synthesis and characterization. *Polym Bull* (55), 123-129, **2005**

Yu Y., D. Nakamura, K. DeBoyace, A.W. Neisius, L.B. McGown "Tunable Thermoassoclation of Binary Guanosine Gels" *J Phys Chem B* (112), 1130-1134, **2008**